



**LIBRARY  
Michigan State  
University**



EVOLUTION OF NUCLEAR SHELL STRUCTURE:  $\beta$ -DECAY AND  
ISOMERIC PROPERTIES OF NUCLEI IN AND NEAR THE  $fp$   
SHELL

By

Heather Lynn Crawford

A DISSERTATION

Submitted to  
Michigan State University  
in partial fulfillment of the requirements  
for the degree of

DOCTOR OF PHILOSOPHY

Chemistry

2010

## ABSTRACT

### EVOLUTION OF NUCLEAR SHELL STRUCTURE: $\beta$ DECAY AND ISOMERIC PROPERTIES OF NUCLEI IN AND NEAR THE $fp$ SHELL

By

Heather Lynn Crawford

One of the fundamental questions in nuclear structure science is how the nucleon single-particle energies evolve with changing proton-to-neutron ratio. The nucleon magic numbers, correctly described by the shell model near the valley of  $\beta$  stability, do not appear to be static across the nuclear landscape. The shifting energies of single-particle orbitals, resulting from variations in nucleon-nucleon interactions such as the tensor monopole interaction, lead to the erosion of some magic numbers, and the appearance of new subshell closures as the driplines are approached.

Near the borders of, and within the  $fp$  shell, relatively low single-particle level densities lead to a number of distinct regions of changing shell structure. The low-energy structure of nuclei near  $N=32$  and  $Z=20$  are stabilized by the presence of a subshell closure at  $N=32$ , a result of an energy gap between the  $\nu 2p_{3/2}$  level and the higher-lying  $\nu 2p_{1/2}$  and  $\nu 1f_{5/2}$  levels. An open question, however, is whether or not the continued upward shift of the  $\nu 1f_{5/2}$  orbital in the Ca isotopes leads to another subshell closure at  $N=34$ . At slightly higher masses, the migration of the  $\nu 1g_{9/2}$  orbital leads to the erosion of the expected  $N=40$  subshell closure, and the apparent development of a new region of deformation in the Cr, Mn and Fe isotopes. The question in this region is how quickly collectivity develops as a function of  $Z$ , as the  $\nu 1g_{9/2}$  orbital drops in energy with decreased occupancy of the proton  $1f_{7/2}$  orbital below  $Z=28$ .

The  $\beta$  decay and isomeric properties of nuclei in and on the border of the  $fp$  shell

have been studied at the National Superconducting Cyclotron Laboratory (NSCL) using the combined experimental set-up of the NSCL  $\beta$  Counting System and 16 detectors from the Segmented Germanium Array. The nuclei studied,  $^{53,54}\text{Ca}$ ,  $^{54,56}\text{Sc}$ ,  $^{50}\text{K}$ , and  $^{61}\text{Cr}$ , were produced in two separate experiments, through the fragmentation of a  $^{76}\text{Ge}$  primary beam by a  $^9\text{Be}$  target. Nuclei were implanted into a double-sided Si microstrip detector, and correlated with subsequent  $\beta$  decays on an event-by-event basis. Detection of  $\gamma$  rays in coincidence with the implant events permitted observation of  $\mu\text{s}$  isomeric states, while those detected in coincidence with decay events permitted elucidation of the populated levels in daughter nuclei.

The low-energy level structures of the neutron-rich  $^{53,54,56}\text{Sc}$  isotopes were investigated and compared with the expectations of the extreme single-particle model, as well as with more advanced shell-model calculations using the GXPF1, GXPF1A and KB3G effective interactions. The results confirm the  $N=32$  subshell closure, but suggest a compression of the  $\nu 2p_{1/2}-\nu 1f_{5/2}$  spacing relative to that assumed in current effective interactions, which may preclude formation of a  $N=34$  subshell closure in the Ca isotopes. The low-energy structure of  $^{61}\text{Mn}$  was probed through the  $\beta$  decay of  $^{61}\text{Cr}$ . The structure was investigated for signs of developing deformation, but results suggest that the effects of the approaching deformation-driving  $\nu 1g_{9/2}$  orbital are not yet significant at  $N=36$  for the Mn isotopes. The observation of an isomer in  $^{50}\text{K}$  permitted investigation of the changing shell structure just below the  $fp$  shell. The isomeric structure in  $^{50}\text{K}$  suggests that the inversion of the  $\pi 1d_{3/2}$  and  $\pi 2s_{1/2}$  orbitals which is known in  $^{47}\text{K}$  may persist above  $N > 28$ , which is at present unexpected in  $sd$ - $fp$  cross-shell interactions.

## ACKNOWLEDGMENTS

First, I want to thank my advisor, Paul Mantica. Thank you for providing the guidance, and having the patience to see me through my Ph.D. I know I sometimes made it more difficult than was necessary, but thanks for understanding that at times that was what I needed to do. You were always, as you say, my cheerleader, and I am grateful for that. Thank you for everything.

I also want to thank Dave Morrissey, Michael Thoennessen, Alexandra Gade and Abby Bickley for serving on my guidance committee, and to acknowledge NSERC of Canada for funding support.

Thank you to my  $\beta$  group-mates, Jill, Josh, and most recently Andrew and Sophia. In particular, Jill and Josh, you led the way for me, and forced me to become a better person in order to meet the standards you set. Thank you for your friendship, and for making graduate school feel more like fun than work. Thanks also to Kei and Geoff, for always being sounding boards, and gamely answering all of my random questions. Nothing that I've accomplished would have been possible without my group.

In my four years here, I've made friends I'll have for life, better friends than I deserve. Thank you for all of the happy hours, the softball (even if I was terrible!), and the random conversations over the last four years. In particular, I'd like to thank a few very good friends - you know who you are. Thank you for believing in me when I couldn't seem to believe in myself, and for pointing out the pitfalls with my umbrella factory back-up plan. You cannot know what your friendship and support has meant to me.

Finally, I have to thank my family. Mom, you wanted credit for a small piece of this work, but you deserve so much more than that. My family is my rock, and even 2301 miles away, I knew you were always right there with me. Thank you for always listening and for your blind faith in me.

# Contents

<b>List of Tables</b> . . . . .	<b>vii</b>
<b>List of Figures</b> . . . . .	<b>ix</b>
<b>1 Introduction</b> . . . . .	<b>1</b>
1.1 Nuclear shell structure . . . . .	1
1.1.1 Evolution of nuclear shell structure . . . . .	6
1.2 Describing the structure of nuclei . . . . .	9
1.2.1 Structure near closed shells . . . . .	10
1.2.2 Collective structures and nuclear deformation . . . . .	16
1.3 Experimental observation of shell closures and nuclear structure . . . . .	17
1.3.1 $E(2_1^+)$ and $B(E2 : 2_1^+ \rightarrow 0_1^+)$ in even-even nuclei . . . . .	18
1.3.2 Tracking single-particle energies and the extreme single-particle model . . . . .	20
1.4 Re-ordering of single-particle states in neutron-rich $fp$ shell nuclei . . . . .	22
1.4.1 $N=32$ and $N=34$ subshell closures . . . . .	22
1.4.2 $N=40$ shell closure and intrusion of the neutron $1g_{9/2}$ orbital . . . . .	25
1.5 Motivation for the measurement . . . . .	31
1.6 Organization of Dissertation . . . . .	32
<b>2 Experimental Techniques</b> . . . . .	<b>33</b>
2.1 $\beta$ decay . . . . .	33
2.1.1 $\beta$ -decay half-lives . . . . .	35
2.1.2 $\beta$ -delayed neutron emission . . . . .	36
2.1.3 Selection rules and $\log ft$ . . . . .	37
2.2 $\gamma$ -ray decay . . . . .	39
2.2.1 Selection rules and lifetimes . . . . .	39
2.2.2 Isomeric $\gamma$ -ray transitions . . . . .	42
2.2.3 Internal conversion . . . . .	43
2.3 Summary of the decay of exotic nuclei . . . . .	44
<b>3 Experimental Setup</b> . . . . .	<b>46</b>
3.1 Isotope production and identification . . . . .	46
3.1.1 NSCL experiment 05101 . . . . .	49
3.1.2 NSCL experiment 07509 . . . . .	50
3.2 Detector apparatus for $\beta$ -decay experiments . . . . .	52
3.3 $\beta$ Counting System . . . . .	52

3.3.1	Electronics . . . . .	55
3.3.2	BCS calibrations . . . . .	60
3.4	Segmented Germanium Array . . . . .	62
3.4.1	Electronics . . . . .	62
3.4.2	SeGA Calibrations . . . . .	64
3.5	Data analysis: Correlations and data fitting . . . . .	69
3.5.1	Implantation-decay correlations . . . . .	70
3.5.2	Decay curve fitting methods . . . . .	76
<b>4</b>	<b>Experimental Results . . . . .</b>	<b>80</b>
4.1	Low-energy structure of neutron-rich ${}_{21}\text{Sc}$ isotopes . . . . .	81
4.1.1	$\beta$ decay of ${}^{53}\text{Ca}$ to ${}^{53}\text{Sc}$ . . . . .	83
4.1.2	$\beta$ decay of ${}^{54}\text{Ca}$ to ${}^{54}\text{Sc}$ . . . . .	86
4.1.3	$\beta$ decay and isomeric structure of ${}^{54}\text{Sc}$ . . . . .	89
4.1.4	$\beta$ decay of ${}^{56}\text{Sc}$ . . . . .	97
4.1.5	Isomerism in ${}^{56}\text{Sc}$ . . . . .	104
4.2	Isomeric Structure of ${}^{50}\text{K}$ . . . . .	109
4.3	Structure of ${}^{61}\text{Mn}$ from $\beta$ decay of ${}^{61}\text{Cr}$ . . . . .	113
<b>5</b>	<b>Discussion . . . . .</b>	<b>121</b>
5.1	Interpretation of the low-energy levels in neutron-rich ${}_{21}\text{Sc}$ . . . . .	121
5.1.1	Low-energy structure of odd- $A$ ${}^{53}\text{Sc}$ . . . . .	122
5.1.2	Low-energy structure of even- $A$ Sc isotopes . . . . .	123
5.2	Re-ordering of proton single-particle states in neutron-rich K isotopes . . . . .	131
5.2.1	Systematics of the ${}_{19}\text{K}$ isotopes around $N=28$ . . . . .	131
5.2.2	Comparison to shell-model calculations using $sd$ - $fp$ cross-shell interactions . . . . .	138
5.3	Onset of collectivity in the ${}_{25}\text{Mn}$ isotopes . . . . .	139
5.3.1	Systematics in odd- $A$ Mn . . . . .	140
5.3.2	Even- $A$ Mn isotopes . . . . .	143
5.3.3	Deformation in comparison to neighboring ${}_{24}\text{Cr}$ and ${}_{26}\text{Fe}$ isotopic chains . . . . .	145
<b>6</b>	<b>Conclusions and Outlook . . . . .</b>	<b>147</b>
6.1	Conclusions . . . . .	147
6.2	Outlook . . . . .	149
6.2.1	Open questions in the $fp$ shell . . . . .	149
6.2.2	The NSCL $\beta$ Counting System with Digital Data Acquisition . . . . .	151
	<b><i>Bibliography</i> . . . . .</b>	<b>154</b>

# List of Tables

2.1	Classification of $\beta$ -decay transitions . . . . .	38
2.2	$\gamma$ -ray selection rules . . . . .	40
2.3	Weisskopf single-particle lifetime estimates for $\gamma$ decay . . . . .	42
3.1	$\gamma$ -ray Transitions Used in the Recalibration of SeGA11 . . . . .	67
4.1	$\beta$ -delayed $\gamma$ rays assigned to the decay of $^{54}\text{Sc}$ . . . . .	90
4.2	$^{56}\text{Sc}$ $\beta$ -delayed $\gamma$ rays . . . . .	98
4.3	$\beta$ and $\beta n$ contributions to the decay of $^{56}\text{Sc}$ . . . . .	104
4.4	Prompt $^{56}\text{Sc}$ $\gamma$ rays . . . . .	105
4.5	Weisskopf half-life estimates for prompt $^{56}\text{Sc}$ $\gamma$ -ray transitions . . . . .	109
4.6	$\gamma$ rays observed in coincidence with $^{50}\text{K}$ implantation events . . . . .	110
4.7	Weisskopf half-life estimates for prompt $^{50}\text{K}$ $\gamma$ -ray transitions . . . . .	113
4.8	$\beta$ -delayed $\gamma$ -ray transitions in the decay of $^{61}\text{Cr}$ . . . . .	116
5.1	Application of the Pandya transform relating neutron particle and hole states in $^{50,52}\text{Sc}$ . . . . .	126
5.2	Calculated transition probabilities for the $3_1^+ \rightarrow 4_1^+$ transition in $^{54}\text{Sc}$ . . . . .	130

# List of Figures

1.1	Observables for atomic and nuclear shell closures . . . . .	2
1.2	Evolution of the nuclear shell model . . . . .	5
1.3	Single-particle states in $^{209}_{82}\text{Pb}_{127}$ . . . . .	11
1.4	Illustration of parameters in j-j coupling . . . . .	15
1.5	Parabolic rule for p-n multiplets . . . . .	16
1.6	Systematics of $E(2_1^+)$ across isotopic chains . . . . .	19
1.7	Monopole shift of the $\nu 1f_{5/2}$ orbital with increasing $\pi 1f_{7/2}$ occupancy	23
1.8	Systematics of $E(2_1^+)$ and $B(E2 : 2_1^+ \rightarrow 0_1^+)$ across isotopic chains around $N=32, N=34$ . . . . .	24
1.9	Systematics of $E(2_1^+)$ around $Z=40, N=54$ and $N=40, Z=28$ . . . . .	27
1.10	Nilsson Diagram for $50 \geq N, Z \geq 20$ . . . . .	30
3.1	Schematic of the NSCL Coupled Cyclotron Facility . . . . .	47
3.2	Particle Identification Plots for NSCL Experiments 05101 and 07509 .	51
3.3	Schematic of the Beta Counting System Detectors . . . . .	53
3.4	Schematic of DSSD Electronics . . . . .	55
3.5	Schematic of SSSD Electronics . . . . .	57
3.6	Schematic of PIN Detector Electronics . . . . .	58
3.7	Schematic of Trigger Electronics . . . . .	59
3.8	$^{228}\text{Th}$ and $^{90}\text{Sr}$ DSSD Calibration Spectra for Illustrative Front and Back Strip . . . . .	61
3.9	Schematic of the Geometric Layout of the SeGA Detectors . . . . .	63
3.10	Schematic of Electronics for SeGA Detectors . . . . .	64

3.11	Residuals for Energy Calibration of Individual SeGA Detectors . . . . .	66
3.12	Residuals for Total SeGA Array Energy Calibration . . . . .	66
3.13	Recalibration of SeGA 11 . . . . .	68
3.14	SeGA Efficiency Calibration . . . . .	69
3.15	Position dependence of rates in NSCL experiment 07509 . . . . .	74
3.16	Comparison of $^{55}\text{Ti}$ $\beta$ -delayed $\gamma$ -ray spectra and half-life curves for analysis including pixels at the edge and over the full DSSD . . . . .	75
4.1	$\gamma$ -ray spectrum collected within 20 $\mu\text{s}$ following a $^{54}\text{Ca}$ implantation .	82
4.2	$\beta$ -delayed $\gamma$ -ray spectrum in the range 0-3 MeV following the decay of $^{53}\text{Ca}$ . . . . .	84
4.3	Decay curves for the $\beta$ decay of $^{53}\text{Ca}$ . . . . .	85
4.4	Decay scheme for decay of $^{53}\text{Ca}$ to states in $^{53}\text{Sc}$ . . . . .	86
4.5	$\beta$ -delayed $\gamma$ -ray spectrum following the decay of $^{54}\text{Ca}$ . . . . .	87
4.6	Decay curves for the decay of $^{54}\text{Ca}$ . . . . .	88
4.7	Decay scheme for the decay of $^{54}\text{Ca}$ to states in $^{54}\text{Sc}$ . . . . .	89
4.8	$\beta$ -delayed $\gamma$ -ray spectrum for the decay of $^{54}\text{Sc}$ . . . . .	90
4.9	$\beta$ -decay curves for the decay of $^{54}\text{Sc}$ , with and without the requirement of a coincident decay $\gamma$ ray . . . . .	92
4.10	Decay Scheme for the decay of $^{54}\text{Sc}$ to states in $^{54}\text{Ti}$ . . . . .	93
4.11	$\gamma\gamma$ coincidence spectra for $\beta$ -delayed $\gamma$ rays following the decay of $^{54}\text{Sc}$	94
4.12	Prompt $\gamma$ -ray spectrum following implantations of $^{54}\text{Sc}$ . . . . .	96
4.13	Decay curve for 110-keV isomeric transition in $^{54}\text{Sc}$ . . . . .	96
4.14	$\beta$ -delayed $\gamma$ -ray spectrum following the decay of $^{56}\text{Sc}$ . . . . .	98
4.15	$\gamma$ -gated decay curves for the decay of $^{56}\text{Sc}$ . . . . .	100
4.16	Decay scheme for $^{56}\text{Sc}$ to states in $^{56}\text{Ti}$ . . . . .	101
4.17	$\gamma\gamma$ coincidence spectra for the decay of $^{56}\text{Sc}$ . . . . .	102
4.18	$\gamma$ -ray spectrum following implantation of $^{56}\text{Sc}$ . . . . .	105
4.19	Decay curve for the $\gamma$ -decaying isomeric state in $^{56}\text{Sc}$ . . . . .	106
4.20	$\gamma\gamma$ coincidences for prompt $\gamma$ rays in $^{56}\text{Sc}$ . . . . .	107

4.21	Decay curves for the $\beta$ decay of $^{56}\text{Sc}$ . . . . .	108
4.22	$\gamma$ -ray spectrum following $^{50}\text{K}$ implantation events . . . . .	111
4.23	$\gamma\gamma$ coincidence spectra for isomeric decay of $^{50}\text{K}$ . . . . .	112
4.24	Proposed low-energy level scheme for $^{50}\text{K}$ . . . . .	114
4.25	Decay curve for the decay of $^{61}\text{Cr}$ to states in $^{61}\text{Mn}$ . . . . .	115
4.26	$\beta$ -delayed $\gamma$ -ray spectrum following the decay of $^{61}\text{Cr}$ . . . . .	116
4.27	Decay scheme for the decay of $^{61}\text{Cr}$ to states in $^{61}\text{Mn}$ . . . . .	118
4.28	$\gamma\gamma$ coincidence spectra for decay of $^{61}\text{Cr}$ . . . . .	119
5.1	Level structure of $^{53}\text{Sc}$ and schematic of coupling to states in $^{52}\text{Ca}$ . .	123
5.2	Experimental level scheme for $^{50,52,54,56}\text{Sc}$ . . . . .	125
5.3	Shell model calculations for the even- $A$ Sc isotopes using the GXPF1, GXPF1A and KB3G effective interactions . . . . .	127
5.4	Energy separation of the $3/2^+$ and $1/2^+$ states in the odd- $A$ K isotopes from $N=20$ to $N=30$ . . . . .	133
5.5	Known states in $^{48}\text{K}$ , and their interpretation within the independent particle model framework . . . . .	135
5.6	Low-energy structure of $^{50}\text{K}$ known from decay of the 172-keV isomeric state . . . . .	137
5.7	Comparison to shell model results for the odd- $A$ $^{25}\text{Mn}$ isotopes . . . .	142
5.8	Low-energy level structure of the even- $A$ $^{60,62,64}\text{Mn}$ isotopes . . . . .	144
5.9	$S_{2n}$ values for the isotopes surrounding Fe near $N=40$ . . . . .	145
6.1	Resolution of $^{228}\text{Th}$ spectrum collected using DDAS vs. analog data acquisition . . . . .	153

# Chapter 1

## Introduction

### 1.1 Nuclear shell structure

The periodicity in the chemical nature of the elements has been represented on the periodic table for more than a century, and is now understood with the essential concept that the electrons surrounding the atomic nucleus are arranged in discrete energy levels, or shells. One of the most direct indicators of this electron shell structure in atoms can be seen by considering the first ionization energy, the energy required to remove an electron from the neutral atom, as a function of atomic number,  $Z$ . Shown in the top panel of Fig. 1.1, the observed trend of ionization energy has discontinuities at specific values of  $Z$ . These discontinuities are understood as arising from the underlying electron shell structure. After filling a given energy orbital, the next electron is placed in a higher energy orbital, and the energy required to remove it decreases substantially.

Analogous to the observed trend in atomic ionization energies, systematic examination of many physical properties of nuclei has revealed periodic trends. Near the valley of stability, bulk properties related to the nuclear mass are suggestive of enhanced relative stability for nuclei with “magic” numbers of protons or neutrons, corresponding to 2, 8, 20, 28, 50, 82, and 126. One can consider, for instance, the one-

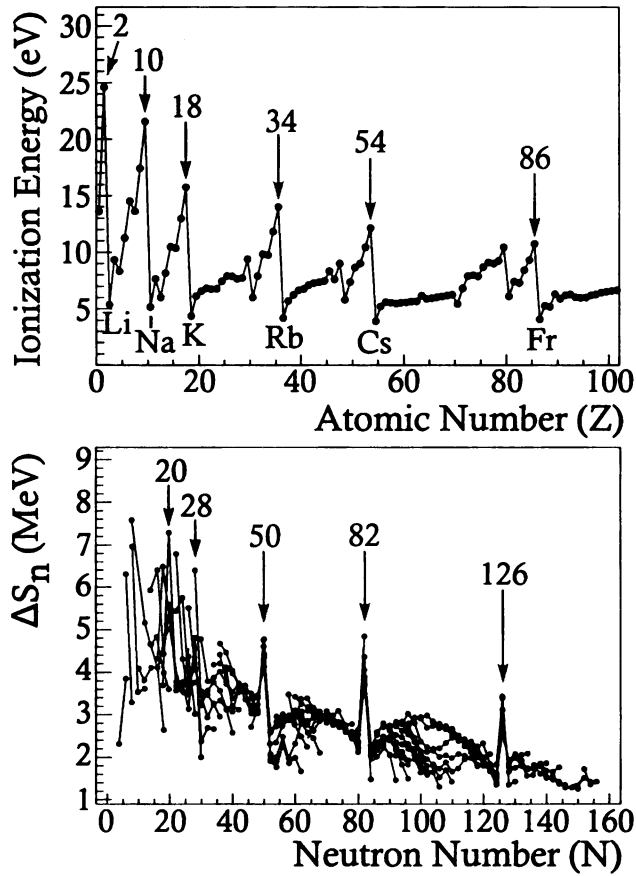


Figure 1.1: (Top) Systematics of the first ionization energies of the atomic elements from hydrogen ( $Z=1$ ) to nobelium ( $Z=102$ ). Data were taken from Ref. [1]. Discontinuities correspond to atomic electron shell closures. (Bottom) Systematics of the difference in neutron separation energy for even-even nuclei  ${}^A_Z X_N$  and their even-odd neighbors. Data were taken from Ref. [2]. Solid lines connect isotopic chains. Discontinuities provide evidence for nuclear shell structure, representing closed neutron shells.

neutron separation energy for a nucleus with mass number  $A$ , and atomic number  $Z$ , which is defined as follows:

$$\begin{aligned}
 S_n(N) &= B({}^A_Z X_N) - B({}^{A-1}_Z X_{N-1}) \\
 &= [M({}^{A-1}_Z X_{N-1}) - M({}^A_Z X_N) + M_n]c^2.
 \end{aligned}
 \tag{1.1}$$

Here,  $B({}_Z^AX_N)$  represents the nuclear binding energy,

$$B({}_Z^AX_N) = [ZM_H + NM_n - M({}_Z^AX_N)]c^2, \quad (1.2)$$

where  $M_H$  is the atomic mass of hydrogen,  $M_n$  is the neutron mass,  $M({}_Z^AX_N)$  is the atomic mass of the given nucleus, and contributions from the differences in the electron binding energies are neglected. The neutron separation energy is analogous to the atomic ionization energy, representing the energy required to remove one neutron from the nucleus. The systematics of the neutron separation energy show periodicity suggesting an underlying shell structure of the nucleus. These shell effects are enhanced by considering the difference in  $S_n$  values between even  $N$  nuclei and their  $N + 1$  neighbors, defined as follows:

$$\begin{aligned} \Delta S_n &= S_n(N) - S_n(N + 1) \\ &= [M({}^{A-1}_ZX_{N-1}) + M({}^{A+1}_ZX_{N+1}) - 2M({}_Z^AX_N)]c^2. \end{aligned} \quad (1.3)$$

The neutron separation energy differences,  $\Delta S_n$ , are plotted in the bottom panel of Fig. 1.1 as a function of neutron number for the isotopes with even numbers of protons and neutrons up to fermium ( $Z=100$ ). The discontinuities corresponding to neutron ‘magic numbers’ are apparent; an analogous examination of proton separation energy systematics similarly highlights the same ‘magic numbers’ for protons.

Given the success in describing atomic structure in terms of electron shells, a similar approach has been employed in nuclear physics to describe the structure of nuclei. However, in the atomic case, electrons move in an “external” field created by the well-understood Coulomb force. As such, the Schrödinger equation for the atomic system can be solved exactly, and electron orbital energies accurately calculated, reproducing the experimentally observed shell closures. The picture is more complicated in the nuclear case, as nucleons move within a field created by the surrounding nucleons,

and the analytical form of the force involved, namely the strong force, is not defined at present [3].

The success of the nuclear shell model rests primarily with the choice of the potential assumed to confine the protons and neutrons within the nucleus. Historically, a starting point has been the harmonic oscillator potential. The energy levels arising from the solution of the Schrödinger equation assuming a harmonic oscillator potential are shown in Fig. 1.2(a). This simple potential reproduces the lowest shell closures, at 2, 8 and 20, however, the higher closures are not in agreement with observation. A more realistic potential, bounded at  $r=R$ , is considered to provide a better approximation.

The Woods-Saxon potential has a shape intermediate between a square well and a harmonic oscillator, and takes the form

$$V(r) = \frac{-V_0}{1 + \exp\left[\frac{(r-R)}{a}\right]}, \quad (1.4)$$

where the parameter  $R$  is the mean nuclear radius,  $a$  represents the diffuseness of the nucleus, and  $V_0$  is the depth of the potential well, usually adjusted to a value of approximately 50 MeV. Solution of the Schrödinger equation assuming this potential again reproduces the lowest shell closures at 2, 8 and 20 but still fails to accurately describe the higher lying magic numbers [see Fig. 1.2(b)].

The missing piece of the puzzle was put in place in the 1940's, when the inclusion of a spin-orbit potential was shown to properly separate subshells and reproduce the experimentally observed magic numbers [5,6]. The spin-orbit potential takes the form:

$$V_{so} = V_{so}(r)\vec{l} \cdot \vec{s}, \quad (1.5)$$

where  $\vec{l}$  represents the orbital angular momentum, and  $\vec{s}$  the intrinsic nucleon spin. The  $\vec{l} \cdot \vec{s}$  term accounts for the interaction of the nucleon spin and its orbital motion,

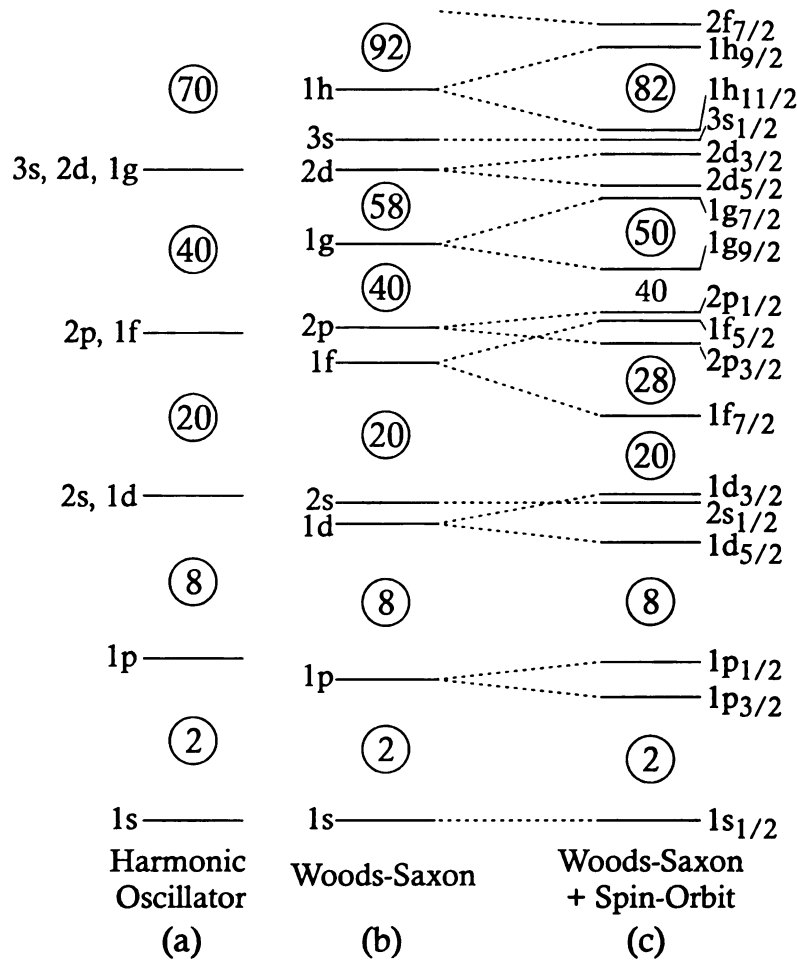


Figure 1.2: Evolution of the nuclear shell model to represent the experimentally observed nucleon “magic” numbers. The first approximation with a harmonic oscillator potential evolved to the more physical Woods-Saxon potential, and finally the inclusion of a spin-orbit potential to reproduce the experimental observations. Figure adapted from Ref. [4].

and leads to a removal of the  $l$ -degeneracy of states, or a splitting of states with  $l > 0$ , based upon the total angular momentum ( $\vec{j} = \vec{l} + \vec{s}$ ) projection. This reordering of the subshell states is shown in Fig. 1.2(c), and the shell closures that develop agree fully with observations of the magic numbers near the valley of  $\beta$  stability.

The nuclear shell model has been further developed and extended to include more subtle aspects of nuclear structure. The basic tenets discussed here, which assumes a spherically symmetric potential, remains the starting point for understanding the level

structures of spherical nuclei near closed shells. However, recent experimental evidence suggests that the shell structure of nuclei, i.e. the ordering and energy separation of single-particle states, is not static across the nuclear landscape, but rather evolves with varying proton-to-neutron ratios. The nature and origins of this re-ordering of single-particle states is the topic of the following section.

### 1.1.1 Evolution of nuclear shell structure

Across the nuclear chart, as progressively more exotic nuclei are probed, there is increasing evidence for an evolution of shell structure. The ordering of single-particle levels as shown in Fig. 1.2(c) has been observed to change slightly with proton-to-neutron ratio, or isospin projection,  $T_z = (N - Z)/2$ , which can change the observed nuclear properties.

At  $Z=4$ , in the relatively light isotopes, breakdown of the  $N=8$  shell closure has been observed in the neutron-rich nucleus  $^{12}_4\text{Be}$  [7]. The last two neutrons in  $^{12}\text{Be}$  are expected to occupy the  $1p_{1/2}$  orbital. However, spectroscopic factors for the removal of a neutron from  $^{12}\text{Be}$  provide direct evidence of significant  $sd$ -shell intruder contributions to the ground state wavefunction, and the disappearance of the  $N=8$  shell closure in this isotope. At slightly heavier masses, the so-called ‘island of inversion’ at  $N=20$  away from stable nuclei, also gives evidence of evolving shell structure. Nuclear ground states have been shown to be dominated by  $\nu(sd)^{-2}(fp)^2$  intruder configurations, suggesting the breakdown of the  $N=20$  shell closure [8, 9] for neutron-rich nuclei with  $10 \leq Z \leq 12$  and  $20 \leq N \leq 22$ . Shell evolution is also seen in the apparent erosion of the  $N=28$  shell closure in the neutron rich  $^{16}\text{S}$  isotopes [10], and the development of a new subshell closure in neutron-rich  $^{20}\text{Ca}$  [11, 12],  $^{22}\text{Ti}$  [13] and  $^{24}\text{Cr}$  [14] isotopes at  $N=32$ . At even higher masses, however, the shifting of single-particle levels is less likely to result in a change in the position of the major shell closures, due to the higher single-particle level densities. None the less, the evolution still occurs – in the region of  $N=50-82$ , and  $Z=40-50$  there is a reordering

of neutron single-particle levels as the  $1g_{7/2}$  orbital rapidly drops in energy between  $^{91}\text{Zr}$  and  $^{131}\text{Sn}$  [15, 16].

These examples highlight the ubiquity of evolving shell structure over the nuclear landscape. It is clear from these instances that there are effects and interactions beyond the scope of the simple shell model which can greatly alter single-particle level energies and ordering. Understanding the origins of and accounting for experimentally observed changes in shell structure are critical for the development of nuclear theory models – an understanding of the phenomena already observed will enhance the reliability of theoretical predictions. One nucleon-nucleon interaction, believed to be a possible cause of shell evolution, is discussed next.

### **Proton-neutron monopole interaction**

One of the suggested reasons for the evolution of nuclear shell structure is the spin-isospin dependent part of the nucleon-nucleon interaction [17]. This is a tensor monopole force, which is additional to the spin-orbit interaction discussed previously, and can alter the effective nucleon single-particle energies (ESPEs). These ESPEs account for the mean effects from all other nucleons, on a nucleon in a given single-particle orbital.

The single-particle energy of an orbital  $j$  is determined by its kinetic energy, and the interaction with the nucleons in the core that produce the mean field [18]. When nucleons are added to a different orbit  $j'$ , the single-particle energy of the original  $j$  orbital is altered. The nucleons in  $j'$  and  $j$  will couple to form states with different total angular momentum,  $J$ , but in considering changing shell structure, it is the shift of single-particle orbitals irrespective of the details of the coupled  $J$  states that is interesting. Thus, the  $J$  dependence is averaged out, and only monopole effects are considered. The monopole component of a nucleon-nucleon residual interaction  $V$  for the effect of the nucleons in  $j'$  on the orbital  $j$  takes the form:

$$V_{jj'}^T = \frac{\sum_J (2J+1) \langle jj' | V | jj' \rangle_{JT}}{\sum_J (2J+1)}, \quad (1.6)$$

where  $\langle jj'|V|jj' \rangle_{JT}$  is the matrix element for  $j$  and  $j'$  coupling to a state with spin  $J$ , and isospin  $T$ . With this interaction, it is possible to evaluate, for example, the effect of  $n_n(j')$  neutrons in the orbital  $j'$  on the single particle energy of the proton orbital  $j$ . The shift in the single-particle energy of the proton orbital  $j$ , denoted  $\Delta\epsilon_p(j)$ , resulting from the presence of  $n_n$  neutrons in the  $j'$  orbital is given by [18]:

$$\Delta\epsilon_p(j) = \frac{1}{2}[V_{jj'}^{T=0} + V_{jj'}^{T=1}]n_n(j'). \quad (1.7)$$

With the inclusion of the tensor monopole shift, a new effective single-particle energy can be defined, which is dependent on the nucleon configuration, and thus changes with proton-neutron ratio. The same arguments hold for the inverse case, the effect of protons in a given orbital on neutron single-particle energies. It should be noted that protons (neutrons) in an orbital  $j$  will also affect the energy of protons (neutrons) in another orbital  $j'$ . However, only  $T = 1$  interactions, which are weaker than  $T = 0$  interactions [18], are relevant in proton-proton or neutron-neutron interactions. Thus, these effects are less significant than those arising from proton-neutron interactions.

As discussed by Otsuka *et al.* [18], there is a general rule for the way in which the proton-neutron tensor monopole force affects the single-particle energies. An attractive interaction is observed between opposite isospin particles (protons and neutrons) in  $j_{<} = l - 1/2$  and  $j'_{>} = l' + 1/2$  orbits (and vice versa,  $j_{>} = l + 1/2$  and  $j'_{<} = l' - 1/2$  orbits), while the interaction between protons and neutrons in  $j_{<} = l - 1/2$  and  $j'_{<} = l' - 1/2$  orbits (and similarly  $j_{>} = l + 1/2$  and  $j'_{>} = l' + 1/2$  orbits) is repulsive. The strength of the interaction is also maximized for  $l \sim l'$ , so a stronger attractive interaction between protons and neutrons in spin-orbit coupling partner orbitals is expected [17].

Nearly all of the examples of evolving nuclear shell structure discussed previously can be partially explained in the framework of the proton-neutron tensor monopole interaction. The disappearing  $N=8$  shell closure in  $^{12}_4\text{Be}$  results from the low occu-

pancy of the  $\pi 1p_{3/2}$  orbital that causes the  $\nu 1p_{1/2}$  orbital to migrate higher in energy, eroding the  $N=8$  gap. The island-of-inversion nuclei can be largely explained by the decreasing attractive interaction between the  $\nu 1d_{3/2}$  orbital and the  $\pi 1d_{5/2}$  orbital as protons are removed from the  $\pi 1d_{5/2}$  level. This reduction causes the  $\nu 1d_{3/2}$  orbital to rise in energy, eroding the  $N=20$  shell closure, and producing a  $N=16$  subshell closure for the lightest nuclei in the region. The region surrounding  $N=34$ ,  $Z=20$  also experiences changes in neutron level ordering driven largely by a reduced monopole interaction between the  $\pi 1f_{7/2}$  orbital and the  $\nu 1f_{5/2}$  orbital, while the heavier nuclei near  $N=50$  show evidence of shell evolution arising from the changing monopole interaction between the  $\pi 1g_{9/2}$  orbital and the spin-orbit partner  $\nu 1g_{7/2}$  orbital.

## 1.2 Describing the structure of nuclei

While one of the goals of nuclear science is to create a single theoretical framework to adequately describe the entire nuclear landscape, the variation in nuclear structure across the chart of the nuclides is significant. The nuclear shell model provides a basis for understanding the overall structure of all nuclei, but important simplifications can be made in certain regions of the nuclear chart. The most basic shell model interpretation, the independent particle model, provides an excellent qualitative description of the low-lying states in nuclei one nucleon from closed shells [19]. A few nucleons from a closed shell, this model can be extended, and residual nucleon-nucleon interactions taken into account, to successfully describe the low-energy structure of nuclei. However, for nuclei far from closed shells, these types of microscopic shell model calculations become intractable. Geometric models provide a better description of the growing collective behavior of mid-shell nuclei, as macroscopic deformations play an increasingly important role in determining the relevant nuclear structure.

## 1.2.1 Structure near closed shells

### The independent particle model

The so-called “independent particle model” describes a nucleus in terms of non-interacting particles orbiting within a central spherically symmetric potential, which is itself produced by all the nucleons. Within this model, nucleons are assumed to sequentially fill the single-particle levels generated by this nuclear potential, in much the same way that electrons are assumed to fill atomic energy levels. Also in analogy to the atomic picture of valence, in which filled electron shells do not contribute to the chemical properties of an element, filled nucleon orbitals are assumed to be inert within the structure of the nucleus. A closed shell will always contribute a total angular momentum and parity,  $J^\pi = 0^+$  in the nuclear case, and so the ground state angular momentum of a nucleus with only one valence particle in a shell  $nlj$  is determined entirely by the single valence nucleon as  $J=j$ , with parity  $\pi=(-1)^l$  [19].

The independent particle model provides a framework for predicting the ground state spin and parity of nuclei one nucleon removed from a closed shell, and has also proven successful in predicting the low-lying excited states in these nuclei. Low-energy levels in such nuclei are formed by simply elevating the valence particle from the ground state orbital to a higher single-particle state. An example of the success of this approach can be found in the structure of  $^{209}_{82}\text{Pb}_{127}$ , as shown in Fig. 1.3. With one valence neutron above the  $N=126$  shell closure, the ground state in  $^{209}\text{Pb}$  is observed to have  $J^\pi=9/2^+$ , as expected with a  $(\nu 2g_{9/2})^1$  configuration. The other six levels corresponding to promotion of the single valence neutron to the other single-particle levels above the  $N=126$  shell closure are all evident in the low-energy structure [see Fig. 1.3(b)]. The neutron spectroscopic factor is near unity for each of these seven states. The spectroscopic factor is a measure of the contribution of a given single-particle configuration to a nuclear state, as determined by comparison of experimental reaction cross-sections with calculations assuming pure single-particle con-

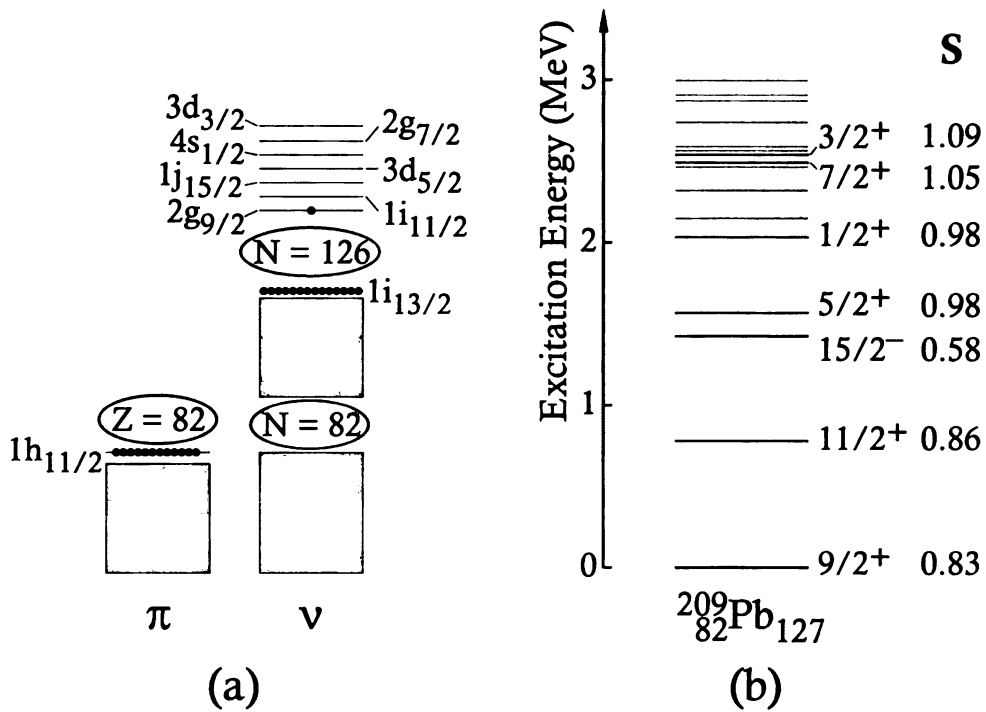


Figure 1.3: (a) Schematic representation of the nucleon configuration for the one-valence neutron nucleus  $^{209}\text{Pb}$ . (b) Experimentally observed levels of  $^{209}\text{Pb}$  below 3 MeV [2]. Black levels correspond to single-particle states arising from occupation of the seven single-particle levels above the  $N=126$  shell gap. The purity of these single particle configurations is supported by the near-unity spectroscopic factors. Grey levels correspond to levels with configurations beyond the scope of the independent particle model.

figurations [20]. Thus, spectroscopic factors near 1 indicate the relative purity of the single-particle states in  $^{209}\text{Pb}$ .

Strictly speaking, the independent particle model is applicable only to nuclei with one valence particle (or hole) outside of a closed shell. However, the fundamental ideas of this model can be extended to nuclei with a few valence particles (or holes) outside of a closed shell inert core. The low-energy structures of such nuclei can be understood by including a residual nucleon-nucleon interaction between valence nucleons above the inert core.

## Few nucleon configurations

A few nucleons outside of a shell closure, the independent particle model can be extended to provide an adequate description of the low-energy states within a nucleus. The simplified idea of the nucleus as consisting of valence nucleons occupying single-particle states above an inert core of closed shells provides a basis for interpreting the structure solely in terms of the interactions among valence particles. However, with more than one valence particle, it is important to consider the residual nucleon-nucleon interaction, which largely determines the observed structure of few-nucleon systems.

Two nucleons occupying orbitals with quantum number  $n_1 l_1 j_1$  and  $n_2 l_2 j_2$  can couple, in the most general case, to produce a multiplet of states with  $|j_1 - j_2| \leq J \leq |j_1 + j_2|$ . If the nucleons are identical and occupy the same orbital, the requirement of an antisymmetric wavefunction limits  $J$  to values from 0 to  $(2j-1)$ , and without a residual nucleon-nucleon interaction, all  $J$  states in a multiplet are expected to be degenerate in energy. Under the effect of a residual interaction,  $V_{12}$ , this degeneracy is broken, and each state  $J$  experiences an energy shift  $\Delta E(j_1 j_2 J)$ , given by [19]:

$$\Delta E(j_1 j_2 J) = \frac{1}{\sqrt{2J+1}} \langle j_1 j_2 J || V_{12} || j_1 j_2 J \rangle, \quad (1.8)$$

where the double-bar indicates summation over all  $M$  states.

The exact form of the residual nucleon-nucleon interaction,  $V_{12}$ , is not known, although it is expected to have a strong attractive short-range component, as well as a long-range component which is of particular importance in producing collective nuclear properties [19]. One example of a commonly used interaction is the so-called ‘pairing plus quadrupole’ interaction, which takes the following form:

$$V_{ppq} = V_{pair} + \kappa r_1^2 r_2^2 P_2(\cos \theta), \quad (1.9)$$

where  $\theta$  represent the angle between the radius vectors to each particle ( $\vec{r}_1$  and  $\vec{r}_2$ ), and  $\kappa$  represents the strength of the quadrupole interaction.  $V_{pair}$  represents the short-range attractive pairing interaction, while the quadrupole component is a first approximation to the long-range component. An even simpler approximation for the residual nucleon-nucleon interaction is a simple delta-function interaction, which only represents the short-range interaction and has been shown to reproduce many of the results from more realistic interactions. The relative spacing of states within proton-proton (p-p) or neutron-neutron (n-n) multiplets, for example, can be well-described by assuming a delta-function residual interaction. Taking the form of the residual interaction to be  $V_{12} = V_0\delta(\vec{r}_1 - \vec{r}_2)$ , where  $\vec{r}_1$  and  $\vec{r}_2$  are the radial coordinates of the two nucleons, and  $V_0$  is the strength of the interaction, Eqn. 1.8 becomes [19]:

$$\begin{aligned} \Delta E(j_1 j_2 J) &= -V_0 F_R(2j_1 + 1)(2j_2 + 1) \begin{pmatrix} j_1 & j_2 & J \\ \frac{1}{2} & \frac{-1}{2} & 0 \end{pmatrix}^2 \text{ if } l_1 + l_2 - J \text{ even} \\ &= 0 \text{ if } l_1 + l_2 - J \text{ odd,} \end{aligned} \quad (1.10)$$

where  $F_R$  is a function of the radial coordinates (i.e.  $n_1 l_1 n_2 l_2$ ) only. Thus, only half of the states in a given p-p or n-n multiplet will be shifted under the influence of a delta-function residual interaction. Further information can be gained by considering that the isospin portion of the nuclear wavefunction for a p-p/n-n configuration is symmetric ( $T=1$ ), which means that the Pauli principle requires the wavefunction to be antisymmetric in either spin or space. A symmetric spin configuration  $S=1$  thus requires the spatial wavefunction to be antisymmetric. However, a delta-function interaction between two nucleons vanishes if  $\vec{r}_1 \neq \vec{r}_2$ , and so will not alter the energy of states with  $S=1$ , and will only affect  $S=0$  states. Given that only half of the states of a p-p or n-n multiplet will be affected by a delta-function residual interaction, as indicated from Eqn. 1.10, a general rule arises describing the splitting of energy levels in p-p and n-n multiplets. If the parity is positive, even  $J$  value are lowered in energy,

with the extreme  $J$  value ( $J_{min} = |j_1 - j_2|$  or  $J_{max} = |j_1 + j_2|$ ) lowered the most, while for negative parity, odd  $J$  values are lowered. If  $j_1 = j_2$ , as in the case of even-even nuclei, the parity of the expected states is positive, and this interaction results in a dramatic lowering of the  $0^+$  state. This interaction is, in fact, the underlying explanation in this model for the fact that even-even nuclei have  $0^+$  ground states [19].

The residual interaction in p-p/n-n multiplets is restricted to  $T=1$  interactions, which simplifies the possible effects of the residual interaction on the relative spacing of states in a multiplet. Proton-neutron (p-n) multiplets however can also include  $T=0$  interactions, which have been observed to be stronger than the  $T=1$  interactions [19]. Thus, a different approach is more appropriate for describing the energy splitting of states within a p-n multiplet under the effect of the nucleon-nucleon residual interaction. Insight into the effect of a residual interaction on the relative ordering of low-lying levels in few nucleon systems can be gained by considering a multipole decomposition of the interaction. Any interaction that depends on the separation between two particles, as the residual interaction is expected to, can be expanded in terms of multipoles [19]. Such a decomposition allows, among other important results, the derivation of the parabolic rule [21] to describe the energies of states in two particle p-n multiplets.

Within a decomposition, each multipole,  $k$  has an angular dependence,  $P_k(\cos \theta)$ , where  $P_k(x)$  are the Legendre polynomials, and  $\theta$  is the angle between the angular momentum vectors for each particle, as shown in Fig. 1.4, and given by the following:

$$\cos \theta = \frac{J(J+1) - j_1(j_1+1) - j_2(j_2+1)}{2\sqrt{j_1(j_1+1)j_2(j_2+1)}}. \quad (1.11)$$

The monopole component,  $k=0$ , is constant, and thus affects all states equally, simply giving an overall energy shift to the entire multiplet of states. This monopole interaction is in fact the same effect discussed previously in Section 1.1.1.

The quadrupole component,  $k=2$ , is proportional to  $P_2(\cos \theta) = \frac{1}{2}(3 \cos^2 \theta)$ , and is

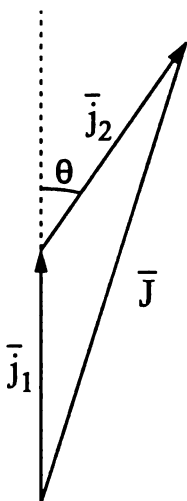


Figure 1.4: Schematic representation of the coupling of two nucleon angular momenta ( $j_1, j_2$ ) values in a geometric representation to a final  $J$ , and the definition of the angle  $\theta$  between them.

maximized for  $\theta = 0^\circ$  and  $180^\circ$ , which corresponds to the alignment or antialignment of the angular momentum vectors of the two constituent particles. Thus, the attractive particle-particle quadrupole interaction lowers the energies of extreme  $J$  values the most, and raises intermediate spins. The  $J$  dependence on the energy splitting between states in a given p-n multiplet is given by the following expression [19], which arises from the  $P_2(\cos \theta)$  proportionality of the  $k=2$  multipole combined with Eqn. 1.11 for the angle  $\theta$ :

$$\begin{aligned} \Delta E(j_1 j_2 J) &\propto \frac{[J(J+1) - j_1(j_1+1) - j_2(j_2+1)]^2}{4j_1(j_1+1)j_2(j_2+1)} \\ &\propto A[J(J+1)]^2 + BJ(J+1) + C, \end{aligned} \quad (1.12)$$

where  $A$ ,  $B$  and  $C$  are independent of  $J$ . This relationship takes the form of a parabola in  $J(J+1)$ , and despite the omission of higher multipoles of the residual interaction, has been shown to provide a good first approximation to experimental data. Figure 1.5 illustrates the parabolic rule applied to the proton-neutron ( $\pi g_{7/2}^1 \nu h_{11/2}^1$ ) multiplet in  $^{122}\text{Sb}$ , and the proton-neutron hole ( $\pi f_{7/2}^1 \nu f_{7/2}^{-1}$ ) multiplet in  $^{48}\text{Sc}$ . The multiplet

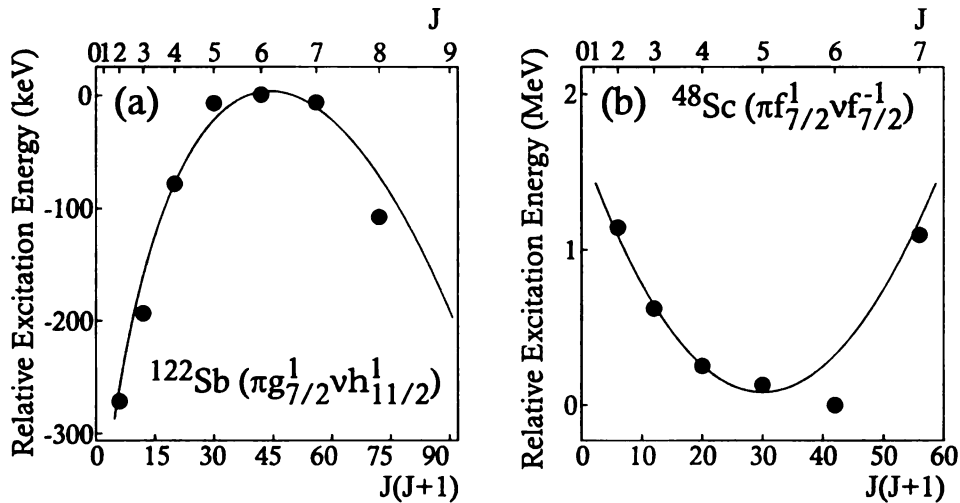


Figure 1.5: Examples of the qualitative success of the parabolic rule describing the level ordering of p-n multiplets. (a) illustrates the p-n particle-particle parabola in  $^{122}\text{Sb}$  [22], while (b) illustrates the p-n particle-hole parabola in  $^{48}\text{Sc}$  [23]. Dots represent experimentally measured energies, while the solid line is a best fit parabola.

under consideration in the case of  $^{48}\text{Sc}$  is actually a particle-hole p-n multiplet. The residual interaction in this case is repulsive, and thus the extreme  $J$  values corresponding to high p-n overlap are pushed higher in energy, while the intermediate spins are lowered.

Moving beyond the case of two valence particles, within the single-particle model it can be assumed that nucleons in a partially filled single-particle orbital will pair to  $J^\pi=0^+$  where possible [19]. Under this assumption the low-lying states of any nucleus near a closed shell can be interpreted, in the independent particle model, as arising from either a single valence nucleon configuration, or a p-n multiplet outside a core of fully paired nucleons.

## 1.2.2 Collective structures and nuclear deformation

The description of nuclei that are more than a few nucleons away from closed shell configurations becomes progressively less practical purely within the shell model framework. These calculations rapidly become intractable for mid-shell nuclei due to the

large numbers of valence nucleons. Additionally, the simplifications made by assuming inert closed shell cores become less appropriate. Significantly more complex excitations develop in these nuclei, which are better described in a more macroscopic framework [19].

Collective interactions between nucleons typically lead to quadrupole (oblate or prolate) deformation of the overall shapes of mid-shell nuclei. The extent of deformation is denoted by a quadrupole deformation parameter,  $\beta_2$ .  $\beta_2 = 0$  in the case of spherical nuclei, while this deformation parameter takes on positive values for prolate deformations, and negative values for oblate deformation. Models which attempt to describe deformation of the nuclear shape, such as the Nilsson model, provide a framework in which to understand the structures of such deformed mid-shell nuclei. The Nilsson model is, in many ways, similar to the spherical shell model discussed earlier, but follows the variation of the energies of the spherical shell-model orbitals in a deformed nuclear potential – it is the single-particle model applicable to deformed nuclei [19].

While the previous sections have discussed a theoretical framework for understanding the structure of nuclei near shell closures, the shell-model framework requires knowledge of the location of shell closures, and the ordering of single-particle states. The following section discusses some of the experimental observables which can provide such information.

### **1.3 Experimental observation of shell closures and nuclear structure**

One of the most critical pieces of information needed to allow development of nuclear structure models and theory is the location of shell and subshell closures across the nuclear landscape. As discussed previously, the location of shell closures is not static across the nuclear chart, and an ongoing experimental focus in nuclear physics is to

locate these shell closures in previously unknown nuclei, and track the migration of single-particle orbitals which lead to this dynamic shell structure.

A number of experimental observables are sensitive to the presence of shell closures across the nuclear landscape. Nuclear masses and binding energies provide the most fundamental mapping of structural evolution across the nuclear landscape. Changes in the trends of neutron-separation energies across isotopic chains, for example, can indicate the presence of neutron shell closures, or the development of deformation, depending on the nature of the observed change. Ground state nuclear moments are also good indicators of shell closures. The nuclear quadrupole moment provides a measure of the nuclear charge distribution, and thus the nuclear shape. Near closed shells, nuclei are expected to be spherical, and ground state quadrupole moments should be small. Away from shell closures, nuclei may be axially deformed, and have large magnitude quadrupole moments. Another indicator for shell closures comes from the excited states of nuclei. Certain characteristics of excited state configurations are expected near closed shells, and such states can be used to identify shell closures, when compared with the systematic behavior in neighboring nuclei. The properties of the first  $2^+$  excited state in even-even nuclei, for instance, are sensitive to the presence of shell closures, as is discussed in the following section.

### 1.3.1 $E(2_1^+)$ and $B(E2 : 2_1^+ \rightarrow 0_1^+)$ in even-even nuclei

Across the nuclear landscape, there are certain pervasive structural patterns that emerge – the near-spherical shape of nuclei near closed shells and the dominance of quadrupole collective nucleon excitations near midshell, for instance. Thus, experimental quantities that are related to the amount of quadrupole collectivity can be good probes of nucleon shell closures. One such measure of quadrupole collectivity in even-even nuclei is the energy of the first  $2^+$  excited state,  $E(2_1^+)$ . The first  $2^+$  excited state in an even-even nucleus is understood as arising from the breaking of a pair of nucleons and excitation of one nucleon of the pair into a higher-lying level. At closed

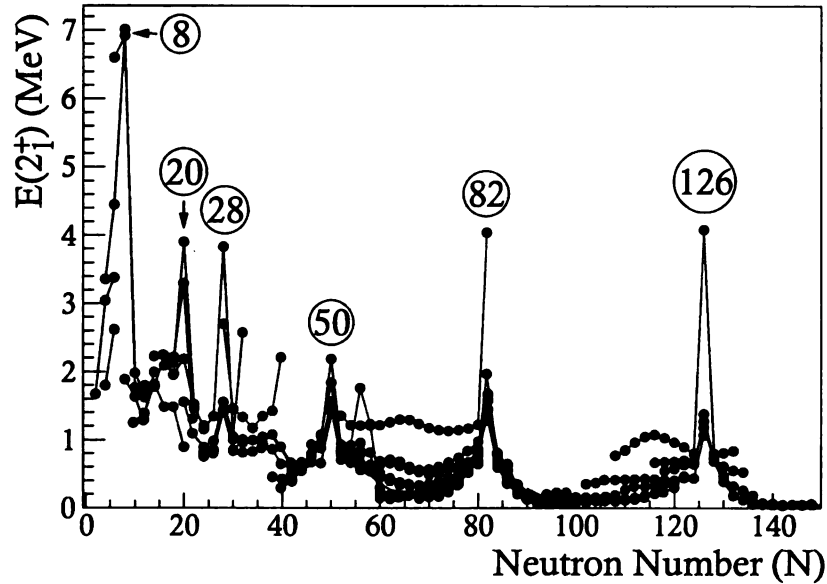


Figure 1.6: Behavior of  $E(2_1^+)$  across isotopic chains. Data were taken from Ref. [25]. Solid lines connect isotopic chains. The trend of increased values of  $E(2_1^+)$  near neutron closed shells is very clear; a similar trend is seen for  $E(2_1^+)$  along isotonic chains for closed proton shells. The same magic numbers seen in the variation of the neutron separation energies in Fig. 1.1 are apparent.

shells there is an observed peak in  $E(2_1^+)$  relative to neighboring nuclei. This reflects the fact that the energy required to break a pair of nucleons and promote one across a shell gap would be significant, while away from the shell closures, multi-state mixing lowers the collective quadrupole states [24]. Macroscopically the curvature of the potential energy surface is lessened, deformation requires less energy, and the energy of the first  $2^+$  state is reduced. Thus, the value of  $E(2_1^+)$  in even-even nuclei, relative to the neighboring even-even nuclei is a good indicator of nuclear shell structure and shell closures. Figure 1.6 illustrates the systematic variation of  $E(2_1^+)$  for even-even nuclei across the nuclear chart, and the appearance of the characteristic peaks in this quantity at closed shells.

Based on the observed trends in the energy of the first  $2^+$  state in even-even nuclei, Grodzins [26, 27] derived an empirical relation some time ago between  $E(2_1^+)$

and the quadrupole deformation parameter  $\beta_2$ :

$$E(2_1^+) = \frac{1225}{A^{7/3}\beta^2} \text{ MeV.} \quad (1.13)$$

At closed shells,  $E(2_1^+)$  values are high, and according to Eqn. 1.13,  $\beta_2$  is small, indicating the near-spherical nature of magic nuclei. Moving away from closed shells,  $\beta_2$  increases as  $E(2_1^+)$  drops, representative of the increasing collectivity and developing deformation of mid-shell nuclei.

A related indicator of quadrupole collectivity, and hence shell closures, in the nuclear chart is the reduced transition matrix element for the E2 transition between the first  $2^+$  excited state and the  $0^+$  ground state in even-even nuclei,  $B(E2 : 2_1^+ \rightarrow 0_1^+)$ . With an inverse relation to the energy of the first excited  $2^+$  state according to the Grodzins rule [26], the  $B(E2 : 2_1^+ \rightarrow 0_1^+)$  value peaks near midshell, and reaches minimum values near closed shells. These two quantities,  $E(2_1^+)$  and  $B(E2 : 2_1^+ \rightarrow 0_1^+)$  are among the most readily accessible in nuclei far from stability. Trends observed in these two independently measured values have served as indicators for shell closures at the far reaches of the nuclear chart (e.g. [13,14,28]).

### 1.3.2 Tracking single-particle energies and the extreme single-particle model

Tracking the evolution of nucleon single-particle energies requires more information than simply the location of shell gaps in the nuclear chart. It is desirable to have a measure of the changing single-particle energies between closed shells. This involves not only identifying states within a nucleus, but also determining the nucleon configurations that contribute to these states. Elucidation of the contributing configurations permits a better appreciation of the shifting single-particle energies that lead to the observed nuclear structure.

One method to obtain information on the wavefunctions contributing to nuclear

states is analysis of nucleon transfer reactions. Stripping reactions and the inverse, nucleon pickup reactions, are direct reactions which are constrained to the nuclear surface, and thus excite specific and limited nucleon degrees of freedom. The cross-sections for such reactions are dominated by the wavefunctions of the transferred nucleons [29]. This property makes single-particle transfer reactions uniquely powerful in characterizing the single-particle character of a nuclear state. Cross-section measurements can be compared to expectations assuming single-particle configurations, and experimental spectroscopic factors can be extracted [30]. These spectroscopic factors provide a measure of the single-particle character of nuclear states, as was mentioned above in the case of  $^{209}\text{Pb}$  (see Fig. 1.3).

While other techniques, including  $\beta$  decay, do not provide access directly to the wavefunctions of nuclear states, information regarding parentage of states can be accessed indirectly by taking advantage of the predictions of the single-particle shell model. Within the framework of this model the spin and parity of the ground state should be representative of the single-particle orbital occupied by the last unpaired nucleon(s). The extreme single-particle model can be extended and predicts certain multiplet configurations corresponding to specific combinations of single-particle levels for nuclei with two unpaired nucleons. The spin, parity and relative energy of low-lying nuclear states can provide guidance for assignment of states as probable members of specific multiplets, and thus insight into the configuration leading to the states. While these inferences are not as robust as the spectroscopic factors from transfer reactions, such interpretations can serve as first steps in understanding the underlying nuclear structure, and relative single-particle energies. It is possible, in this way, to qualitatively track the relative ordering of single-particle orbitals. Liddick *et al.* [31] relied on such qualitative observations in the region of  $N=34$ , and gained insight into the  $\pi 1f_{7/2}-\nu 1f_{5/2}$  monopole migration.

## 1.4 Re-ordering of single-particle states in neutron-rich $fp$ shell nuclei

The previous sections have discussed the general usefulness of the shell model in describing the structure of the atomic nucleus, as well as the nucleon-nucleon forces which are believed to drive the evolution of this structure across the nuclear chart. Specific regions of evolving structure within the  $fp$  shell are highlighted in this section.

### 1.4.1 $N=32$ and $N=34$ subshell closures

As discussed in Section 1.1.1, the proton-neutron tensor monopole interaction has a strong influence on evolving shell structure across the nuclear landscape. One region mentioned previously is that near  $Z=20$  and  $N=34$ . The monopole interaction in this region is that between the  $1f_{5/2}$  ( $l-1/2$ ) neutron orbital and the  $1f_{7/2}$  ( $l+1/2$ ) proton orbital. The low-energy structures of neutron-rich nuclei with neutrons occupying the  $1f_{7/2}$ ,  $2p_{3/2}$ ,  $2p_{1/2}$  and  $1f_{5/2}$  orbitals are strongly influenced by the occupation of the proton  $1f_{7/2}$  orbital, as illustrated in Figure 1.7. With increasing  $\pi 1f_{7/2}$  occupancy in moving from  ${}_{20}\text{Ca}$  to  ${}_{28}\text{Ni}$ , the energy of the  $5/2^-$  level, which has a large contribution from the  $\nu 1f_{5/2}$  orbital, drops, moving much closer to the  $3/2^-$  ( $\nu 2p_{3/2}$ ) ground state.

Along with the sizeable spin-orbit splitting between the  $\nu 2p_{3/2}$  and  $\nu 2p_{1/2}$  states, the monopole migration of the  $\nu 1f_{5/2}$  orbital suggests that, for nuclei with low occupancy of the  $\pi 1f_{7/2}$  orbital, e.g., the  ${}_{20}\text{Ca}$ ,  ${}_{22}\text{Ti}$  and  ${}_{24}\text{Cr}$  isotopes, there is a sufficient gap in energy between the  $\nu 2p_{3/2}$  and  $\nu 2p_{1/2}$  states to produce an  $N=32$  subshell closure. This expectation has been borne out experimentally in the  ${}_{20}\text{Ca}$  [11, 12],  ${}_{22}\text{Ti}$  [13] and  ${}_{24}\text{Cr}$  [14] isotopes in the systematic variation of the  $E(2_1^+)$  as a function of neutron number, shown in Fig. 1.8(a). The rise in  $E(2_1^+)$  at  $N=32$  relative to the nearest even-even neighbors for the even-even Ca, Ti and Cr isotopes is clear. Further support for the  $N=32$  subshell closure below  $Z=28$  comes from the small  $B(E2 : 2_1^+ \rightarrow 0_1^+)$  transition probabilities measured for  ${}_{22}^{54}\text{Ti}_{32}$  [28] and  ${}_{24}^{56}\text{Cr}_{32}$  [32] [see

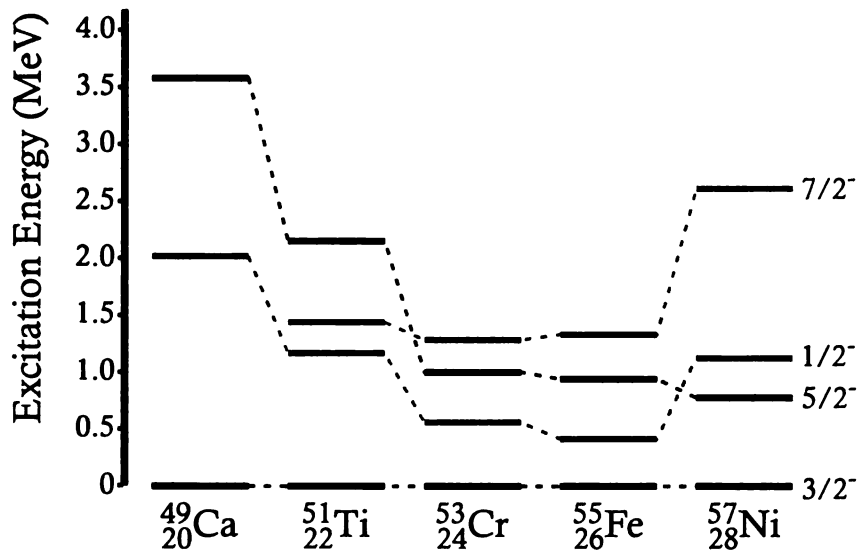


Figure 1.7: Evolution of the low-energy states in the  $N=29$  isotones from  $Z=20$  to  $Z=28$ . The monopole shift of the  $\nu 1f_{5/2}$  orbital with increasing occupation of the  $\pi 1f_{7/2}$  orbital is suggested by the decreasing energy of the  $5/2^-$  state along the chain.

Fig. 1.8(b)]. The high-spin structures of  $^{50,52,54}\text{Ti}$  [13] are also indicative of a sizeable  $N=32$  gap. The separation between the  $6_1^+$  and the closely spaced  $8_1^+$ ,  $9_1^+$  and  $10_1^+$  levels in  $^{54}\text{Ti}$  has been interpreted as an indication of the substantial cost to promote a  $\nu 2p_{3/2}$  neutron across the  $N=32$  gap to either of the  $\nu 2p_{1/2}$  or  $\nu 1f_{5/2}$  orbitals [13].

The experimentally-confirmed  $N=32$  subshell closure has been well-reproduced by shell-model calculations in the  $fp$  shell using several effective interactions [33–35]. Beyond  $N=32$ , the GXPF1 interaction [33] further predicts a subshell closure at  $N=34$  for the  $_{20}\text{Ca}$  and  $_{22}\text{Ti}$  isotopes, arising from the continued upward monopole shift of the  $\nu 1f_{5/2}$  orbital [33]. Experimental evidence, however, is inconsistent with the prediction of  $N=34$  as a subshell closure in the  $_{22}\text{Ti}$  isotopes. Measurement of  $E(2_1^+)$  for  $^{56}\text{Ti}_{34}$  by Liddick *et al.* [36] placed the first  $2^+$  level at 1127 keV, nearly 400 keV drop lower than the  $E(2_1^+)=1495$  keV observed for  $^{54}\text{Ti}_{32}$  [13] [see Fig. 1.8(b)]. This result, at odds with the expectation of a  $N=34$  subshell closure for the  $_{22}\text{Ti}$  isotopes, spurred the development of the new GXPF1A effective shell model interaction [34]. To improve the description of the low-energy structure of  $^{56}\text{Ti}$ , five of the two-body

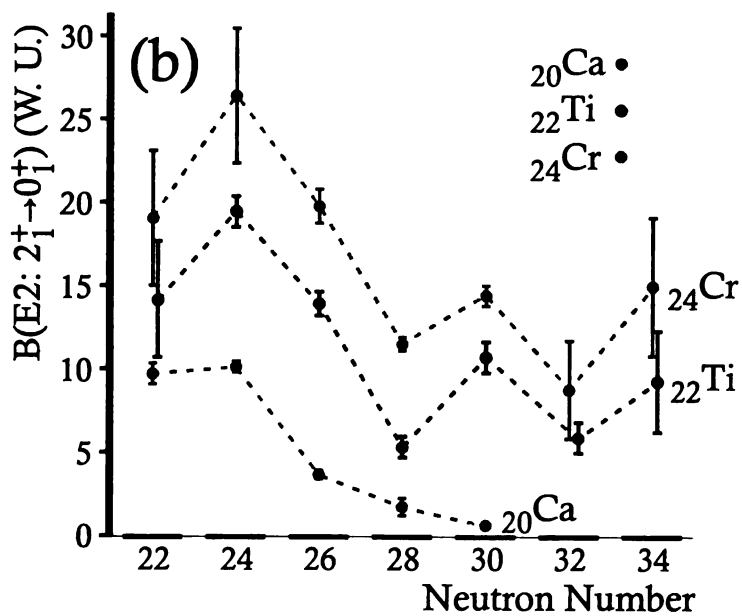
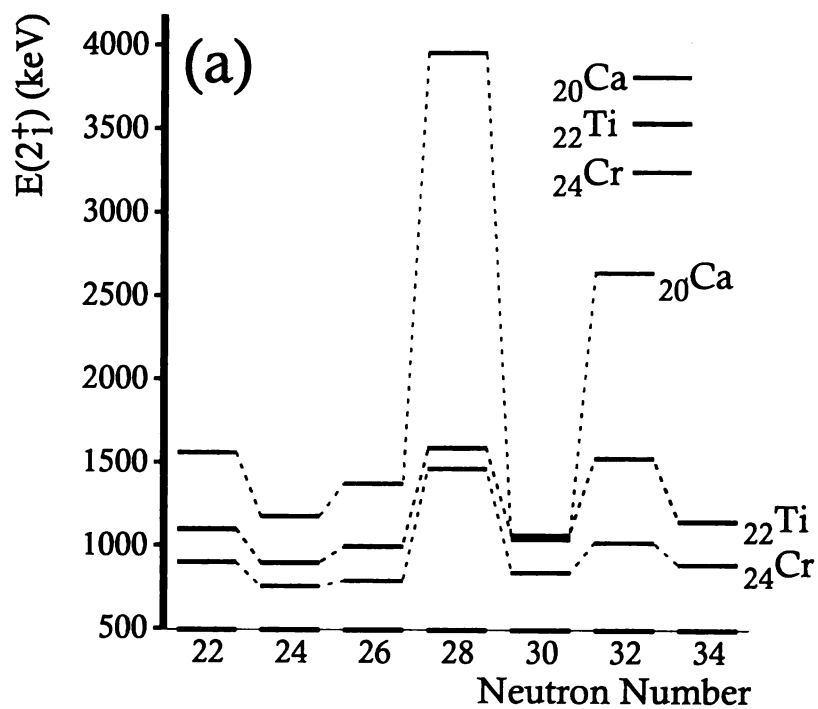


Figure 1.8: Behavior of (a)  $E(2_1^+)$  and (b)  $B(E2: 2_1^+ \rightarrow 0_1^+)$  across the  $^{20}\text{Ca}$ ,  $^{22}\text{Ti}$  and  $^{24}\text{Cr}$  isotopic chains in the region of  $N=32,34$ .

matrix elements were altered to reduce the strength of the monopole interaction in nuclei with  $N > 32$ . These modifications produced an effective interaction that provides improved agreement with experimental data for isotopes in the region, and continues to predict a  $N=34$  subshell closure for the  ${}_{20}\text{Ca}$  isotopes, which have no protons in the  $\pi 1f_{7/2}$  orbital and thus a maximum separation between the  $\nu 1f_{5/2}$  and  $\pi 1f_{7/2}$  [34]. The most direct method of addressing the possible  $N=34$  subshell closure in the Ca isotopes would be to measure  $E(2_1^+)$  for  ${}_{20}^{54}\text{Ca}_{34}$  directly. Low production yields have kept such a measurement elusively out of reach at the present time.

#### 1.4.2 $N=40$ shell closure and intrusion of the neutron $1g_{9/2}$ orbital

According to the shell model orbital ordering shown in Fig.1.2(c), the  $1g_{9/2}$  single-particle orbital is well-separated from the  $1g_{7/2}$ ,  $2d_{5/2}$ , and other higher-energy orbitals, giving rise to a well-established  $N, Z=50$  shell closure. A less pronounced shell closure at  $N, Z=40$ , arising from an energy separation between the  $1g_{9/2}$  orbital and the lower-lying  $fp$  shell levels is also expected within the simple spherical shell-model framework.

Near  $N \sim Z$  however, there is little evidence of the suggested magicity at  $N$  or  $Z=40$ . The self-conjugate nucleus  ${}_{40}^{80}\text{Zr}_{40}$ , for example, shows no evidence of magicity, as it has a rotational-like yrast structure [37], and a large quadrupole deformation,  $\beta_2=0.39$  [38], suggestive of a highly collective structure. This structure is similar to that of  ${}_{38}^{76}\text{Sr}_{38}$ , which again has a rotational-like yrast structure, and a large quadrupole deformation, with  $\beta_2 > 0.4$  [39]. The dominance of a deformed structure rather than the expected spherical ‘doubly-magic’ structure of  ${}_{40}^{80}\text{Zr}_{40}$  is explained by the shape-polarizing effect of a well-stabilized deformed shell gap at  $N, Z=38$  [40]. At large prolate deformation ( $\beta_2 \simeq 0.4$ ) a significant gap forms at  $N=38$  between Nilsson orbitals arising from the  $1g_{9/2}$  orbital. Energetically, unless stabilized by a large

spherical shell gap (for instance at  $N, Z = 28$  or  $50$ ), it is preferential for a nucleus to assume a quadrupole deformation and occupy the local energy minimum at nucleon number  $38$ . These deformed shell gaps strongly stabilize the highly deformed  $N=Z=38$   $^{76}\text{Sr}$  core, and lead to a situation in which the  $^{80}\text{Zr}$  deformed configuration is more stable than the spherical configuration, even with a subshell closure at  $N, Z=40$ . The stability of the deformed  $^{76}\text{Sr}$  core is also believed to be responsible for the particle stability of the proton-rich nucleus  $^{77}_{39}\text{Y}_{38}$  [41].

Except for the collectivity at  $N \sim Z$ , the expected shell gap at nucleon number  $40$  is evident for both protons and neutrons in the neutron-rich nuclei. Figure 1.9(a) shows  $E(2_1^+)$  for the neutron-rich  $_{40}\text{Zr}$  isotopes relative to their nearest neighbor even-even isotones over a range of neutron numbers from  $N=50$  to  $N=58$ .  $^{90}\text{Zr}_{50}$ ,  $^{96}\text{Zr}_{56}$  and  $^{98}\text{Zr}_{58}$  all show evidence of an increase in  $E(2_1^+)$  relative to the nearest isotonic even-even neighbours, supporting the presence of a  $Z=40$  subshell gap. However, this quasi-magic gap is eroded with the addition of neutrons beyond  $N=58$ , due to the attractive monopole interaction between  $\nu 1g_{7/2}$  neutrons and  $\pi 1g_{9/2}$  protons [15].

The bulk of evidence for the expected  $N=40$  subshell gap comes from studies of  $^{68}_{28}\text{Ni}_{40}$  and its nearest-neighboring isotopes. As is shown in Figure 1.9(b), the energy of the first  $2^+$  state in  $^{68}\text{Ni}$  is  $2.033$  MeV [45], significantly higher than in the neighboring  $^{66}\text{Ni}$  and  $^{70}\text{Ni}$  isotopes, providing an experimental signature indicative of a subshell closure at neutron number  $N=40$ . Further evidence for the  $N=40$  subshell closure in the Ni isotopes comes from the  $E(4_1^+)/E(2_1^+)$  ratio, which reaches a local minimum at  $^{68}\text{Ni}$ , and the low transition probability [46, 47] for excitation to the first excited  $2^+$  state.

While in the Ni isotopes there are numerous indicators for the goodness of the  $N=40$  subshell closure, with the addition or removal of protons away from the magic number  $Z=28$ , the  $N=40$  closure is rapidly washed out. Figure 1.9(b) shows the systematics of  $E(2_1^+)$  for the even- $Z$   $_{24}\text{Cr}$  through  $_{32}\text{Ge}$  isotopic chains surrounding  $N=40$ . The  $E(2_1^+)$  values for the  $_{24}\text{Cr}$ ,  $_{26}\text{Fe}$ ,  $_{30}\text{Zn}$  and  $_{32}\text{Ge}$  isotopes all decrease with

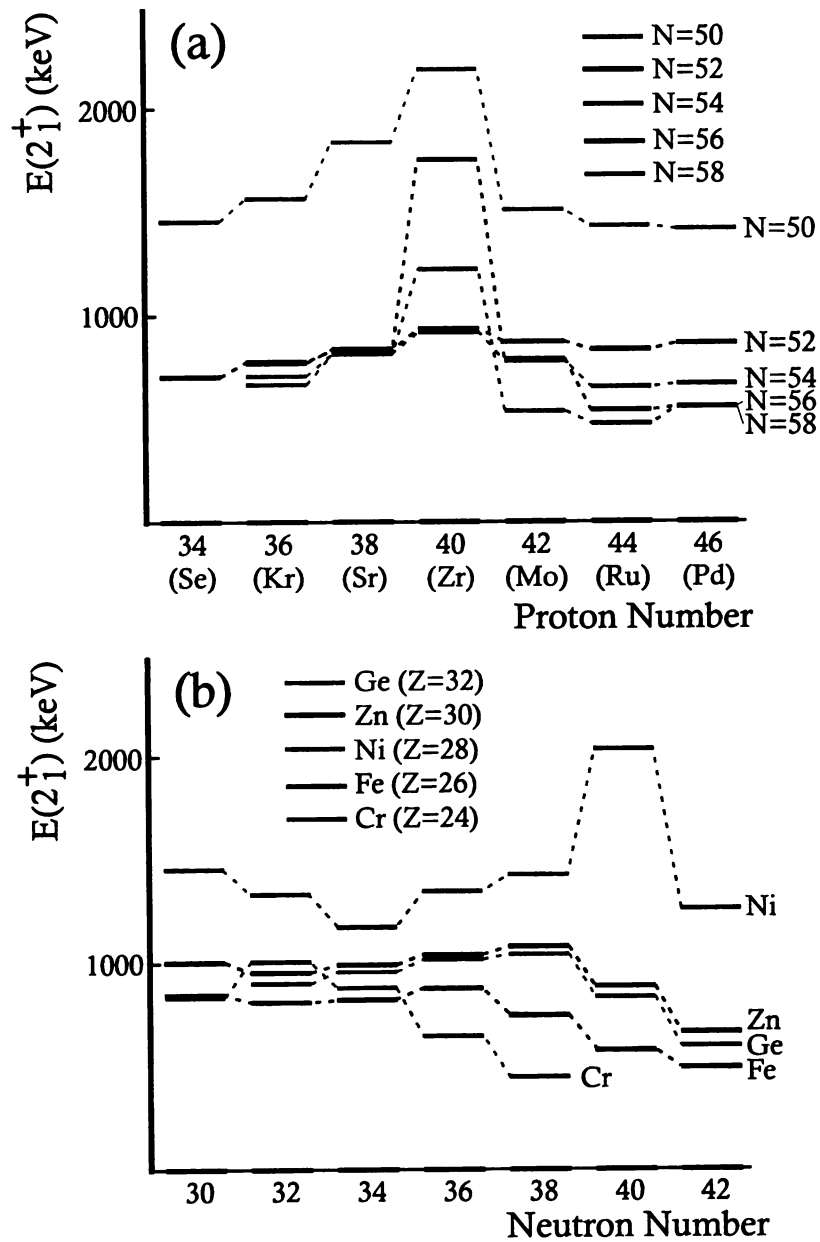


Figure 1.9: Systematic variation of  $E(2_1^+)$  for the (a) isotonic chains in the region of  $Z=40$ , and (b) neutron-rich  ${}_{24}\text{Cr}$ ,  ${}_{26}\text{Fe}$ ,  ${}_{28}\text{Ni}$ ,  ${}_{30}\text{Zn}$  and  ${}_{32}\text{Ge}$  isotopic chains in the region around  $N=40$ . Data were taken from Refs. [14, 25, 42–44].

increasing neutron number, even through  $N=40$ . Deformation of the ground state is well-known in the case of the higher- $Z$   ${}_{32}\text{Ge}$  isotopes. As discussed by Leenhardt *et al.* [48], systematics of  $B(E2: 2_1^+ \rightarrow 0_1^+)$  support the trends seen in  $E(2_1^+)$ , and suggest that the  ${}_{30}\text{Zn}$  isotopes are a transitional region between the spherical  ${}_{28}\text{Ni}$  isotopes and the well-deformed  ${}_{32}\text{Ge}$  isotopes.

Collectivity has also been observed to develop near  $N=40$  for the isotopes below  $Z=28$ . Hannawald *et al.* [42] identified the first  $2^+$  state in  ${}^{66}\text{Fe}_{40}$  at  $E(2_1^+)=573$  keV following  $\beta$  decay from  ${}^{66}\text{Mn}$ . This low excitation energy was taken to be an indication of collectivity near the ground state, and a quadrupole deformation parameter of  $\beta_2=0.26$  was obtained from the Grodzins relation [26]. A recent measurement has extended the data for the  ${}_{26}\text{Fe}$  isotopes past  $N=40$ , identifying the first excited state in  ${}^{68}\text{Fe}_{42}$  at 517 keV in a 2p knockout reaction [43]. This is the most neutron-rich Fe isotope studied, and shows that the decreasing trend of  $E(2_1^+)$  for the  ${}_{26}\text{Fe}$  isotopes continues past  $N=40$ .

The systematic decrease of  $E(2_1^+)$  is even more pronounced in the  ${}_{24}\text{Cr}$  isotopes [see Fig. 1.9(b)]. The low  $E(2_1^+)$  values in  ${}^{60}\text{Cr}_{36}$  and  ${}^{62}\text{Cr}_{38}$  are indicative of deformation, leading to deduced values of  $\beta_2=0.27$  and 0.31 respectively [44]. Deformation is also suggested by the reported large quadrupole deformation lengths for  ${}^{60,62}\text{Cr}$  obtained in the analysis of proton inelastic scattering [49, 50]. While data are not yet available for the low-energy structure of  ${}^{64}\text{Cr}_{40}$ , the trend of lowering  $E(2_1^+)$  values is predicted [51] to continue at and beyond  $N=40$ , as observed already in the  ${}_{26}\text{Fe}$  isotopes.

Understanding the origin of collectivity, which apparently develops in the region of  $N=40$  in nuclei above and below  $Z=28$ , requires a knowledge of the interactions at work. The strength of the  $N=40$  subshell closure is dependent on the energy separation between the  $1f_{5/2}, 2p_{1/2}$  neutron orbitals and the higher-lying  $1g_{9/2}$  orbital. The strong repulsive monopole p-n interaction between protons in the  $\pi 1f_{7/2} (l+1/2)$  orbit and neutrons in the  $\nu 1g_{9/2} (l+1/2)$  orbit decreases with the removal of  $\pi 1f_{7/2}$

protons ( $Z < 28$ ), as does the attractive  $\pi 1f_{7/2} (l + 1/2) - \nu 1f_{5/2} (l - 1/2)$  interaction, which causes a narrowing of the  $\nu 1g_{9/2} - \nu 1f_{5/2}$  energy separation. This effectively weakens the  $N=40$  subshell closure, which may only manifest itself in  $^{68}\text{Ni}$  due to reinforcement by the spherical  $Z=28$  closed shell [52].

In addition to the weakening of the spherical  $N=40$  subshell closure by the monopole interaction, the first two Nilsson substates of the  $\nu 1g_{9/2}$  orbital are steeply downsloping in energy with increasing quadrupole deformation, as is shown in Fig. 1.10. The reduced energy gap at  $N=40$  is insufficient to maintain the nucleus in a spherical configuration [48], as occupation of the deformed levels is energetically preferential, and collective deformed ground states develop, further eroding the  $N=40$  subshell closure. Thus, the  $1g_{9/2}$  neutron orbital plays a strong role in determining collectivity near  $N=40$ , as its approach to the Fermi surface permits development of ground states with significant quadrupole deformation. The decrease in energy of  $9/2^+$  states in odd- $A$  Cr isotopes approaching  $N=40$  [53–55] offers further evidence of the  $1g_{9/2}$  orbital approaching the Fermi surface.

Considering Figure 1.9(b) in more detail, the decrease in  $E(2_1^+)$  suggests an onset of deformation in the  $^{24}\text{Cr}$  isotopes beginning at  $N=36$ , while in the  $^{26}\text{Fe}$  isotopes, such evidence for deformation first appears at  $N=38$ . The point at which collectivity sets in in this region will add to the understanding the effect of the neutron  $1g_{9/2}$  orbital on the structure of nuclei at the extremes of the  $fp$  shell. The neutron-rich  $^{24}\text{Cr}$  and  $^{26}\text{Fe}$  isotopes have been investigated, but scant data are available for the neighbouring odd- $Z$   $^{25}\text{Mn}$  isotopes near to  $N=40$ . An understanding of the onset of deformation for the  $^{25}\text{Mn}$  isotopes would contribute significantly to the understanding of the evolving structure in the region near  $N=40$ .

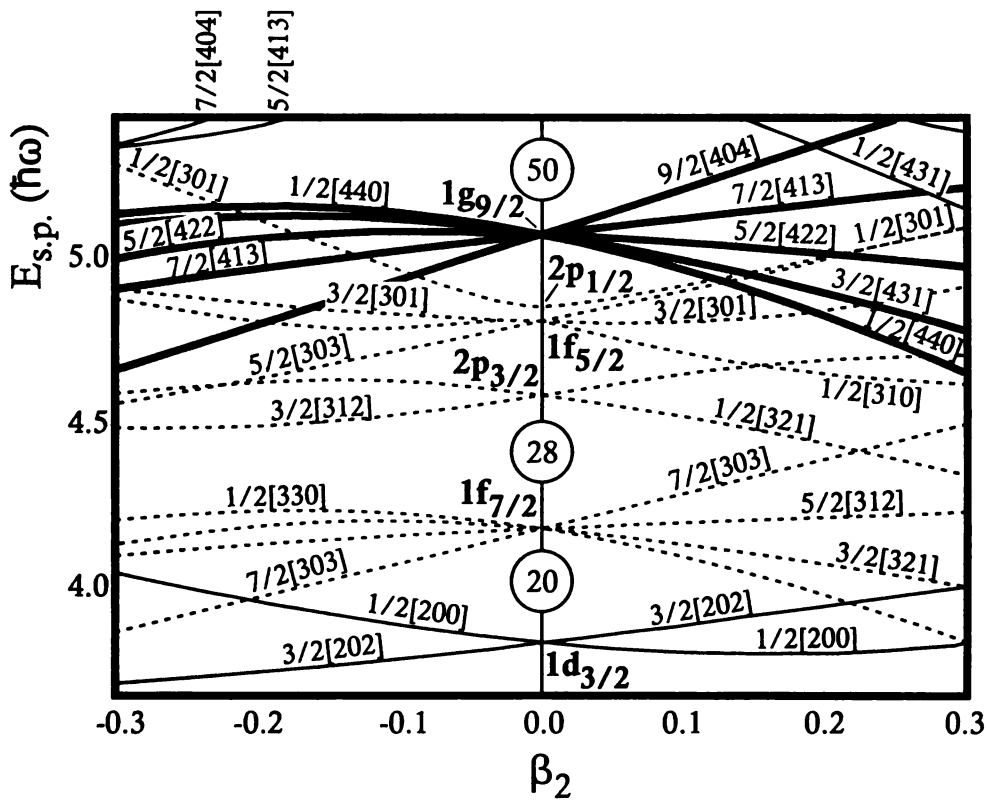


Figure 1.10: Nilsson diagram for the neutron orbitals between 20 and 50. The Nilsson substates arising from the  $1g_{9/2}$  orbital are highlighted in bold red, and with increasing deformation, the lowest two substates are observed to be steeply downsloping. Figure adapted from Ref. [2].

## 1.5 Motivation for the measurement

The motivation for the present study was to more fully understand the evolution of the single particle energies in the neutron-rich nuclei of the  $fp$  shell. Within the  $fp$  shell, and at its upper and lower borders, the evidence of evolving single-particle level ordering has been described. Further experimental data are required to constrain nuclear theory, and help in the development of cross-shell interactions, which are believed to be critical for the description of nuclei on the border of major shells.

Near  $N=32,34$ ,  $\beta$  decay of the  $^{53,54}_{20}\text{Ca}$  isotopes was investigated to gain insight into the low-energy structures of the daughter  $^{53,54}_{21}\text{Sc}$  isotopes. Isomeric decay of states in  $^{54,56}\text{Sc}$  provided additional information for these isotopes. The odd- $Z$   $_{21}\text{Sc}$  nuclei are nuclei with a few nucleons more than a closed shell, and, as discussed previously, the low-energy level schemes can be described in terms of proton-neutron multiplets. Within this simple framework, insight into the neutron configurations in the Sc isotopes can be gained. An improved understanding of the situation in the  $_{21}\text{Sc}$  isotopes may shed light on the case of the  $_{20}\text{Ca}$  isotopes, and the open question of a  $N=34$  subshell closure at  $^{54}\text{Ca}$ .

At higher  $Z$ , the onset of deformation for nuclei with  $Z < 28$  approaching  $N=40$  is also interesting. As discussed,  $_{26}\text{Fe}$  and  $_{24}\text{Cr}$  isotopes have been well studied, but the location of the onset of deformation for the intermediate  $_{25}\text{Mn}$  isotopes is not clear. While extensive level schemes up to high-spin have been deduced for the lighter  $^{57-60}_{25}\text{Mn}$  isotopes [56], no level structures are available for Mn isotopes with  $N > 38$ . In-beam  $\gamma$  rays have been recently observed for neutron-rich  $^{59-63}\text{Mn}$  produced by multinucleon transfer between a  $^{70}\text{Zn}$  projectile and a  $^{238}\text{U}$  target [57]. For the most neutron-rich  $^{63}\text{Mn}$  only a single  $\gamma$  ray was assigned. Five  $\gamma$  rays were assigned to  $^{62}\text{Mn}$ , completing the low-energy level scheme proposed previously from  $\beta$  decay [58], a structure which is complicated by the presence of two  $\beta$ -decaying states.  $\gamma$  rays have been assigned from both  $\beta$  decay [59] and in-beam work [57] in the case of

$^{61}\text{Mn}$ . Transitions identified in the former  $\beta$  decay by Sorlin *et al.* were not placed in a level scheme, while only yrast states have been identified in the latter in-beam work. The present work studied the  $\beta$  decay of  $^{61}\text{Cr}$  to states in  $^{61}\text{Mn}$  to produce a more complete level scheme for this nucleus. Comparison with shell model calculations in different valence spaces were found to provide insight into the onset of collectivity, and the monopole migration of the deformation inducing  $\nu 1g_{9/2}$  orbital with decreasing occupancy of the  $\pi 1f_{7/2}$  orbital.

The low-energy isomeric structure of  $^{50}_{19}\text{K}_{31}$  was also studied, and provided insight into the evolution of the proton single particle  $1d_{3/2}$  and  $1s_{1/2}$  states just below the  $fp$  shell. The insight gained in this region of the nuclear chart does not clarify current open questions, but rather adds to mounting evidence for structural evolution outside the predictions of current theoretical treatments.

## 1.6 Organization of Dissertation

An introduction to the concepts of nuclear shell structure and the need for studying neutron-rich nuclei was presented in this chapter, including the motivation for the present measurement. The principles of the measurement techniques of  $\beta$  and  $\gamma$  decay are presented in Chapter 2, as well as an explanation of how they pertain to nuclear structure. Details of the experimental setup are presented in Chapter 3, including a description of the detectors. The results for the low-energy level structures of  $^{50}\text{K}$ ,  $^{53,54,56}\text{Sc}$  and  $^{61}\text{Mn}$  are presented in Chapter 4, and the implications of these results discussed in Chapter 5. Chapter 6 includes a summary of this work, and a discussion of the possibilities for future studies using both  $\beta$  decay and other complementary techniques.

# Chapter 2

## Experimental Techniques

$\beta$ -delayed  $\gamma$ -ray spectroscopy is a powerful method to probe the structure of the most exotic nuclei, including short-lived nuclei near the driplines. A highly sensitive technique,  $\beta$  decay itself can provide valuable information on half-lives, decay  $Q$  values, and branching information, even in cases with very few events. The branching of the  $\beta$ -decay process populates states in a daughter nucleus selectively, based on the relative angular momenta and parities of the parent and daughter states. The excited states populated in a daughter nucleus most often de-excite by the emission of  $\gamma$  rays. The energy of the emitted  $\gamma$  rays provides information on the excitation energy of the states populated in the  $\beta$  decay, another key observable in nuclear structure studies. This chapter details the relevant processes of  $\beta$  and  $\gamma$  decay, and outlines how their combined use permits access to details of the structure of exotic nuclei.

### 2.1 $\beta$ decay

$\beta$  decay, in the most qualitative sense, describes the process of the conversion of a proton in the nucleus into a neutron, or vice versa. During this process, the atomic number ( $Z$ ) and neutron number ( $N$ ) of the nucleus is changed, but the mass number ( $A$ ) remains the same. Thus,  $\beta$  decay moves nuclei along isobaric chains towards

stability. One of the earliest observed radioactive decay modes,  $\beta$  decay is governed by the weak force, and encompasses three distinct decay processes:

$$\beta^- : {}^A_Z X_N \rightarrow {}^A_{Z+1} Y_{N-1}^+ + \beta^- + \bar{\nu} + Q_\beta, \quad (2.1)$$

$$\beta^+ : {}^A_Z X_N \rightarrow {}^A_{Z-1} Y_{N+1}^- + \beta^+ + \nu + Q_\beta, \text{ and} \quad (2.2)$$

$$\text{Electron Capture} : {}^A_Z X_N + e^- \rightarrow {}^A_{Z-1} Y_{N+1}^- + \nu + Q_\beta, \quad (2.3)$$

where  $e^-$  is an orbital electron,  $\beta^\pm$  is a beta particle,  $\nu$  is a neutrino,  $\bar{\nu}$  is an anti-neutrino, and  $Q_\beta$  represents the characteristic amount of energy released for a given  $\beta$  decay process [3]. The energy released,  $Q_\beta$ , must be greater than zero for  $\beta$  decay to occur. On the neutron-rich side of stability  $\beta^-$  decays occur, driving nuclei towards stability along an isobaric chain by converting neutrons to protons within the nucleus. On the neutron-deficient side of the line of stability, both  $\beta^+$  and electron capture processes can occur, though  $\beta^+$  is only observed in nuclei with a sufficiently large  $Q_\beta$ , due to a 1.022 MeV threshold for the creation of an  $e^-$ - $\beta^+$  pair.

Electron capture is the process in which an orbital electron is captured by the nucleus, and combines with a bound proton to achieve the transformation of a nucleus  ${}^A_Z X_N$  into  ${}^A_{Z-1} Y_{N+1}$ . The  $Q_\beta$  for electron capture is given by  $Q_{EC} = [m({}^A_Z X_N) - m({}^A_{Z-1} Y_{N+1})]c^2 - B_n$ , where  $B_n$  is the binding energy of the captured  $n$ -shell electron [3]. Only one particle, a neutrino, is emitted in the electron captures process. Due to the extremely small neutrino mass, and the fact that neutrinos have no charge, it is nearly impossible to observe this particle directly. Thus, electron capture processes are typically observed by monitoring secondary radiation. The captured electron is most often an inner shell (i.e. K or L shell) electron, and its capture during the decay process creates a vacancy, which is filled by electrons from higher shells. These downward transitions result in emission of characteristic X rays or Auger electrons, which can provide a signature for the electron capture process.

The other possibility for neutron-deficient nuclei to move towards stability along

an isobaric chain is  $\beta^+$  decay. The  $Q_\beta$  value for  $\beta^+$  decay is given by  $Q_{\beta^+} = [m({}_Z^A X_N) - m({}_{Z-1}^A Y_{N+1}) - 2m_e]c^2$ , and thus there is an energy threshold for  $\beta^+$  decay, requiring an atomic mass difference of at least two electron rest masses, 1.022 MeV, between the parent and daughter species. As was the case in electron capture, a neutrino is emitted during the decay, but a second particle, a  $\beta^+$ , is also emitted. It is very difficult to detect the neutrino, but it is possible to detect the  $\beta^+$ , either directly, through its interaction with atomic electrons in a detection medium, or by detection of the two 511-keV  $\gamma$  rays which result when the positron thermalizes and annihilates with an electron.

On the neutron-rich side of stability, the relevant  $\beta$ -decay process is  $\beta^-$  decay. The  $Q_\beta$  value for this decay is the simplest case, given by the difference in the atomic masses of the parent and daughter,  $Q_{\beta^-} = [m({}_Z^A X_N) - m({}_{Z+1}^A Y_{N-1})]c^2$ . As was the case in  $\beta^+$  decay, this process involves emission of two particles, an anti-neutrino and a high-energy electron or  $\beta^-$  particle. The  $\beta^-$  can be detected directly through its interaction with atomic electrons in the detection medium. It is this decay mode that is of interest in the present study of neutron-rich nuclei.

### 2.1.1 $\beta$ -decay half-lives

One of the most fundamental quantities describing a  $\beta$ -decay process is the rate at which the decay occurs.  $\beta$  decay is governed by first-order rate law, and the number of nuclei,  $N$ , in a sample at a time  $t$  is given by:

$$N(t) = N_0 e^{-\lambda t}, \quad (2.4)$$

where  $N_0$  is the number of nuclei originally in the sample, and  $\lambda$  is the decay constant characteristic of the decay. Physically,  $\lambda$  represents the probability per unit time for the decay of a given nucleus [3]. The decay constant,  $\lambda$ , is closely related to the more

often quoted half-life,  $T_{1/2}$  as:

$$T_{1/2} = \frac{\ln(2)}{\lambda}. \quad (2.5)$$

The half-life corresponds to the average time required for half of the nuclei in a sample to decay. Governed by the weak interaction, the half-life of  $\beta$ -decay processes ranges from a few milliseconds to seconds or even longer. The longest-lived  $\beta$ -decaying nuclei have half-lives in excess of  $10^{18}$  years. The half-life of a  $\beta$ -decay process depends strongly on the energy of the decay processes, and differences (i.e. spin and parity) between the parent initial state and the final state in the daughter. The dependence on the initial and final state structures can be qualitatively understood, and relates to the selection rules for  $\beta$  decay, which are discussed in Section 2.1.3. The next section addresses the process of  $\beta$ -delayed neutron emission, a decay mode which can be a significant part of the decay of neutron-rich nuclei.

### 2.1.2 $\beta$ -delayed neutron emission

Neutron emission is a decay process involving direct emission of a neutron from a nucleus according to the following equation:



where  $Q_n$  represents the mass-energy difference between the initial and final states. When the daughter nucleus,  ${}^{A-1}_Z X_{N-1}$ , is left in its ground state,  $Q_n = -S_n$ , where  $S_n$  is the neutron separation energy, a measure of how much energy is required to remove a neutron from a given nucleus, as discussed in Chapter 1 (see Eqn. 1.1). In general the neutron separation energy becomes lower with the addition of neutrons along an isotopic chain. Thus, for the most neutron-rich nuclei, neutron separation energies are quite low, and in fact when the separation energy reaches zero, the nucleus is said to be at the neutron dripline. Not being subject to the Coulomb force, and thus without a Coulomb barrier, the last neutron is simply not confined within a nucleus at the

neutron dripline.

While the ground state of a  $\beta$ -decay daughter nucleus may be bound with respect to neutron emission (i.e.  $S_n > 0$ ), there are many cases in  $\beta^-$  decay in which the decay populates states in the daughter which are above the neutron separation energy, or neutron threshold. When this occurs, the emission of a neutron from the excited state of the daughter can proceed rapidly, as neutron emission is mediated by the strong force and competes favorably with  $\gamma$ -ray emission mediated by the electromagnetic interaction. Following neutron emission, excited states in the  $\beta n$  daughter may be populated, and further de-excite through emission of  $\gamma$  radiation characteristic of that nucleus. It is possible to identify  $\beta$ -delayed neutron emission in the decay of neutron-rich nuclei through the detection of these characteristic  $\gamma$  rays.

### 2.1.3 Selection rules and $\log ft$

$\beta^-$  decay involves the emission of two particles, a  $\beta^-$ , or high energy electron, and an anti-neutrino. These emitted particles are leptons with intrinsic spin  $S=1/2$ , and can carry additional orbital angular momentum. If the spins of the two emitted particles are antiparallel, they are coupled to  $S_\beta=0$ , and the system undergoes what is called Fermi decay [3]. The other possibility, that the spins of the electron and neutrino are aligned parallel, coupling to  $S_\beta=1$ , is called Gamow-Teller decay. The orientation of the electron and anti-neutrino spins provides the first classification of  $\beta$  decay – whether the electron and/or neutrino carry additional angular momentum further divides the  $\beta$ -decay process.

The so-called allowed  $\beta$  decay describes the situation in which the electron and neutrino carry no orbital angular momentum ( $l=0$ ). With  $S_\beta=0$ , an allowed Fermi decay has no change in the nuclear spin,  $\Delta J = |J_i - J_f| = 0$ . Additionally, with  $l=0$ , there is no change in parity between the initial and final states,  $\pi = (-1)^l$  in this case.  $S_\beta=1$  for allowed Gamow-Teller decays, and one unit of angular momentum is carried by the electron and neutrino, even with zero additional units of orbital

Table 2.1:  $\beta$  decay selection rules for allowed and forbidden transitions. Table adapted from Ref. [4].

Transition Type	$\Delta\pi$	$\Delta l$	$\Delta J$	$\log ft$
Superallowed	No	0	0	2.9 - 3.7
Allowed	No	0	0, 1	4.4-6.0
First forbidden	Yes	1	0, 1, 2	6 - 10
Second forbidden	No	2	1, 2, 3	10 - 13
Third forbidden	Yes	3	2, 3, 4	$\geq 15$

angular momentum ( $l=0$ ). Allowed Gamow-Teller decays thus have  $\vec{J}_i = \vec{J}_f + 1$ , and so  $|J_f - 1| \geq J_i \geq |J_f + 1|$ , or  $\Delta J=0,1$ . Again, with  $l = 0$ , there is no change in parity between final and initial states in allowed Gamow-Teller decay. Since  $\Delta J=0$  is allowed in both cases, most transitions are mixed Fermi and Gamow-Teller decays, except when  $J_i = J_f = 0$ , in which case only Fermi decay is possible [3]. This special case is called a “super-allowed” decay.

Allowed  $\beta$ -decay transitions are among the fastest, although other transitions in which the electron/neutrino carry non-zero orbital angular momentum ( $l > 0$ ) are possible. These so-called ‘forbidden’ transitions are not completely forbidden as the name suggests, but are slower and thus much less likely to occur than allowed transitions. The degree of forbiddenness increases with  $l$  – first forbidden decays have the electron and neutrino emitted with  $l=1$ , while  $l=2$  corresponds to second forbidden decays, etc. Table 2.1 summarizes the selection rules for  $\beta$  decay up to third forbidden decays.

The comparative half-life, or  $ft$  value provides a method for comparing the  $\beta$ -decay probabilities in different nuclei. The dependence of the  $\beta$ -decay rate on specific nuclear properties such as the Coulomb interaction based on the atomic number of the daughter,  $Z$ , and the maximum energy of the  $\beta$  transition are incorporated into the value of  $f$ , the Fermi integral [3]. With these well-understood dependencies removed, differences in  $ft$ , or the more commonly reported  $\log ft$ , represent differences between the initial and final nuclear states. Values for the Fermi integral are tabulated

for ranges of  $Z$  and the maximum  $\beta$  energy,  $E_{max}$ , but approximate values can be obtained using the empirical expression for  $\log f_{\beta^-}$  [60]:

$$\log f_{\beta^-} = 4.0 \log E_{max} + 0.78 + 0.02Z - 0.005(Z - 1) \log E_{max}. \quad (2.7)$$

The value of  $t$  in  $\log ft$  is the partial half-life for the decay to a specific state in the daughter nucleus. If the parent nucleus has a total half-life  $T_{1/2}^{total}$ , then the partial half-life for decay populating a specific state  $i$  in the daughter is given by [3]:

$$T_{1/2}^{partial,i} = \frac{T_{1/2}^{total}}{BR_i}, \quad (2.8)$$

where  $BR_i$  is the branching ratio to the state  $i$  in the daughter.

## 2.2 $\gamma$ -ray decay

Following  $\beta$  decay, the daughter nucleus may be left in an excited state. Internal transition or colloquially,  $\gamma$ -ray decay, is the process by which an excited nucleus can release excess energy in the form of electromagnetic radiation, or a photon. From a schematic perspective, the emitted electromagnetic radiation connects two states within the nucleus, each of which have definite spin,  $J$ , and parity,  $\pi$ . The emitted photon must connect the states in energy, and conserve both spin and parity. This results in strict selection rules for  $\gamma$ -ray transitions.

### 2.2.1 Selection rules and lifetimes

Photons have no intrinsic spin, and thus the orbital angular momentum,  $\lambda$ , carried by a photon is constrained by the spins of the initial ( $J_i$ ) and final ( $J_f$ ) nuclear states as:

$$|J_i - J_f| \leq \lambda \leq (J_i + J_f)\hbar. \quad (2.9)$$

Table 2.2:  $\gamma$ -ray decay selection rules and multiplicities up to  $\lambda=3$ . Table adapted from Ref. [4].

Radiation Type	Name	$\lambda=\Delta J$	$\Delta\pi$
E1	Electric dipole	1	Yes
M1	Magnetic dipole	1	No
E2	Electric quadrupole	2	No
M2	Magnetic quadrupole	2	Yes
E3	Electric octupole	3	Yes
M3	Magnetic octupole	3	No

While there may be a number of possible  $\lambda$  values, or multiplicities for  $\gamma$ -rays connecting two nuclear states, the transition rate is strongly dependent on  $\lambda$ , and the lowest possible  $\gamma$ -ray multipolarity will be favored. However, the required conservation of parity plays a significant role in determining the type of  $\gamma$ -ray transition which occurs.

Each nuclear state corresponds to a distinct distribution of matter and charge, and thus an electromagnetic transition connecting two nuclear states necessarily corresponds to a change in the distribution of protons and neutrons within that nucleus [4]. A shift in the charge distribution produces an electric field, while a shift in the distribution of current gives rise to a magnetic field. Thus, de-exciting  $\gamma$ -ray transitions can be classified as either electric or magnetic in nature. Electric transitions are characterized by a parity dependence on  $\lambda$  of  $\Delta\pi=(-1)^\lambda$ , while for magnetic transitions, the parity change is  $\Delta\pi=(-1)^{\lambda+1}$ . Combined with the angular momentum requirements, the resulting  $\gamma$ -ray selection rules are summarized in Table 2.2.

Based upon the type and multipolarity of a de-exciting  $\gamma$ -ray transitions, estimates can be made for the expected lifetime of the parent state. The decay constant for the emission of a photon from a well-defined single state with excess energy is given by what is known as Fermi's golden rule [4]. The transition rate,  $T(E\lambda)$  or  $T(M\lambda)$ , for

a  $\gamma$ -ray transition with energy  $E_\gamma$  can be written as follows [4]:

$$T(E\lambda) = \alpha\hbar c \frac{8\pi(\lambda+1)}{\lambda[(2\lambda+1)!!]^2} \left(\frac{E_\gamma}{\hbar c}\right)^{2\lambda+1} \frac{1}{\hbar} B(E\lambda), \quad (2.10)$$

$$T(M\lambda) = \alpha\hbar c \left(\frac{\hbar}{2m_p c}\right)^2 \frac{8\pi(\lambda+1)}{\lambda[(2\lambda+1)!!]^2} \left(\frac{E_\gamma}{\hbar c}\right)^{2\lambda+1} \frac{1}{\hbar} B(E\lambda), \quad (2.11)$$

where  $\alpha$  is the fine structure constant,  $\hbar$  is Plank's constant divided by  $2\pi$ ,  $c$  is the speed of light,  $m_p$  is the mass of the proton and  $B(E\lambda)$  and  $B(M\lambda)$  are the reduced electric and magnetic transition probabilities respectively, which contain all of the nuclear wavefunction information.

To obtain useful estimates of the transition rates for  $\gamma$ -ray transitions, estimates of the reduced transition probabilities are required. However, these values depend strongly on nuclear models. A commonly-used value was derived for the extreme single-particle model, discussed earlier in Section 1.2.1. Assuming that the transition involves the change of a single particle in a uniform density nucleus, then the so-called Weisskopf single-particle estimates for the reduced transition probabilities are given by the following [4]:

$$B_W(E\lambda) = \frac{(1.2)^{2\lambda}}{4\pi} \left(\frac{3}{\lambda+3}\right)^2 A^{2\lambda/3} e^2 (fm)^{2\lambda}, \quad (2.12)$$

$$B_W(M\lambda) = \frac{10}{\pi} (1.2)^{2\lambda-2} \left(\frac{3}{\lambda+3}\right)^2 A^{(2\lambda-2)/3} \left(\frac{e\hbar}{2m_p c}\right)^2 (fm)^{2\lambda-2}. \quad (2.13)$$

Combination of the Weisskopf single-particle transition probability estimates with the expressions for the  $\gamma$ -ray transition rates yields the so-called Weisskopf estimates for  $\gamma$ -ray decay transition rates. The Weisskopf estimates for the lifetimes of certain types of  $\gamma$ -ray transitions are given in Table 2.3.

Table 2.3: Weisskopf single-particle lifetimes estimates for electric and magnetic  $\gamma$  transitions up to multipolarity 3 [4].  $A$  represents the mass number of the nucleus, while  $E_\gamma$  is the  $\gamma$  energy in MeV.

Radiation Type	Weisskopf Estimate for Transition Lifetime ( $s^{-1}$ )
E1	$1.0 \times 10^{14} A^{2/3} E_\gamma^3$
M1	$5.6 \times 10^{13} E_\gamma^3$
E2	$7.3 \times 10^7 A^{4/3} E_\gamma^5$
M2	$3.5 \times 10^7 A^{2/3} E_\gamma^5$
E3	$34 A^2 E_\gamma^7$
M3	$16 A^{4/3} E_\gamma^7$

## 2.2.2 Isomeric $\gamma$ -ray transitions

The possibility exists in nuclei for excited states to be relatively long-lived, or isomeric. Isomeric states are those which have unexpectedly long lifetimes compared to other nearby states in the nucleus. While there is no clear lifetime cut-off for classifying a nuclear state as isomeric, for example states with lifetimes  $> 10^{-9}$  s can be considered isomeric, particularly in comparison to the typical lifetime for nuclear states of order  $10^{-15}$  s.

When low-lying states in a nucleus have very different angular momenta and there are no intermediate states, the  $\gamma$ -ray decay from the higher-lying state will be hindered due to the large change in angular momentum, a result predicted even by the Weisskopf single-particle estimates. This leads to long-lived nuclear excited states, or isomeric states. When this long lifetime arises due to a large change in angular momentum between the excited state and lower-lying states, this is known as spin isomerism. Also evident from the expressions for the Weisskopf single-particle lifetime estimates is a strong  $\gamma$ -ray energy dependence. Low-energy  $\gamma$ -ray transitions may be long-lived, particularly in heavy nuclei with large mass number.

There are other sources of hindered  $\gamma$ -ray transition probabilities which can lead to nuclear isomerism. As an example, in highly-deformed nuclei, the projection of the total angular momentum onto the nuclear symmetry axis,  $K$ , is an approximately

conserved quantum number. As such, selection rules emerge for transitions allowed based on  $\Delta K$ , and  $K$  isomerism is possible when transitions are inhibited by a large  $\Delta K$  [19].

Aside from large changes in quantum numbers hindering  $\gamma$ -ray transitions, isomers can arise when transitions to lower states involve a significant change in nucleon configuration, even without a large change in angular momentum. The overlap between initial and final states can be poor, and thus hinder the transition. These are called structural isomers and are analogous to the molecular isomers in chemical systems. As such, the presence (or absence) of nuclear isomers can provide critical insight into nuclear structure.

### 2.2.3 Internal conversion

A competing process to  $\gamma$ -ray decay, internal conversion, occurs when an excited nucleus de-excites by interacting electromagnetically with an orbital electron, and ejecting it [3]. This process involves no direct electromagnetic radiation (no photons are involved), and the ejected electrons will have discrete energies, related to the transition energy according to:

$$E_{IC} = E_{\text{transition}} - E_{\text{electron binding energy}}. \quad (2.14)$$

Since orbital electrons occupy discrete shells, within a conversion electron spectrum, separate lines will appear corresponding to ejection of K, L, M, etc. shell electrons.

To quantify the process of internal conversion, and its competition with  $\gamma$ -ray decay, an internal conversion coefficient ( $\alpha$ ) is defined as follows:

$$\alpha = \frac{\text{number of internal conversion decays}}{\text{number of } \gamma\text{-ray decays}} = \frac{\lambda_{IC}}{\lambda_{\gamma}}. \quad (2.15)$$

As there are contributions to the internal conversion process from electrons in a

number of electron shells, the total probability of decay,  $\alpha_{total}$  is given by summing  $\alpha$  for all possible atomic electrons. However,  $\alpha_{total}$  is usually dominated by contributions from ejection of inner (i.e. K and L) shell electrons.

Compilations for internal conversion coefficients are available [61], which provide the internal conversion coefficient for each atomic electron shell, as well as the total value. Internal conversion is expected to compete most strongly with  $\gamma$ -ray decay for heavy elements (high  $Z$ ), and low transition energies (low  $E$ ) [3].

## 2.3 Summary of the decay of exotic nuclei

Governed by the selection rules presented in Table 2.1, the allowed  $\beta$  decay of a state in the parent nucleus selectively populates states in the daughter according to  $\Delta J = 0, 1$ . Usually the  $\beta$ -decaying state is the ground state, though isomeric states may also undergo  $\beta$  decay. If the spin and parity of the decaying state is known, the selectivity of the  $\beta$ -decay process immediately provides limitations for the possible  $J^\pi$  values of the states populated in the decay.

Following the  $\beta$ -decay process, excited states populated in the daughter will de-excite by  $\gamma$ -ray emission to the ground state, or if the populated state is above the neutron separation threshold for the nucleus, by neutron emission to states in the  $\beta n$  daughter.  $\beta$ -delayed neutron emission can be identified and quantified by monitoring the  $\gamma$ -rays emitted when states in the  $\beta n$  daughter de-excite, as discussed in Section 2.1.3. Emitted  $\gamma$  rays provide information not only on the energy of states in the daughter, but can also limit spin and parity values, when combined with other information. The most intense  $\gamma$ -ray transitions will, in general, correspond to low multipolarity transitions, usually limiting non-isomeric transitions to  $\Delta J = 1, 2$ . This requirement can further constrain possible  $J^\pi$  values for states populated in the decay based on the observed  $\gamma$ -ray transitions connecting to other states. Considering energetics,  $\gamma$  rays may de-excite a state directly to the nuclear ground state, in which

case the  $\gamma$ -ray energy is equal to the excitation energy of the state. Alternatively,  $\gamma$  rays may occur in cascade, through an intermediate state. Level energies can be determined by looking for  $\gamma$  energy sums in the case of  $\gamma$ -cascades. Often, there is more than one possible cascade, and identifying  $\gamma$ -ray transition sums can help in building up nuclear level schemes.  $\gamma$ - $\gamma$  coincidence measurements also provide invaluable information in determining  $\gamma$ -ray cascades, while  $\gamma$ -ray transition intensities can additionally constrain the possibilities.

Prompt, or isomeric  $\gamma$ -rays can be similarly used to determine low-energy level schemes of parent nuclides. Summing relationships and  $\gamma$ -ray intensities provide valuable input for assembling level structures from prompt  $\gamma$ -ray data.

The very powerful techniques of  $\beta$ -delayed  $\gamma$ -ray spectroscopy and prompt  $\gamma$ -ray spectroscopy were used to study the low-energy level structures of neutron-rich nuclei in the  $fp$  shell in the present work. The next chapter will detail the experimental set-up used for the present study.

# Chapter 3

## Experimental Setup

The motivation for nuclear structure studies of exotic neutron-rich radioactive isotopes was presented in Chapter 1, focusing on important cases in the  $fp$  shell. The second chapter presented the fundamentals of  $\beta$  and  $\gamma$  decay, discussing the selectivity of these processes and the utility of  $\beta$ -delayed and prompt  $\gamma$ -ray spectroscopy. This chapter focuses on the more practical aspects of the experimental set-up used in two  $\beta$ -decay experiments that studied neutron-rich  $fp$  shell nuclei at the National Superconducting Cyclotron Laboratory (NSCL) at Michigan State University. Production and separation of the short-lived isotopes of interest using fragmentation and in-flight separation is discussed. The details of the experimental end-station detectors, including the  $\beta$  counting system (BCS) and Segmented Germanium Array (SeGA) are presented, including a description of the readout electronics and calibrations performed for each detector system. Details of the procedure for implantation-decay correlations and elements of data analysis are also included.

### 3.1 Isotope production and identification

Only a handful of very long-lived radioisotopes are naturally abundant on Earth. Thus, to study unstable nuclei, it is necessary to produce these species in an artificial

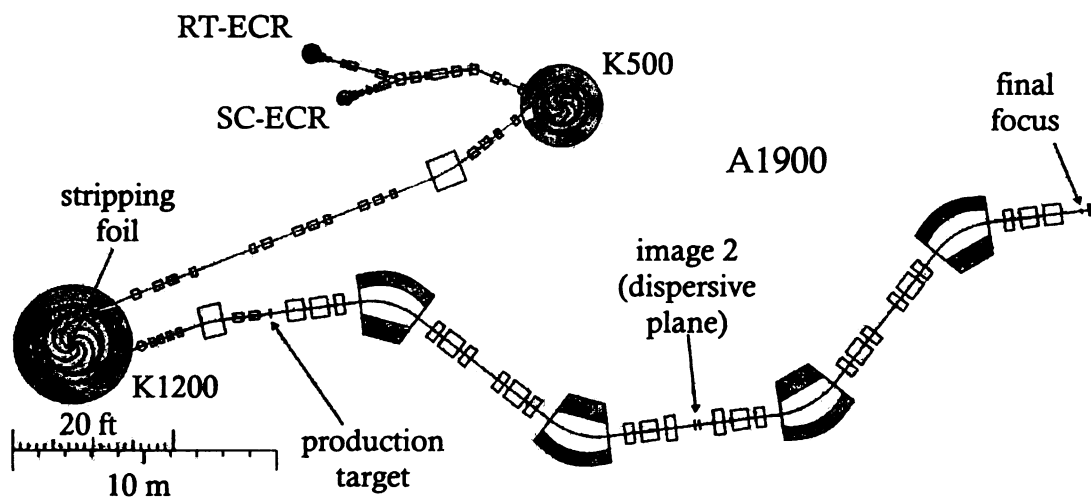


Figure 3.1: Schematic of the NSCL Coupled Cyclotron Facility, showing the K500 and K1200 cyclotrons and the A1900 fragment separator.

way. At NSCL, secondary beams of exotic rare isotopes are produced using the projectile fragmentation technique. The fragmentation process involves the interaction of a medium-energy primary beam (100-160 MeV/nucleon) on a stationary target. The primary beam is a stable isotope that is first ionized in one of the NSCL's electron cyclotron resonance (ECR) ion sources. The primary beam of ions is then accelerated by the coupled K500 and K1200 cyclotrons, shown schematically in Fig. 3.1. After extraction out of the K1200 cyclotron, the primary beam has an energy in the range 100 to 160 MeV/nucleon. The beam is then impinged on a production target. Typically the production targets are thin  $^9\text{Be}$  foils with thicknesses of order hundreds of  $\text{mg}/\text{cm}^2$ . Beryllium is used because of its high number density and robust physical properties. Fragmentation of the primary beam in the production target, in which a range of nucleons is abraded from the heavy beam, results in the production of nuclei between the  $A$  and  $Z$  of the primary beam and hydrogen. As fragmentation reactions are mostly peripheral reactions, there is a relatively small momentum transfer [4], and the surviving larger-mass fragments emerge from the thin production target with energies close to that of the primary beam. These secondary beam components are forward focused and continue into the A1900 fragment separator [62].

Given the large variety of ions produced in the fragmentation process, and the low production rates for the most exotic nuclei, it is critical to efficiently separate the ions of interest from all others produced. This is accomplished at NSCL using the A1900 fragment separator [62]. The A1900 separator is a large acceptance, achromatic, high resolution separator. Fragments entering the separator after the production target are separated by a combination of magnetic selection and energy loss ( $B\rho-\Delta E-B\rho$ ). Ions of a single magnetic rigidity,  $B\rho = mv/q$ , are selected in the first stage of the separator. Since ions emerge from the production target with approximately the same velocity ( $v$ ), this first separation selects ions with nearly the same mass/charge ( $m/q$ ) ratio. At the second intermediate image of the separator, the dispersive image (image 2, or I2), maximum horizontal dispersion of the beam is present and the ions pass through a wedge-shaped energy degrader. The ions entering the wedge have the same  $B\rho$ , but experience an energy loss proportional to  $Z^2$  in the wedge material, and thus exit the wedge degrader with different energies, and different momenta. A second  $B\rho$  separation stage in the second half of the separator then provides isotopic resolution [63].

The rate and purity of the secondary beam are determined by the composition and thickness of the production target and wedge degrader, as well as the momentum acceptance settings. Variably-adjustable slits are located at each of the three intermediate images of the separator, and can be narrowed to limit the momentum acceptance of the separator below the maximum  $\Delta p/p \sim 5\%$ .

The A1900 is a versatile device, and can be tuned to accommodate the needs of a wide variety of experiments. Many experiments require a high level of purity in the secondary beam, while others have more stringent requirements in terms of the overall fragment rate. The two experiments discussed in this dissertation made use of so-called “cocktail beams”, with multiple component nuclei, as the overall beam rate, and not beam purity, was most important.

Regardless of the specific requirements of a given experiment, a critical experi-

mental necessity is particle identification. Nearly all experiments at NSCL use the combination of energy loss in a thin detector and time-of-flight (TOF) to identify secondary beam particles. The general requirement for particle identification is thus two detectors separated by some distance over which to measure a time of flight. The BCS set-up measures energy loss in a silicon PIN detector, which is a part of the BCS detector telescope, described in detail in the following section. The time-of-flight measurement with the BCS uses the signal from the energy-loss PIN as a start, and either the cyclotron RF signal, or a signal from a plastic scintillator at image 2 of the A1900, as a stop signal. The plastic scintillator can also be used to provide an event-by-event momentum correction to the time-of-flight for those experiments in which the A1900 is operated with a large momentum acceptance. The I2 scintillator is read out by two photomultiplier tubes, one on each end, permitting determination of the approximate position of fragments in the scintillator. The position information is used to correct time-of-flight measurements for the differing path lengths and velocities of ions when a large momentum acceptance is used. Such time-of-flight corrections were necessary for both experiments discussed in this dissertation.

This section has described in general terms the production, separation and identification of exotic nuclei at NSCL. The following subsections present the specific details for production of the cocktail beams used in NSCL experiments 05101 and 07509, the experiments discussed in this dissertation.

### 3.1.1 NSCL experiment 05101

The main focus of NSCL experiment 05101 was the study of neutron-rich  ${}_{20}\text{Ca}$  isotopes, and settings of the A1900 magnetic rigidities were optimized for  ${}^{54}\text{Ca}$  and  ${}^{54}\text{K}$  production. Some data, however, were taken with an incorrect target setting, which resulted in a secondary beam of isotopes in the region of  ${}^{60}\text{V}$ . The fragmentation process used to produce these neutron-rich nuclei was the interaction of a  ${}^{76}\text{Ge}$  beam with a Be target. The primary beam of  ${}^{76}\text{Ge}$  was ionized to  $12^+$  in the room-temperature

ECR ion source and accelerated to 11.6 MeV/nucleon in the K500 cyclotron. Following foil stripping to a charge state of  $30^+$ , the  $^{76}\text{Ge}$  primary beam was accelerated to a full energy of 130 MeV/nucleon by the K1200 and impinged on a 47-mg/cm<sup>2</sup>  $^9\text{Be}$  target, located at the object position of the A1900 separator. Secondary fragments were separated through the A1900 with magnetic rigidity settings of  $B\rho=4.403$  Tm before the wedge, and  $B\rho=4.134$  Tm following a 300 mg/cm<sup>2</sup> Al wedge located at the intermediate image of the separator. The full momentum acceptance of the A1900 ( $\Delta p/p\sim 5\%$ ) was used for fragment collection. Given the large momentum acceptance used in the experiment, the plastic scintillator at the dispersive image of the A1900 (I2) was used for event-by-event momentum correction, and as the stop for the time-of-flight measurement. The start of the TOF measurement was provided by the signal of the most upstream PIN detector in the BCS silicon telescope, PIN01, described in the next section. The secondary cocktail beam consisted of  $\sim 10$  isotopes, including  $^{60}\text{V}$ , delivered to the experimental end-station of the BCS + SeGA located in the N3 vault. The particle identification plot for this setting is shown in Fig. 3.2(a).

### 3.1.2 NSCL experiment 07509

The isotopes of interest in NSCL experiment 07509 were those centered only around  $^{54}\text{Ca}$ . The primary beam of  $^{76}\text{Ge}$  was accelerated to 130 MeV/A in the same manner as in NSCL experiment 05101, which was detailed in section 3.1.1. The beam was impinged on a 352-mg/cm<sup>2</sup> thick Be production target, and the projectile-like fragments entered into the A1900 fragment separator. The first half of the separator was set to a magnetic rigidity of 4.103 Tm. A thin 45 mg/cm<sup>2</sup> Al wedge was placed at the A1900 intermediate image to provide differential energy loss. The second half of the separator was set to a magnetic rigidity of 4.030 Tm to optimize production and separation of  $^{54}\text{Ca}$ . The A1900 was operated with a maximum momentum acceptance of  $\sim 5\%$ . In total 24 isotopes, including  $^{54}\text{Ca}$ , were directed to the experimental end station set up in the S2 vault. As was the case in experiment 05101, the TOF

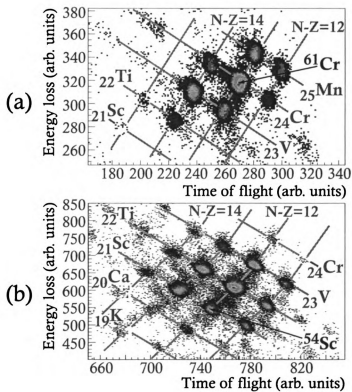


Figure 3.2: Particle identification plots for the relevant experimental settings in NSCL experiment (a) 05101, and (b) 07509. In both cases, time of flight measurements were started by the signal from the most upstream PIN detector of the BCS, and stopped by a signal from the I2 scintillator. Energy loss was measured in the upstream PIN detector of the BCS. The particle groups were identified by their subsequent decay.

measurement was started by the signal from the upstream PIN detector of the BCS, PIN01, and stopped by the delayed signal from the I2 scintillator. The I2 scintillator was also used to provide event-by-event momentum correction for the TOF. The particle identification plot for experiment 07509 is shown in Fig. 3.2(b).

## 3.2 Detector apparatus for $\beta$ -decay experiments

The experimental apparatus for both experiments discussed here consisted of the NSCL  $\beta$  counting system (BCS), and detectors from the SeGA. Secondary beam fragments were implanted into the detectors of the BCS, which provided triggers for both implantation and  $\beta$ -decay events.  $\gamma$  rays were detected in the SeGA detectors, and  $\gamma$ -ray events were recorded for both implantation and decay processes. The following sections describe the end-station systems in detail for NSCL experiments 07509 and 05101. The end-station set-ups for these two experiments were nearly identical. However, the minor differences between the set-ups will be noted when present.

## 3.3 $\beta$ Counting System

The NSCL  $\beta$  counting system (BCS) [64] consists of a stack of Si detectors. A schematic of the BCS detectors as set-up in NSCL experiment 07509 is shown in Fig. 3.3. The centerpiece of the system is a highly-segmented double-sided Si microstrip detector (DSSD), into which the secondary beam is implanted. The high segmentation of the implantation detector permits event-by-event correlation of fragment implantations with their subsequent  $\beta$  decays. The detectors of this system as set-up for NSCL experiment 07509 are described in this section. The readout electronics, calibration procedures and calibration results are also described.

The central detector of the BCS was a 4 cm by 4 cm,  $40\times 40$  DSSD, manufactured by Micron Semiconductors. The segmentation of the detector with  $40\times 1$  mm strips

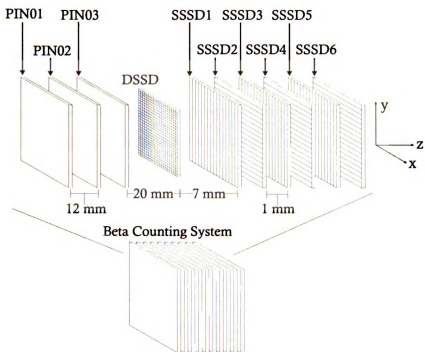


Figure 3.3: Schematic diagram of the silicon detectors which constitute the NSCL  $\beta$  Counting System. The arrangement of detectors for experiments 07509 and 05101 were as pictured; for details regarding detector thicknesses, see the text. Figure adapted from Ref. [65].

on the front and  $40 \times 1$  mm perpendicular strips on the back resulted in electrical segmentation into 1600 individual pixels, each of which act as an individual detector. Fragments were continuously implanted in this detector, and implantations were correlated with decays on an event-by-event basis. The correlation requirements are described in detail in Section 3.5 at the end of this chapter. A DSSD detector thickness of  $995 \mu\text{m}$  was used in NSCL experiment 07509, while the implantation detector used in experiment 05101 had a nominal thickness of  $979 \mu\text{m}$ .

Downstream of the implantation detector were six  $5 \text{ cm}$  by  $5 \text{ cm}$ , 16-strip single-sided silicon strip detectors (SSSDs), which constituted the  $\beta$  calorimeter. Segmented in only one direction, the orientation of strips in the SSSDs was alternated between the horizontal ( $x$ ) and vertical ( $y$ ) directions for adjacent detectors, as is shown in Fig. 3.3. This arrangement of detectors allowed for two-dimensional position information for any particles moving downstream of the DSSD. The thicknesses of SSSD1 through SSSD6 for NSCL experiment 07509 were  $975 \mu\text{m}$ ,  $981 \mu\text{m}$ ,  $977 \mu\text{m}$ ,  $989 \mu\text{m}$ ,  $988 \mu\text{m}$ , and  $985 \mu\text{m}$  respectively. For experiment 05101, the thicknesses were  $981 \mu\text{m}$ ,  $977 \mu\text{m}$ ,  $975 \mu\text{m}$ ,  $988 \mu\text{m}$ ,  $989 \mu\text{m}$ , and  $985 \mu\text{m}$  for SSSD1-SSSD6 respectively.

A stack of three silicon PIN detectors were placed upstream of the DSSD, which acted as active energy degraders and provided the energy loss and timing information required for particle identification. The thicknesses of the three PIN detectors were  $297 \mu\text{m}$  for PIN01,  $297 \mu\text{m}$  for PIN02, and  $488 \mu\text{m}$  for PIN03, during NSCL experiment 07509. Experiment 05101 had thicknesses of  $991$ ,  $997$  and  $309 \mu\text{m}$  for PIN01, PIN02, and PIN03, respectively.

A passive aluminum energy degrader was placed upstream of the PIN detectors to ensure fragments were stopped near the center of the DSSD implantation detector. A  $7.5 \text{ cm} \times 7.5 \text{ cm}$  Al degrader foil was held on a rotating mount, that was used to adjust the angle, and thus the effective thickness, of the foil with respect to the beam. The Al degrader thickness for experiment 07509 was  $4 \text{ mm}$ , while experiment 05101 only required a degrader with a thickness of  $2.3 \text{ mm}$ .

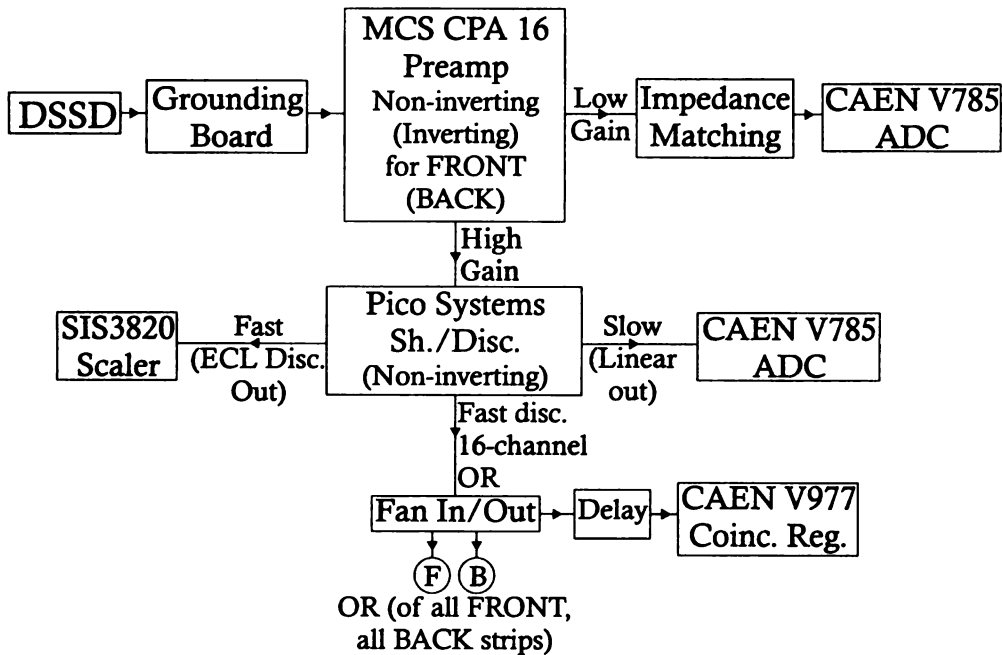


Figure 3.4: Schematic diagram of the signal processing electronics for the DSSD of the BCS.

### 3.3.1 Electronics

A schematic diagram of the signal processing electronics for the DSSD is shown in Figure 3.4. Signals for the front and back segments were carried from the detector within the vacuum chamber to feedthroughs on a backplate by separate ungrounded 50-pin ribbon cables. Outside the vacuum, 50-pin ribbon cables carried signals for the front and back of the DSSD to a grounding board. On the ground board, signals from each strip were paired with ground signals, and were grouped in units of 16 to match the input channel density of the conventional analog electronics. The grouping performed on the ground board created blocks with F1-16, F17-32, F33-40, B1-16, B17-32 and B33-40, where F and B represent front and back strips respectively, and numbers refer to the strip number of the detector.

One of the challenges of using a single detector to detect both implantation events and  $\beta$  decays is the dynamic range required to measure both types of events. Ion implantation deposited energies of order several GeVs, while  $\beta$  decays deposited much

lower energies, of order a few hundred keVs. The BCS overcomes this challenge by using dual-gain preamplifiers from Multi Channel Systems (MCS). The 16-channel preamps have a high-gain amplification for the lower-energy  $\beta$  signals of 2 V/pC, and a low-gain amplification for the high-energy implantation signals of 0.1 V/pC. The 50  $\Omega$  low-gain signals from the MCS preamps were impedance matched to the 1 k $\Omega$  inputs of 32-channel CAEN 785 VME analog-to-digital converters (ADCs). The high-gain signals from the preamplifiers required further signal processing to amplify the small signal. The high-gain outputs of the MCS preamps were sent into PicoSystems programmable CAMAC shaper/discriminator modules. These 16-channel modules have programmable discriminator thresholds and gains, and analog energy and digital timing outputs for each channel. A logical OR of the discriminator output of all 16 channels is also available from each module. Analog energy signals were sent to VME CAEN 785 ADCs, where each block of 16 high-gain signals and the corresponding low-gain signals were digitized in a single ADC module. The digital timing outputs were sent to SIS 3820 VME scaler modules for rate monitoring on a channel-by-channel basis. The logical OR of the 16 channels was used to define the master trigger logic, as discussed at the end of this section, and also sent to a VME CAEN V977 coincidence register for sparse readout. A given 32-channel ADC contained both high- and low-gain signals from one block of 16 DSSD channels. The coincidence register reduced the event size by allowing restriction of the ADC digitization to those modules that had data above threshold.

Shown in Fig. 3.5 is a schematic of the electronics for the six SSSDs downstream of the implantation DSSD. Signals from each of these 16-strip detectors were carried, with paired grounds, by 34-pin ribbon cables from the detector to the backplate feedthroughs, and from the backplate to MCS preamps identical to those used with the DSSD. However, in the case of the SSSDs, only high-gain signals were processed. Similar to the DSSD electronics, the SSSD signals were amplified and discriminated using PicoSystems shaper/discriminator modules. Analog energy signals were sent to

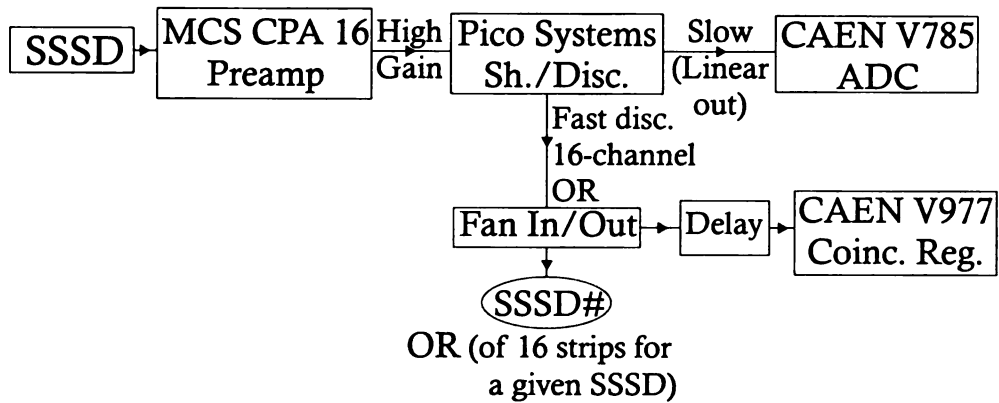


Figure 3.5: Schematic diagram of the signal processing electronics for the SSSDs of the BCS.

VME CAEN 785 ADCs, with two SSSDs worth of signals in a single ADC, in pairs of SSSDs 1 and 2, 3 and 4, and 5 and 6. The individual channel discriminator outputs were not monitored in scalars. However, the OR of the 16 discriminator outputs was sent to the VME CAEN V977 coincidence register allowing sparse readout of the ADCs, as was the case in the DSSD electronics. Additionally, for NSCL experiment 07509, a logical OR was taken of the ORs of the discriminator signals from SSSD5 and SSSD6. This signal was used to veto the master gate trigger against light particles that did not stop in the DSSD, and increase the data acquisition live time. Such a veto was not required in NSCL experiment 05101.

The electronics for all three upstream PIN detectors were essentially identical. The signal from each detector was sent through a four-channel Tennelec TC178 preamplifier, and then a Tennelec TC248 shaping amplifier. The slow unipolar output from the shaping amplifier was then sent to a VME CAEN 785 ADC, while the fast timing output was analyzed by a Tennelec TC455 constant fraction discriminator (CFD). One of the CFD outputs from PIN01 was sent to a coincidence register. The set bit for PIN01 was used to control the readout of the ADC containing the signals from all three PIN detectors, as well as signals derived from the PIN detectors, including those from time-to-amplitude converters (TACs) used to measure time-of-flight. Timing signals from the CFDs of all three PIN detectors were distributed to VME SIS

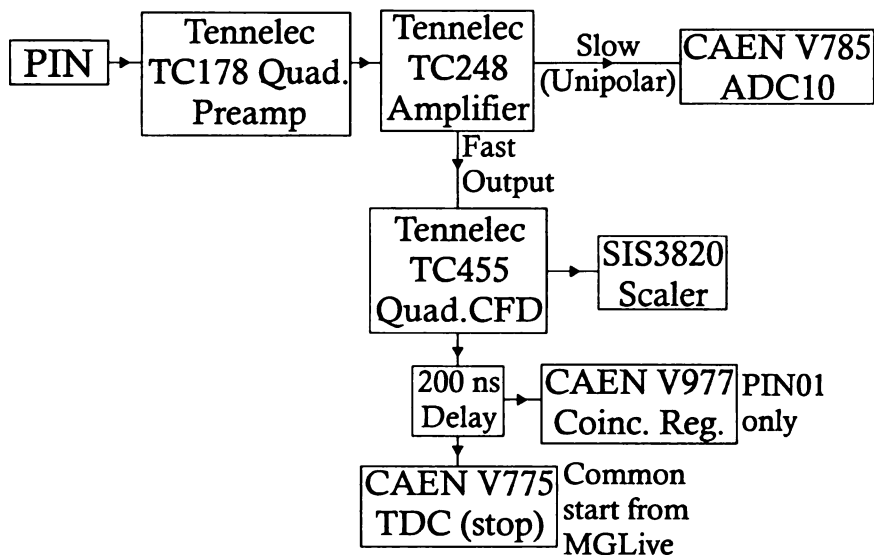


Figure 3.6: Schematic diagram of the signal processing electronics for the three PIN detectors used in NSCL experiments 07509.

3820 scaler modules for rate monitoring, and to time-to-digital converters (TDCs) as a stop signal, where the module was gated with a common start derived from the master trigger of data acquisition. Figure 3.6 is a schematic of the electronics for the PIN detectors.

The master-gate trigger (MG) for data readout was derived using the discriminator signals from the implantation detector, the DSSD. The MG for experiment 07509 was generated in hardware by taking a logical OR of all of the front strips logically ANDed with a logical OR of all of the back strips of the DSSD. The MG was vetoed by the logical OR of signals from SSSD5 and SSSD6. The MG was more complicated in the case of NSCL experiment 05101. The MG was generated by a logical OR of: (1) DSSD front AND back, as described for 07509, (2) signal above threshold in any of the 16 strips of the most upstream SSSD01, and (3) signal above threshold in the most upstream PIN01. A master gate live (MGLive) signal was derived in both experiments from MG by requiring a hardware logical AND with a signal from the data acquisition computer indicating not-busy. The MGLive signal was used to trigger data acquisition, as well as to generate digitization gates for all ADCs, TDCs, and

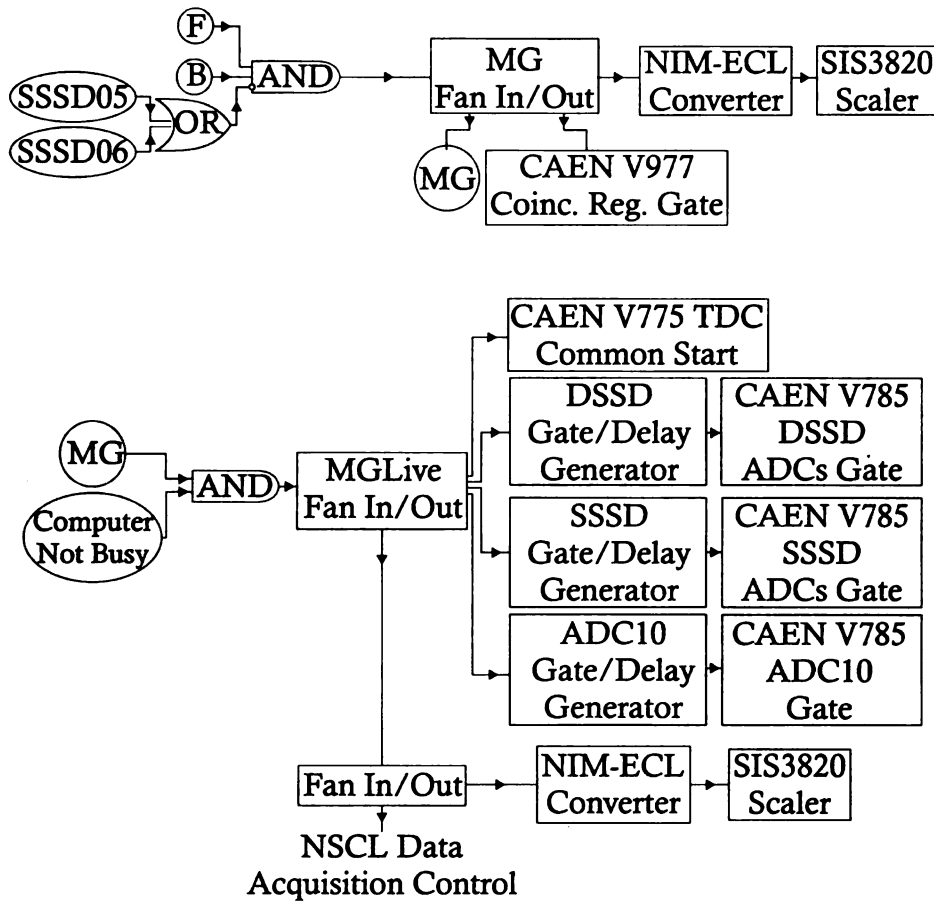


Figure 3.7: Schematic diagram of the trigger electronics for data acquisition of NSCL experiment 07509.

the coincidence register. A schematic of the trigger electronics for 07509 is shown in Fig. 3.7.

A critical requirement for  $\beta$ -decay experiments with continuous implantation is the ability to correlate implantations and their subsequent decays, and have a measure of the time elapsed between the events. To this end, each event included a timestamp generated by a SIS3820 scaler module specially configured to act as a 50-MHz clock. The 32-bit clock data word, which had a resolution of 20 ns per clock tick, was scaled into a 24-bit parameter in software. This clock parameter, with a resolution of 5.12  $\mu$ s per scaled tick, was sufficient for the measurement of  $\beta$ -decay half-lives in the ms regime.

### 3.3.2 BCS calibrations

Each of the silicon detectors of the Beta Counting System was calibrated for energy using a  $^{228}\text{Th}$   $\alpha$  source. An  $\alpha$  spectrum was collected from the  $^{228}\text{Th}$  source for each detector, containing sufficient statistics ( $\sim 100$  counts/peak) to allow position determination of the four main  $\alpha$  peaks below 8 MeV, in all strips including those at the edge of the detector. Each strip was gain matched by adjusting a slope parameter to place the lowest-energy (5.4 MeV)  $\alpha$  peak at channel 350 in a 9-bit histogram in each strip of the detector. Calibrated spectra included, in addition to gain-matching, adjustment by an offset determined by the pedestal of the ADC. A simple shift was applied to each strip to align the first data channel for each strip at zero. Histograms of the raw energy parameter for a representative strip (strip 20) on the front and back of the DSSD are shown in Figures 3.8(a) and (b), respectively. Calibrated spectra for the same detector strips following the gain-matching and offset adjustment, are presented in Figures 3.8(c) and (d).

A  $^{90}\text{Sr}$  source was used to set energy thresholds for each silicon detector. The  $\beta$  decay of  $^{90}\text{Sr}$  has an end-point energy of 546 keV, but the daughter  $^{90}\text{Y}$ , which also undergoes  $\beta$  decay, has an end-point energy of 2.280 MeV [2]. The signal induced in a 1 mm thick Si detector for such  $\beta$  energies is a  $\Delta E$  signal of order hundreds of keV. Thus, the thresholds of detectors deep within the stack of the BCS detectors could be checked even after other detectors were in place. Hardware thresholds were set for each BCS detector (the DSSD and SSSDs) by comparing the analog output triggered by the CFD output for the same detector channel on a digital oscilloscope. Spectra were then collected for each strip using the  $^{90}\text{Sr}$  source, and software thresholds were established based upon the position of the noise signal. The calibrated  $^{90}\text{Sr}$  spectra for DSSD front strip 20 and back strip 20 are shown in Figures 3.8(e) and (f), respectively. The arrow in the figures indicates the position of the software threshold, which was applied when determining the signals contributing to sums, etc., in data analysis.

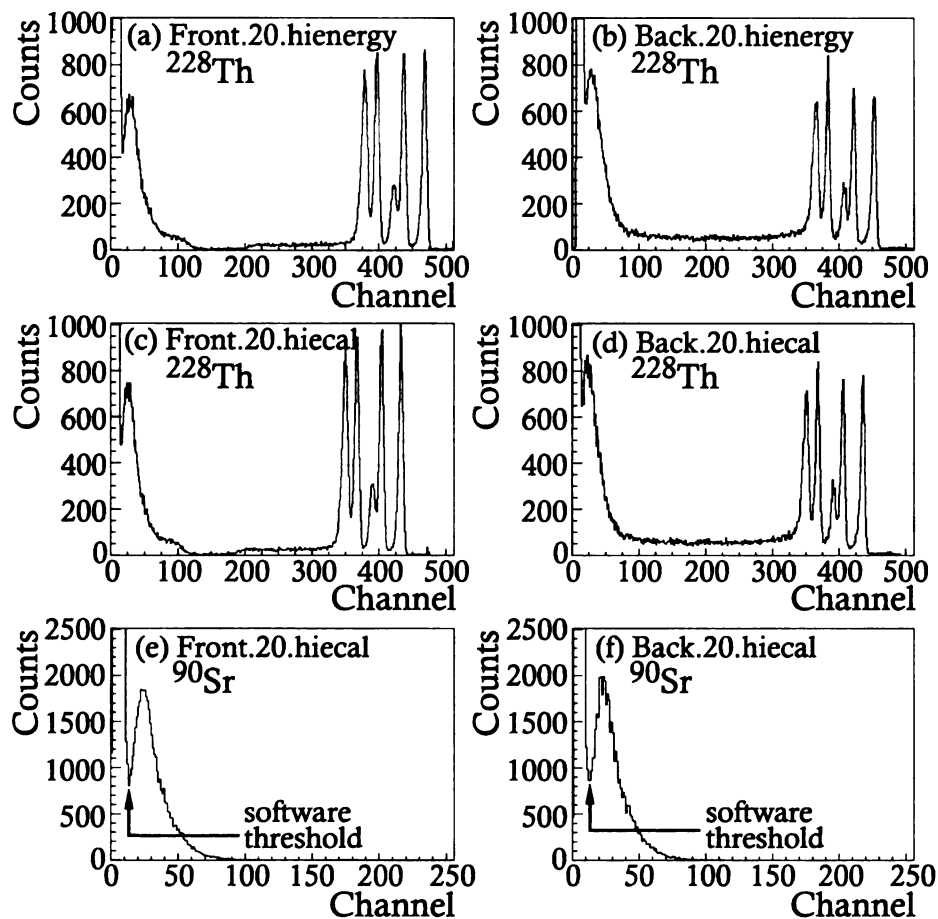


Figure 3.8: Calibration spectra for a representative front and back DSSD strip from NSCL experiment 07509. (a) and (b) are the raw ADC spectra for a  $^{228}\text{Th}$  source on the front and back of the detector respectively, while (c) and (d) are the same spectra following gain-matching and offset adjustment. (e) and (f) are calibrated  $^{90}\text{Sr}$  spectra for the front and back strips of the DSSD respectively, from which software thresholds were set.

## 3.4 Segmented Germanium Array

Detectors from SeGA [66] were used for monitoring prompt and  $\beta$ -delayed  $\gamma$  rays during NSCL experiments 07509 and 05101. Each SeGA detector consists of a single cylindrically symmetric, n-type high-purity Ge crystal, with a diameter of 7 cm, and a length of 8 cm. The core electrode lies along the central axis of the detector. The outside surface of each crystal is electrically segmented into 4 quadrants azimuthally, and  $8 \times 10$  mm thick slices longitudinally. The high segmentation of the SeGA detectors is useful for in-beam  $\gamma$ -ray spectroscopy experiments with fast beams, where a Doppler correction to the  $\gamma$ -ray detected energy is critical for achieving the best possible resolution [66]. However for the case of  $\beta$ -delayed  $\gamma$ -ray spectroscopy, the nuclei are stopped before  $\gamma$ -ray emission. Therefore determination of the position of interaction from the segmentation of SeGA is not required, and only the central contact signal for each SeGA detector was read out during NSCL experiments 07509 and 05101.

A total of 16 SeGA detectors were mounted in a close-packed geometry surrounding the beam pipe containing the BCS detectors, as shown in Fig. 3.9. The detectors were arranged in two concentric circles of eight detectors each, a configuration known as  $\beta$ -SeGA or barrel-SeGA. The crystal of each detector was oriented with its long axis parallel to the beam pipe, face to face with a detector in the opposite ring. The array was positioned such that the implantation detector of the BCS defined the plane between the two rings of detectors. The electronics for the SeGA detectors, and details of the energy and efficiency calibrations for the array are described in the next sections.

### 3.4.1 Electronics

A schematic of the SeGA electronics is presented in Figure 3.10. Two identical output signals are available from each SeGA detector from the internal preamplifier attached

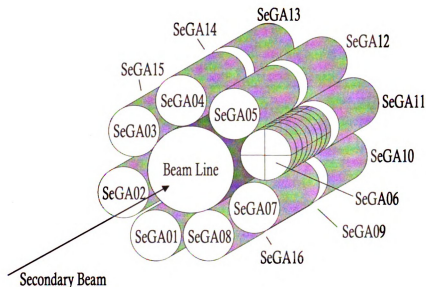


Figure 3.9: Geometric arrangement of the 16 SeGA detectors surrounding the beam pipe containing the BCS silicon detectors.

to the central contact signal. These two identical signals were distributed through different pathways to provide both timing and energy signals. One signal was sent to an Ortec 863 timing fraction analyzer (TFA) for fast shaping, and then into a Tennelec TC455 constant fraction discriminator. One of the CFD outputs was delayed, and used as the stop signal for a Philips CAMAC 7186H TDC that was started by the MGLive signal. A second CFD output was sent to a VME SIS3820 scaler module for rate monitoring. The other central contact preamplifier signal was processed by an Ortec 572 shaping amplifier and the unipolar output was digitized by a four-channel Ortec AD413A CAMAC ADC. The ADC was gated by a signal derived from the MGLive trigger. The width of this gate was set to  $20 \mu\text{s}$  to permit the detection of isomers with half-lives in the  $\mu\text{s}$  range following implantation events. The time between implantations and photon emission was measured by a time-to-amplitude converter (TAC), which was started on the MGLive signal, and stopped by an OR of all of the SeGA CFD outputs.

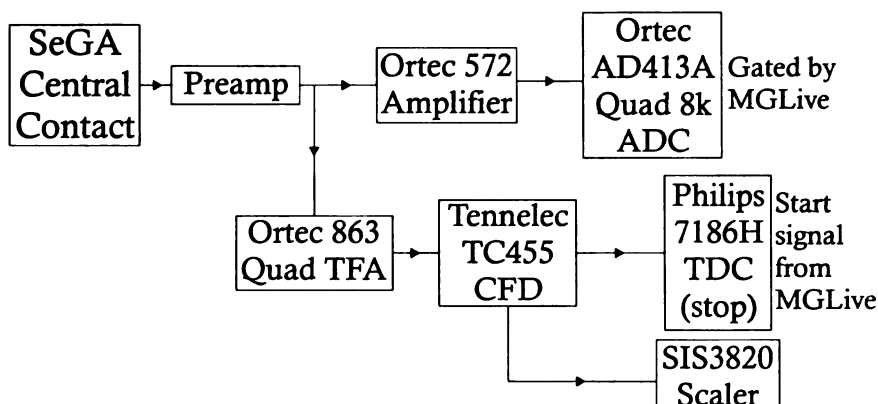


Figure 3.10: Schematic diagram of the signal processing electronics for SeGA detectors.

### 3.4.2 SeGA Calibrations

Energy calibrations were completed for the entire array of SeGA detectors before, during, and after NSCL experiment 07509. Two calibration sources were used to calibrate the full 4-MeV range of the  $\gamma$ -ray histogram: a  $^{56}\text{Co}$  source, for the high-energy calibration, and a NIST-Standard Reference Material (SRM) source, containing the radionuclides  $^{154,155}\text{Eu}$  and  $^{125}\text{Sb}$ , suitable from 40 keV to 1500 keV. Energy calibration data were collected by triggering the data acquisition system on a logical OR of the CFD outputs for each of the 16 SeGA detectors. Calibration sources were placed outside of the beampipe and moved during the run to ensure that each detector accumulated sufficient statistics,  $\sim 50$  counts in the 2.6 MeV peak of  $^{56}\text{Co}$ , to perform the calibration. The calibration spectra were analyzed using the Oak Ridge Data Analysis and Manipulation Module (DAMM) to determine the centroid and associated error for the location of each  $\gamma$ -ray transition, based on a Gaussian fit. Energy calibration parameters were obtained from a third-order polynomial fit to the centroid for each peak as a function of the known  $\gamma$ -ray transition energy. A third-order polynomial was required to account for both non-linearity of the detector response at low energies, and a previously observed [67] non-linearity in the response of the Ortec AD413 ADCs between low ( $< 1.5$  MeV) and high energies. Application of calibration parameters in

software provided calibrated energy histograms for each SeGA detector. The energy resolution of all detectors was  $\leq 3.5$  keV full-width at half-maximum (FWHM) for the 1.3 MeV transition in  $^{60}\text{Co}$ . During experiment 07509, one of the detectors of SeGA exhibited poor gain stability, even shifting gain during a single hour-long run. Due to the instability of this detector, it was omitted from all analysis, leaving a 15-detector array for this experiment. All 16 detectors of the array were included in analysis for the case of experiment 05101.

The residuals from the energy calibration applied to each SeGA detector are presented in Figure 3.11. The residual is defined as the difference between the known  $\gamma$ -ray transition energy and the value deduced from the calibrated spectrum. Vertical error bars are the error in the centroid resulting from the fit of a Gaussian to a given peak in the calibrated energy spectrum. The residuals for the summed spectrum of all 15 SeGA detectors is given in Fig. 3.12. A conservative systematic error of  $\pm 0.25$  keV was attributed to the energy calibration of the SeGA detectors. This error encompasses the complete distribution of the residuals, and corresponds to approximately twice the root-mean square residual value. The errors quoted for  $\gamma$ -ray energies in the present work were determined by adding, in quadrature, this error from the energy calibration ( $\pm 0.25$  keV), and the error in the centroid of the peak locations as determined using DAMM.

One of the SeGA detectors, SeGA11, had to be recalibrated due to a gain shift during the course of experiment 07509. Well-known  $\gamma$ -ray transitions from nuclides in the cocktail beam made a recalibration possible. The  $\gamma$ -ray transitions used to recalibrate SeGA11 during experiment 07509 are summarized in Table 3.1. The residuals of the fit to these known transitions before the new energy calibration was implemented is depicted in Fig. 3.13(a), while the residuals with the corrected calibration are shown in (b). The recalibration did not alter the  $\pm 0.25$  keV systematic error for the full array attributed to the energy calibration. The gains of all other detectors were checked for gain shifts by monitoring the location of well-known transitions in

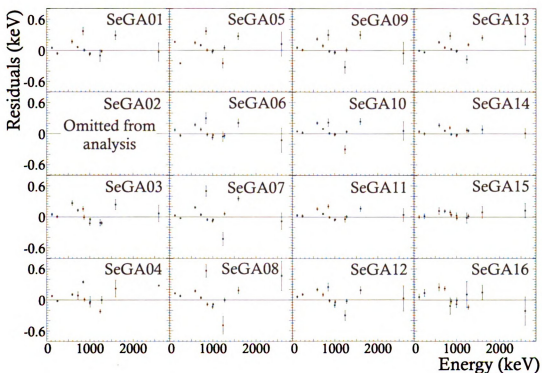


Figure 3.11: Residual plots for the 15 individual SeGA detectors included in the analysis of data from experiment 07509. The residual is defined as  $E_{\gamma}^{known} - E_{\gamma}^{exp}$ .

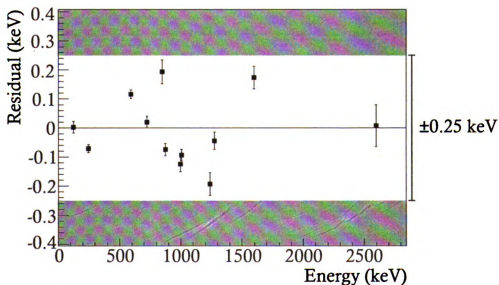


Figure 3.12: Residual plot for the sum of all 15 SeGA detectors used in experiment 07509. A systematic error of  $\pm 0.25$  keV (marked by the shaded bands) was attributed to the SeGA energy calibration.

Table 3.1: Known  $\gamma$ -ray transitions used to perform a re-calibration of SeGA11 during experiment 07509.

Source of Transition	$E_\gamma$ (keV)
$^{54}\text{Sc}$ isomer decay	$110\pm 1.0$ [68]
$^{57}\text{Ti}$ decay	$174.8\pm 0.4$ [69]
$^{57}\text{V}$ decay	$267.8\pm 0.3$ [70]
$^{55}\text{Ti}$ decay	$323.4\pm 0.4$ [71]
$^{56}\text{V}$ decay	$668.4\pm 0.3$ [70]
$^{55}\text{Ti}$ decay	$672.5\pm 0.4$ [71]
$^{57}\text{V}$ decay	$692.4\pm 0.4$ [70]
$^{58}\text{V}$ decay	$879.8\pm 0.4$ [70]
$^{54}\text{Sc}$ decay	$1001.2\pm 0.5$ [31]
$^{56}\text{V}$ decay	$1006.1\pm 0.3$ [70]
$^{58}\text{V}$ decay	$1056.4\pm 0.4$ [70]
$^{54}\text{Sc}$ decay	$1494.8\pm 0.8$ [31]
$^{57}\text{Ti}$ decay	$1861.5\pm 0.4$ [69]
$^{58}\text{V}$ decay	$2217.5\pm 0.4$ [70]

the data, but no other corrections were necessary.

Absolute peak detection efficiencies were deduced for each SeGA detector by placing the SRM standard source at the position of the DSSD within the vacuum chamber. Two calibration data sets were collected in parallel for each detector, one set using the NSCL data acquisition system (DAQ) triggered on the output of the CFD for the SeGA detector of interest, and the other using a PC-based multi-channel analyzer (MCA). The PC-based MCA collected data independent of the DAQ trigger, and recorded data for a dead-time adjusted total of 3600 s, thus assuring a true measurement of the absolute detector efficiency. The DAQ system was known to have a trigger rate dependence, but ambiguity in the ADC dead-time correction made absolute efficiency determination less certain. Thus, the two independent systems were used to cross-check one another and ensure a good determination of the  $\gamma$ -ray efficiency of the array. Peak efficiencies were deduced by comparison of the observed emission rates as detected by SeGA with the known activity of the isotopes in the SRM source. A relative efficiency measurement for photon energies above 1.5 MeV was also completed using a  $^{56}\text{Co}$   $\gamma$ -ray source. Data was taken using only the DAQ system, triggered by

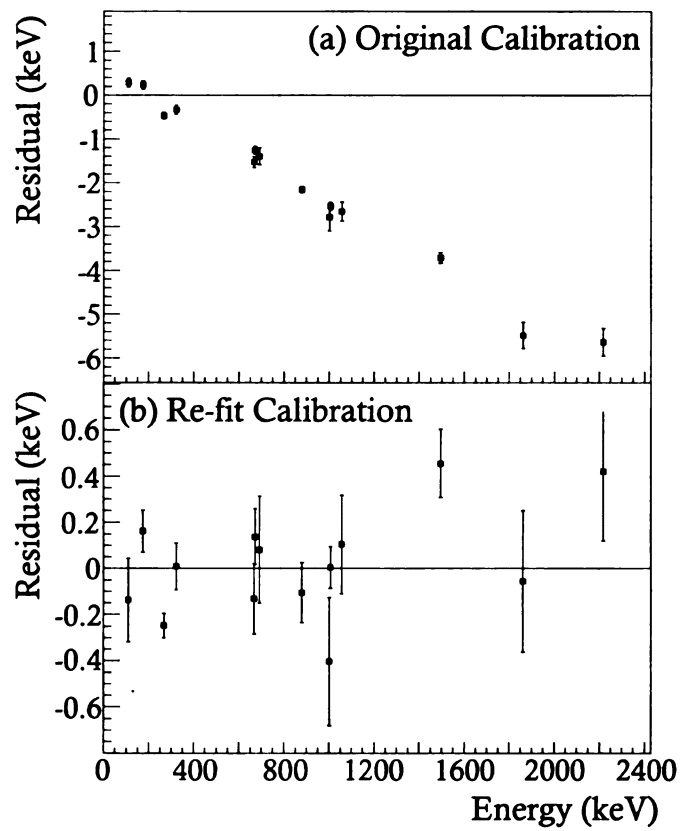


Figure 3.13: Residuals for the energy calibration of SeGA11 during gain-shifted runs using (a) the original energy calibration, and (b) a re-fit energy calibration based upon known  $\gamma$ -ray transitions within the data.

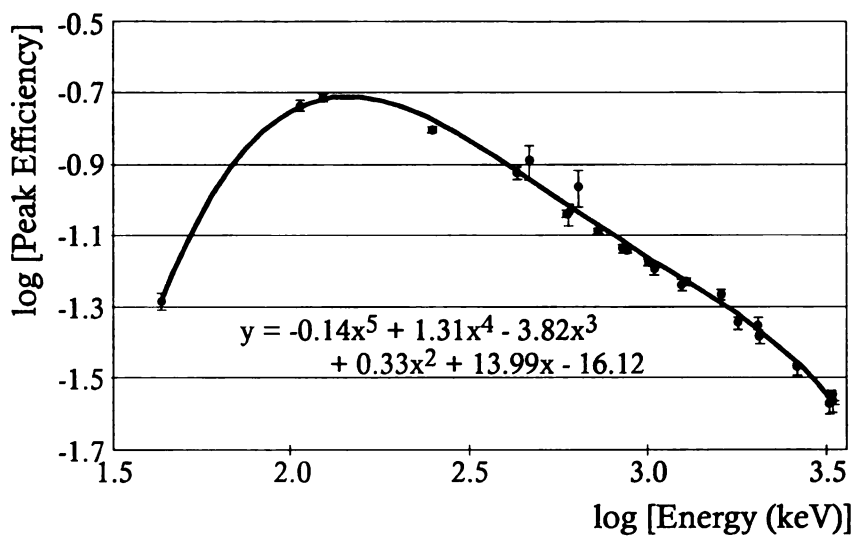


Figure 3.14: Peak detection efficiency curve for NSCL experiment 07509. Data points represent measured efficiencies using the NSCL data acquisition system. Data were fitted with a fifth-order polynomial, denoted by the solid line.

a logical OR of the individual SeGA detector CFD outputs for the relative efficiency measurement. Peak efficiencies were deduced from the  $^{56}\text{Co}$  data by assuming the same absolute efficiency for the 873.2 keV transition in  $^{154}\text{Eu}$  from the SRM source and the 846.7 keV transition in  $^{56}\text{Co}$ , and normalizing the other transitions in  $^{56}\text{Co}$  to this value based on known relative intensities. The resulting efficiency curve for SeGA for experiment 07509 is shown in Figure 3.14, and was fitted with a fifth-order polynomial. The peak efficiency for the array corresponds to 6.6 % at 1 MeV and 3 % at 3 MeV. Similar peak efficiencies were obtained, and an analogous efficiency curve produced for NSCL experiment 05101.

### 3.5 Data analysis: Correlations and data fitting

The previous sections of this chapter provided details of the physical experimental set-up used in NSCL experiments 05101 and 07509, including the beam delivery, detector systems, and electronics. This section describes the other critical component of correlation experiments with continuously implanted beams: the logic and methods

used to build up correlations from the data and to extract the values of interest, including half-lives and decay branching ratios, in a robust manner.

### 3.5.1 Implantation-decay correlations

The method of continuous implantation  $\beta$ -decay spectroscopy relies on the ability to correlate individual implantation events with their subsequent  $\beta$  decays. The method makes use of both position and time information to perform the correlations.

Each event was evaluated in software to determine the nature of the event. Raw signals from each detector were calibrated and compared to software-defined upper and lower thresholds. Software flags were set to indicate valid data for those detectors in which signals satisfied the threshold requirements. Additionally, for the segmented detectors in which multiple strips may have had valid signals for a given event, the energies observed in each strip were evaluated to localize the event to a single strip. The spatial position, or pixel  $(x, y)$  of an event in the DSSD was defined to be the front and back strip with the largest recorded energy signal.

Implantation events were identified as those with a valid signal in each of the upstream PIN detectors (PIN1, PIN2 and PIN3) as well in the low-gain histograms of both a front and back strip of the DSSD. Implantation events additionally required the absence of a valid signal in SSSD1. When these conditions were met for a given event, the event was positively identified as an implantation and the  $\Delta E$ , time-of-flight and time-stamp information was stored within a two-dimensional array in software, in the array element corresponding to the  $(x, y)$  position of the pixel of the DSSD to which the implantation had been localized.

Decay events were identified as those events which had no valid signal in any of the upstream PIN detectors but had a valid signal in the high-gain histograms of both a front and back strip of the DSSD. Once an event was assigned as a decay, a series of checks were made based on time and position to correlate the decay event with a previous implantation. The  $(x, y)$  position of the decay event was checked to

see the last time that an implantation event occurred at the same geometric location within the DSSD. Only identical  $(x, y)$  coordinates were considered in the case of experiment 07509 (implantation rates of  $\sim 100$  Hz). When rates were sufficiently low, as in the case of the other experiment 05101 (average implantation rate  $\sim 30$  Hz), the correlation position was extended to also allow correlation of a decay with an implantation in any of the eight nearest neighbor pixels  $(x \pm 1, y \pm 1)$ . If an implantation event had occurred, an additional check was made to ensure that there had not been back-to-back implantations in that pixel within a short time frame, which could cause ambiguity in assigning a decay to one implantation over the other. Once the integrity of the implantation was verified, the time between the decay event and the implantation was checked to ensure that the event had occurred within a pre-defined correlation time window for each isotope, established as some multiple of the expected decay half-life. With the geometric and temporal conditions met, the decay event was considered to be positively correlated with a previous implantation.

Decay curves were constructed for all isotopes by histogramming the time difference between the implanted ion of interest and the correlated  $\beta$  decay. Decay curves were fitted as described in Section 3.5.2 and the half-lives deduced for each isotope. Additionally, by integrating the decay curve for the parent isotope contribution, the total number of detected  $\beta$  decays for the parent was deduced. Combined with the total number of implanted ions from the particle identification spectrum, the average  $\beta$ -detection efficiency of the DSSD was calculated for each isotope. The average  $\beta$ -detection efficiency for all isotopes studied in NSCL experiment 07509 using a single-pixel correlation was found to be  $11.4 \pm 0.4\%$ .

The basic requirements for correlation of an implantation and its subsequent decay are well established. However, there are a number of variables which can be adjusted to optimize the correlation efficiency based on the experimental conditions and expected properties of the decay. The correlations are determined entirely by the constraints set by the geometry and timing in analysis. The following section describes the adjustable

variables in the correlation procedure, and the choices made in the present analysis based on implantation rates.

### **Implantation rates and correlation limits**

As discussed in the previous section, the two time frames critical to the correlation procedure are the minimum time between back-to-back implantations in a pixel, and the correlation time window, corresponding to the maximum elapsed time over which an implantation would be correlated with a decay. These time windows were adjusted in the data analysis on an isotope-by-isotope basis to optimize the correlations, using the expected half-life of the parent isotope. The correlation time windows were chosen to be approximately ten half-lives of the parent nuclide, permitting a good determination of the parent, subsequent generations, and the background contributions to a decay curve. The minimum time between back-to-back implantations was set to match the correlation time.

To minimize random correlations certain conditions related to the rate of events in the detector must be met. The implantation rate must be sufficiently low that, on average, the time between back-to-back implantations in a pixel is greater than the length of the correlation time window. The overall implantation rate for experiment 07509 was  $\sim 100$  Hz. However, these implantation events were not distributed evenly over the detector surface. The beam profile was such that pixels near the center of the detector experienced a higher implantation rate than those at the edge of the detector. An average of less than 5 s separated implantations in the most central pixels of the implantation DSSD. The average time between implantations for each pixel of the surface of the DSSD is shown in Fig. 3.15(a). However, for most nuclei included in experiment 07509, even the highest implantation rate allows a sufficiently long correlation time window. A more significant problem was posed by the build-up of activity from subsequent generations in pixels with higher implantation rates. With an average of four  $\beta$  decays to reach stability from each implanted fragment,

the accumulated activity in the detector creates a background of random correlations in all spectra. In Figure 3.15(b) is shown the average number of observed  $\beta$ -decay events occurring in a one-second time interval in each pixel of the detector. Assuming the average  $\beta$ -detection efficiency of  $11.4 \pm 0.4\%$ , the average rate of  $\beta$  decays is more than 3/s in the most central pixels. The higher background rates increase the chance of random correlations, and both  $\gamma$ -ray spectra and half-life curves will have pixel-dependent background contributions.

The non-uniformity of the beam profile was used to provide an alternate analysis of decays which required a longer correlation time window. A cut was made in position based upon the time between back-to-back implantations, and only a subset of pixels corresponding to those with  $>100$  s between back-to-back implantations was used for the primary analysis of isotopes with longer half-lives. The pixels satisfying the cut are shown in Fig. 3.15(c). The back-to-back implantation rate requirement was used in software to limit analysis to the  $\sim 800$  pixels, or half of the detector surface on the edge of the detector with lower rates. Imposing this restriction did not affect the average  $\beta$ -detection efficiency for a single-pixel correlation, but did result in a reduction of statistics by a factor of ten.

The benefits of making a restriction on the back-to-back implantation rate are best illustrated in an example. The  $\beta$  decay of  $^{55}\text{Ti}$  is reported to have a half-life of  $1.3 \pm 0.1$  s, and 9  $\gamma$ -ray transitions have been previously reported [71].  $^{55}\text{Ti}$  was a component of the cocktail beam in NSCL experiment 07509, and its decay was examined for both the subset of pixels of the DSSD shown in Fig. 3.15(c), and all pixels, with a correlation time window of 5 s. The resulting  $\beta$ -delayed  $\gamma$ -ray spectra are presented in Figs. 3.16(a) and (b) respectively. The known transitions in  $^{55}\text{Ti}$  and its daughter  $^{55}\text{V}$  are marked by the filled circles. The background contribution to the spectrum of Fig. 3.16(a) is reduced in the spectrum of Fig. 3.16(b), while the known transitions are apparent in both spectra. The half-life curve is also affected by background, as illustrated in Figs. 3.16(c) and (d). The decay curve generated from

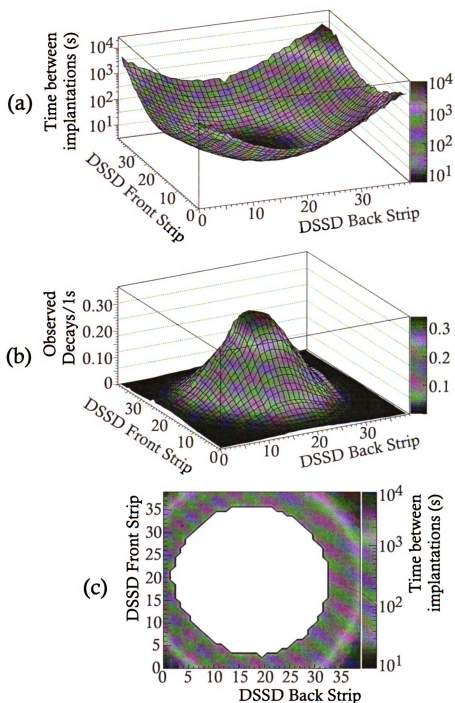


Figure 3.15: Rate profiles over the surface of the implantation DSSD. (a) shows the average time, in seconds, between implantations for each pixel of the DSSD. (b) is the average number of decay events in a given pixel within a 1 second time interval. (c) illustrates the pixels of the DSSD in which the time between implantations is  $\geq 100$  s. This rate requirement, which encompasses  $1/2$  of the DSSD pixels, was applied in analysis to select a subset of pixels.

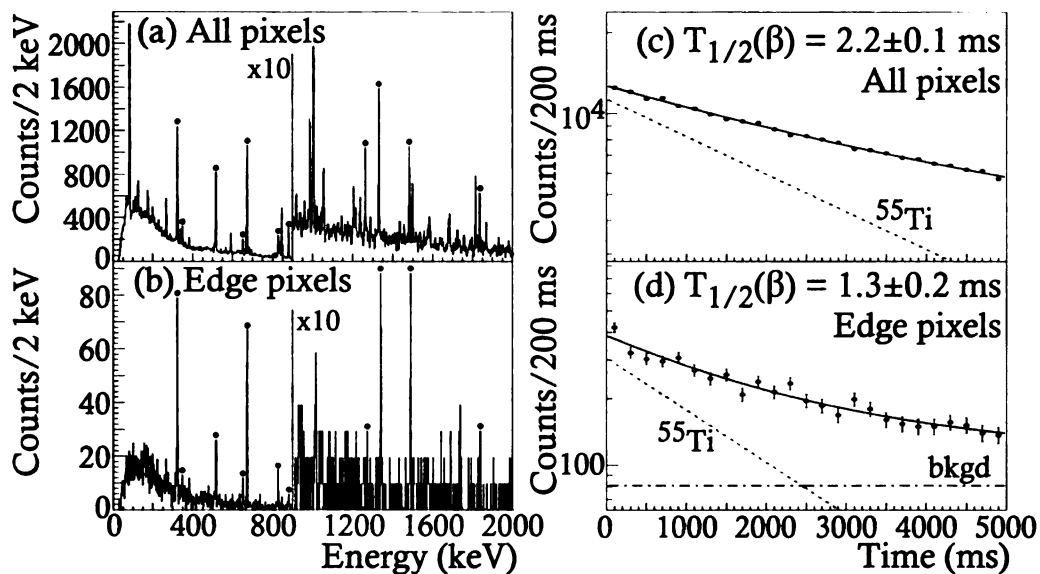


Figure 3.16: (a) and (b):  $\beta$ -delayed  $\gamma$ -ray spectra following the decay of  $^{55}\text{Ti}$  for data taken from (a) all pixels of the DSSD, and (b) only pixels near the edge of the DSSD, in which the time between implantations was  $\geq 100$  s. (c) and (d):  $\beta$ -decay curves derived from data using (c) all pixels of the DSSD, and (d) pixels near the edge of the DSSD.

all data in Fig. 3.16(c) was fitted with an exponential decay for the parent, the growth and decay of the daughter  $^{55}\text{V}$ , and a constant background. The resulting fit gave a half-life a factor of two longer than the known value. The decay curve resulting from data in the edge pixels only [see Fig. 3.16(d)] was fitted in the same manner and the deduced half-life is in good agreement with literature [71].

Primary analysis for data from NSCL experiment 07509 was restricted to the subset of pixels with low implantation rates as described above when the required correlation time window was greater than 1 s. This includes the analysis of the  $\beta$  decays of  $^{53}\text{Ca}$  and  $^{54}\text{Sc}$ , discussed in the next chapter. The restriction to a subset of DSSD pixels allowed a clean analysis of the decay properties of these longer-lived isotopes. However, it would be preferable in future experiments to further defocus the beam over the detector surface to reduce the implantation rate in the central detector pixels. The loss in statistics due to fragments missing the detector would likely be less than that arising from limiting the analysis region. The implantation

rate was considerably lower for NSCL experiment 05101; the total implantation rate was  $\sim 30$  Hz. It was therefore not necessary to limit the analysis to any specific region of the DSSD.

### 3.5.2 Decay curve fitting methods

One of the key values that can be extracted from  $\beta$ -decay spectroscopy data is the half-life of implanted nuclei. A critical step in extracting a half-life from continuous implantation data is the correct correlation of implantation events with their subsequent decays, which was described in the previous section. Equally important, however, is the method used to fit the decay curve data with functions describing not only the decay of the parent nucleus of interest, but also contributions from decay of the daughter isotope(s) and randomly correlated background events, which must be included due to the  $<100\%$   $\beta$ -detection efficiency of the DSSD.

Typically, fitting techniques require the minimization of a “goodness of fit” parameter, which often takes the form of a  $\chi^2$  value. A commonly used parameter is the Gaussian  $\chi^2$ , defined as follows [72]:

$$\chi_{\text{Gaussian}}^2 = \sum_i^N \frac{(y_i - y_{fit}(\mathbf{a}))^2}{\sigma_i^2}, \quad (3.1)$$

where  $y_i$  represents the  $i^{\text{th}}$  data point, with associated variance  $\sigma_i$ , and  $y_{fit}(\mathbf{a})$  is the fit to the data point, which is a function of the set of fit parameters,  $\mathbf{a}$ . The best fit parameters are determined by minimizing the value of  $\chi^2$  iteratively, by considering the numerical derivatives of  $\chi^2$  with respect to each of the fit parameters,  $a$ .

Data from low count-rate experiments follow Poisson statistics [4], and the use of  $\chi_{\text{Gaussian}}^2$  is not appropriate. An alternative method for nuclear counting experiments with low statistics is to use the maximum likelihood of the Poisson probability

distribution. The likelihood function ( $\mathcal{L}$ ) for Poisson statistics is given by [73]:

$$\mathcal{L} = \prod_i^N P_P(y_i, \mu) = \prod_i^N \frac{\mu^{y_i} e^{-\mu}}{y_i!}, \quad (3.2)$$

where  $P_P(y_i, \mu)$  is the probability of measuring a value of  $y_i$ , when the true mean of the distribution is given by  $\mu$ , for  $N$  events. Taking the natural logarithm of Eqn. 3.2, the log-likelihood function is given by:

$$\ln \mathcal{L} = \sum_{i=1}^N [y_i \ln \mu - \mu - \ln y_i!]. \quad (3.3)$$

With some rearrangement of Eqn 3.3, a version of the  $\chi^2$  statistic derived from maximizing the log-likelihood function for Poisson distributed data can be expressed as:

$$\chi_{LL}^2 = 2 \sum_i^N [y_{fit} - y_i \ln(y_{fit}) + \ln(y_i!)], \quad (3.4)$$

where  $y_{fit}$  is the fit to the data point  $y_i$ . Minimization of this  $\chi_{LL}^2$  correctly determines the fit parameters for Poisson distributed data, irrespective of the procedure used to histogram the event data.

Results are discussed in the next chapter which include half-lives deduced using two distinct methods: a curve fitting method based within the ROOT data analysis framework [74], which optimized a fit to the binned decay curve data, and a maximum likelihood approach, where each instance of a correlated decay event is evaluated and associated with a specific member of a decay chain, or to background. Both of these methods used the Poisson statistical approach and are outlined in more detail in the following sections.

## Functional curve fit with ROOT

The majority of cases under consideration in the present study had good statistics, and the half-lives were deduced from the decay curve data using a traditional curve-fitting approach. A ROOT-based fitting program was written that provided a graphical user interface and the option to customize the fitting function based on the properties of a given decay. Fit functions were based on the Bateman equations for nuclear decay processes including parent, daughter, and grand-daughter decays as required, with the option of including  $\beta$ -delayed neutron branching and the associated  $\beta n$  daughter decays. Two fitting algorithms were available with the ROOT package: minimization of a Gaussian  $\chi^2$ , defined as in Eqn. 3.1, and maximization of the Poisson likelihood function by minimization of the  $\chi_{LL}^2$  statistic as defined in the previous section. The latter method was applied for all decay curve fits discussed in Chapter 4.

## Maximum likelihood analysis

The Maximum Likelihood (MLH) fitting method was based upon the maximization of a custom log-likelihood function defined for a given data set. As applied to the analysis of nuclear decay half-lives, the MLH method provides a mathematically correct description of the probability of observing chains of decay events, and thus makes use of all available information, on an event-by-event basis, to deduce the unknown decay properties. The MLH method and its application to low-statistics  $\beta$ -decay data are described in detail elsewhere [65].

No  $\beta$  decays in the present work were analyzed using the MLH method to deduce a half-life value. However, the method was adapted to treat low-statistics isomer  $\gamma$ -ray decay data for  $^{50}\text{K}$ , discussed in the next chapter. The nature of  $\gamma$ -ray decay, with discrete energy transitions, allowed simplification of the MLH method as compared to the treatment of  $\beta$  decay. As it is possible to discriminate  $\gamma$ -ray decays based on energy, there are essentially only two options for the identity of a decay event – a real parent  $\gamma$ -ray decay, or a random background event. Contributions from the decays

of subsequent generations in the likelihood function can thus be excluded. Gating on a specific  $\gamma$ -ray energy also significantly reduces the background rates associated with any given isomer decay event. The elimination of contributions from subsequent decays and background greatly simplifies the MLH method, reducing the Poisson log-likelihood maximization technique to treatment of individual data points.

# Chapter 4

## Experimental Results

The previous chapters have outlined the techniques of  $\beta$  decay and  $\beta$ -delayed and prompt  $\gamma$ -ray spectroscopy, as well as the details of the experimental set-up for NSCL experiments 05101 and 07509. Results from these experiments are presented in this chapter.

Prompt  $\gamma$ -ray information provided information on  $\mu$ s isomers for nuclei implanted in both experiments.  $\beta$ -decay half-lives and  $\beta$ -delayed  $\gamma$ -ray spectra were also obtained from implantation-decay correlations as described in the previous chapter.  $\gamma\gamma$  matrices were constructed for events with  $\gamma$  multiplicities of two or higher, allowing analysis of  $\gamma$  coincidence information. These data were used to establish level schemes. Combined, the data obtained permitted considerable expansion of the knowledge of the neutron-rich  $fp$  shell nuclei.

Experiment 07509 included over 20 neutron-rich nuclei in the region surrounding  $^{54}\text{Ca}$ , and provided new information on the quantum structure of the neutron-rich  $^{53,54,56}_{21}\text{Sc}$  isotopes, both through the decay of the parent  $^{53,54}_{20}\text{Ca}$  nuclides, as well as via prompt  $\gamma$ -ray emission from isomeric states in the even- $A$   $^{54,56}\text{Sc}$  isotopes themselves. Prompt  $\gamma$  rays from  $^{50}_{19}\text{K}$  were also observed in experiment 07509, providing information on the low-energy structure of this nuclide. New data for the low-energy structure of neutron-rich  $^{61}_{25}\text{Mn}$  was obtained from experiment 05101, via  $\beta$  decay from

the parent  ${}^{61}_{24}\text{Cr}$  isotope. This chapter presents results, including  $\beta$ -decay half-lives,  $\beta$ -delayed  $\gamma$ -ray information and prompt  $\gamma$ -ray information, for  ${}^{50}\text{K}$ , neutron-rich  ${}_{21}\text{Sc}$  and  ${}_{20}\text{Ca}$  isotopes from  $N=32$  to  $N=35$ , and  ${}^{61}\text{Cr}$ .

## 4.1 Low-energy structure of neutron-rich ${}_{21}\text{Sc}$ isotopes

The presence of subshell gap at  $N=32$ , the result of a sizeable energy spacing between the  $\nu 2p_{3/2}$  single-particle orbital and the higher-lying  $\nu 2p_{1/2}$  and  $\nu 1f_{5/2}$  orbitals, has been observed experimentally in the  ${}_{20}\text{Ca}$ ,  ${}_{22}\text{Ti}$  and  ${}_{24}\text{Cr}$  isotopes. Additional to this subshell closure, the possibility exists in the  ${}_{20}\text{Ca}$  isotopes for a  $N=34$  subshell closure, resulting from the continued upward shift of the  $\nu 1f_{5/2}$  orbital attributed to a reduced monopole interaction. Confirmation of the presence or absence of a  $N=34$  subshell closure in the Ca isotopes has been the focus of a number of experimental efforts in the  $fp$  shell. The primary goal of experiment 05101 was to investigate the  $\beta$  decay of  ${}^{54}\text{K}$  to states in  ${}^{54}\text{Ca}$ , with the hopes of populating the first  $2^+$  excited state in  ${}^{54}\text{Ca}$ . Observation of the  $\gamma$ -ray de-exciting the  $2^+_1$  state in  ${}^{54}\text{Ca}$  would have provided a direct measurement of the excitation energy of the state, and when considered in the systematics of the  ${}_{20}\text{Ca}$  isotopes, potentially the first evidence for a  $N=34$  subshell closure. However, only 73  ${}^{54}\text{K}$  implantations were observed after one week of running time. The production yields proved prohibitively low for a successful  $\beta$ - $\gamma$  measurement during the allotted time.

Experiment 07509 was also motivated by the possibility of observing the  $\gamma$ -ray decay of the  $2^+_1$  state in  ${}^{54}\text{Ca}$  and measuring  $E(2^+_1)$ . Within the data of experiment 05101, 3 counts were observed at 327 keV in the  $\gamma$ -ray spectrum collected within 15  $\mu\text{s}$  following  ${}^{54}\text{Ca}$  implantations. Could an isomeric state be present in  ${}^{54}\text{Ca}$ ? The possibility for such an isomer arises when low-energy  $4^-$  and  $5^-$  negative parity states, an outcome of the coupling of the  $\nu 2p_{1/2}$  and  $\nu 1g_{9/2}$  orbitals, are considered.

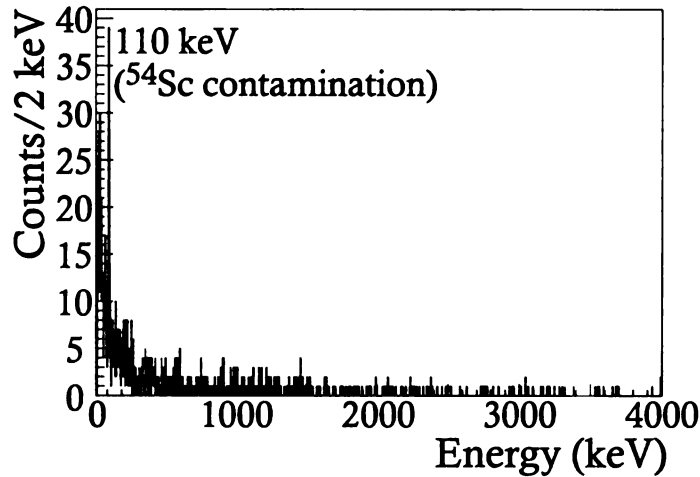


Figure 4.1:  $\gamma$ -ray spectrum collected within 20  $\mu\text{s}$  following a  $^{54}\text{Ca}$  implantation. No evidence of an isomer decay is observed. The peak at 110 keV is due to random correlations with the  $\gamma$  ray in the isomer decay of  $^{54}\text{Sc}$ .

The isomeric decay from a  $5^-$  state in  $^{54}\text{Ca}$  would be expected follow the sequence  $5^- \rightarrow 3_1^+ \rightarrow 2_1^+ \rightarrow 0_1^+$ . Thus, the goal of experiment 07509 was to investigate the possible isomeric decay of  $^{54}\text{Ca}$ , and measure the energies of the  $\gamma$ -ray transitions involved, in particular that of the  $2_1^+ \rightarrow 0_1^+$  transition, expected to be  $\geq 2$  MeV. The  $\gamma$ -ray spectrum collected within 20  $\mu\text{s}$  following a  $^{54}\text{Ca}$  implantation in experiment 07509 is shown in Fig. 4.1. No evidence of an isomer was observed.

While the structure of  $^{54}\text{Ca}$  has proven difficult to probe directly at present, the possibility of an  $N=34$  subshell closure at  $Z=20$  can be investigated indirectly by considering the level structures of neighboring isotopes, e.g. the  $_{21}\text{Sc}$  isotopes. The low-energy structure of the Sc isotopes should be described by the coupling of the single valence  $f_{7/2}$  proton to the valence neutrons. Thus, the low-energy levels in the  $_{21}\text{Sc}$  isotopes surrounding  $N=34$  should be sensitive to the neutron single-particle energy spacings, and may shed light on the possible  $N=34$  subshell closure in the Ca isotopes.

Four neutron-rich  $_{21}\text{Sc}$  isotopes from  $N=32$  to  $N=35$  were included in the cocktail beam delivered to the NSCL  $\beta$  counting system in experiment 07509, as well as three  $_{20}\text{Ca}$  isotopes from  $N=32$  to  $N=34$ . The  $_{20}\text{Ca}$  isotopes provided access, via



their  $\beta$  decays and  $\beta$ -delayed  $\gamma$ -ray emissions, to the low-energy structure of their daughter  ${}_{21}\text{Sc}$  isotopes. Prompt  $\gamma$ -ray emission in  ${}^{54}\text{Sc}$  complemented the decay data, providing additional insight into the low-energy structure of this isotope. Prompt  $\gamma$  rays provided the only access into the low-lying levels of  ${}^{56}\text{Sc}$ , for which the parent  ${}^{56}\text{Ca}$  was not produced with sufficient yield to permit  $\beta$ - $\gamma$  analysis. The results for the low-energy structures of the Sc isotopes, determined both from decay of the Ca isotopes and prompt  $\gamma$ -ray emission from the Sc isotopes themselves, are presented in the following sections.

#### 4.1.1 $\beta$ decay of ${}^{53}\text{Ca}$ to ${}^{53}\text{Sc}$

The  $\beta$ -delayed  $\gamma$ -ray spectrum for  ${}^{53}\text{Ca}$  in the range 0 to 3 MeV for decay events within 5 s following an implantation event is shown in Fig. 4.2. Due to the length of the correlation time window used in the analysis of the  ${}^{53}\text{Ca}$  decay, this spectrum includes only decays correlated with implantations isolated in pixels towards the edge of the implantation detector, as discussed in Section 3.5.1. One transition is apparent in this spectrum at  $2109.0 \pm 0.3$  keV, and has been assigned to the  $\beta$  decay of  ${}^{53}\text{Ca}$ . This newly assigned transition has recently been confirmed in one-proton knockout from  ${}^{54}\text{Ti}$  [75].

The decay curve constructed from  ${}^{53}\text{Ca}$ -correlated  $\beta$  decays with the additional requirement of a coincident 2109-keV  $\gamma$  ray is presented in Fig. 4.3(a). Extraction of the half-life from the full data without a  $\gamma$ -ray coincidence requirement is complicated by uncertain quantities, including daughter half-lives and neutron branching ratios, which must be included in the fitting function. It is therefore desirable to additionally gate the decay curve on a known  $\gamma$  ray, to remove contributions from both background and subsequent decays in the decay chain. The newly observed 2109-keV  $\gamma$  ray could be used in the case of  ${}^{53}\text{Ca}$ , and the full statistics of the DSSD could be used in this case – the additional 2109-keV  $\gamma$ -ray coincidence requirement reduced background events, allowing extraction of a clean decay curve. The  $\gamma$ -gated decay curve was

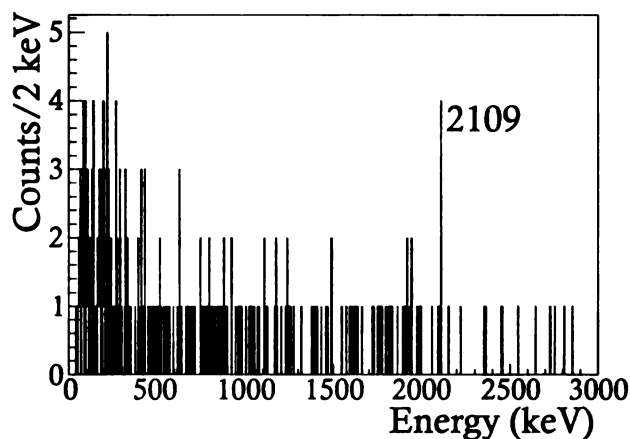


Figure 4.2:  $\beta$ -delayed  $\gamma$ -ray spectrum in the energy range 0-3 MeV following the decay of  $^{53}\text{Ca}$ . The spectrum is limited to include  $\gamma$  rays coincident only with  $\beta$  decays in the subset of pixels near the edge of the DSSD. The transition assigned to the  $\beta$  decay of  $^{53}\text{Ca}$  is marked by its energy in keV.

fitted with a single exponential decay and a constant background, yielding a half-life value of  $461 \pm 90$  ms. This value is higher than the value of  $230 \pm 60$  ms previously reported by Mantica *et al.* [76]. However, as noted in Ref. [76], the possibility of a second  $\beta$ -decaying state in  $^{53}\text{Ca}$ , which could account for the discrepancy between the present result and previous measurements, cannot be excluded. A fit to the decay curve without the additional  $\gamma$  requirement is required to determine the total number of observed  $^{53}\text{Ca}$   $\beta$  decays. The fit to the un-gated decay curve, considering only decay correlated with implantations towards the edge of the implantation detector, and fixing the half-life at 461 ms, is presented in Fig. 4.3(b).

An absolute  $\gamma$  intensity of  $56 \pm 12\%$  was determined for the 2109-keV transition from a Gaussian fit to the peak in Fig. 4.2, the absolute efficiency of the 15-detector geometry of SeGA ( $4.3 \pm 0.2\%$ ), and the number of  $^{53}\text{Ca}$   $\beta$  decays (252) that were correlated with fragment implantations, as determined from the fit to the decay curve of Fig. 4.3(b). The absolute intensity of the 2109-keV transition suggests that the majority of  $\beta$  intensity from the decay of  $^{53}\text{Ca}$ , excluding  $\beta n$  contributions, proceeds through an excited state depopulated by this transition. The 2109-keV transition is thus proposed to directly feed the  $^{53}\text{Sc}$  ground state, and the associated 2109-keV

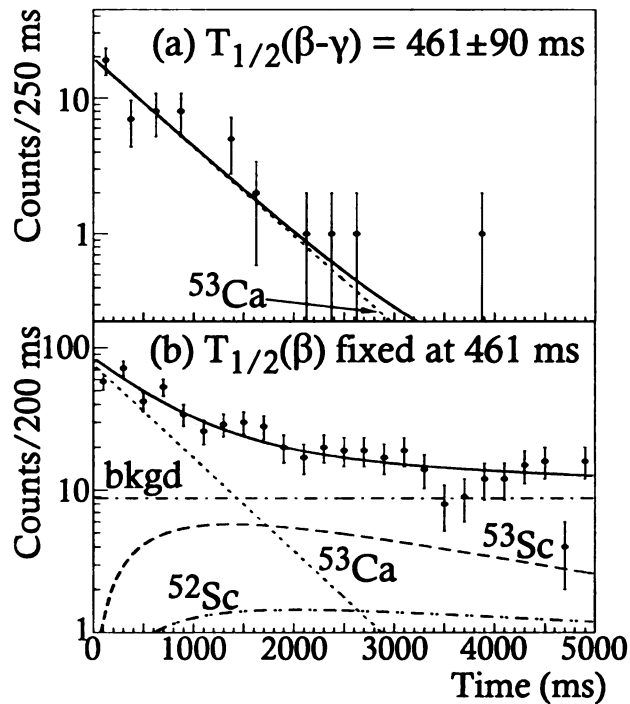


Figure 4.3:  $\beta$ -decay curves for the decay of  $^{53}\text{Ca}$ . (a) Decay curve constructed considering  $\beta$ -decay events correlated with  $^{53}\text{Ca}$  implantations over the entire surface of the DSSD, with the additional requirement of a coincident 2109-keV decay  $\gamma$  ray. These data were fitted with a single exponential decay and a constant background. (b) Decay curve constructed considering only data in the subset of pixels near the edge of the DSSD, with a correlation time of 5 s. Data were fitted with an exponential decay of the parent, with the half-life fixed at 461 ms, growth and decay of the  $\beta$  and  $\beta n$  daughters, assuming a 40% neutron-branching ratio [77] and a constant background.



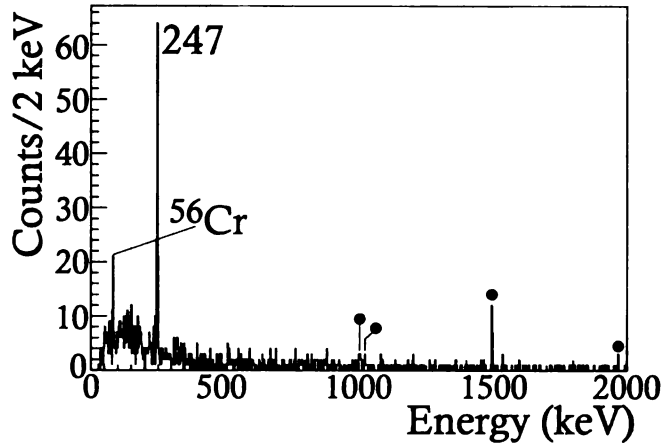


Figure 4.5:  $\beta$ -delayed  $\gamma$ -ray spectrum following the decay of  $^{54}\text{Ca}$  to states in  $^{54}\text{Sc}$ , in the range of 0-2 MeV. Observed transitions assigned to the decay of  $^{54}\text{Ca}$  are marked by their energy in keV, while transitions in the  $\beta$  decay of the daughter  $^{54}\text{Sc}$  are marked by a filled circle.

assigned  $J^\pi=(1)^+$  based on the apparent allowed  $\beta$  decay to this level from the  $0^+$   $^{54}\text{Ca}$  ground state. As discussed by Mantica *et al.* [76], the 247-keV state populated in the decay of  $^{54}\text{Ca}$  de-excites promptly (within a few ns). A prompt 247-keV transition from a  $1^+$  state to the  $^{54}\text{Sc}$  ground state precludes a  $J^\pi=4^+$  assignment for the  $^{54}\text{Sc}$  ground state, as Weisskopf estimates for a 247-keV M3 transition would suggest a half-life of order days. The observed  $\beta$ -feeding pattern to states in  $^{54}\text{Ti}$  from  $^{54}\text{Sc}$  had previously limited the ground state spin and parity to  $(3,4)^+$  [31]. The present result suggests a  $3^+$  assignment for the ground state spin and parity of  $^{54}\text{Sc}$  – a 247-keV E2 transition is expected to have a half-life in the ns range, consistent with the observed prompt nature of the transition. The unobserved  $\beta$  intensity of  $35\pm 9\%$  can be attributed to a possible  $\beta n$  branch in the  $^{54}\text{Ca}$  decay, as direct feeding to the  $(3)^+$  ground state of  $^{54}\text{Sc}$  is unlikely from the  $0^+$  ground state of  $^{54}\text{Ca}$ .

The decay curve derived from  $^{54}\text{Ca}$ -correlated  $\beta$  decays within 1 s of an implantation event is shown in Fig. 4.6(a). The decay curve of Fig. 4.6(a) was fitted with a single exponential decay for the parent  $^{54}\text{Ca}$ , exponential growth and decay of the  $\beta$  daughter isotope,  $^{54}\text{Sc}$  ( $T_{1/2} = 526 \pm 15$  ms, see Section 4.1.3), and a constant background component. The deduced half-life for the decay of  $^{54}\text{Ca}$  was  $101\pm 9$  ms,

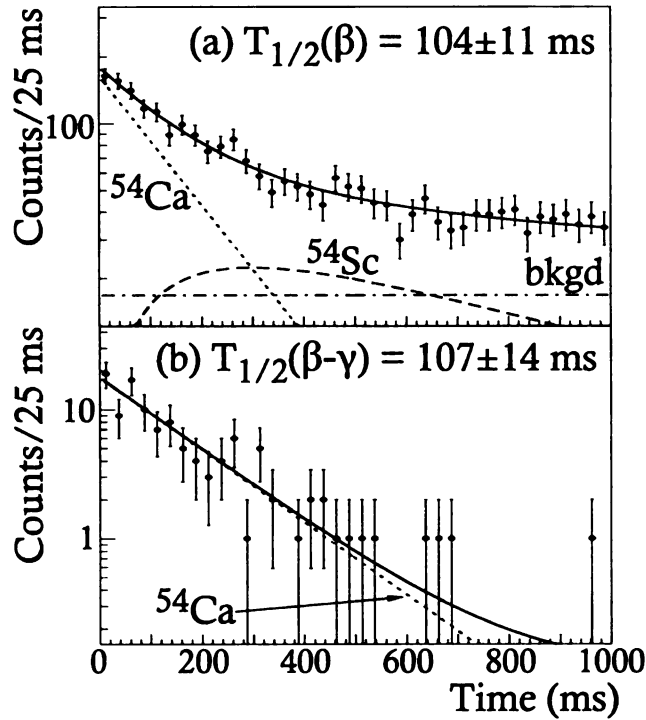


Figure 4.6:  $\beta$ -decay curves for the decay of  $^{54}\text{Ca}$ . (a) Decay curve constructed from  $^{54}\text{Ca}$ -correlated  $\beta$ -decay events over the entire DSSD surface, using a correlation time of 1 s. These data were fitted with an exponential decay of the parent, growth and decay of the  $\beta$  daughter, and a constant background. (b) The decay curve for  $^{54}\text{Ca}$ , with the additional requirement of a 247-keV decay  $\gamma$  ray coincident with the  $\beta$  decay. The curve was fitted with a single exponential decay and a constant background.

within  $1\sigma$  of the value of  $86 \pm 7$  ms reported by Mantica *et al.* [76]. The difference in the deduced half-life value is a result of the new, longer half-life for the  $^{54}\text{Sc}$  daughter nucleus (see Section 4.1.3). A fit to the present data using the previous  $^{54}\text{Sc}$  half-life of  $360 \pm 60$  ms [31] used by Mantica *et al.* gave a half-life value of  $88 \pm 13$  ms. Shown in Fig. 4.6(b) is the decay curve obtained by requiring a coincidence with the 247-keV  $\beta$ -delayed  $\gamma$  ray observed in the  $^{54}\text{Ca}$  decay. The 247-keV  $\gamma$ -gated decay curve yields a half-life value of  $107 \pm 14$  ms, again consistent with both the un-gated decay curve and the previous value reported by Mantica *et al.* [76]. The proposed decay scheme for levels in  $^{54}\text{Sc}$  populated following the  $\beta$  decay of  $^{54}\text{Ca}$  is shown in Fig. 4.7.

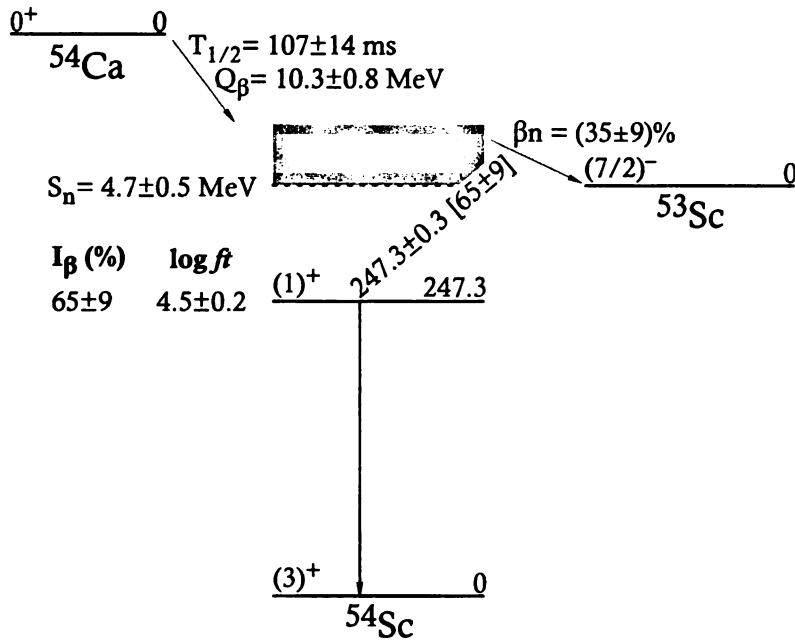


Figure 4.7: Decay scheme for  $^{54}\text{Ca}$ . The energy of each state is given in keV, and the number in square brackets following the  $\gamma$ -ray energy is the absolute  $\gamma$ -ray intensity.  $Q_{\beta}$  and  $S_n$  were deduced from data in Ref. [80].

### 4.1.3 $\beta$ decay and isomeric structure of $^{54}\text{Sc}$

Analysis of the  $\beta$  decay of  $^{54}\text{Sc}$  used a correlation time of 5 s, with primary analysis restricted to the subset of pixels towards the edge of the implantation DSSD, as discussed in Section 3.5.1. The  $\beta$ -delayed  $\gamma$ -ray spectrum for  $^{54}\text{Sc}$  in the range 0 to 3 MeV is presented in Fig. 4.8. Twelve transitions were identified in this spectrum. The four lowest energy transitions were eliminated as candidates for transitions in the decay of  $^{54}\text{Sc}$  on the basis of their apparent half-lives, and likely belong to the decay of the daughter nucleus,  $^{54}\text{Ti}$ .  $\gamma\gamma$  analysis indicates that these four transitions are in coincidence with one another, and the lowest energy transition at 108 keV corresponds to a known transition in  $^{54}\text{V}$  [68]. The remaining eight transitions are assigned to the  $\beta$  decay of  $^{54}\text{Sc}$ , and are summarized in Table 4.1. The transitions observed at 1002, 1021 and 1495 keV were observed previously in  $\beta$  decay [31] and deep-inelastic studies [81].

The decay curve for  $^{54}\text{Sc}$ -correlated decay events including decay events over the

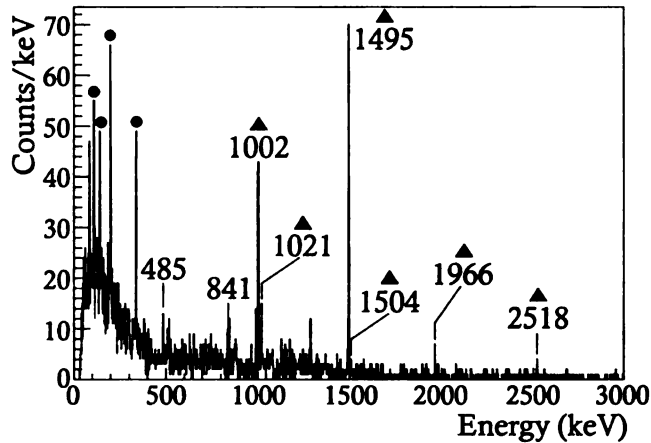


Figure 4.8:  $\beta$ -delayed  $\gamma$ -ray spectrum following the decay of  $^{54}\text{Sc}$ , for  $\gamma$ -ray transitions in the energy range 0-3 MeV. Transitions in the decay of  $^{54}\text{Sc}$  are marked by their energies in keV, while transitions belonging to the decay of the daughter are marked by a filled circle. Transitions marked by shaded triangles were used to gate the  $\beta$ -decay curve of Fig. 4.9(a).

Table 4.1: Energies and absolute intensities of  $\beta$ -delayed  $\gamma$  rays assigned to the  $\beta$  decay of  $^{54}\text{Sc}$ . The half-life deduced from a  $\gamma$ -gated decay curve, considering data over the entire surface of the DSSD, is also included for all transitions in which statistics were sufficient to fit a curve.

$E_\gamma$ (keV)	$I_\gamma^{absolute}$ (%)	Initial State (keV)	Final State (keV)	Half-life (ms)
$484.6 \pm 0.4$	$4 \pm 1$	3000	2516	$564 \pm 99$
$840.5 \pm 0.4$	$7 \pm 2$	3338	2497	$620 \pm 104$
$1002.4 \pm 0.3$	$40 \pm 4$	2497	1495.0	$522 \pm 28$
$1020.8 \pm 0.4$	$9 \pm 2$	2517	1495.0	$556 \pm 53$
$1495.0 \pm 0.3$	$79 \pm 5$	1495.0	0	$525 \pm 19$
$1504.0 \pm 0.3$	$2 \pm 1$	3000	1495	$521 \pm 113$
$1965.7 \pm 0.4$	$7 \pm 1$	3460	1495	$458 \pm 100$
$2517.5 \pm 0.3$	$5 \pm 1$	2517	0	—

entire surface of the DSSD, with the additional requirement of a coincident 1002, 1021, 1495, 1504 or 1966-keV  $\gamma$  transition, is presented in Fig. 4.9(a). A fit to these data using a single exponential decay and constant background yielded a half-life for  $^{54}\text{Sc}$  of  $526 \pm 15$  ms, longer than the value  $360 \pm 60$  ms determined by Liddick *et al.* [31]. One possible explanation for the discrepancy between the present half-life requiring a coincident decay  $\gamma$  ray, and the previous value would be the presence of a second  $\beta$ -decaying state in  $^{54}\text{Sc}$ . However, as noted by Liddick *et al.* [31], the ordering of low-energy states predicted by the shell model is not supportive of a  $\beta$ -decaying isomer. Additionally, decay curves gated on individual  $\gamma$  transitions yielded half-life values in good agreement with one another (see the last column of Table 4.1, which is not indicative of an isomer).

Another possible explanation for the discrepancy between the half-lives is the deconvolution of the previously observed  $\beta$ -decay curve. A half-life of  $2.1 \pm 1.0$  s, used in the present analysis, was determined in the 07509 data set for the daughter  $^{54}\text{Ti}$  and is in agreement with, though slightly longer than the literature value [82]. Additionally, the unobserved  $\beta$  intensity in the present work is suggestive of a neutron-branching contribution of  $\sim 20\%$ . Inclusion of these factors, not considered by Liddick *et al.* [31], would result in an underestimation of the parent half-life in the previous work.

The proposed levels in  $^{54}\text{Ti}$  populated by the  $\beta$  decay of  $^{54}\text{Sc}$  are shown in Fig. 4.10. Placement of the 1002-, 1021- and 1495-keV transitions follows the assignments made in previous work [31,81], and is confirmed by both the absolute  $\gamma$ -ray intensities of the transitions, and observed  $\gamma\gamma$  coincidences. The new transitions with energies 484, 840, 1505 and 1965 keV were placed on the basis of the observed  $\gamma\gamma$  coincidences, as shown in Fig. 4.11. Energy-sum relationships were used to place both the 1505-keV cross-over transition connecting the states with energies 3000 and 1495 keV, and the 2517-keV transition between the 2517-keV level and the ground state.

The apparent  $\beta$  feeding and  $\log ft$  values deduced from the absolute  $\gamma$  intensities are included in Fig. 4.10.  $J^\pi$  for the states with energies 1495, 2496 and 2517 keV are

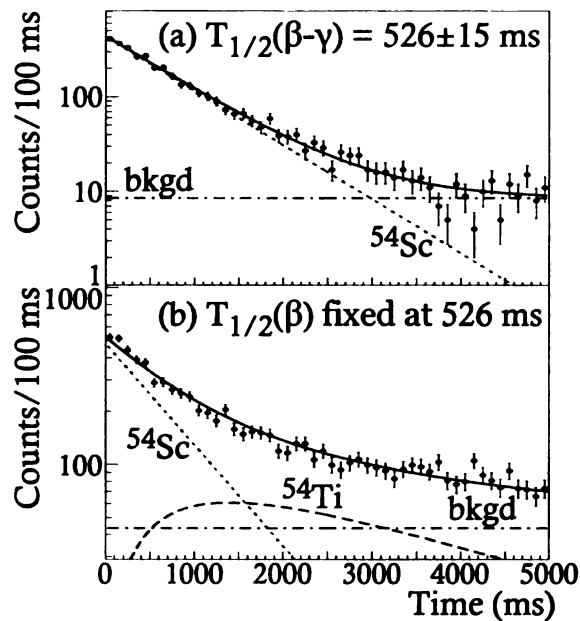


Figure 4.9: Decay curves for the  $\beta$  decay of  $^{54}\text{Sc}$  to states in  $^{54}\text{Ti}$  using a correlation time of 5 s. (a) Decay curve, considering data over the entire surface of the DSSD, with the additional requirement of a coincident 1002, 1021, 1495, 1504, 1966 or 2518-keV  $\gamma$  ray (marked by the shaded triangles in Fig. 4.8). These data were fitted with a single exponential decay and constant background. (b)  $^{54}\text{Sc}$   $\beta$ -decay curve constructed considering  $\beta$  decays localized to the subset of pixels on the edge of the DSSD. The decay curve was fitted with a function including a single exponential decay, growth and decay of the daughter,  $\beta n$  daughter and granddaughters, and constant background, assuming a neutron branching ratio of 20%. The half-life of the parent  $^{54}\text{Sc}$  was fixed at 526 ms, as determined from the  $\gamma$ -gated decay curve.

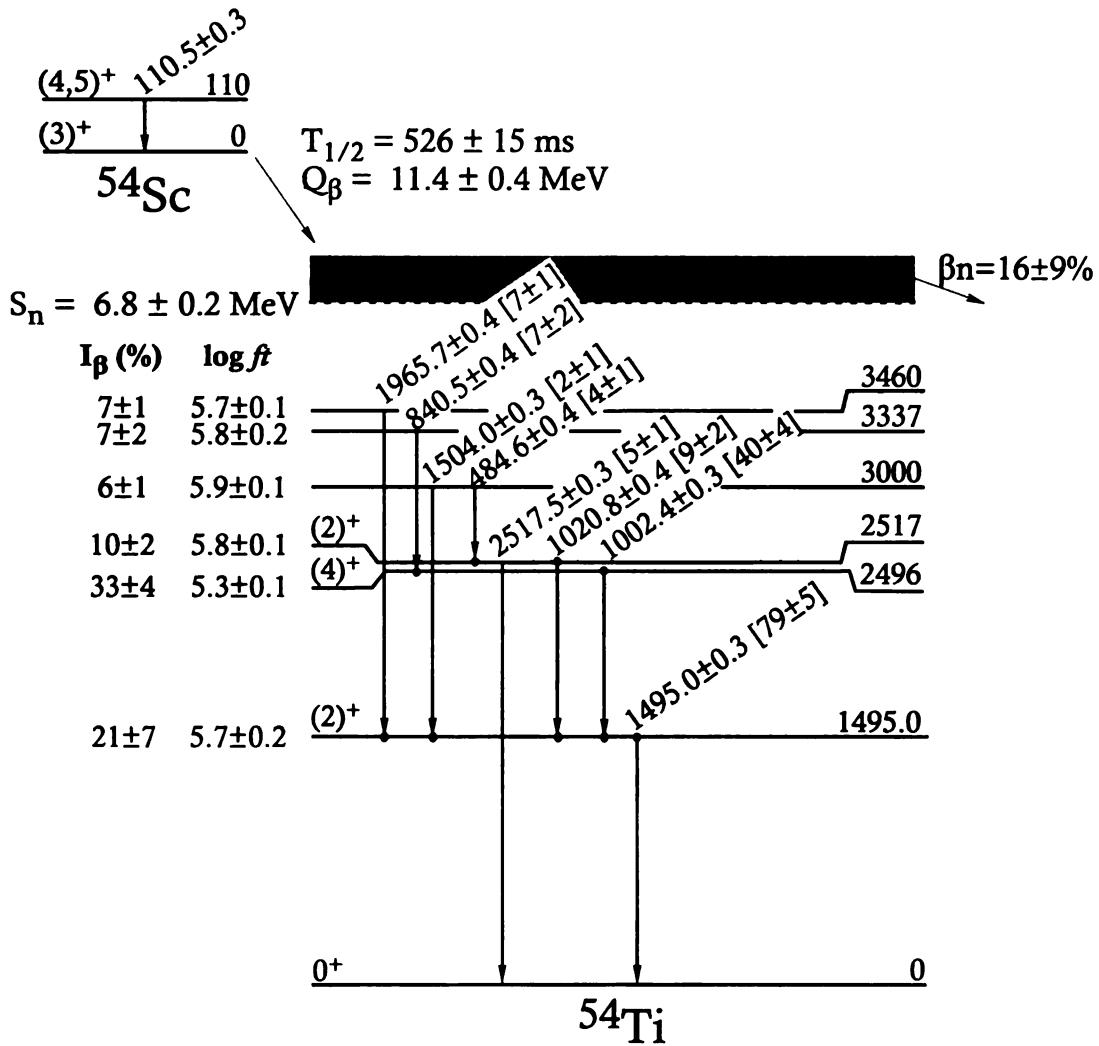


Figure 4.10: Proposed decay scheme for  $^{54}\text{Sc}$  to states in  $^{54}\text{Ti}$ . The energy of each state is given in keV. The number in brackets following the  $\gamma$ -ray transition energy is the absolute  $\gamma$ -ray intensity. Apparent  $\log ft$  values were deduced from the apparent  $\beta$  branches, the  $^{54}\text{Sc}$  half-life, decay  $Q$  value, and the excitation energy of the populated states [79].

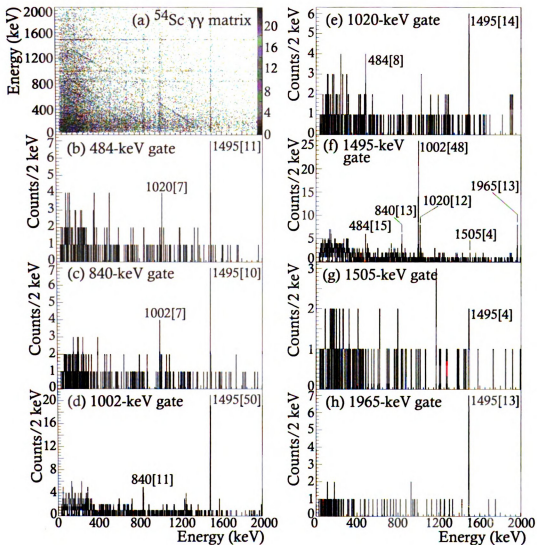


Figure 4.11: (a) Two-dimensional  $\gamma\gamma$  coincidence matrix for  $\gamma$  rays observed in coincidence with  $^{54}\text{Sc}$ -correlated decay events over the entire surface of the DSSD.  $\gamma$  coincidence spectra gated on the (b) 485 keV, (c) 840 keV, (d) 1002 keV, (e) 1021 keV, (f) 1495 keV, (g) 1504 keV and (h) 1965-keV transitions in coincidence with a  $^{54}\text{Sc}$ -correlated  $\beta$ -decay event. The number in square brackets following the energy is the number of counts in the peak.

adopted from previous works [31, 81]. Apparent allowed feeding to both the  $2^+$  and  $4^+$  states suggest a  $J^\pi$  assignment of  $3^+$  for the  $^{54}\text{Sc}$  ground state, in agreement with the assignment made based on the  $\beta$  decay of  $^{54}\text{Ca}$  into  $^{54}\text{Sc}$ , discussed in Section 4.1.2. No direct feeding is therefore expected to the  $0^+$   $^{54}\text{Ti}$  ground state. The missing  $\beta$  intensity can be accounted for by a  $\beta n$  branch of  $16 \pm 9\%$  in the decay. An allowed  $\beta$  decay from the  $(3)^+$   $^{54}\text{Sc}$  ground state limits the spin of the newly-placed states with energies 3000, 3337 and 3460 keV to  $J^\pi = 2^+, 3^+$  or  $4^+$ .

The  $\gamma$ -ray spectrum collected within a 20- $\mu\text{s}$  window following a  $^{54}\text{Sc}$  implantation event is shown in Fig. 4.12. Observation of a 110-keV isomeric transition in  $^{54}\text{Sc}$  was first reported by Grzywacz *et al.* [68], where the 110-keV transition was assigned E2 multipolarity, based on Weisskopf estimates. As shown in Fig. 4.12, the 110-keV isomeric transition was observed with high statistics and an improved half-life for this isomeric state was deduced. The prompt  $\gamma$ -ray energy is shown as a function of time after implantation of  $^{54}\text{Sc}$  fragments into the DSSD in Fig. 4.13(a). The 110-keV transition is visible, with an intensity decaying with time. Fig. 4.13(b) is a projection of the data in Fig. 4.13(a) onto the time axis, showing the time dependency of the 110-keV transition. This decay curve was fitted with a single exponential function with a half-life for this isomeric state of  $2.77 \pm 0.02 \mu\text{s}$ . The present half-life value agrees with measurement of Grzywacz *et al.* [68], but significantly improves the precision.

The improved precision of the half-life for the 110-keV isomeric transition in  $^{54}\text{Sc}$  allowed confirmation, through comparison with Weisskopf estimates, of the E2 multipolarity assignment for this transition. The  $(3)^+$  spin and parity assignment for the  $^{54}\text{Sc}$  ground state, and an E2 isomeric transition limits  $J^\pi$  of the 110-keV state to  $J = 1, 5$ . A spin of  $J=1$  is excluded by the non-observation of feeding to this state by the  $\beta$  decay of  $^{54}\text{Ca}$ . Thus, under the assumption of an E2 multipolarity for the transition, the 110-keV isomeric state in  $^{54}\text{Sc}$  is tentatively assigned a spin and parity of  $J^\pi=(5)^+$ , as was originally suggested by Grzywacz *et al.* [68]. However, this assignment assumes a single-particle nature for the final and initial states. The situation

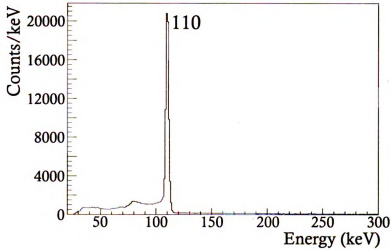


Figure 4.12:  $\gamma$ -ray spectrum in the range of 0-300 keV collected within the first 20  $\mu\text{s}$  following a  $^{54}\text{Sc}$  implantation event. The  $\gamma$ -ray transition is marked by its energy in keV.

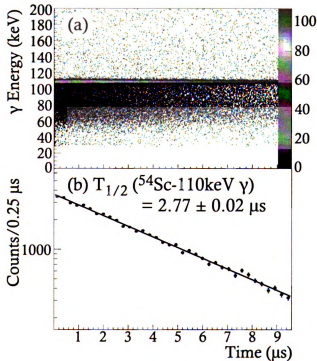


Figure 4.13: Time dependence of the 110-keV isomeric transition in  $^{54}\text{Sc}$ . (a) The prompt  $\gamma$ -ray energy plotted as a function of time following a  $^{54}\text{Sc}$  implantation. (b) A projection of (a) onto the time axis. The data were fitted with a single exponential decay to deduce a half-life for the isomeric state in  $^{54}\text{Sc}$ .

is less certain when more complicated wavefunctions involving configuration mixing are considered. As will be discussed further in Section 5.1.2, a  $4^+$  spin and parity assignment for the 110-keV isomeric state may also be possible.

#### 4.1.4 $\beta$ decay of $^{56}\text{Sc}$

The analysis of the  $\beta$  decay of  $^{56}\text{Sc}$  only required a correlation time of 1 s, and the full DSSD implantation detector could be used in the analysis. The  $\beta$ -delayed  $\gamma$ -ray spectrum for  $^{56}\text{Sc}$  in the range 0 to 2 MeV is shown in Fig. 4.14. Nine transitions in this spectrum have been assigned to the decay of  $^{56}\text{Sc}$ , and are summarized in Table 4.2. Two additional transitions were assigned to the decay of the granddaughter nuclide,  $^{56}\text{V}$  ( $T_{1/2} = 216 \pm 4$  ms [70]) – no transitions are known in the decay of the daughter  $^{56}\text{Ti}$  ( $T_{1/2} = 200 \pm 5$  ms [71]). The transitions with energies 592, 690, 751, 1129 and 1161 keV agree well with  $\gamma$  rays previously observed in both  $\beta$  decay [31] and deep inelastic in-beam experiments [81]. In Ref. [31], it was noted that the transition at  $592.3 \pm 0.5$  keV was within the error of a known transition in  $^{55}\text{Ti}$  [83], and the possibility of  $\beta$ -delayed neutron emission was suggested. In addition to the 592-keV transition, another known transition in  $^{55}\text{Ti}$ , at 1204 keV, is present in the  $\beta$ -delayed  $\gamma$ -ray spectrum, confirming  $\beta$ -delayed neutron emission in the decay of  $^{56}\text{Sc}$ .

Liddick *et al.* [31] proposed two  $\beta$ -decaying states in  $^{56}\text{Sc}$ : a low-spin state with  $T_{1/2} = 35 \pm 5$  ms, and a higher-spin state with slightly longer  $T_{1/2} = 60 \pm 7$ . Given the different spin values, the two  $\beta$ -decaying states were observed to populate different levels in the  $^{56}\text{Ti}$  daughter.  $\gamma$ -gated decay curves were generated for each  $\gamma$ -ray transition identified in Fig. 4.14 and fitted with a single exponential decay plus constant background. The  $\gamma$ -gated decay curves are presented in Figure 4.15, and the resultant half-life values are summarized in Table 4.2. The values deduced from decay curves gated on the 690 and 1161-keV transitions were  $73 \pm 10$  ms and  $78 \pm 9$  ms respectively, consistent within  $1\sigma$  of the previous half-life determination for the higher-spin isomer,  $60 \pm 7$  ms [31]. The transitions assigned to the  $\beta n$  decay also have half-lives consistent

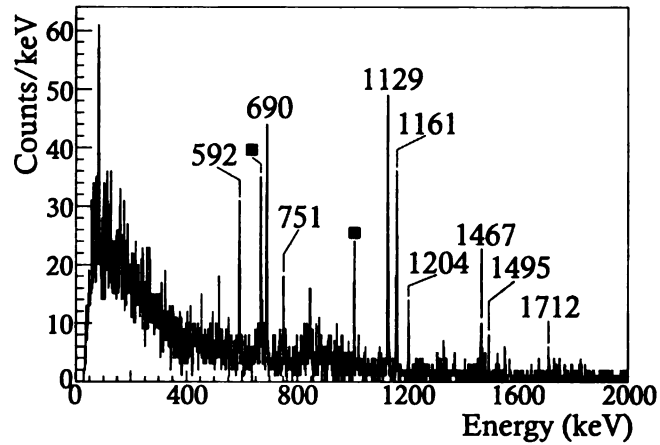


Figure 4.14:  $\beta$ -delayed  $\gamma$ -ray spectrum in the range of 0-2 MeV following the decay of  $^{56}\text{Sc}$  to states in  $^{56}\text{Ti}$ . Transitions marked by their energies in keV are those assigned to the decay of  $^{56}\text{Sc}$ . Transitions marked by a shaded square are attributed to the  $\beta$  decay of the grand-daughter nuclide,  $^{56}\text{V}$ .

Table 4.2: Energies and relative intensities of  $\beta$ -delayed  $\gamma$  rays observed following a  $^{56}\text{Sc}$ -correlated decay event and assigned to the decay of  $^{56}\text{Sc}$ . Observed half-lives for  $\gamma$ -gated decay curves are also included.

$E_\gamma$ (keV)	$I_\gamma^{absolute}$ (%)	Decay Mode	Initial State (keV)	Final State (keV)	$T_{1/2}$ (ms)
$591.7 \pm 0.3$	$14 \pm 2$	$\beta n$	591.7	0	$78 \pm 25$
$689.6 \pm 0.3$	$18 \pm 2$	$\beta$	2979	2289	$73 \pm 10$
$750.9 \pm 0.4$	$8 \pm 2$	$\beta$	1880	1128.7	$24 \pm 7$
$1128.7 \pm 0.3$	$48 \pm 4$	$\beta$	1128.7	0	$51 \pm 6$
$1160.6 \pm 0.3$	$30 \pm 3$	$\beta$	2289	1128.7	$78 \pm 9$
$1203.5 \pm 0.3$	$8 \pm 1$	$\beta n$	1795	591.7	$68 \pm 19$
$1466.8 \pm 0.3$	$6 \pm 1$	$\beta$	-	-	$60 \pm 13$
$1494.8 \pm 0.3$	$3 \pm 1$	$\beta$	4474	2979	$150 \pm 44$
$1711.6 \pm 0.3$	$3 \pm 1$	$\beta$	-	-	$29 \pm 10$

with decay from the higher-spin state, as do the transitions with energies 1467 and 1495 keV.

The half-life of the lower-spin  $\beta$ -decaying state in  $^{56}\text{Sc}$  was previously deduced to be  $35 \pm 5$  ms from a two-component fit to the decay curve gated on the 1129-keV  $\gamma$  transition, which depopulates a state fed directly and/or indirectly by both  $\beta$ -decaying states in  $^{56}\text{Sc}$ . Two newly-identified  $\gamma$ -ray transitions with energies 751 and 1712 keV were found to have half-lives similar to that extracted previously for the lower-spin isomer. These two  $\gamma$  rays apparently depopulate states fed exclusively by the lower-spin isomer. The weighted average of the half-lives for the 751- and 1712-keV transitions yields a half-life for the lower-spin isomer of  $26 \pm 6$  ms.

Levels in  $^{56}\text{Ti}$  and  $^{55}\text{Ti}$  populated in the decay of the two  $\beta$ -decaying states in  $^{56}\text{Sc}$  are shown in Fig. 4.16. The states in  $^{55}\text{Ti}$  are known from the  $^{55}\text{Sc}$   $\beta$  decay in NSCL experiment 07509 [84], previous  $\beta$ -decay studies [31], and deep inelastic work [83]. The three states at 1129, 2290 and 2980 keV in  $^{56}\text{Sc}$  were previously identified and tentatively assigned spin and parities [31,81], which are shown in Fig. 4.16.  $\gamma\gamma$  coincidences [see Fig. 4.17(a),(c),(d)] also confirm the placement of the 690-, 1129- and 1160-keV  $\gamma$  transitions associated with these three levels. The observed  $\gamma\gamma$  coincidences between the 1129- and 751-keV transitions [see Fig. 4.17(b),(c)] suggest the placement of an additional state populated by the lower-spin  $\beta$ -decaying state at 1880 keV.  $\gamma\gamma$  coincidences between the 1495- and 690-keV transitions [see Fig. 4.17(a),(e)] suggest that the higher-spin  $\beta$ -decaying state populates a level at 4474 keV, in addition to populating the two states at 2290 and 2980 keV. Only the 1467- and 1712-keV  $\gamma$  transitions remain unplaced in the present level scheme for  $^{56}\text{Ti}$ .

Absolute  $\gamma$ -ray intensities were determined for the  $\beta$ -delayed  $\gamma$ -ray transitions in the  $^{56}\text{Sc}$  decay by comparison of the number of observed  $\gamma$  rays, adjusted for the absolute efficiency of SeGA, with the number of observed  $^{56}\text{Sc}$  decay events. Typically, the number of parent decays is obtained from the decay curve fit, as previously described in Section 3.5.1. However, a precise value for  $^{56}\text{Sc}$  could not be obtained using this

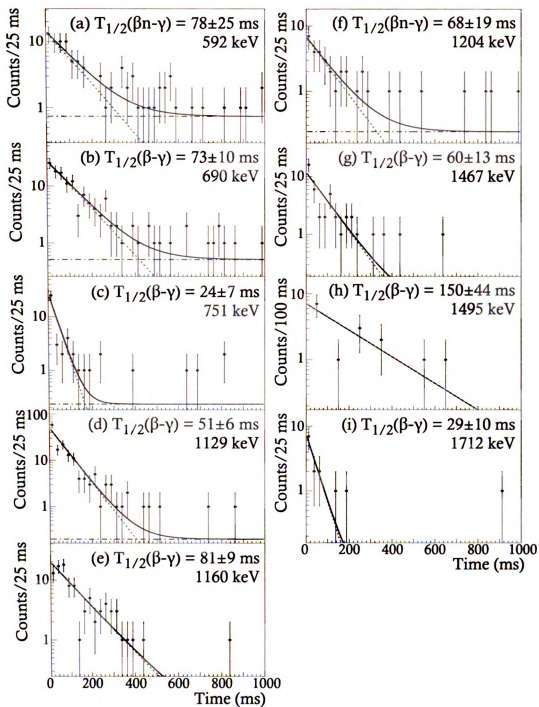


Figure 4.15: Decay curves for  $^{56}\text{Sc}$  using a correlation time of 1 s, and data over the entire surface of the DSSD, with the additional requirement of a coincident decay  $\gamma$ -ray transition. Decay curves are gated on the (a) 592-keV, (b) 690-keV, (c) 751-keV, (d) 1129-keV, (e) 1160-keV, (f) 1204-keV, (g) 1467-keV, (h) 1495-keV and (i) 1712-keV  $\gamma$  rays in the decay. All curves were fitted with a single exponential decay (dotted line) and a constant background component (dot-dashed line).

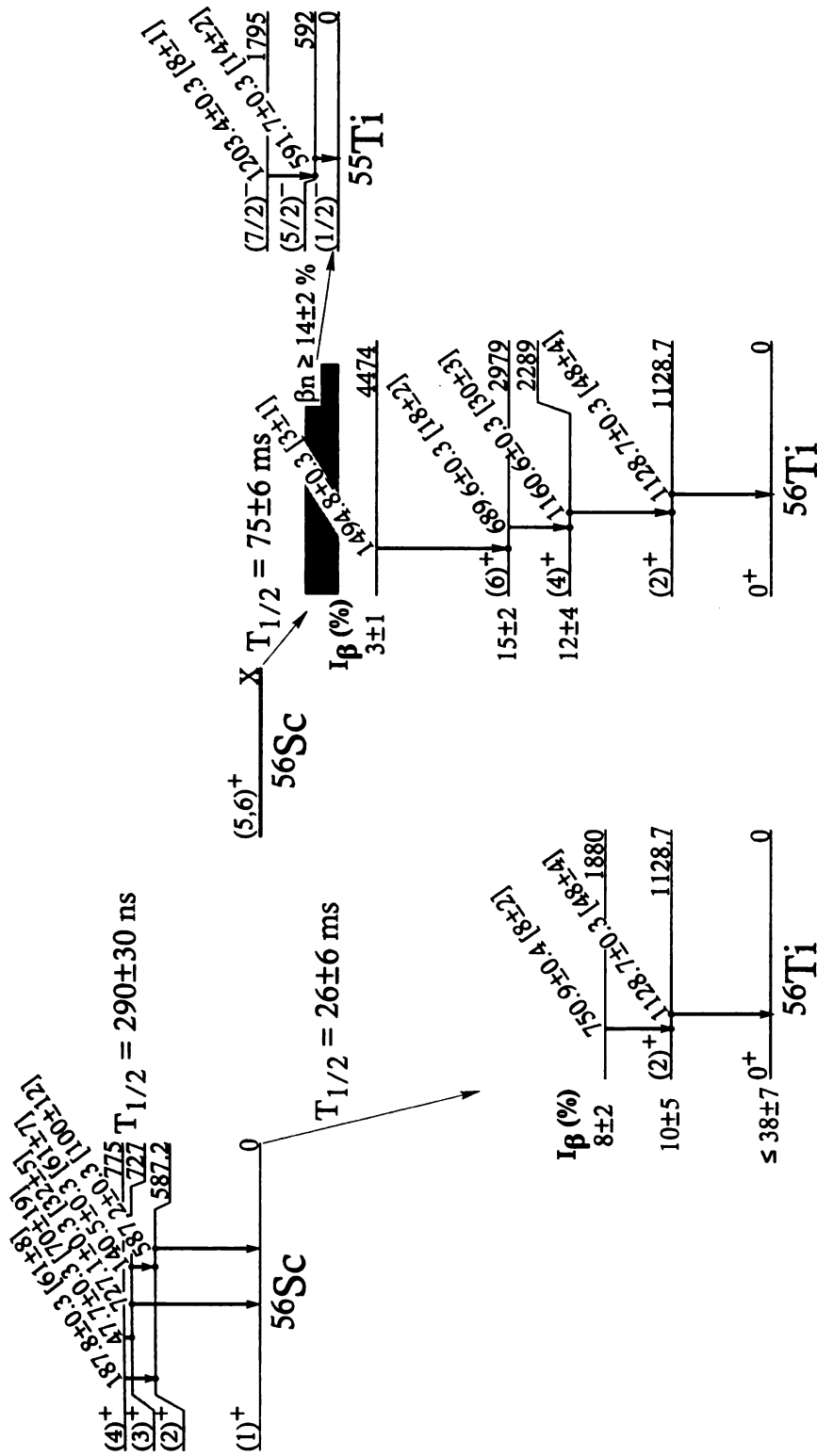


Figure 4.16: Proposed level scheme for  $^{56}\text{Sc}$ , following the  $\gamma$  decay of the isomeric transition at 775 keV, and levels in  $^{55,56}\text{Ti}$  populated following the  $\beta$  decay of  $^{56}\text{Sc}$ . The numbers in brackets following the isomeric  $\gamma$ -ray energies are the relative  $\gamma$  intensities. The number following the  $\beta$ -delayed  $\gamma$ -ray energies is the absolute  $\gamma$ -ray efficiency. The relative energies of the two  $\beta$ -decaying states is not known. The energy of the higher-spin  $\beta$ -decaying state, denoted by "X" may be negative if it is the ground state.  $Q_{\beta}$  for this decay is  $13.7 \pm 0.7$  MeV, and the neutron separation energy in  $^{56}\text{Ti}$  is  $5.3 \pm 0.2$  MeV [80].

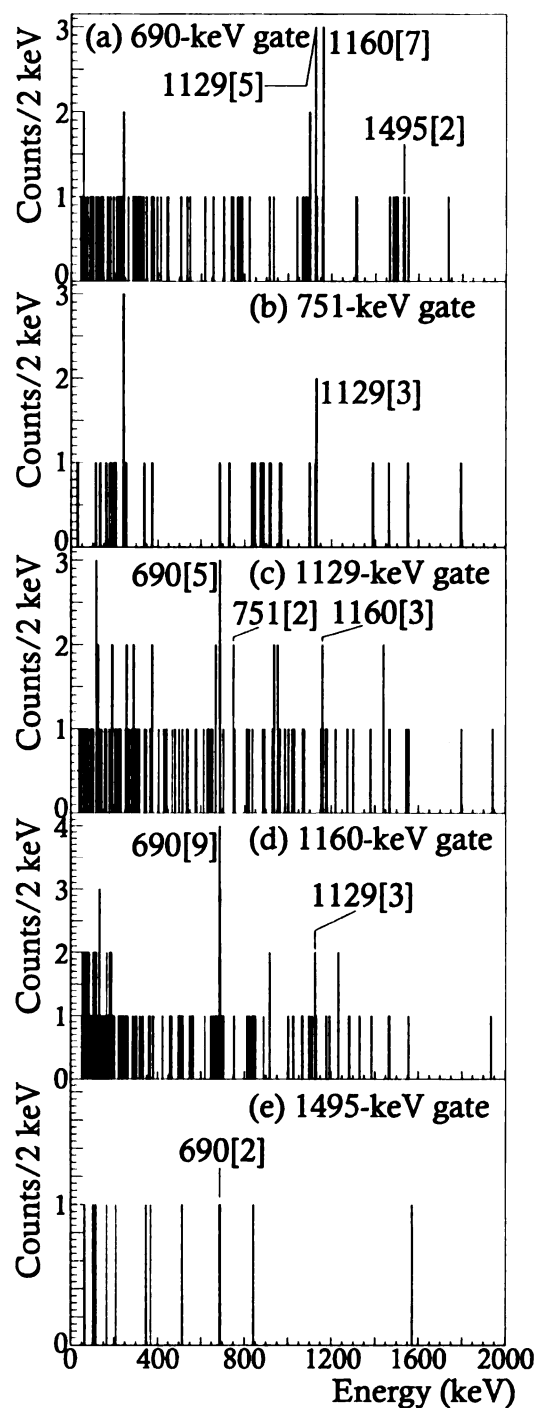


Figure 4.17:  $\gamma\gamma$  coincidence spectra gated on the (a) 690-keV, (b) 751-keV, (c) 1129-keV, (d) 1160-keV, and (e) 1495-keV transitions in coincidence with  $^{56}\text{Sc}$ -correlated  $\beta$ -decay events. These coincident spectra include data within a 1 s correlation time, for implants collected over the entire surface of the DSSD. The numbers in square brackets following the energies are the number of counts in the peaks.

approach. The presence of the two  $\beta$ -decaying states in this case results in a decay curve fit with a large number of free parameters. Instead, the number of  $^{56}\text{Sc}$  decays was determined using the total number of implantations, taken from the particle identification, and the average  $\beta$ -detection efficiency of  $11.4 \pm 0.4\%$ . The absolute  $\gamma$ -ray intensities are included in Table 4.2, and in the decay scheme of Fig. 4.16. Apparent  $\beta$  branches were deduced from the absolute  $\gamma$ -ray intensities. Decay from the higher-spin isomer apparently populates both the  $4^+$  and  $6^+$  states in  $^{56}\text{Ti}$ . This suggests that the higher-spin isomer has  $J^\pi = 5^+$ , in contradiction to the previous assignment of  $(6,7)^+$  by Liddick *et al.* [31]. However, the large  $Q_\beta$  value for the decay allows the  $(4)^+$  state at 2289 keV to be populated by cascades from above, resulting in the observed intensity difference between the 690- and 1161-keV transitions. Given this possibility, the higher-spin  $\beta$ -decaying state has been tentatively assigned as  $(5,6)^+$ . The state with an energy of 4474 keV, also populated by the higher-spin  $\beta$ -decaying state, has  $J^\pi$  limited to  $4^+$ ,  $5^+$ ,  $6^+$  or  $7^+$ , depending on the spin and parity of the higher-spin  $\beta$ -decaying state in  $^{56}\text{Sc}$ .

Decay from the lower-spin  $\beta$ -decaying state in  $^{56}\text{Sc}$  apparently directly feeds the first excited  $2^+$  state in  $^{56}\text{Ti}$ , which limits the spin and parity of this  $\beta$ -decaying state to  $1^+$ ,  $2^+$  or  $3^+$ . The  $J^\pi$  for the  $^{56}\text{Sc}$  ground state can be further restricted if there is direct  $\beta$  feeding to the  $^{56}\text{Ti}$  ground state. The absolute intensity of the 592-keV transition in the  $\beta n$  daughter  $^{55}\text{Ti}$  suggests a lower-limit for the neutron branching ratio of  $14 \pm 2\%$ . Even under the assumption that the two unplaced  $\gamma$  transitions directly populate the  $^{56}\text{Ti}$  ground state, there is  $29 \pm 7\%$  of the  $\beta$  intensity unaccounted for. Two scenarios can account for the missing intensity: either direct feeding to the  $^{56}\text{Ti}$  ground state or  $\beta n$  decay populating the ground state of  $^{55}\text{Ti}$  directly. Each possibility was investigated by reanalyzing the  $\beta$  decay of  $^{56}\text{Sc}$  with the longer correlation time of 5 s. With a longer correlation time, it was possible to compare the intensities of  $\gamma$ -ray transitions in the decay of the  $\beta n$  daughter  $^{55}\text{Ti}$  (672.5 keV,  $I_\gamma^{absolute} = 44 \pm 4\%$ ), and the  $\beta\beta$  granddaughter  $^{56}\text{V}$  (668.4 keV,  $I_\gamma^{absolute} = 26 \pm 2\%$ ). Within a 5 s correlation

Table 4.3: Determination of the  $\beta$  and  $\beta n$  contributions to the decay of  $^{56}\text{Sc}$ , based on the observation of  $\gamma$ -ray transitions in subsequent decays within the  $\beta$  and  $\beta n$  decay chains.

$^{56}\text{Sc}$ Decay Mode	Signature Decay	$E_\gamma$ (keV)	$I_\gamma^{absolute}$ (%)	Counts (5 s Correlation Time)	Number of Observed Decays	% of $^{56}\text{Sc}$ Decays
$\beta$	$^{56}\text{V} \rightarrow ^{56}\text{Cr}$	$668.4 \pm 0.3$	$26 \pm 2$	$94 \pm 12$	$362 \pm 54$	$71 \pm 14$
$\beta n$	$^{55}\text{Ti} \rightarrow ^{55}\text{V}$	$672.5 \pm 0.4$	$44 \pm 4$	$64 \pm 10$	$145 \pm 26$	$29 \pm 6$

time, >90% of the  $^{55}\text{Ti}$  ( $T_{1/2} = 1.3 \pm 0.1$  s [71]) populated in  $\beta n$  decays would have decayed, while  $^{56}\text{Ti}$  ( $T_{1/2} = 200 \pm 5$  ms [71]) populated in the  $\beta$  decay of  $^{56}\text{Sc}$  would have decayed into  $^{56}\text{V}$  ( $T_{1/2} = 216 \pm 4$  ms [70]), which would also have decayed. Thus, the ratio of  $\beta$  to  $\beta n$  decays in  $^{56}\text{Sc}$  can be determined by the ratio of the intensities of the 668- and 673-keV transitions, which are detected with nearly the same efficiency in SeGA.

The results of the  $\beta n/\beta\beta$  analysis are summarized in Table 4.3. Approximately 70% of the decays of  $^{56}\text{Sc}$  populate states in  $^{56}\text{Ti}$ . Thus, the missing  $\beta$ -intensity cannot be fully accounted for by  $\beta n$  decay to the ground state of  $^{55}\text{Ti}$ , and there is apparent direct population of the  $0^+$   $^{56}\text{Ti}$  ground state. The higher-spin  $(5,6)^+$   $\beta$ -decaying state cannot populate the  $^{56}\text{Ti}$  ground state directly, and so the lower-spin isomer must decay directly to the  $^{56}\text{Ti}$  ground state. The apparent feeding of the  $0^+$   $^{56}\text{Ti}$  ground state and the first  $2^+$  excited state thus suggests a spin and parity for the lower-spin  $\beta$ -decaying state of  $J^\pi=1^+$ . Direct feeding from the  $(1)^+$   $\beta$ -decaying state limits  $J^\pi$  of the state at 1880 keV to  $(0,1,2)^+$ .

#### 4.1.5 Isomerism in $^{56}\text{Sc}$

The  $\gamma$ -ray spectrum collected within a 20- $\mu\text{s}$  time window following the implantation of  $^{56}\text{Sc}$  is presented in Fig. 4.18. Five transitions were observed, and are summarized in Table 4.4. Those transitions with energies 140, 188, and 587 keV are in agreement with the three transitions previously reported by Liddick *et al.* [31].

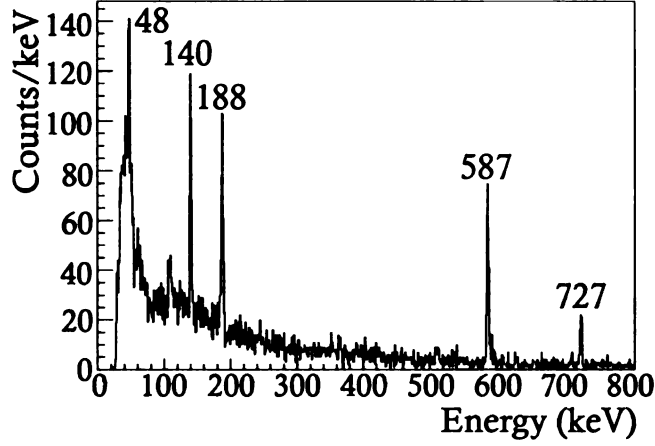


Figure 4.18: The prompt  $\gamma$ -ray spectrum collected within the first 20  $\mu\text{s}$  following a  $^{56}\text{Sc}$  implantation. The  $\gamma$  rays assigned to the isomer decay in  $^{56}\text{Sc}$  are marked by their energies in keV. The additional peak visible in the spectrum at 110 keV is contamination from the isomer decay of  $^{54}\text{Sc}$ .

Table 4.4: Energies and relative intensities of isomeric  $\gamma$  rays observed in the 20  $\mu\text{s}$  window following a  $^{56}\text{Sc}$  implantation event. Relative  $\gamma$  intensities are corrected for internal conversion [61], based on the transition multipolarity and energy. Transition multiplicities were assigned based on Weisskopf half-life estimates.

$E_\gamma$ (keV)	$I_\gamma^{\text{relative}}$ (%)	Transition Multipolarity	Total Internal Conversion Coefficient ( $\alpha_{\text{total}}$ )	Initial State (keV)	Final State (keV)
$47.7 \pm 0.3$	$70 \pm 19$	M1	$(1.16 \pm 0.02) \times 10^{-1}$	775	727
$140.5 \pm 0.3$	$61 \pm 7$	M1	$(6.6 \pm 0.1) \times 10^{-3}$	727	587
$187.8 \pm 0.3$	$61 \pm 8$	E2	$(2.63 \pm 0.04) \times 10^{-2}$	775	587
$587.2 \pm 0.3$	$100 \pm 12$	M1	$(2.34 \pm 0.04) \times 10^{-4}$	587	0
$727.1 \pm 0.3$	$32 \pm 5$	E2	$(2.45 \pm 0.04) \times 10^{-4}$	727	0

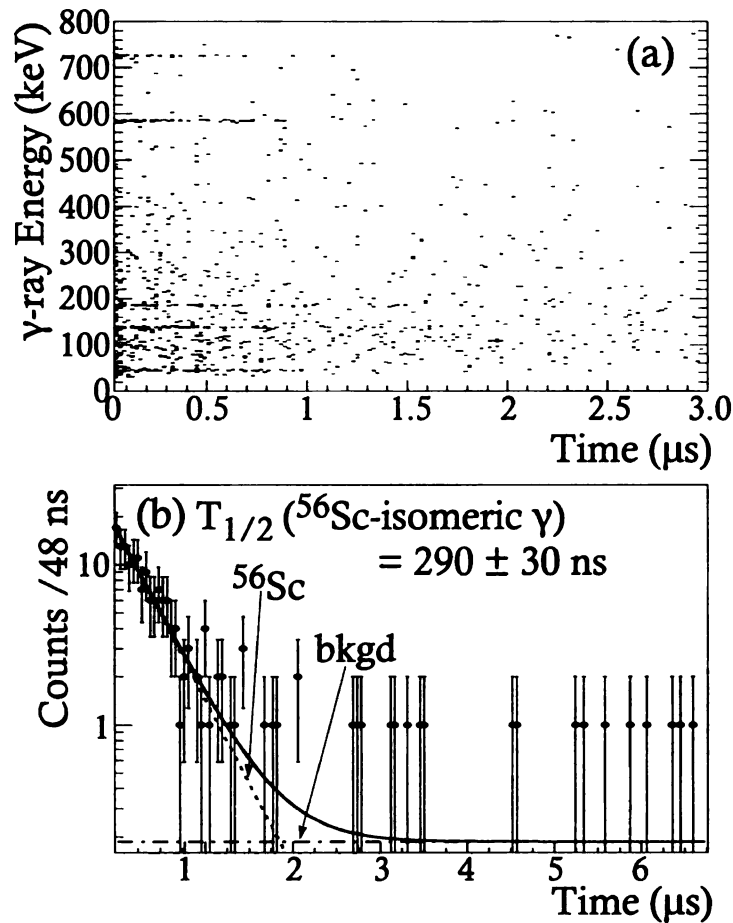


Figure 4.19: Time evolution of the prompt  $\gamma$ -ray transitions in  $^{56}\text{Sc}$ . (a) Prompt  $\gamma$ -ray energy plotted as a function of the time elapsed following a  $^{56}\text{Sc}$  implantation event. (b) Projection of (a) onto the time axis, gated on the five prompt  $\gamma$ -ray transitions. The data were fitted with a single exponential decay and a constant background.

The observed  $\gamma$ -ray energy is presented as a function of the time elapsed between a  $^{56}\text{Sc}$  implantation and prompt  $\gamma$ -ray emission in Fig. 4.19(a). The five transitions with energies 48, 140, 188, 587 and 727 keV appear to decay with the same half-life. Figure 4.19(b) contains a projection of the data of Fig. 4.19(a), gated on the five isomeric transitions, onto the time axis. The resulting decay curve was fitted with a single exponential decay and a constant background with a half-life for the isomeric state in  $^{56}\text{Sc}$  of  $290 \pm 30 \text{ ns}$ .

The low-energy structure of  $^{56}\text{Sc}$  populated by isomeric decay, presented in Fig. 4.16, was established based on the observed  $\gamma\gamma$  coincidences (see Fig. 4.20), and relative

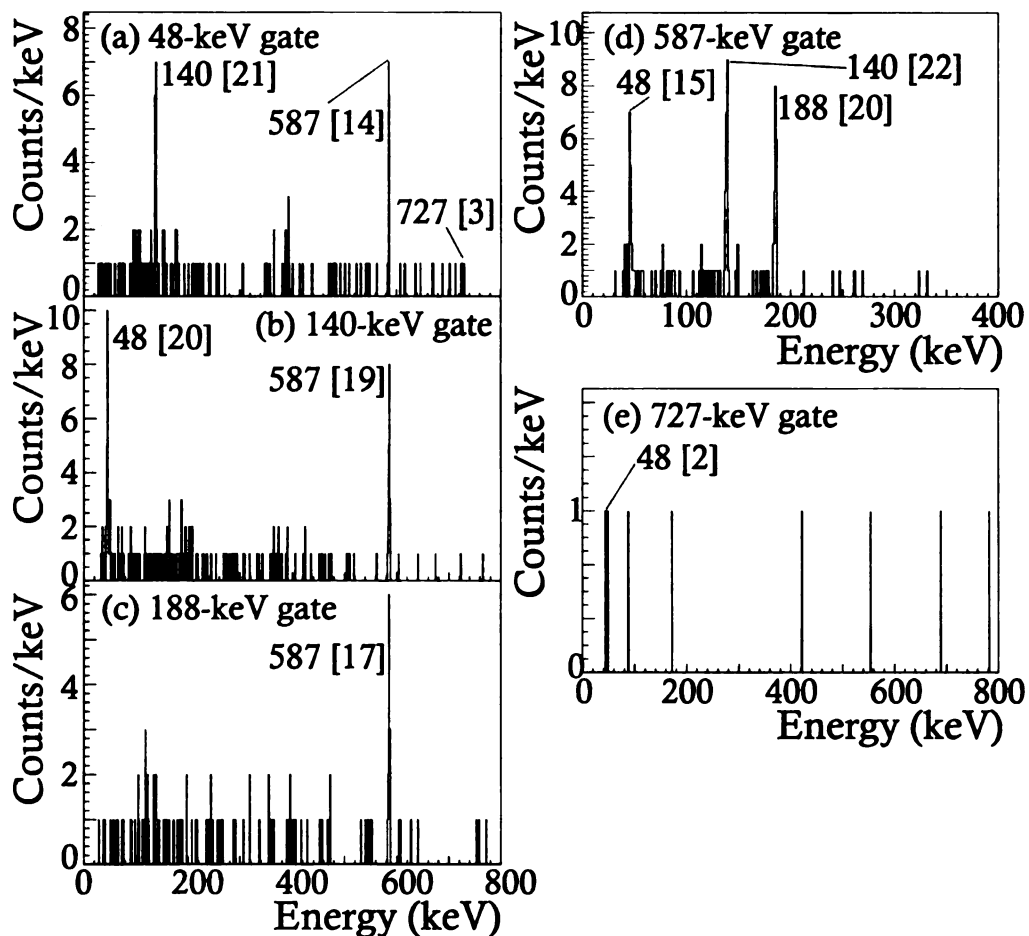


Figure 4.20:  $\gamma\gamma$  coincidence spectra for the (a) 48-keV, (b) 140-keV, (c) 188-keV, (d) 587-keV and (e) 727-keV transitions in the 20- $\mu$ s time window following a  $^{56}\text{Sc}$  implantation. The number of coincident counts are given by the numbers in square brackets following the transition energies.

transition intensities corrected for internal conversion. Energy-sum relationships to the cross-over transitions with energies 188 and 727 keV provided further support for the proposed level scheme.

A novel approach was taken to determine which of the two  $\beta$ -decaying states in  $^{56}\text{Sc}$  is populated by the isomeric decay. A half-life curve was constructed including only  $\beta$ -decay events correlated with  $^{56}\text{Sc}$  implantations that were in turn coincident with one of the five prompt  $\gamma$  rays. The resulting decay curve is presented in Fig. 4.21. A fit to these data with a single exponential decay for the  $^{56}\text{Sc}$  parent, growth and decay of the daughter ( $^{56}\text{Ti}$ ,  $T_{1/2} = 200 \pm 5$  ms [71]) and grand-

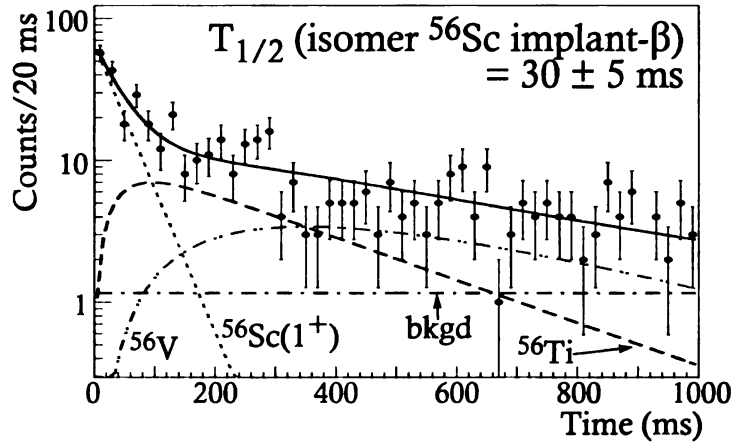


Figure 4.21: Decay curve for  $^{56}\text{Sc}$ -correlated  $\beta$  decays considering only  $^{56}\text{Sc}$  implantations coincident with identified isomeric  $\gamma$ -ray transitions. The decay curve was fitted with a single exponential decay, growth and decay of the  $\beta$ -decay daughter and granddaughter, and a constant background.

daughter ( $^{56}\text{V}$ ,  $T_{1/2} = 216 \pm 4$  ms [70]), and constant background yielded a half-life of  $30 \pm 5$  ms, consistent with decay of the lower-spin  $\beta$ -decaying state, previously assigned  $J^\pi = (1)^+$  (see Section 4.1.4). Knowledge of the quantum numbers of the lowest-energy state of the isomer ‘band’ permits tentative  $J^\pi$  assignments for the remaining low-lying levels populated in the isomeric decay of the isomeric state in  $^{56}\text{Sc}$ . The 188-keV transition, which directly depopulates the isomeric level, has E2 multipolarity, based on Weisskopf estimates (see Table 4.5). The 48-keV transition is assigned multipolarity M1, on the basis of the observed favourable competition with the 188-keV transition, and comparison with Weisskopf estimates. It follows that the 140-keV transition must also have M1 multipolarity. The observed intensities of the 727-keV and 140-keV transitions depopulating the isomeric state then suggest the former transition to be E2, which according to Weisskopf estimates, will proceed at a comparable rate to the 140-keV M1 transition. Finally, the remaining 587-keV transition must have M1 multipolarity. These assignments lead to the tentatively assigned  $J^\pi = (2)^+$ ,  $(3)^+$  and  $(4)^+$  values for the states in  $^{56}\text{Sc}$  at 587, 727 and 775 keV excitation energy above the base state, assuming that the base state has  $J^\pi = (1)^+$ .

Table 4.5: Weisskopf half-life estimates for the five prompt  $\gamma$ -ray transitions observed in  $^{56}\text{Sc}$ .

$E_\gamma$ (keV)	Weisskopf single particle half-lives					
	E1	M1	E2	M2	E3	M3
47.7	4.7 ps	114 ps	209 $\mu\text{s}$	5.9 ms	4.0 hours	$1.5 \times 10^6$ years
140.5	184 fs	4.5 ps	942 ns	27 $\mu\text{s}$	7.6 s	92 years
187.8	77 fs	1.9 ps	221 ns	6.3 $\mu\text{s}$	990 ms	6.7 years
587.2	2.5 fs	61 fs	738 ps	21 ns	339 $\mu\text{s}$	2.1 hours
727.1	1.3 fs	32.2 fs	254 ps	7.2 ns	76 $\mu\text{s}$	1084 s

## 4.2 Isomeric Structure of $^{50}\text{K}$

The neutron-rich  $_{19}\text{K}$  isotopes with  $N \geq 20$  are situated on the border of two major shells, with protons occupying the high-lying  $sd$ -shell single-particle orbitals, and neutrons filling low-lying  $fp$ -shell orbitals. The low-energy levels in the K isotopes are thus sensitive to the relative spacing of the proton single-particle orbitals below the  $Z=20$  shell closure. Recent evidence [85,86] suggests an evolution of the energies of the  $\pi 1d_{3/2}$  and  $\pi 2s_{1/2}$  states for the K isotopes with  $N > 28$  outside of the predictions of the most current  $sd$ - $fp$  cross-shell effective interactions. The low-energy levels in  $^{50}_{19}\text{K}_{31}$  are thus interesting to better understand the evolution of the proton single-particle states below  $Z=20$  with increasing neutron excess.

Isomerism in  $^{50}\text{K}$  was first reported by Lewitowicz *et al.* [87], with more details included in the work of Daugas [88]. The prompt  $\gamma$ -ray spectrum for  $^{50}\text{K}$  implantations collected in this work is presented in Fig. 4.22(a). Three transitions are apparent in this spectrum, at 43, 128 and 172 keV, and their details are summarized in Table 4.6. The observed transitions are in agreement with those previously observed by Daugas [88]. However, the additional two transitions with energies  $70 \pm 1$  keV and  $101 \pm 1$  keV also reported in Ref [88] are not apparent in the  $\gamma$ -ray spectrum depicted in Fig. 4.22(a). Fragment- $\gamma\gamma$  coincidences, shown in Fig. 4.23, indicate a coincidence relationship between the 43- and 128-keV transitions, however, the ordering of these transitions is not uniquely determined. The third transition at 172 keV in the spec-

Table 4.6: Energies, relative intensities and half-lives for the  $\gamma$  rays observed within the 20  $\mu$ s following a  $^{50}\text{K}$  implantation event. Relative intensities are corrected for internal conversion [61], based on the transition multipolarity and energy. Transition multiplicities were assigned based on comparison to Weisskopf half-life estimates as discussed in the text. Half-lives for individual  $\gamma$ -ray transitions were determined using the MLH method. A weighted average of the MLH values is also presented, as well as the results of a fit to the data for all three transitions using the ROOT fitting program.

$E_\gamma$ (keV)	$I_\gamma^{\text{relative}}$ (%)	Transition Multipolarity	Total Internal Conversion Coefficient ( $\alpha_{\text{total}}$ )	Number of Counts for $T_{1/2}$	MLH Half-life (ns)
$42.8 \pm 0.3$	$84 \pm 22$	M1	$0.107 \pm 0.003$	4	$65^{+75}_{-30}$
$128.4 \pm 0.3$	$75 \pm 15$	M1	$0.0059 \pm 0.0002$	21	$135^{+37}_{-27}$
$172.2 \pm 0.3$	$100 \pm 19$	E2	$0.0287 \pm 0.0008$	11	$229^{+125}_{-69}$
MLH Weighted average:					$154^{+34}_{-26}$ ns
ROOT fit:					$158 \pm 27$ ns

trum in Fig. 4.22(a) is placed as the cross-over transition, based on the energy-sum relationship.

The time evolution of the  $^{50}\text{K}$   $\gamma$  rays is given in Figure 4.22(b). The three transitions observed in Fig. 4.22(a) are apparent, though statistics are low. The number of counts are further reduced when considering only  $\gamma$  rays with decay times greater than 1  $\mu$ s, after the background of prompt  $x$ -rays which occurs upon fragment implantation into the DSSD. The  $\gamma$ -ray spectrum with this cut on the decay time is shown in Fig. 4.22(c), and the low statistics are evident. The total number of counts for each of the three transitions is summarized in Table 4.6.

An MLH analysis was used to extract the isomer half-life information due to the low statistics for the observed  $\gamma$  rays. The likelihood function (see Section 3.5) was evaluated for each event, and maximized to yield a half-life value for each of the three  $\gamma$  rays assigned to the decay of the  $^{50}\text{K}$  isomeric state. The resultant half-lives are listed in Table 4.6. The half-lives are consistent with one another, and a weighted average yields a value of  $154^{+34}_{-26}$  ns for the isomeric state with energy 172 keV in  $^{50}\text{K}$ .

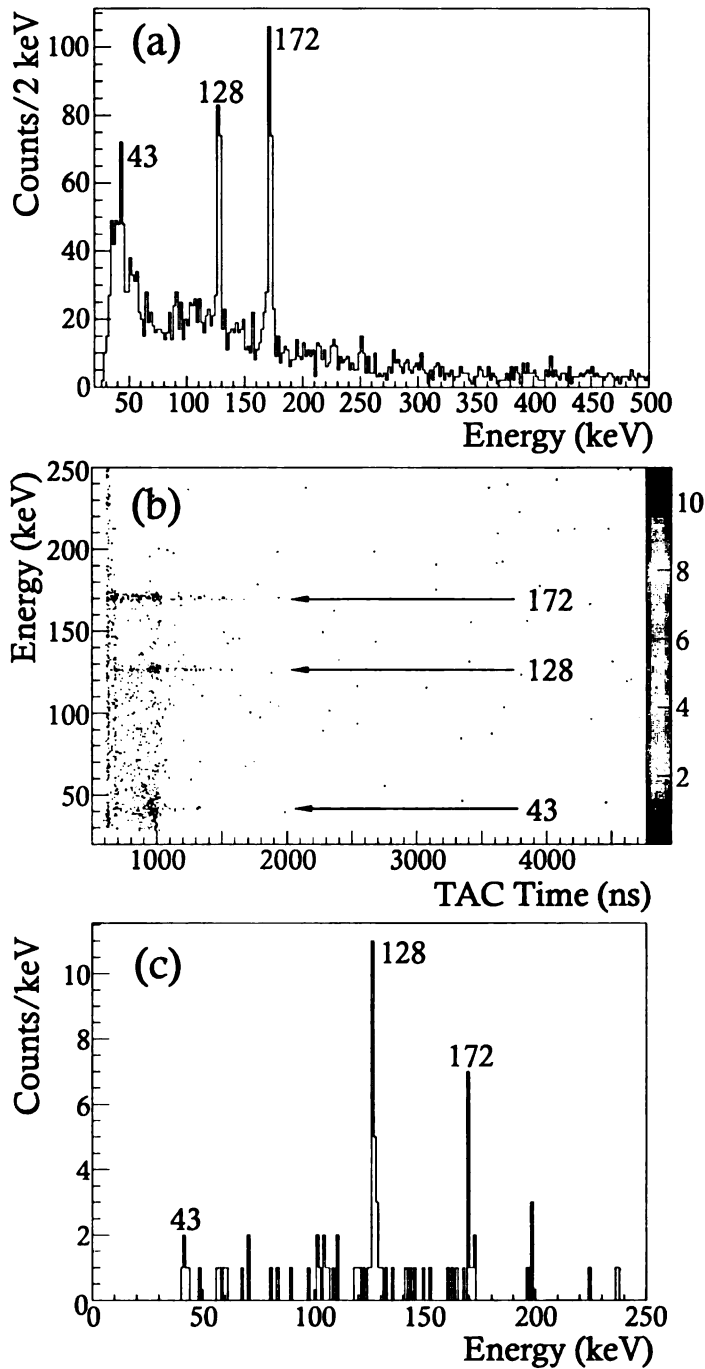


Figure 4.22: (a)  $\gamma$ -ray spectrum observed within the  $20 \mu\text{s}$  window following a  $^{50}\text{K}$  implantation event, in the energy range of 0-500 keV. The transitions assigned to the isomeric decay of  $^{50}\text{K}$  are marked by their energies in keV. (b) Time evolution of the  $\gamma$  rays observed following  $^{50}\text{K}$  implantations. The three observed transitions are marked by arrows. (c)  $\gamma$ -ray energy spectrum of (a) with the requirement of a TAC time greater than  $1.0 \mu\text{s}$ , beyond the x-ray flash. The three counts with energy 199 keV in this spectrum are background.

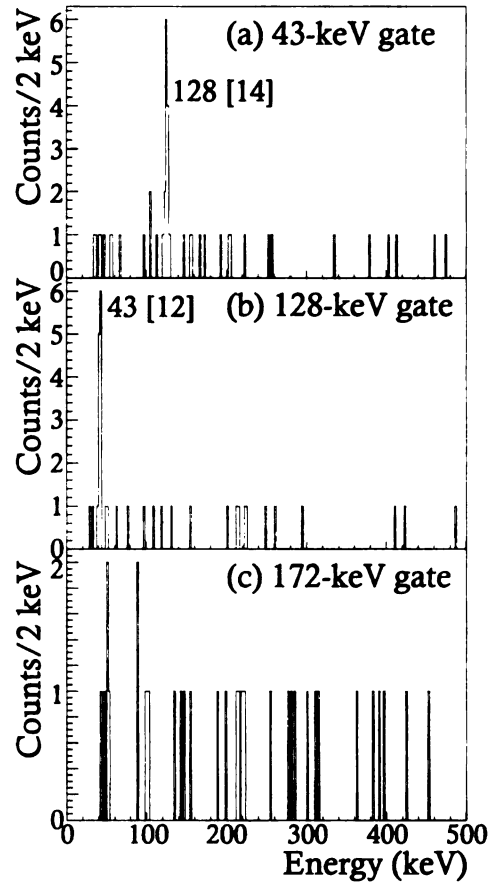


Figure 4.23:  $\gamma\gamma$  coincidence spectra gated on the (a) 43-keV, (b) 128-keV and (c) 172-keV  $\gamma$  rays observed within 20  $\mu$ s following a  $^{50}\text{K}$  implantation event. The numbers in square brackets following the energy of a peak are the number of counts in that peak.

Table 4.7: Weisskopf half-life estimates for the three prompt  $\gamma$ -ray transitions observed in  $^{50}\text{K}$ .

$E_\gamma$ (keV)	Weisskopf single particle half-lives					
	E1	M1	E2	M2	E3	M3
42.8	6.5 ps	158 ps	359 $\mu\text{s}$	10 ms	8.6 hours	$4.1 \times 10^6$ years
128.4	241 fs	5.9 ps	1.5 $\mu\text{s}$	42 $\mu\text{s}$	14.2 s	206 years
172.2	100 fs	2.4 ps	340 ns	9.6 $\mu\text{s}$	1.8 s	14.7 years

The results of a decay curve fit, using the ROOT program with Poisson analysis, to the summed data for all three transitions yields a value of  $158 \pm 27$  ns, consistent with the average MLH result. Both half-life values agree with the value of  $125 \pm 40$  ns reported by Daugas [88].

Comparison of the deduced lifetime with the Weisskopf estimates (see Table 4.7) suggests an E2 multipolarity for the 172-keV transition. The competition of the 43-128 keV  $\gamma$ -ray cascade with the direct ground state transition from the isomeric 172-keV state suggests that the multiplicities of the 43- and 128-keV transitions are M1. The low-energy level scheme for  $^{50}\text{K}$  is presented in Fig. 4.24. Spins and parities for the low-energy states populated in the prompt  $\gamma$ -ray decay of  $^{50}\text{K}$  are discussed in detail in Chapter 5.

### 4.3 Structure of $^{61}\text{Mn}$ from $\beta$ decay of $^{61}\text{Cr}$

Below the  $Z=28$  shell closure and approaching  $N=40$ , there is evidence in both the  $^{24}\text{Cr}$  and  $^{26}\text{Fe}$  isotopic chains of increasing collectivity, which develops below  $Z=28$  with the approach of the  $1g_{9/2}$  neutron orbital to the Fermi surface. While the onset of collectivity has been investigated in the  $^{24}\text{Cr}$  and  $^{26}\text{Fe}$  isotopic chains, data in the intermediate  $^{25}\text{Mn}$  isotopes is less abundant. The level structure of  $^{61}\text{Mn}$  will extend the information in the Mn isotopic chain, and provide insight into the development of collective behavior for  $Z=25$ .

Implanted  $^{61}\text{Cr}$  fragments were correlated with their subsequent  $\beta$  decays by re-

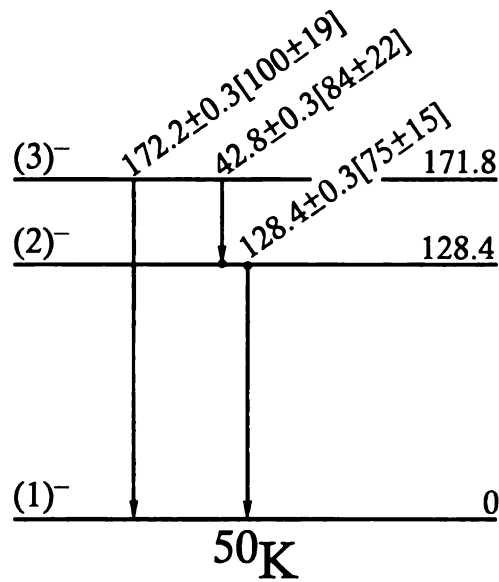


Figure 4.24: Proposed low-energy level scheme for  $^{50}\text{K}$ . The numbers in square brackets following the  $\gamma$ -ray transition energies are the relative transition intensities. The order of the two  $\gamma$ -ray cascade is not uniquely determined – the tentative  $2^-$  state may alternately be located at an excitation energy of 42.8 keV.

quiring the presence of a high-energy implantation event in a single pixel of the DSSD, followed by a low-energy  $\beta$  event in the same or any of the eight neighbouring pixels, using a correlation time of 3 s. The decay curve for  $^{61}\text{Cr}$ -correlated  $\beta$  decays given in Fig. 4.25 was fitted with a single exponential decay combined with an exponential growth and decay of the short-lived daughter,  $^{61}\text{Mn}$ , whose half-life was taken to be  $670 \pm 40$  ms from Ref. [89]. A constant background was also included as a free parameter in the fit. A half-life of  $233 \pm 11$  ms was deduced for the ground-state  $\beta$  decay of  $^{61}\text{Cr}$ . This new value compares favorably with the previous measurement by Sorlin *et al.* [59] of  $251 \pm 22$  ms, but is more than  $1\sigma$  shorter than the  $270 \pm 20$  ms value reported earlier by Ameil *et al.* [90].

The  $\beta$ -delayed  $\gamma$ -ray spectrum from the decay of  $^{61}\text{Cr}$  is shown in Fig. 4.26. The spectrum covers the energy range 0 to 2.5 MeV. The seven transitions assigned to the decay of  $^{61}\text{Cr}$  are listed in Table 4.8. The peaks observed with energies of 207 and 629 keV in Fig. 4.26 are known transitions in the decay of the  $^{61}\text{Mn}$  daughter [91]. The 1028- and 1205-keV transitions from the decay of the grand-daughter  $^{61}\text{Fe}$  [92] are

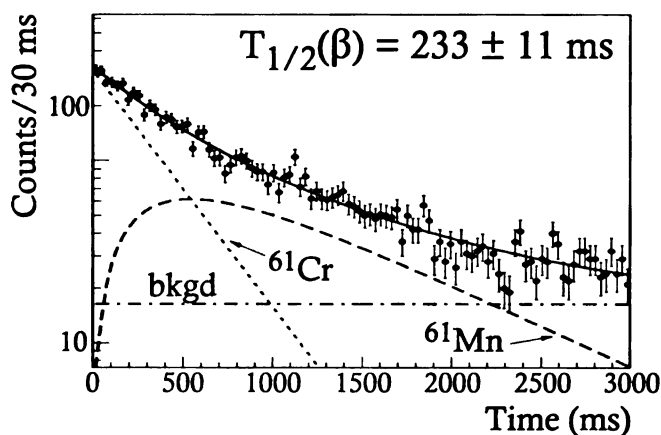


Figure 4.25: Decay curve for the  $\beta$  decay of  $^{61}\text{Cr}$  to  $^{61}\text{Mn}$ , constructed from decays correlated with  $^{61}\text{Cr}$  implantations using a 3 s correlation time. The data were fitted with a single exponential decay for the parent, growth and decay of the daughter, and a constant background.

also seen in Fig. 4.26. The peaks at 355, 535, 1142 and 1861 keV correspond in energy to the transitions previously reported by Sorlin *et al.* [59]. However, the transition observed in that work at 1134 keV was not apparent in the present work, see Fig. 4.26. The three additional  $\gamma$ -ray transitions at 157, 1497, and 2378 keV can be assigned for the first time to the decay of  $^{61}\text{Cr}$ . It is worth noting that two transitions with energies 155 and 355 keV had previously been assigned to the  $\beta$  decay of  $^{62}\text{Cr}$  [58]. Observation of these transitions in Fig. 4.26 suggests that they are associated with levels in  $^{61}\text{Mn}$ , and their observation in Ref. [58] may be evidence for  $\beta$ -delayed neutron decay of the  $^{62}\text{Cr}$  ground state. The in-beam  $\gamma$ -ray spectra for  $^{61}\text{Mn}$  and  $^{62}\text{Mn}$  obtained by Valiente-Dobón *et al.* [57] include transitions with energies of 157 and 155 keV, respectively, supporting the present assignment of the 157-keV  $\gamma$ -ray transition in Fig. 4.26 to the decay of  $^{61}\text{Cr}$ .

The proposed decay scheme for levels in  $^{61}\text{Mn}$  populated following the  $\beta$  decay of  $^{61}\text{Cr}$  is presented in Fig. 4.27. The  $\beta$ -decay  $Q$  value was taken from Ref. [80]. Absolute  $\gamma$ -ray intensities were deduced from the number of observed  $^{61}\text{Cr}$   $\gamma$  rays, the  $\gamma$ -ray peak efficiency, and the number of  $^{61}\text{Cr}$  implants correlated with  $\beta$  decays, as derived from the fit of the decay curve in Fig. 4.25. The two- $\gamma$  cascade involving

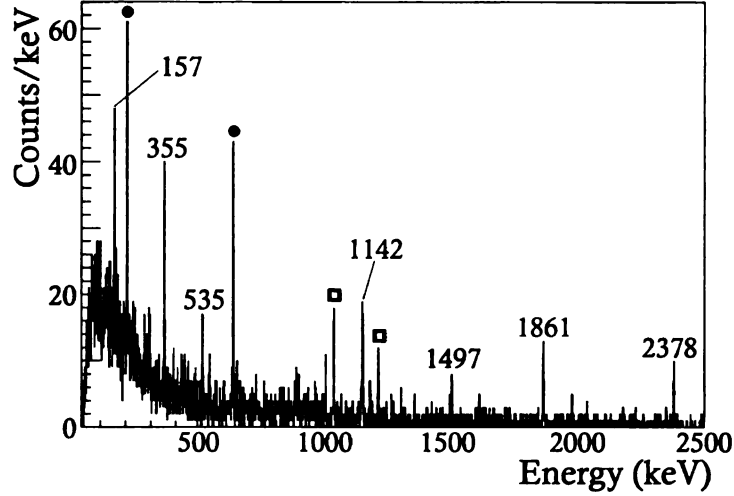


Figure 4.26:  $\beta$ -delayed  $\gamma$ -ray spectrum for the  $\beta$  decay of  $^{61}\text{Cr}$ , in the energy range of 0-2.5 MeV. Transitions marked by their energies in keV are assigned to the decay of  $^{61}\text{Cr}$ . Transitions marked by a filled circle are known transitions in the daughter  $^{61}\text{Mn}$ , while transitions marked by a square belong to the decay of the  $^{61}\text{Fe}$  granddaughter.

Table 4.8: Energies and absolute intensities of the  $\beta$ -delayed  $\gamma$  rays assigned to the decay of  $^{61}\text{Cr}$ . The initial and final states for those transitions placed in the proposed  $^{61}\text{Mn}$  level scheme are also indicated.

$E_\gamma$ (keV)	$I_\gamma^{\text{absolute}}$ (%)	$E_{\text{initial}}$ keV	$E_{\text{final}}$ keV	Coincident $\gamma$ rays (keV)
$157.2 \pm 0.5$	$9 \pm 2$	157	0	
$354.8 \pm 0.4$	$16 \pm 2$	1497	1142	535, 1142
$534.6 \pm 0.5$	$5 \pm 1$	2032	1497	355
$1142.2 \pm 0.4$	$21 \pm 2$	1142	0	355
$1497.3 \pm 0.5$	$9 \pm 2$	1497	0	
$1860.8 \pm 0.4$	$20 \pm 2$	1861	0	
$2378.2 \pm 0.4$	$11 \pm 1$	2378	0	

the 1142- and 355-keV transitions was confirmed by  $\gamma\gamma$  coincidence relationships (see Fig. 4.28). However, the ordering of the two transitions is not uniquely determined. The arrangement shown in Fig. 4.27 was based on the absolute intensities of the 1142- and 355-keV transitions. No evidence was found for  $\gamma$  rays in coincidence with the 157-keV ground-state transition within the statistical uncertainty of the measurement. Two counts in the 355-keV coincidence spectrum of Fig. 4.28(b) suggested placement of the 535-keV line in cascade from a higher-lying level at 2032 keV. This tentative placement is represented in Fig. 4.27 by a dashed line.

The apparent  $\beta$ -decay feeding to levels in  $^{61}\text{Mn}$  was deduced from the absolute  $\gamma$ -ray intensities. The deduced values, along with apparent  $\log ft$  values, are also given in Fig. 4.27. The observed  $\beta$  branches all have apparent  $\log ft$  values between 4 and 6, consistent with allowed transitions. The 1142-keV level was found to have a small  $\beta$  branching with a large error, and might not be directly populated by the  $\beta$  decay of  $^{61}\text{Cr}$ .

A ground-state spin and parity assignment of  $5/2^-$  was assigned to  $^{61}\text{Mn}$  by Runte *et al.* [91], based on the systematic trends of ground-state  $J^\pi$  values for the less neutron-rich, odd- $A$  Mn isotopes. The first excited state at 157 keV has been tentatively assigned  $J^\pi=7/2^-$  from the in-beam  $\gamma$ -ray results. Allowed  $\beta$  feeding to the lowest two states would then limit the  $J^\pi$  quantum numbers of the  $^{61}\text{Cr}$  ground state to values of  $5/2^-$  or  $7/2^-$ . Gaudefroy *et al.* [58] tentatively assigned the ground state of  $^{61}\text{Cr}$  to be  $J^\pi=5/2^-$  on the basis of the observed  $\beta$ -decay properties of the progenitor,  $^{61}\text{V}$ , and such an assignment is adopted in Fig. 4.27. It is likely that the 1142-keV state has low spin, either  $J^\pi=1/2^-$  or  $J^\pi=3/2^-$ . The level at 1142 keV is apparently weakly fed by  $\beta$  decay, was not identified in the yrast structure of  $^{61}\text{Mn}$  [57], and does not depopulate to the  $7/2^-$  level at 157 keV within the statistical uncertainty of this measurement. The 1497-keV level is tentatively assigned a  $J^\pi$  of  $3/2^-$  or  $5/2^-$  because of the apparent allowed  $\beta$ -decay branch and the favorable competition between the two depopulating  $\gamma$  rays that suggests that both transitions

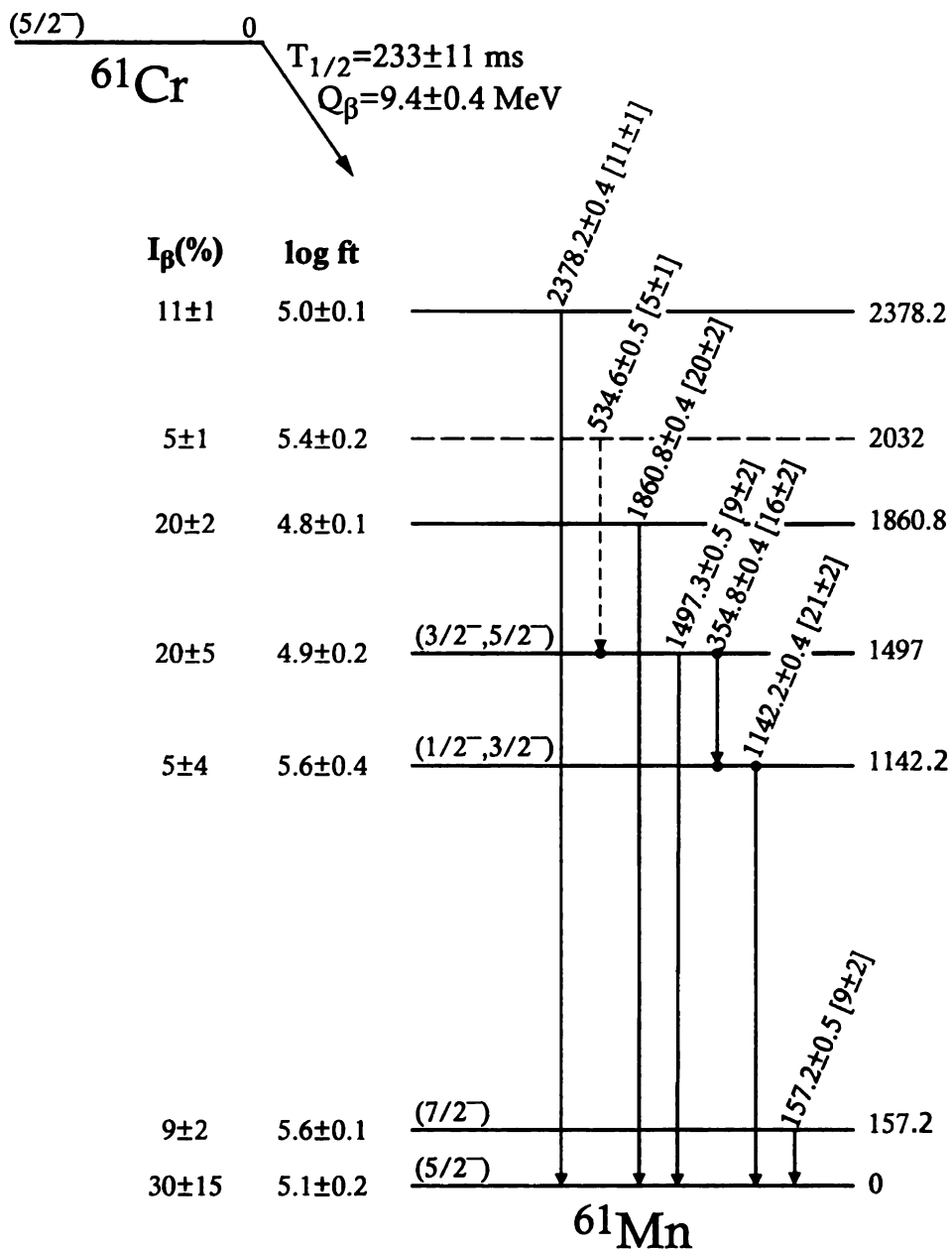


Figure 4.27: Decay scheme for the  $\beta$  decay of  $^{61}\text{Cr}$  to states in  $^{61}\text{Mn}$ . The number in brackets following the  $\gamma$ -ray energy is the absolute intensity.  $Q_\beta$  was determined from data in Ref. [80].

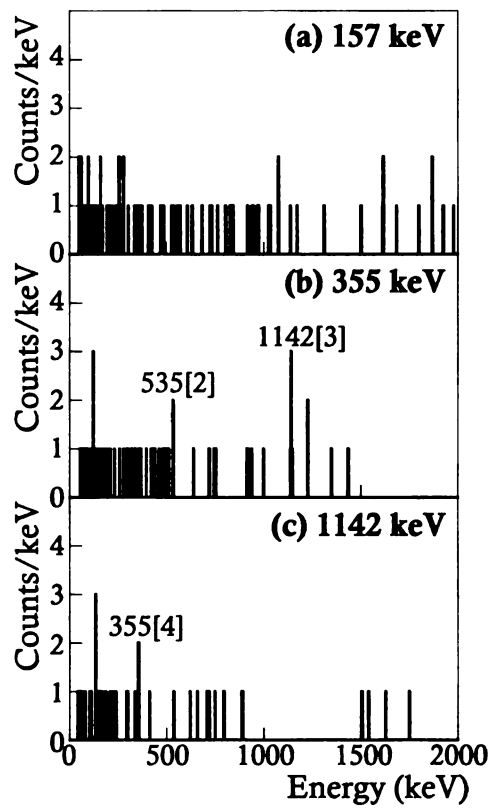


Figure 4.28:  $\gamma\gamma$ -coincidence spectra for the decay of  $^{61}\text{Cr}$ , gated on the (a) 157-keV, (b) 355-keV and (c) 1142-keV  $\gamma$ -ray transitions. These coincident spectra include data within a 3 s correlation time, for implants collected over the entire surface of the DSSD. In square brackets following the energy for each peak is the number of counts in that peak.

have M1 multipolarity. The proposed levels at excitation energies of 1861 and 2378 keV are apparently fed by allowed  $\beta$  decay as well, and can take  $J^\pi$  values in a range from  $3/2^-$  to  $7/2^-$ .

# Chapter 5

## Discussion

### 5.1 Interpretation of the low-energy levels in neutron-rich ${}_{21}\text{Sc}$

One of the more interesting questions with regard to nuclear structure in the  $fp$  shell is that of the possible  $N=34$  subshell closure in the  ${}_{20}\text{Ca}$  isotopes. The maximum upward monopole shift of the  $\nu 1f_{5/2}$  orbital with the completely empty  $\pi 1f_{7/2}$  orbital in the Ca isotopes may result in a significant gap between the  $\nu 1f_{5/2}$  orbital and the lower-lying  $\nu 2p_{1/2}$  orbital, creating a subshell gap at  $N=34$  similar to that previously observed at  $N=32$ . As discussed previously in Section 4.1, a number of experiments have been performed to probe the structure of  ${}^{54}\text{Ca}$  directly, with the hope of determining whether or not a subshell closure exists at  $N=34$  for the  $Z=20$  Ca isotopes. However, these experiments have proven difficult, and to date, no direct measurement has been successful.

Having one proton in addition to the Ca isotopes, the low-energy structure of the  ${}_{21}\text{Sc}$  isotopes may provide insight into the neutron single-particle energy spacing near  $N=34$ , and thus into the possible  $N=34$  subshell closure in Ca. The low-energy structures of  ${}^{53,54,56}\text{Sc}$  have been determined in the present work, by considering both the  $\beta$  decay of the parent nuclei  ${}^{53,54}\text{Ca}$ , as well as the isomeric decay of  ${}^{54,56}\text{Sc}$ .

The low-lying levels of these  ${}_{21}\text{Sc}$  isotopes will be discussed in the context of the extreme single-particle model, as a coupling of the odd  $1f_{7/2}$  proton to the valence neutron configurations in the  ${}_{20}\text{Ca}$  core isotopes. The success or failure of simple coupling schemes to explain the observed low-energy structure of the Sc isotopes can also provide indirect indications of the presence or absence of subshell closures in the Ca core nuclei.

Below, the structures of the neutron-rich Sc isotopes are discussed in the framework of the simple coupling of the valence proton and neutrons. The experimental levels are then compared to the results of more realistic shell-model calculations.

### 5.1.1 Low-energy structure of odd- $A$ ${}^{53}\text{Sc}$

The low-energy structure of  ${}^{53}\text{Sc}$  can be interpreted as a weak coupling of the valence  $\pi f_{7/2}$  proton to states in  ${}^{52}\text{Ca}$ , which, assuming a robust  $N=32$  subshell closure, can be viewed as a doubly magic core [12]. Coupling of the valence proton to the first  $2^+$  state in  ${}^{52}\text{Ca}$  should produce a quintet of states in  ${}^{53}\text{Sc}$  with  $J^\pi$  values ranging from  $3/2^-$  to  $11/2^-$ , at energies centered around  $\sim 2.6$  MeV. Studies of  ${}^{53}\text{Sc}$  produced in deep inelastic reactions [93] have populated  $9/2^-$  and  $11/2^-$  states near this energy, which are likely members of the  $\pi f_{7/2} \otimes 2^+$  multiplet (see Fig. 5.1). The  $\beta$  decay of  ${}^{53}\text{Ca}$  was observed to populate only one state in  ${}^{53}\text{Sc}$ . The population of a single state in the decay of  ${}^{53}\text{Ca}$  is expected for allowed  $\beta$  decay from the presumed  $1/2^-$   ${}^{53}\text{Ca}$  ground state, since the decay should only populate the  $3/2^-$  state of the  $\pi f_{7/2} \otimes 2^+$  multiplet. Thus, the single new level at 2109 keV is a likely candidate for the  $3/2^-$  member of the  $\pi f_{7/2} \otimes 2^+$  multiplet. The three known levels in  ${}^{53}\text{Sc}$ , shown in Fig. 5.1, reside at above 2 MeV, as expected within the weak coupling framework. While not all states of the expected quintet have been identified, this simple scheme describes the three known levels well. The apparent success of the weak coupling description for  ${}^{53}\text{Sc}$  provides support for the robust nature of the  $N=32$  subshell closure in the  ${}_{20}\text{Ca}$  isotopes.

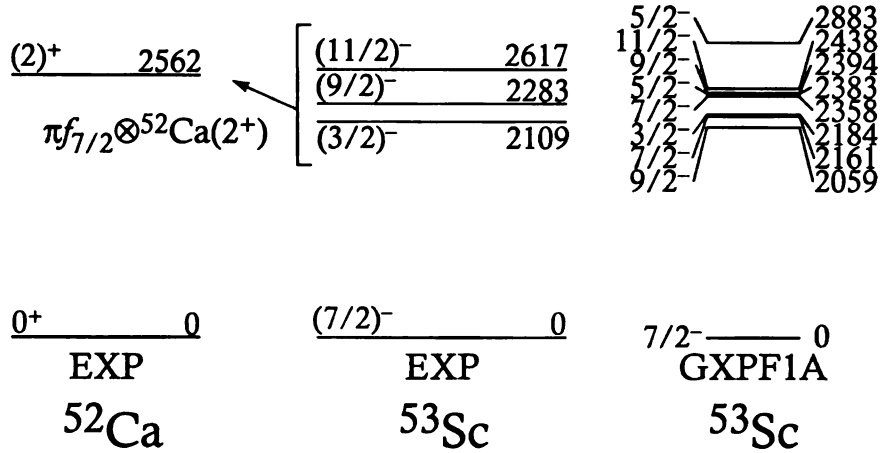


Figure 5.1: The comparison of the known levels in  ${}^{53}\text{Sc}$  [75, 93] to states in  ${}^{52}\text{Ca}$  suggests that  ${}^{53}\text{Sc}$  is accurately described by weak coupling of the odd  $\pi f_{7/2}$  proton to the  ${}^{52}\text{Ca}$  core. The experimental states are also in good agreement with predictions of shell-model calculations using the GXPF1A effective interaction [94].

A more advanced approach to describe the low-energy structure of  ${}^{53}\text{Sc}$  comes from considering more realistic wavefunctions, that allow configuration mixing. Shell-model calculations using the GXPF1A effective interaction [34] were performed for  ${}^{53}\text{Sc}$  [94], and are presented in Fig. 5.1. The calculated levels are in good agreement with the three known excited states, although there are significantly more calculated levels. Additional experimental work is required to identify the remaining levels and complete the expected  $\pi f_{7/2} \otimes 2^+$  multiplet in  ${}^{53}\text{Sc}$ .

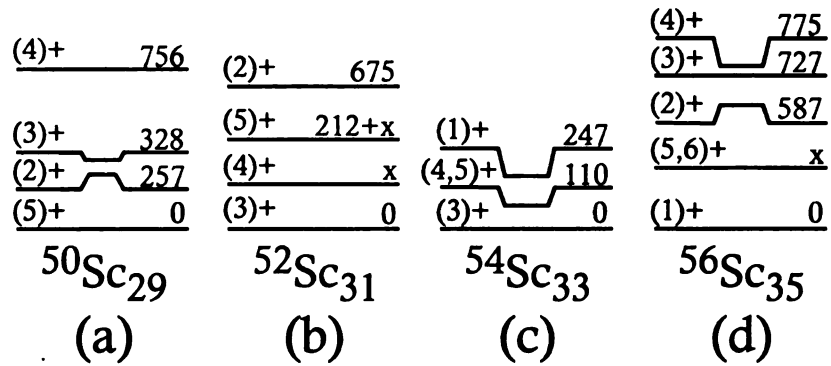
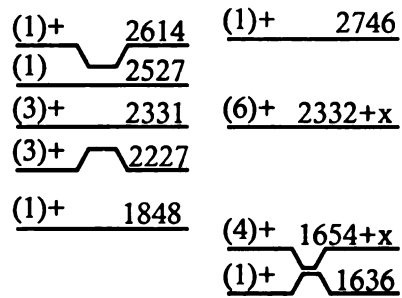
### 5.1.2 Low-energy structure of even- $A$ Sc isotopes

The structure of the even- $A$  (odd-odd)  ${}_{21}\text{Sc}$  isotopes can be described by coupling the valence  $\pi f_{7/2}$  proton particle with  $p_{3/2}$ ,  $p_{1/2}$ ,  $f_{5/2}$ , and at higher energies,  $g_{9/2}$ , valence neutron configurations. The success of such a description is shown most directly by considering the cases of  ${}^{50}\text{Sc}$  and  ${}^{52}\text{Sc}$ , where this simple interpretation explains many aspects of the known low-energy structures.

${}^{50}\text{Sc}$  has one proton and one neutron outside of the doubly magic  ${}^{48}\text{Ca}$  core, and the lowest energy levels can be described by coupling a valence  $\pi f_{7/2}$  proton and  $\nu p_{3/2}$

neutron. The low-energy structure, known from  $\beta$  decay [95], transfer reactions [96], and charge exchange reactions [97] is summarized in Fig. 5.2(a). The four states lowest in energy with  $J^\pi = 2^+$  to  $5^+$  arise from the configuration  $(\pi f_{7/2})^1 \otimes (\nu p_{3/2})^1$ . The particle-particle coupling rules [21] predict the arrangement of the states of this multiplet in a downward-opening parabola, which agrees with the experimental energy level ordering. Promotion of the valence neutron in  $^{50}\text{Sc}$  to the  $\nu p_{1/2}$  level gives the configuration  $(\pi f_{7/2})^1 \otimes (\nu p_{1/2})^1$ , producing only two states with  $J^\pi = 3^+, 4^+$ . Two  $3^+$  states are identified in the level scheme of  $^{50}\text{Sc}$  above 2 MeV, and either is a candidate for the  $3^+$  member of this doublet. The energy spacing between multiplets arising from configurations involving the  $\nu p_{3/2}$  and  $\nu p_{1/2}$  states depends on the  $\nu p_{3/2} - \nu p_{1/2}$  single-particle spacing, and thus the  $\nu p_{3/2} - \nu p_{1/2}$  spin-orbit splitting. The apparent separation of these two multiplets in  $^{50}\text{Sc}$  is on the order of 2 MeV, a gap sufficient to account for an established  $N=32$  subshell closure in  $_{21}\text{Sc}$ .

The structure of  $^{52}\text{Sc}$  can be similarly described by the coupling of a valence  $\pi f_{7/2}$  proton particle and  $\nu p_{3/2}$  neutron hole, taking  $^{52}\text{Ca}$  as the inert core [93]. States in this odd-odd nucleus have been identified in  $\beta$  decay studies [11], in-beam  $\gamma$ -ray spectroscopy following secondary fragmentation [98] and deep-inelastic work [93,99]. The known levels are presented in Fig. 5.2(b). Shell model calculations for  $^{52}\text{Sc}$  using the GXPF1, GXPF1A and KB3G effective interactions are presented in Fig. 5.3(a). As discussed in Refs. [93,99], the lowest-lying quartet of states in  $^{52}\text{Sc}$  can be associated with the configuration  $(\pi f_{7/2})^1 \otimes (\nu p_{3/2})^{-1}$ . The four states with  $J^\pi = 2^+ - 5^+$ , should form an upward-opening parabola, since the coupling involves a proton particle and neutron hole. The lowest  $3^+$  and  $4^+$  states in this parabola are expected to be close in energy. The energy separation between these states has not been established experimentally, but is likely to be small [99]. The Pandya transform [100] can be applied to relate the particle-particle  $(\pi f_{7/2})^1 \otimes (\nu p_{3/2})^1$  states of  $^{50}\text{Sc}$  to the particle-hole  $(\pi f_{7/2})^1 \otimes (\nu p_{3/2})^{-1}$  states in  $^{52}\text{Sc}$ . The Pandya relationship assumes the validity of  $jj$  coupling and is based on the simple form of the coefficients of fractional parent-



$^{50}\text{Sc}_{29}$

(a)

$^{52}\text{Sc}_{31}$

(b)

$^{54}\text{Sc}_{33}$

(c)

$^{56}\text{Sc}_{35}$

(d)

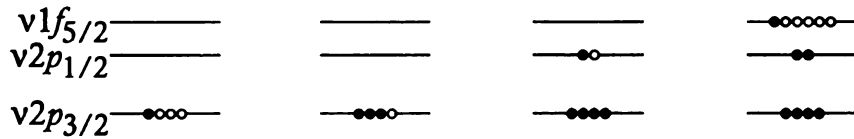


Figure 5.2: Experimentally known levels in the even- $A$  (a)  $^{50}\text{Sc}_{29}$ , (b)  $^{52}\text{Sc}_{31}$ , (c)  $^{54}\text{Sc}_{33}$ , and (d)  $^{56}\text{Sc}_{35}$  isotopes. Also included are the expected ground-state neutron configurations in the  $fp$ -shell orbitals above the  $N=28$  shell closure.

Table 5.1: Results of the application of the Pandya transform to the low-lying  $\pi f_{7/2}^1 \otimes \nu p_{3/2}^1$  neutron-particle states in  $^{50}\text{Sc}$  to predict the  $\pi f_{7/2}^{-1} \otimes \nu p_{3/2}^1$  neutron-hole states in  $^{52}\text{Sc}$ .

$^{50}\text{Sc} (\pi f_{7/2}^1 \nu p_{3/2}^1)$		$^{52}\text{Sc} (\pi f_{7/2}^1 \nu p_{3/2}^{-1})$			
$J^\pi$	Experimental Energy (keV)	$J^\pi$	Calculated Energy (keV)	Experimental Energy (keV)	$\Delta(E_{calc} - E_{exp})$ (keV)
$3^+$	0	$3^+$	26	0	26
$2^+$	257	$4^+$	0	x	-x
$3^+$	328	$5^+$	229	212+x	17-x
$4^+$	756	$2^+$	880	675	105

age (the probability of a given  $J$  state arising from a specific nucleon configuration) relating one- and two-hole states [100]. The results of this transform applied to  $^{50}\text{Sc}$  to the corresponding states in  $^{52}\text{Sc}$  are presented in Table 5.1. For a small energy separation between the  $3^+$  and  $4^+$  states (x) in  $^{52}\text{Sc}$ , the transform provides excellent agreement, suggesting that the configurations of these low-lying levels in both nuclei are fairly pure. Calculations using the GXPF1 effective interaction [12] support the relative purity of the four lowest-energy levels (see Fig. 5.3).

At higher excitation energies in  $^{52}\text{Sc}$ , the coupling of the  $\pi f_{7/2}$  proton to an excited  $\nu p_{1/2}$  neutron to give a pair of states with  $J^\pi=3^+, 4^+$  accounts for the observed  $4^+$  state in  $^{52}\text{Sc}$  at  $\sim 1.7$  MeV. The  $6^+$  state at  $\sim 2.3$  MeV in  $^{52}\text{Sc}$  has been shown in shell-model calculations to also have parentage that includes this configuration, although the extent of this contribution varies between shell-model interactions. Calculations using the GXPF1A interaction [99] suggest that the primary parentage of the 2.3-MeV  $6^+$  state is  $(\pi f_{7/2})^1 \otimes (\nu(p_{3/2}^2 p_{1/2}^1))$ , while the  $(\pi f_{7/2})^1 \otimes (\nu(p_{3/2}^2 f_{5/2}^1))$  configuration is predicted to dominate the first  $8^+$  state in  $^{52}\text{Sc}$ , experimentally observed at  $\sim 3.6$  MeV [99] [see Fig. 5.3(a)]. Experimentally, the energy separation between states dominated by the  $(\pi f_{7/2})^1 \otimes (\nu p_{3/2})^{-1}$  and  $(\pi f_{7/2})^1 \otimes (\nu(p_{3/2}^2 p_{1/2}^1))$  configurations appears to be  $\sim 2$  MeV, again corresponding to the spin-orbit splitting between the  $\nu p_{3/2}$  and  $\nu p_{1/2}$  single-particle states, in agreement with the results for  $^{50}\text{Sc}$ . As

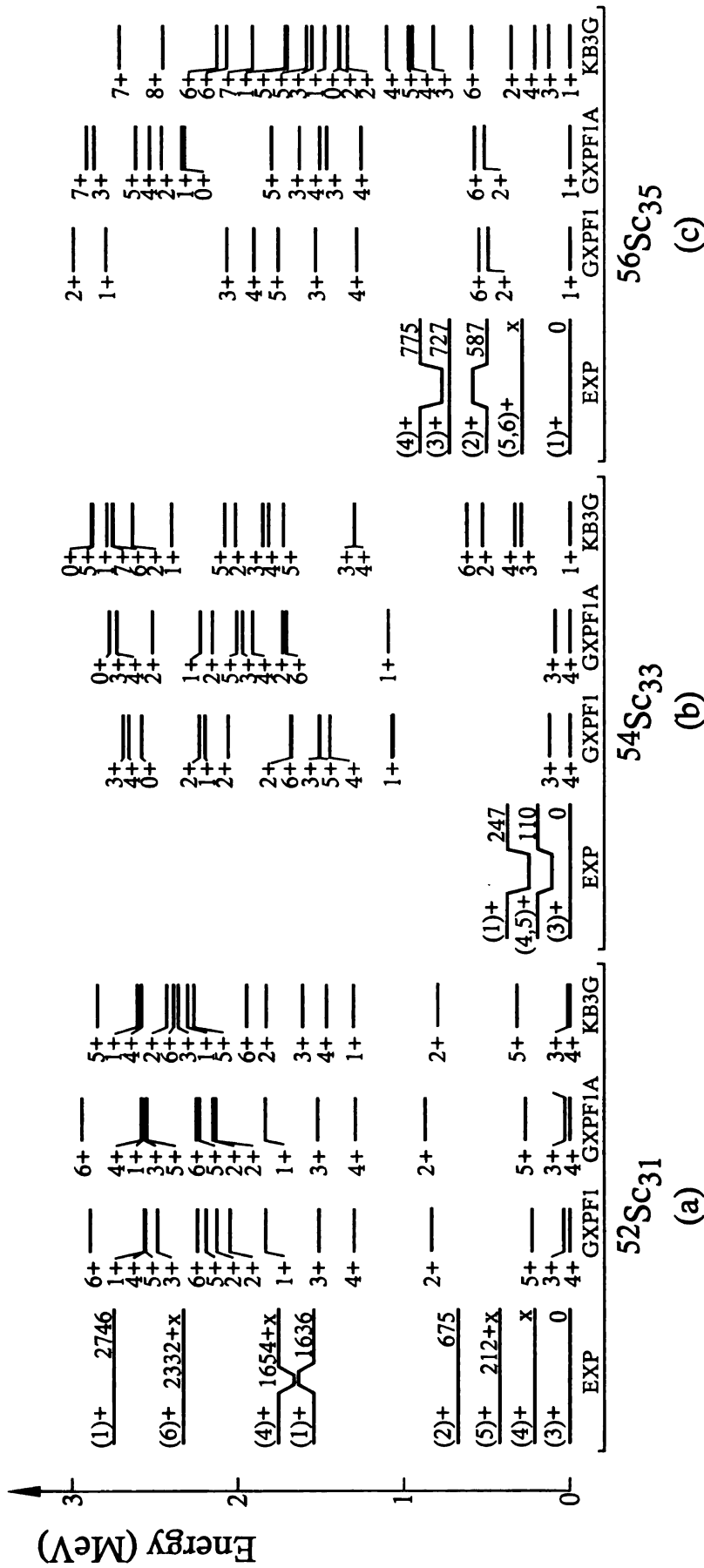


Figure 5.3: Comparison of the experimentally-known levels below 3 MeV in the even- $A$  (a)  $^{52}\text{Sc}$ , (b)  $^{54}\text{Sc}$  and (c)  $^{56}\text{Sc}$  isotopes with shell model calculations using the GXPF1 [33], GXPF1A [34] and KB3G [35] effective interactions.

noted by Fornal *et al.* [99], the apparent separation between the  $\nu p_{1/2}$  and  $\nu f_{5/2}$  single-particle states, as inferred from the energy spacing between the  $6^+$  and  $8^+$  states in  $^{52}\text{Sc}$ , is slightly smaller than that assumed in the GXPF1A interaction.

The low-energy structure of  $^{54}\text{Sc}$ , with two additional neutrons, should be significantly different. The  $\nu p_{3/2}$  orbital is now fully occupied, and the  $^{54}\text{Sc}$  structure at low energy should reflect coupling of the valence  $f_{7/2}$  proton particle to either a  $p_{1/2}$  or  $f_{5/2}$  neutron, again taking  $^{52}\text{Ca}$  as an inert core. The  $\nu p_{1/2}$  single-particle level is expected to lie below the  $\nu f_{5/2}$  state in the  $_{21}\text{Sc}$  isotopes, based on the observations in  $^{52}\text{Sc}$ . Assuming this ordering, the  $(\pi f_{7/2})^1 \otimes (\nu p_{1/2})^1$  coupling yields a doublet of states with  $J^\pi = 3^+, 4^+$ , which is expected to be lowest in energy in  $^{54}\text{Sc}$ . Shell model results [31,94] predict the  $3^+$  and  $4^+$  states of this configuration to be close in energy, and thus the spin and parity of the  $^{54}\text{Sc}$  ground state is not clear from a theory perspective. The ground state of  $^{54}\text{Sc}$  has been tentatively assigned  $J^\pi = 3^+$  in the present work (see Sections 4.1.2 and 4.1.3). Considering the situation purely in terms of the proton-neutron coupling, it may be natural to assume that the isomeric 110-keV level corresponds to the  $4^+$  state arising from the  $(\pi f_{7/2})^1 \otimes (\nu p_{1/2})^1$  configuration. However, within the simple coupling framework it is difficult to understand why the in-multiplet M1 transition is hindered strongly enough to yield the experimental isomer half-life of 2.8  $\mu\text{s}$ . In this case, the two other states identified in  $^{54}\text{Sc}$ , the isomeric  $(5)^+$  level and higher-lying  $(1)^+$  state, may arise from the configuration  $(\pi f_{7/2})^1 \otimes (\nu f_{5/2})^1$ . This coupling results in a sextet of states ranging from  $J^\pi = 1^+$  to  $6^+$ , and the particle-particle coupling would produce a downward-facing parabola. There are however, inconsistencies in the level ordering compared with the spin and parity assignments made in  $^{54}\text{Sc}$ . The  $1^+$  state lies above the possible  $5^+$  state in energy in the level scheme as presented in Fig. 5.2(c), a result which is inconsistent with the expectations of the particle-particle parabola, and calculations using the GXPF1, GXPF1A and KB3G effective interaction [see Fig. 5.3(b)]. An alternative  $J^\pi$  assignment for the states in  $^{54}\text{Sc}$  with a  $4^+$  ground state and  $6^+$  110-keV isomeric

level is a possibility, but the placement of the  $6^+$  level below the  $1^+$  level is also unexpected would also contradict the shell-model predictions. The apparent experimental level ordering could be better explained if the  $(\pi f_{7/2})^1 \otimes (\nu p_{3/2})^{-1}$  configuration was the origin of the  $3^+$  and  $5^+$  states. However, as demonstrated for the lighter Sc isotopes, the  $\nu p_{3/2} - \nu p_{1/2}$  spin-orbit splitting is a fairly constant  $\sim 2$  MeV, so that the  $\nu f_{7/2} - \nu p_{3/2}$  multiplet should reside at  $\sim 2$  MeV in  $^{54}\text{Sc}$ .

An alternative to the  $5^+$  assignment for the 110-keV isomeric state is a  $4^+$  assignment. While not expected based on comparison of the deduced isomer lifetime with Weisskopf single-particle estimates, which favor an E2 multipolarity for the 110-keV transition, a  $4^+$  spin and parity cannot be excluded for the 110-keV state. Calculations using the GXPF1 [33], GXPF1A [34] and KB3G [35] interactions all predict a doublet of states near the  $^{54}\text{Sc}$  ground state with  $J^\pi = 3^+$  and  $4^+$ . The transition probabilities,  $B(M1 : 3^+ \rightarrow 4^+)$  and  $B(E2 : 3^+ \rightarrow 4^+)$  calculated with these three interactions are shown in Table 5.2, along with the calculated partial half-lives. In all cases, the M1 component would dominate the transition. However, the  $B(M1 : 3^+ \rightarrow 4^+)$  values are small, giving rise to half-lives of order nanoseconds or longer – much slower than the picoseconds expectation from the single-particle Weisskopf estimate. The  $B(M1 : 3^+ \rightarrow 4^+)$  value is very sensitive to the degree of mixing in the wavefunctions for the  $3^+$  and  $4^+$  states [94]. With increased configuration mixing, there is increased suppression of the  $B(M1 : 3^+ \rightarrow 4^+)$  value, hindering the transition. A  $4^+$  spin and parity assignment is in better agreement with the expectation for the level ordering in  $^{54}\text{Sc}$ . However, more work is required to make a firm spin assignment for the 110-keV isomeric state in  $^{54}\text{Sc}$ .

The  $1^+$  state at energy 247 keV in  $^{54}\text{Sc}$  can only be explained by the  $(\pi f_{7/2})^1 \otimes (\nu f_{5/2})^1$  configuration. Even if this is the only member of the multiplet identified, the energy separation between the ground state with  $(\pi f_{7/2})^1 \otimes (\nu p_{1/2})^1$ , and the excited state with  $(\pi f_{7/2})^1 \otimes (\nu f_{5/2})^1$ , appears to be small. Shell model results using the GXPF1 and GXPF1A effective interactions [31, 94] predict a  $\nu p_{1/2} - \nu f_{5/2}$  separation of more

Table 5.2: Calculated transition probabilities and half-lives for the transition between the  $3^+$  and  $4^+$  states in  $^{54}\text{Sc}$ , using the GXPF1, GXPF1A and KB3G shell-model effective interactions. The Weisskopf single-particle estimates for the half-life of a 110-keV transition are also included.

	GXPF1	GXPF1A	KB3G	Single-Particle
$B(M1 : 3^+ \rightarrow 4^+) (\mu_N^2)$	0.02611	0.00369	0.00080	
$T_{1/2}(M1) (\text{s})$	$8.10 \times 10^{-10}$	$1.56 \times 10^{-8}$	$8.94 \times 10^{-7}$	$9.30 \times 10^{-12}$
$B(E2 : 3^+ \rightarrow 4^+) (e^2 fm^4)$	5.07	6.24	6.96	
$T_{1/2}(E2) (\text{s})$	$4.05 \times 10^{-6}$	$1.72 \times 10^{-5}$	$1.03 \times 10^{-3}$	$2.89 \times 10^{-6}$

than 1 MeV, which manifests itself in  $^{54}\text{Sc}$  as an expanded low-energy level structure, seen in Fig. 5.3(b). The compression in the experimentally established structure of  $^{54}\text{Sc}$  suggests a  $\nu p_{1/2}$ - $\nu f_{5/2}$  single-particle energy separation smaller than that assumed in the GXPF1 and GXPF1A effective interactions, and is inconsistent with a robust  $N=34$  subshell closure.

Another rapid structure change should be evident in the heavier  $^{56}\text{Sc}$  nucleus, since the addition of two neutrons to  $^{54}\text{Sc}$  will fill the  $\nu p_{1/2}$  single-particle orbital. The unpaired valence neutron will then occupy the  $\nu f_{5/2}$  state. Under this assumption, the lowest energy states in  $^{56}\text{Sc}$  would have a  $(\pi f_{7/2})^1 \otimes (\nu f_{5/2})^1$  configuration. The resulting sextet of states with  $J^\pi=1^+$  to  $6^+$  should be arranged in a downward facing parabola, with the  $4^+$  state at the vertex. The challenge in comparing these expectations in  $^{56}\text{Sc}$  to the new data is that the absolute energies of the two  $\beta$ -decaying states are not known. The states expected at low energy in  $^{56}\text{Sc}$  with  $J^\pi=1^+$ ,  $2^+$  and  $(5,6)^+$  are likely attributed to the  $(\pi f_{7/2})^1 \otimes (\nu f_{5/2})^1$  configuration. The  $3^+$  and  $4^+$  states cannot be trivially assigned the same configuration, as they may also arise from the  $(\pi f_{7/2})^1 \otimes (\nu p_{1/2})^1$  coupling, depending on the relative position of the  $\nu p_{1/2}$  and  $\nu f_{5/2}$  single-particle orbitals. In fact, significant mixing would be expected between the  $3^+/4^+$  states in the  $\pi f_{7/2}$ - $\nu f_{5/2}$  and  $\pi f_{7/2}$ - $\nu p_{1/2}$  multiplets if there is only a small energy gap between the  $\nu f_{5/2}$  and  $\nu p_{1/2}$  effective single-particle energies, as suggested in  $^{54}\text{Sc}$ . This mixing can also be seen in the calculated levels [94], even with

a large  $\nu p_{1/2}$ - $\nu f_{5/2}$  gap.

## 5.2 Re-ordering of proton single-particle states in neutron-rich K isotopes

The neutron-rich  ${}_{19}\text{K}$  isotopes with  $N \geq 20$  sit on the border of two major shells, with protons occupying the nearly full  $sd$  shell below  $Z=20$ , and neutrons occupying the next major shell, the  $fp$  shell. As such, shell-model descriptions of the neutron-rich K isotopes remain challenging, as cross-shell interactions are required to describe the interaction of valence  $sd$ -shell protons and  $fp$ -shell valence neutrons. Interactions which account for excitations of nucleons across the shell gaps are even more challenging than those within a given shell. However, new interactions do exist which attempt to accurately reproduce the cross-shell interactions between the  $sd$  and  $fp$  shells [101–103]. The results of shell-model calculations using such interactions will be discussed for the region surrounding  ${}^{50}\text{K}$  in the following sections. However, the structure of the neutron-rich K isotopes will first be described in terms of coupling of the valence nucleons, and the expected shifts in nucleon single-particle energies resulting from the monopole interaction. The systematics of the neutron-rich  ${}_{19}\text{K}$  isotopes surrounding the  $N=28$  shell closure are examined within this framework in the next section.

### 5.2.1 Systematics of the ${}_{19}\text{K}$ isotopes around $N=28$

As discussed in Chapter 1, the tensor monopole interaction between protons and neutrons is attractive between  $j_< (l - 1/2)$  and  $j_> (l + 1/2)$  orbital pairs and repulsive for  $j_<-j_<$  or  $j_>-j_>$  orbital pairs. The strength of the interaction is maximized between single-particle orbitals with similar  $l$  values [17]. Considering the effect of  $1f_{7/2} (l+1/2)$  neutrons on the proton  $sd$ -shell orbitals, it is apparent that the tensor

monopole interaction with the  $1d_{3/2}$  ( $l-1/2$ ) proton orbital will be attractive, while the interaction will be repulsive for the  $1d_{5/2}$  ( $l+1/2$ ) proton orbital. The  $2s_{1/2}$  proton orbital should exhibit no tensor monopole shift, since there are no partner orbitals for  $l=0$ . Thus, based solely on the energy shifts expected due to the tensor monopole interaction, the  $1d_{3/2}$  proton orbital is expected to decrease in energy relative to the  $2s_{1/2}$  orbital with increasing neutron  $1f_{7/2}$  occupancy. This expectation appears to be borne out in the experimental data for the even- $N$  K isotopes between  $N=20$  and  $N=28$ . The first  $3/2^+$  state in the odd- $A$  K isotopes can be associated with the  $1d_{3/2}^{-1}$  proton-hole configuration, while the first  $1/2^+$  state is associated with the  $2s_{1/2}^{-1}$  proton-hole (equivalently, the  $2s_{1/2}^1$  proton-particle) configuration. This relationship has been confirmed in the case of  $^{39}\text{K}$  in the analysis of proton pick-up reactions with  $^{40}\text{Ca}$  [104]. Thus, the relative energy of the  $3/2_1^+$  and  $1/2_1^+$  experimental levels is directly related to the separation between the proton  $1d_{3/2}$  and  $2s_{1/2}$  single-particle orbitals. A change in the energy separation of the  $1d_{3/2}$  and  $2s_{1/2}$  proton-hole states in the odd- $A$  K isotopes with increasing  $\nu 1f_{7/2}$  occupancy is apparent in Fig. 5.4. The  $\pi 2s_{1/2}^{-1}$  state, which is initially well-separated from the  $\pi 1d_{3/2}^{-1}$  ground state in  $^{39}\text{K}$ , rapidly drops in energy relative to the  $\pi 1d_{3/2}^{-1}$  state as the neutron  $1f_{7/2}$  orbital is filled. In fact, in  $^{47}\text{K}_{28}$ , with a full  $\nu 1f_{7/2}$  orbital, the proton  $1d_{3/2}$  orbital has dropped below the  $\pi 2s_{1/2}$  orbital, and  $^{47}\text{K}$  has been experimentally confirmed to have a ground state  $J^\pi$  of  $1/2^+$  [105], corresponding to a  $2s_{1/2}^{-1}$  proton hole configuration.

Moving past the  $N=28$  shell closure, neutrons begin to occupy the  $2p_{3/2}$  orbital. The tensor monopole interaction between the  $2p_{3/2}$  neutron orbital and the  $1d_{3/2}$  proton orbital, while attractive, is weaker than the  $\nu 1f_{7/2}$ - $\pi 1d_{3/2}$  tensor interaction. Again, the  $\pi 2s_{1/2}$  orbital should exhibit no tensor monopole shift. However, a second component to the monopole interaction, known as the central force [106], plays a significant role in the evolution of the relative spacing of the  $2s_{1/2}$  and  $1d_{3/2}$  proton orbitals in this region [107]. The central force is an attractive interaction between protons and neutrons, which does not have the spin dependence of the tensor monopole

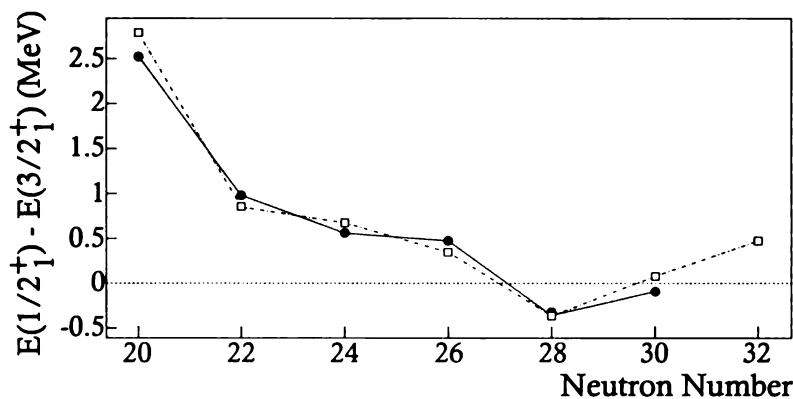


Figure 5.4: Systematic behavior of the separation between the  $3/2^+$  and  $1/2^+$  states in the odd- $A$  potassium isotopes between  $N=20$  and  $N=30$ . The observed energy separation is directly related to the separation between the  $1d_{3/2}$  and  $2s_{1/2}$  proton orbitals in the K isotopes. Experimental data points are indicated by filled circles, while predictions using the SDPF-U effective interaction [101] are represented by the open squares.

force. The central force does have an  $l$  dependence, and like the tensor force it is maximized for similar  $l$ . Below  $N=28$ , the central force between the  $\nu 1f_{7/2}$  and  $\pi 1d_{3/2}$  orbitals is stronger than that between the  $\nu 1f_{7/2}$  and  $\pi 2s_{1/2}$ . The central force contribution, in that case, reinforced the tensor monopole interaction and lowered the  $\pi 1d_{3/2}$  state relative to the  $\pi 2s_{1/2}$  state. However, above  $N=28$ , the central force between the  $\nu 2p_{3/2}$  and  $\pi 2s_{1/2}$  orbitals is expected to be stronger than the combined tensor monopole and central forces between the  $\nu 2p_{3/2}$  and  $\pi 1d_{3/2}$  orbitals. Thus, with the addition of neutrons to the  $2p_{3/2}$  orbital, the  $\pi 2s_{1/2}$  orbital is expected to drop in energy relative to the  $\pi 1d_{3/2}$  orbital, and the inversion of the proton orbitals, which was observed between  $^{45}\text{K}_{26}$  and  $^{47}\text{K}_{28}$ , reverses. The open question is how quickly this reversal occurs, which is related to the strength of the monopole interaction between the neutron and proton orbitals in the  $fp$  and  $sd$  shells respectively. An examination of the experimentally known low-energy structures of the K isotopes beyond  $N=28$  can provide first insight into this question.

States in the nucleus  $^{48}\text{K}$ , which has one neutron beyond  $N=28$ , are known from deep-inelastic work [108] and recent multinucleon transfer reactions [85] and are shown in Fig. 5.5. The ground state of this nucleus was initially assigned a spin and parity

of  $2^-$  on the basis of the expectations from the shell model and observed  $\beta$  feeding to states in  $^{48}\text{Ca}$  [109]. However, Broda *et al.* [85] re-assigned the ground state of  $^{48}\text{K}$  as  $J^\pi=1^-$  following analysis of multi-nucleon transfer and deep-inelastic reaction data. Such an assignment is still consistent with  $^{48}\text{K}$   $\beta$ -decay results since direct  $\beta$  decay to  $3^-$  states in  $^{48}\text{Ca}$  is not observed. Taking the  $J^\pi$  re-assignments from Ref. [85], the ground state and first excited state at energy 143 keV in  $^{48}\text{K}$  can be interpreted as arising from the coupling of the  $2p_{3/2}$  neutron with the  $2s_{1/2}$  proton hole, which gives rise to a  $1^-$  state (the ground state) and a  $2^-$  state (the 143-keV state). The higher-energy states in  $^{48}\text{K}$  at 279 keV and 728 keV should correspond to the  $2^-$  and  $3^-$  states of the  $(\nu 2p_{3/2})^1 \otimes (\pi 1d_{3/2})^{-1}$  multiplet. The  $0^-$  and  $1^-$  members of this multiplet are unknown at this time. The expectation of an upward-opening parabola for the particle-hole coupling would place the  $0^-$  and  $1^-$  levels above the  $2^-$  state at 279 keV. The separation between the  $1d_{3/2}$  and  $2s_{1/2}$  proton hole states in  $^{48}\text{K}$  appears to be of order a few hundred keV, consistent with a narrowing of the  $\pi 1d_{3/2}$ - $\pi 2s_{1/2}$  gap with the addition of a single  $2p_{3/2}$  neutron. This interpretation suggests that the  $\pi 1s_{1/2}$  level remains above the  $1d_{3/2}$  level in  $^{48}\text{K}_{29}$ .

The addition of two neutrons in the K isotopes beyond  $N=28$  corresponds to the odd- $A$  nucleus  $^{49}\text{K}$ . Recent data [86] for  $^{49}\text{K}$  from multinucleon transfer suggest that the proton  $2s_{1/2}$  orbital still remains above the  $1d_{3/2}$  orbital, as indicated in the systematics shown in Fig. 5.4. In this nucleus, the  $\pi 1d_{3/2}$ - $\pi 2s_{1/2}$  energy separation has narrowed further to only 92 keV.

Moving further to  $^{50}\text{K}$ , one can explore the relative position of the  $\pi 1d_{3/2}$  and  $\pi 2s_{1/2}$  orbitals with three neutrons now in the  $2p_{3/2}$  orbital. The low-energy levels in  $^{50}\text{K}$  from the present work are presented in Fig. 5.6. Assuming that the proton  $2s_{1/2}$  orbital has dropped further in energy and is again below the  $\pi 1d_{3/2}$  orbital, the ground state configuration in  $^{50}\text{K}$  would arise from the  $(\nu 2p_{3/2})^{-1} \otimes (\pi 1d_{3/2})^{-1}$  configuration. This configuration would account for the  $0^-$  ground state as previously assigned based on the  $\beta$  decay of  $^{50}\text{K}$  to states in  $^{50}\text{Ca}$  [110]. However, it is difficult

(7<sup>+</sup>)      3586

(5<sup>+</sup>)      2177

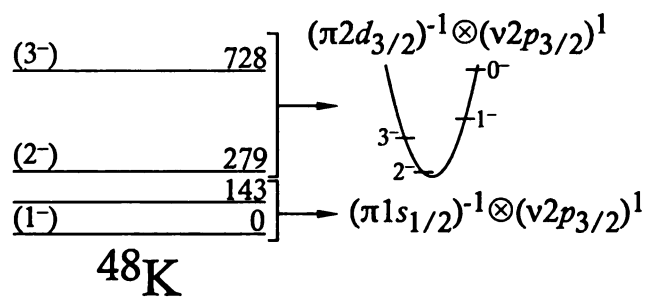


Figure 5.5: Known states in  $^{48}\text{K}$  [85, 108], and the possible origin of the low-lying states in the simple framework of the independent particle model.

to understand the presence of the observed isomer in  $^{50}\text{K}$  if the low-lying states all arise from the  $(\nu 2p_{3/2})^{-1} \otimes (\pi 1d_{3/2})^{-1}$  configuration. As discussed in Section 4.2, the deduced half-life of  $154_{-26}^{+34}$  ns for the  $^{50}\text{K}$  isomeric state at 172 keV is consistent with an E2 multipolarity for the 172-keV transition. The observed high level of competition between the direct 172-keV ground state transition and the two  $\gamma$ -ray cascade suggests that the first M1 transition of the cascade must be hindered. Such hindrance is unexpected for an in-multiplet M1 transition.

An alternative is that the ground state in  $^{50}\text{K}$  has the  $(\nu 2p_{3/2})^{-1} \otimes (\pi 2s_{1/2})^{-1}$  configuration. The ground state would be expected then to have a spin and parity of  $1^-$ , with the first excited state being the  $J^\pi=2^-$  state of the  $2s_{1/2}$  proton-hole configuration. The isomeric state could then be explained as the  $(\nu 2p_{3/2})^{-1} \otimes (\pi 1d_{3/2})^{-1}$  configuration. The isomeric state would most likely correspond to the  $3^-$  state of this multiplet. The M1 transition connecting the  $3^-$  isomeric state and the lower-lying  $2^-$  state would be hindered as a result of the forbidden nature of a  $\pi 1d_{3/2}-\pi 2s_{1/2}$  transition. Such a hindrance would explain the observed competition between the direct 172-keV E2 ground-state transition, and the two  $\gamma$ -ray cascade. Thus, a  $J^\pi=1^-$  ground state in  $^{50}\text{K}$ , arising from a  $2s_{1/2}$  proton hole configuration, seems to provide a more satisfactory understanding for the observed isomerism in  $^{50}\text{K}$  than any state arising from a  $(1d_{3/2})^{-1}$  configuration. Such a result would suggest that, even with three  $2p_{3/2}$  neutrons, the  $\pi 2s_{1/2}$  orbital remains above the  $\pi 1d_{3/2}$  orbital. The relative energy of states arising from the two proton-hole configurations would suggest a  $\pi 1d_{3/2}-\pi 2s_{1/2}$  gap comparable to that in  $^{48}\text{K}$ , of order a few hundred keV. However, to resolve the uncertainty in this situation, a direct measurement of the ground state spin and parity is necessary.

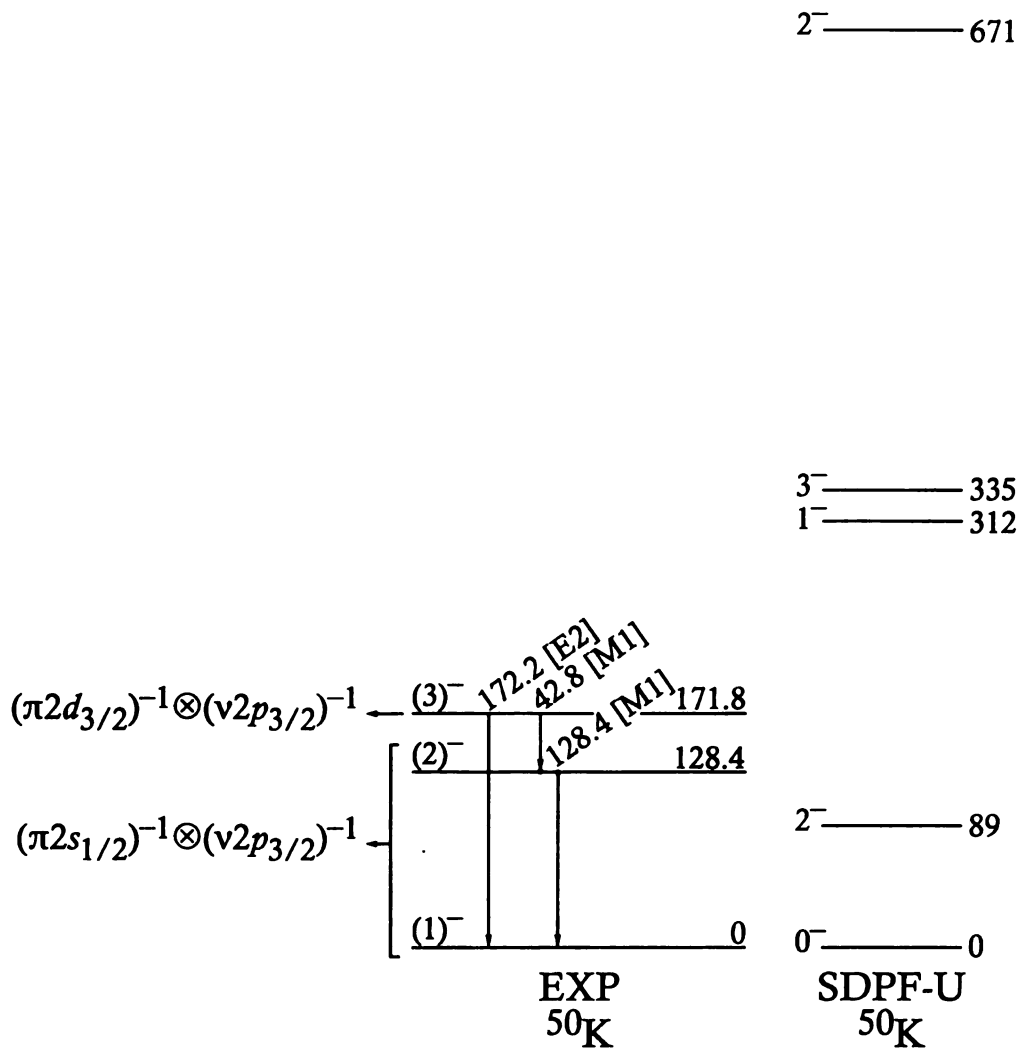


Figure 5.6: Proposed low-energy level scheme for  $^{50}\text{K}$ , and the possible origin of the low-lying states in the simple framework of the independent particle model. The energy of the suggested  $2^-$  state is not uniquely determined, and may alternately be located at energy 42.8 keV. The states below 1 MeV, calculated using the SDPF-U [101] effective interaction are also shown.

## 5.2.2 Comparison to shell-model calculations using $sd$ - $fp$ cross-shell interactions

There has been significant work in recent years on the development of shell-model effective interactions for calculations in the  $sd$ - $fp$  valence space, due primarily to the experimental observation of a weakening  $N=28$  shell closure [111,112]. These new effective interactions consist of three basic components: (a) a proton-proton interaction in the  $sd$  shell, (b) a neutron-neutron interaction in the  $fp$  shell, and (c) a cross-shell proton-neutron interaction. Generally, standard interactions are used for the intra-shell parts, such as the USD interaction for the  $sd$  shell [113], and the KB [114] or GXPF1A [34] interactions in the  $fp$  shell. The most uncertain part of the  $sd$ - $fp$  shell model calculations is the cross-shell component.

Utsuno *et al.* [102] have recently developed a new  $sd$ - $fp$  shell interaction that makes use of the USD interaction in the  $sd$  shell, and the GXPF1B interaction (a slight modification of the GXPF1A interaction with a better  $1p_{3/2}$ - $1p_{1/2}$  energy gap around the Ca isotopes [102]) in the  $fp$  shell. The cross-shell part of the interaction is built up from three components: a central force, a spin-orbit force and a tensor force. Results for the K isotopes using this effective interaction have been found to be consistent with experiment through  $^{47}\text{K}$  [102], correctly predicting the inversion of the  $\pi 2s_{1/2}$  and  $\pi 1d_{3/2}$  single-particle orbitals.

Another recent  $sd$ - $fp$  shell effective interaction has been developed by Nowacki and Poves [101]. Their SDPF-U interaction is a refinement of the previous SDPF-NR effective interaction [115], which makes use of the USD interaction in the  $sd$  shell, the KB interaction in the  $fp$  shell, and the  $G$  matrix calculations of Kahana, Lee and Scott for the cross-shell interaction. The monopole part of the cross-shell interaction was empirically modified to produce the correct evolution of effective single-particle states by fitting to a number of reference states across the region of interest. Results from this interaction for the  $^{19}\text{K}$  isotopes are in good agreement with experiment up

to and including  $N=28$ , correctly predicting the inversion of the  $\pi 2s_{1/2}$  and  $\pi 1d_{3/2}$  single particle orbitals in  $^{47}\text{K}$  [101]. However, immediately beyond  $N=28$ , the SDPF-U effective interaction predicts a  $3/2^+$  ground state in  $^{49}\text{K}_{30}$ , in contradiction with recent experimental results [86]. The separation between the  $\pi 2s_{1/2}$  and  $\pi 1d_{3/2}$  single particle orbitals predicted by the SDPF-U interaction for  $N > 30$  continues to increase [101] and is inconsistent with the suggested  $(\nu 2p_{3/2})^{-1} \otimes (\pi 2s_{3/2})^{-1}$  ground state configuration in  $^{50}\text{K}$ . Shell-model calculations for  $^{50}\text{K}$  were performed using the SDPF-U effective interaction [94] and are presented in Fig. 5.6. The apparent discrepancy between theory and experiment may be related to the  $2p_{3/2}-1d_{3/2}$  and  $2p_{3/2}-1s_{1/2}$  monopole strengths. These monopole interactions largely determine the evolution of the  $\pi 2s_{1/2}-\pi 1d_{3/2}$  single-particle energy spacing with the filling of the  $\nu 2p_{3/2}$  orbital beyond  $N=28$ . Additionally, the  $2p_{3/2}-1d_{3/2}$  and  $2p_{3/2}-2s_{1/2}$  monopole strengths were changed between the SDPF-U interaction and the previous SDPF-NR interaction, which had correctly reproduced the  $1/2^+$   $^{49}\text{K}$  ground state [101]. Additional data will be required to better constrain the cross-shell effective interactions, and improve the predictive power of *sd-fp* shell interactions.

### 5.3 Onset of collectivity in the $^{25}\text{Mn}$ isotopes

Approaching  $N=40$  below the  $Z=28$  shell closure, an increase in collectivity has been inferred at low energy for the neutron-rich  $^{24}\text{Cr}$  and  $^{26}\text{Fe}$  nuclei. The apparent onset of deformation in these isotopes has been associated with the presence of the neutron  $1g_{9/2}$  single-particle orbital near the Fermi surface as  $N=40$  is approached. The observed structural changes in this region are again attributed in part to the tensor monopole interaction. The repulsive interaction between  $1f_{7/2}$  ( $l+1/2$ ) protons and  $1g_{9/2}$  ( $l+1/2$ ) neutrons is reduced with the removal of  $1f_{7/2}$  protons below  $Z=28$ , and the  $1g_{9/2}$  orbital drops in energy towards the Fermi surface. The role of the  $\nu 1g_{9/2}$  orbital in driving deformation, as a function of nuclear charge, will be critical

to assessing the persistence of the  $N=50$  shell gap in  $^{78}\text{Ni}$  and other neutron-rich nuclei in this region of the nuclear chart.

As noted in Chapter 1, the systematic variation in  $E(2_1^+)$  values [Fig. 1.9(b)] suggest that collectivity sets in already at  $N = 36$  for the Cr isotopes, while first evidence for such effects in the Fe isotopes occurs at  $^{64}\text{Fe}$ , which has  $N = 38$ . Therefore, the low-energy structure of  $^{61}\text{Mn}$ , with  $N = 36$ , might exhibit features at low energy suggestive of a change in collectivity when compared to other odd- $A$  Mn isotopes nearer to stability. The  $\beta$  decay of  $^{61}\text{Cr}$  to states in  $^{61}_{25}\text{Mn}_{36}$  was studied in the present work. The newly identified states extend the systematics of the odd- $A$  Mn isotopes through  $N=36$ , and can be investigated for signs of developing collectivity.

### 5.3.1 Systematics in odd- $A$ Mn

The systematic variation of the known energy levels of the odd- $A$  Mn isotopes with  $A = 57 - 63$  is shown in Fig. 5.7. The levels below 2 MeV for  $^{57}\text{Mn}$  were taken from  $\beta$  decay of  $^{57}\text{Cr}$  [116], in-beam  $\gamma$ -ray spectroscopy [117], and the  $(d, ^3\text{He})$  transfer reaction [118].  $\beta$  decay populates seven excited states below 2 MeV, as well as the  $^{57}\text{Mn}$  ground state. The states directly fed by  $\beta$  decay are all assumed to have negative parity, since the  $^{57}\text{Cr}$  parent has ground state  $J^\pi = 3/2^-$ . The negative parity yrast states observed in  $^{57}\text{Mn}$  were populated by a heavy-ion induced fusion-evaporation reaction, that provided tentative spin assignments of the levels up to  $J = 25/2$ . The  $(d, ^3\text{He})$  transfer reaction provided unambiguous  $J^\pi$  assignments to the negative parity states below 2 MeV at 84, 851, and 1837 keV, based on angular distribution data. Positive parity was deduced for the excited states with energies 1753 and 1965 keV. Based on the spectroscopic strengths for proton pickup [118], the first  $7/2^-$ ,  $1/2^+$ , and  $3/2^+$  levels in  $^{57}\text{Mn}$  were deduced to carry  $\sim 40\%$  of the summed single-particle strength from shell model expectations.

Valiente-Dobón *et al.* [57] studied neutron-rich Mn isotopes by in-beam  $\gamma$ -ray spectroscopy following deep inelastic collisions of a  $^{70}\text{Zn}$  beam on a  $^{238}\text{U}$  target.

Negative-parity yrast states were identified up to  $J = 15/2$  in  $^{59}\text{Mn}_{34}$  and  $J = 11/2$  in  $^{61}\text{Mn}_{36}$ . Only a single transition, with an energy of 248 keV, was assigned to the structure of  $^{63}\text{Mn}_{38}$ . The non-yrast levels in  $^{59,61}\text{Mn}$  shown in Fig. 5.7 were identified in  $\beta$ -decay work. The  $\beta$  decay of  $^{59}\text{Cr}$  to levels in  $^{59}\text{Mn}$  was most recently reported by Liddick *et al.* [69]. The ground state spin and parity of the parent  $^{59}\text{Cr}$ , tentatively assigned to be  $J^\pi = 1/2^-$ , restricts the range of states in  $^{59}\text{Mn}$  accessible by allowed  $\beta$  decay to those with  $J^\pi = 1/2^-, 3/2^-$ . The ground state of  $^{59}\text{Mn}$  is known to have  $J^\pi = 5/2^-$  [119]. The non-yrast  $J^\pi$  values for  $^{59}\text{Mn}$  were inferred from the  $\beta$ - and  $\gamma$ -decay patterns. The present work has expanded the knowledge of states in  $^{61}\text{Mn}$ , identifying three new states, in addition to the three previously known yrast states [57].

The negative parity yrast structures below 2 MeV in odd- $A$   $^{57,59,61}\text{Mn}$  exhibit little variation as a function of neutron number. These levels are consistent with shell model calculations reported in Ref. [57] employing the GXPF1A, KB3G and  $fpg$  effective interactions. The authors of Ref. [57] do note, however, that the proper ordering of the  $9/2^-$  and  $11/2^-$  levels at  $\sim 1$  MeV is reproduced for all three isotopes only by the  $fpg$  interaction. The experimental energy gap between the ground state, with  $J^\pi = 5/2^-$ , and the  $7/2^-$  first excited state exhibits a regular increase from  $^{57}\text{Mn}$  (83 keV) to  $^{65}\text{Mn}$  (272 keV) [58]. Both the GXPF1A and  $fpg$  shell model interactions reproduce the observed trends well.

The shell model calculations in Ref. [57] were extended to include non-yrast states below 2 MeV. The calculations were performed with the code ANTOINE [120] using the GXPF1A [34] and  $fpg$  [46] effective interactions. The full  $fp$  model space was utilized for the calculations with the GXPF1A interaction. The valence space for the calculations with the cross shell interaction  $fpg$  was limited to 2 neutron excitations from the  $fp$  shell to the  $1g_{9/2}$  orbital. As compared to Ref. [57], truncation of the basis states was necessary to reach convergence for the higher density of states at lower spin for the most neutron-rich Mn isotopes considered here. However, in those

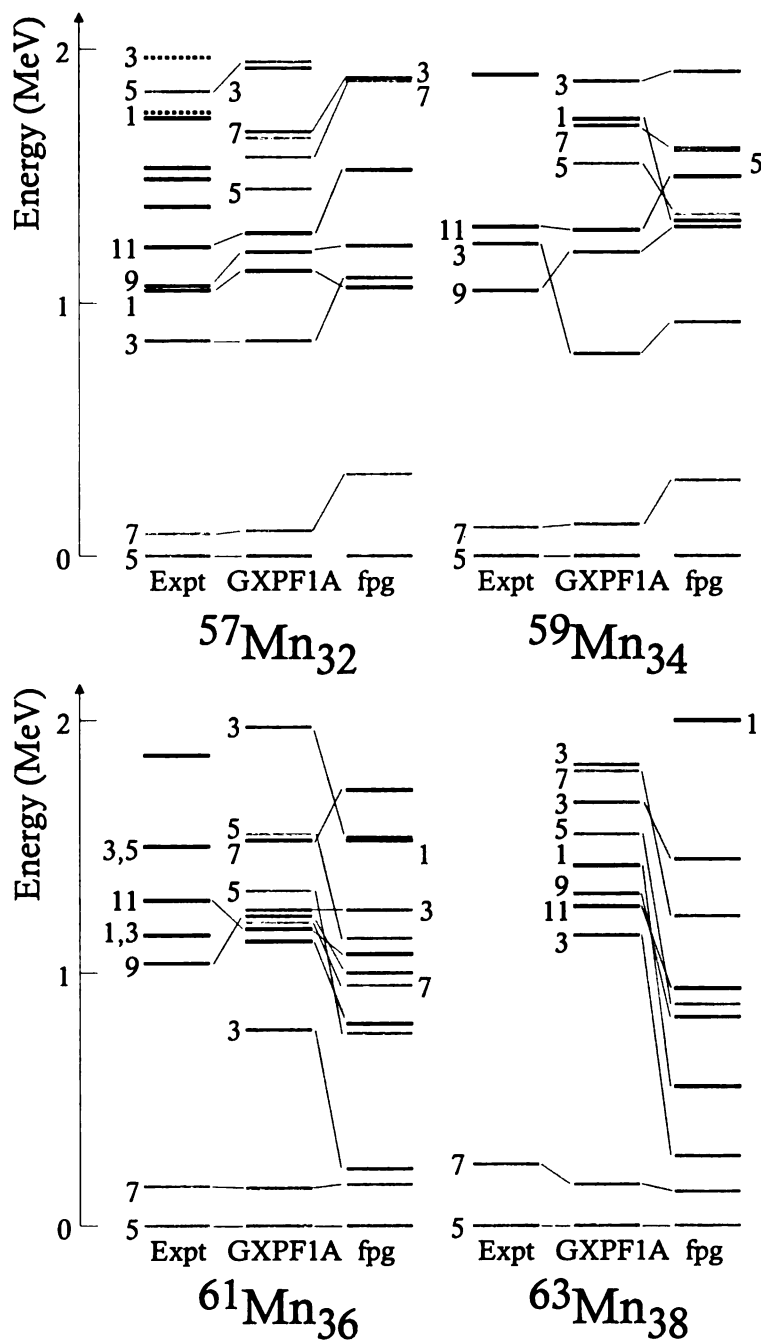


Figure 5.7: Systematic variation of the low-energy levels of the neutron-rich, odd- $A$   $^{25}\text{Mn}$  isotopes, along with the results of shell model calculations with the GXPF1A and  $fpg$  interactions. Only levels below 2 MeV are presented. In addition, the shell model results shown are limited to the three lowest energy levels calculated for  $J^\pi = 1/2^- - 7/2^-$ , and the yrast levels for  $J^\pi = 9/2^-$  and  $11/2^-$ . Levels with assumed negative parity are shown as solid lines, and those with positive parity are presented as dotted lines. Spins are given as  $2I$  and, in nearly all cases, are tentative as discussed in the text.

cases where the calculations were completed with both 2 and 6 neutron excitations allowed from the  $fp$  shell, similar results were obtained.

The low density of levels below 1 MeV is persistent in  $^{57,59,61}\text{Mn}$ , and agrees well with the shell model results with the GXPF1A effective interaction. The only excited state in this energy range is the  $7/2^-$  level, which is expected to carry a reduced  $1f_{7/2}$  single-particle component with the addition of neutrons [118]. The low-spin level density below 1 MeV is shown to increase at  $^{61}\text{Mn}$  in the shell model results with the  $fp_g$  interaction. Here, the influence of the  $1g_{9/2}$  neutron orbital becomes apparent at  $N = 36$ . However, this is not borne out in the observed level structure. The regular behavior of the low-energy levels of the odd- $A$   $^{25}\text{Mn}$  isotopes through  $N = 36$  follows the similar trend observed in the even-even  $^{26}\text{Fe}$  isotopes, where the possible onset of collectivity at low energy is not evident until  $N = 38$  is reached.

### 5.3.2 Even- $A$ Mn isotopes

Although no new data for the even- $A$  Mn isotopes are reported in this work, the systematic variation of these states provides additional support for the delayed onset of collectivity in the Mn isotopes. Only a few excited states in the odd-odd  $^{60,62}\text{Mn}$  were established based on  $\beta$ -decay studies [58, 121]. The low-energy levels in these isotopes are shown in Figure 5.8. Two  $\beta$ -decaying states are known in both isotopes, but the location and ordering of the proposed  $1^+$  and  $4^+$  states has not been established in  $^{62}\text{Mn}_{37}$  [58]. Good agreement was noted between shell model results with the GXPF1 interaction and both the low-energy structure and  $\beta$ -decay properties of  $^{60}\text{Mn}_{35}$  [121]. The low-energy structure of  $^{62}\text{Mn}$  built on the  $1^+$   $\beta$ -decaying state shows marked similarity to that in  $^{60}\text{Mn}$ , albeit the excited  $2^+$  and  $1^+$  states are both shifted  $\sim 100$  keV lower in energy with the addition of two neutrons. Although Valiente-Dobón *et al.* reported a number of in-beam  $\gamma$  rays associated with the depopulation of yrast levels in both  $^{60}\text{Mn}$  and  $^{62}\text{Mn}$ , no level structures were proposed due to the lack of coincidence data [57]. Again, the systematic variation of the (few)

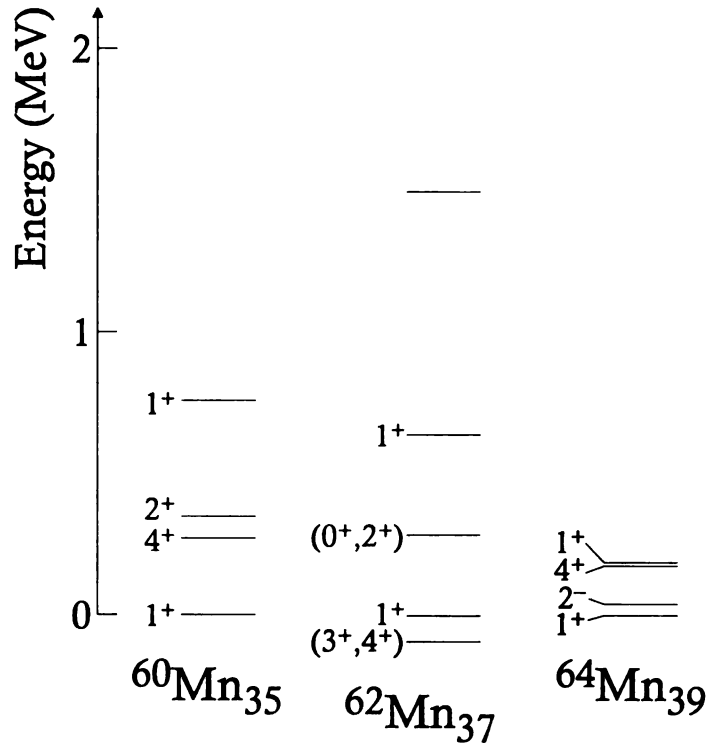


Figure 5.8: Experimentally known low-energy level structures for the even- $A$  Mn isotopes from  $N=35$  through  $N=39$ . The location and ordering of the proposed  $1^+$  and  $(3^+, 4^+)$  states in  $^{52}\text{Mn}$  is unknown – for the purposes of the figure, the  $1^+$  states were aligned for all isotopes.

excited levels established in the odd-odd Mn isotopes through  $N = 37$  does not suggest a sudden onset of collectivity, in line with the trend established for the yrast states of even-even  $_{26}\text{Fe}$  isotopes.

Beyond  $N=37$ , low-energy levels in  $^{64}\text{Mn}$  are known from the  $\beta$  decay of  $^{64}\text{Cr}$  [122]. A low-lying  $2^-$  state has been identified at 40 keV in  $^{64}\text{Mn}$ , as shown in Fig. 5.8. Identification of such an unnatural parity state is an indication for the approach of the  $\nu 1g_{9/2}$  level close to the Fermi surface in this isotope. This structural signature provides the first indication of the approaching deformation-inducing  $1g_{9/2}$  orbital in the Mn chain. Additional spectroscopic measurements in this isotopic chain are required to more fully characterize the onset of deformation in the Mn isotopes.

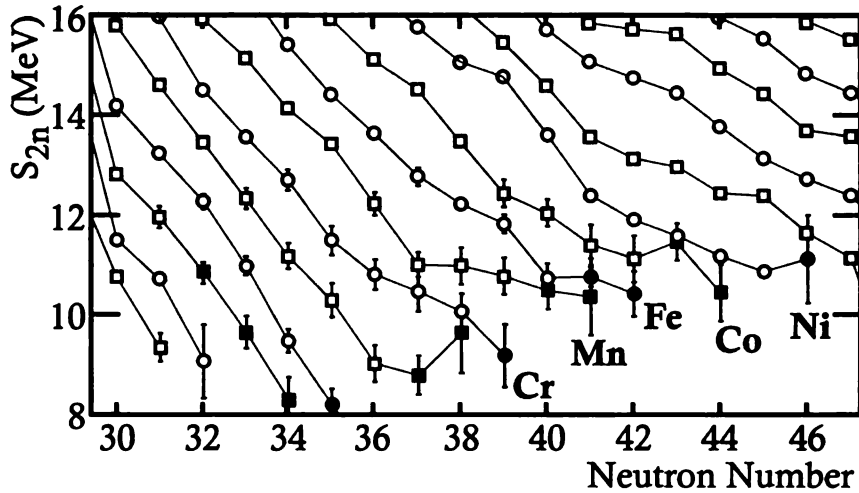


Figure 5.9: Two neutron separation energies in the  $N=40$  region. Hollow symbols indicate masses taken from the 2003 Atomic Mass Evaluation [80], while filled symbols are masses measured recently using the time-of-flight method at NSCL [123]. Figure was adapted from Ref. [123].

### 5.3.3 Deformation in comparison to neighboring ${}_{24}\text{Cr}$ and ${}_{26}\text{Fe}$ isotopic chains

The low density of states in  ${}^{61}\text{Mn}$  has been shown to agree with the results of shell model calculations in the  $fp$  model space without the need to invoke neutron excitations into the  $1g_{9/2}$  orbital. There is no compelling evidence for the onset of collectivity in the  ${}_{25}\text{Mn}$  isotopes through  $N=37$ . However, at  $N=39$ , there is evidence of the influence of the  $1g_{9/2}$  neutron orbital, in the form of a  $2^-$  unnatural parity state at low energy in  ${}^{64}\text{Mn}$ . These observations are consistent with the behavior of the neutron-rich  $Z+1$   ${}_{26}\text{Fe}$  isotopes, where no indication of collectivity was observed until  $N=38$ . While spectroscopic information is not available beyond  $N=39$  in the Mn isotopes, nuclear mass systematics in the region surrounding  $N=40$  have recently been extended in the Cr, Mn and Fe isotopes [123]. The systematics of the mass observables, such as the two-neutron separation energies ( $S_{2n}$ ), are sensitive to deformation effects, as discussed in Chapter 1. Two-neutron separation energies are shown in Figure 5.9 for the isotopes surrounding  $N=40$  and  $Z=25$ .

As discussed by Estradé [123], a reduction in the slope of the  $S_{2n}$  values as a function of neutron number has been observed to coincide with the onset of deformation in the Fe isotopes. The reduced slope corresponds to extra neutron binding as deformation sets in. The reduction in the slope begins in the  ${}_{25}\text{Mn}$  isotopes at  $N=37$ , in agreement with the spectroscopic observations to date. A change in the slope of the two neutron separation energies for the Fe isotopes is observed at  $N=40$ , coinciding with the onset of deformation in the  $Z=26$  isotopic chain. The Cr isotopes present a less clear case. A subtle change in the slope begins at  $N=36$ , in agreement with the earlier onset of deformation in the even-even  ${}_{24}\text{Cr}$  isotopes evident in the systematic variation of the  $2_1^+$  states. Thus, mass systematics appear to agree with spectroscopic observations for the onset of deformation in the Cr, Mn and Fe isotopes. Collectivity, resulting from the lowering of the  $\nu 1g_{9/2}$  orbital closer to the Fermi surface, occurs earliest in the  ${}_{24}\text{Cr}$  isotopes, while the onset of deformation in the  ${}_{25}\text{Mn}$  isotopic chain occurs later, more like the situation in the  ${}_{26}\text{Fe}$  isotopes. With the removal of additional  $1f_{7/2}$  protons below  ${}_{24}\text{Cr}$ , in the  ${}_{22}\text{Ti}$  and  ${}_{20}\text{Ca}$  isotopes, the  $\nu 1g_{9/2}$  orbital is expected to be lowered further, and collectivity may develop even sooner. The lowering of the  $\nu 1g_{9/2}$  may also lead to a new “island of inversion” surrounding  ${}_{22}^{62}\text{Ti}_{40}$ , as first suggested by Brown [124], and discussed by Tarasov *et al.* in light of enhanced production cross sections in the region near  ${}^{62}\text{Ti}$  [125].

# Chapter 6

## Conclusions and Outlook

### 6.1 Conclusions

The low-energy level structures of nuclei within and near the  $fp$  shell have been investigated using  $\beta$ -delayed and prompt  $\gamma$ -ray spectroscopy, to find evidence for changing nuclear shell structure.

The low-energy levels of neutron-rich  ${}^{53,54,56}_{21}\text{Sc}$  were investigated through the  $\beta$  decay of the parent nuclides  ${}^{53,54}\text{Ca}$ , as well as through prompt isomeric  $\gamma$ -ray emission from  ${}^{54,56}\text{Sc}$ . These nuclei reside in the vicinity of the known  $N=32$  subshell closure, a result of the large gap between the  $\nu 2p_{3/2}$  orbital and the higher-lying  $\nu 2p_{1/2}$  and  $\nu 1f_{5/2}$  orbitals. The low-energy structures of the Sc isotopes were analyzed in the extreme single-particle model framework, as a coupling of the valence  $1f_{7/2}$  proton to states in the corresponding  ${}_{20}\text{Ca}$  core. Such a description worked well for  ${}^{53}\text{Sc}$ , where the valence proton weakly couples to states in doubly-magic  ${}^{52}_{20}\text{Ca}_{32}$ . The success of this description provided further confirmation for the validity of the  $N=32$  subshell closure in the Ca isotopes. Interpretation of the low-energy levels in the even- $A$  Sc isotopes as resulting from the coupling of a  $1f_{7/2}$  proton and valence neutrons to a Ca core provided information on the separation between the  $\nu 2p_{1/2}$  and  $\nu 1f_{5/2}$  orbitals. The energy separation between these orbitals is proposed by some shell-

model interactions to be sufficient to produce a new subshell closure at  $N=34$  in the Ca isotopes. While more work is required to complete the relevant multiplets of states in  $^{54,56}\text{Sc}$ , early indications suggest that the low-energy levels in the Sc isotopes are compressed relative to shell-model predictions and that a significant  $N=34$  subshell gap does not exist between the  $p_{1/2}$  and  $f_{5/2}$  neutron levels in the  $^{21}\text{Sc}$  isotopes. More information is required for the  $^{20}\text{Ca}$  isotopes, specifically at  $^{54}\text{Ca}$  to determine conclusively whether the removal of the final  $f_{7/2}$  proton is sufficient to create a substantial subshell closure at  $N=34$ .

The low-energy isomeric structure in  $^{50}_{19}\text{K}$ , with protons in the  $sd$  shell and neutron occupying the  $fp$  shell, was investigated using prompt  $\gamma$ -ray spectroscopy. The observed isomeric structure of  $^{50}\text{K}$  was suggestive of a re-ordering of the proton single particle states below the  $Z=20$  shell closure. The isomeric structure was best explained with a  $\nu 2p_{3/2} \otimes \pi 2s_{1/2}$  configuration for the ground state in  $^{50}\text{K}$ , which gives rise to a  $1^-$  ground state spin and parity. This is inconsistent with previous assignment of  $0^-$  for the ground state of  $^{50}\text{K}$ , based on  $\beta$ -decay measurements [110]. The predictions of the most recent  $sd$ - $fp$  cross-shell effective interactions, the SDPF-U interaction from Nowacki and Poves [101], and the newest interaction from Utsuno *et al.* [102], are also inconsistent with the suggested  $1^-$  ground state in  $^{50}\text{K}$ . Theoretical work is required to reconcile the predictions of these cross-shell interactions with the recent experimental results in the K isotopes. Additional spectroscopic information is also required for the K isotopes beyond  $N=28$  to provide the constraints necessary to more fully understand the monopole interactions involved at work, and the evolution of the proton single-particle energies below  $Z=20$  in the region.

The  $\beta$  decay of  $^{61}\text{Cr}$  was studied to extract details on non-yrast excited states in the daughter nucleus  $^{61}_{25}\text{Mn}_{36}$ . This nucleus is situated near  $N=40$ , in a region where evidence of collectivity has been observed in the neutron-rich  $^{24}\text{Cr}$  and  $^{26}\text{Fe}$  isotopes, with an apparent onset at  $N=36$  and  $N=38$  respectively. The structure of the neutron-rich Mn isotopes is important to determine the onset of deformation in

the  $Z=25$  isotopic chain, and improve the understanding of the role of the  $\nu 1g_{9/2}$  orbital in enhancing deformation. The dependence of single-particle energy shifts on the proton number  $Z$  in this region can also be probed through study of the low-energy levels in the Mn isotopes. The low-energy level scheme for  $^{61}\text{Mn}$ , deduced following  $\beta$  decay of  $^{61}\text{Cr}$ , features five new excited states above a 1-MeV excitation energy. However, the low-energy structure below 1 MeV did not resemble that from the shell model results that consider the  $1g_{9/2}$  orbital. The low density of states below 1 MeV is a consistent feature observed in the odd- $A$  Mn isotopes with  $A = 57, 59, 61$ , and follows the results of shell model calculations restricted to the  $fp$  model space. There is also little variation in the yrast structures of these odd- $A$  Mn isotopes up to  $J = 15/2$ , as reported by Valiente-Dobón *et al.* [57]. No compelling evidence was found for the onset of collectivity in the low-energy structures of the Mn isotopes through  $N = 37$ . The only evidence for the onset of collectivity in the Mn isotopes comes at  $N=39$ , where a unnatural parity states suggests the approach of the  $\nu 1g_{9/2}$  orbital close to the Fermi surface. These observations are consistent with the behavior of the even-even,  $Z + 1$   $^{26}\text{Fe}$  isotopes, but not with that of the even-even  $Z - 1$   $^{24}\text{Cr}$  isotopes, where possible onset of collectivity at low energy has been suggested from the  $E(2_1^+)$  energy at  $N = 36$ . Little data are available for both yrast and non-yrast levels in the  $^{25}\text{Mn}$  isotopes beyond  $N = 36$ . Such data will be critical to evaluate the role of the neutron  $1g_{9/2}$  orbital in defining the structural properties of the neutron-rich Mn isotopes.

## 6.2 Outlook

### 6.2.1 Open questions in the $fp$ shell

While the results presented here have provided information on the nuclear structure in and around the  $fp$  shell, a number of questions remain. Further experiments are necessary in these regions may serve to provide the information critical to clarify the

situation.

The present work has provided information on the low-energy level structures of the neutron rich  $^{53,54,56}\text{Sc}$  isotopes in the region surrounding  $N=34$ . However, the actual parentage of the low-energy states in  $^{54}\text{Sc}$  and  $^{56}\text{Sc}$  needs to be confirmed. Firm assignments for the spin and parity of these low-energy states, and determination of the purity of the single-particle configurations would serve to more fully characterize these nuclei. A measurement of the angular distribution, or internal conversion of the isomeric 110-keV transition in  $^{54}\text{Sc}$  would provide the required information to confirm the multipolarity of the transition, and establish the spin and parity of the 110-keV state. Neutron knock-out reactions into both  $^{54}\text{Sc}$  and  $^{56}\text{Sc}$  would access the neutron spectroscopic factors for the low-energy states in these nuclei. Spectroscopic factors will be critical in providing the final confirmation for the parentage of the low-energy states in  $^{54,56}\text{Sc}$ , and providing the most robust check for shell-model calculations. However, due to the close energy spacing in the low-lying levels of  $^{54,56}\text{Sc}$ , these experiments may benefit from the improved resolution expected using next-generation  $\gamma$ -ray detector arrays, with sub-segment position resolution. The direct study of the low energy states of neutron-rich  $^{54,56}\text{Ca}$  isotopes is also critical, but will likely have to wait for next generation accelerator facilities due to the low production cross-sections for these isotopes.

Evidence for the inversion of the  $2d_{3/2}$  and  $1s_{1/2}$  proton orbitals in the potassium isotopes beyond  $N=28$  is based on indirect measurements. The present data in  $^{50}\text{K}$  is suggestive of a  $1^-$  ground state, arising from a configuration involving a  $2s_{1/2}$  proton hole. The tentative assignment suggests that the  $\pi 2s_{1/2}$  orbital remains above the  $\pi d_{3/2}$  past  $N=28$ . However, absolute confirmation of the ground state spin could be obtained through a measurement of the ground state hyperfine splitting in  $^{49,50}\text{K}$ . Measurement of the ground-state  $g$ -factors in the K isotopes beyond  $N=28$  would also provide valuable information. Such a measurement using  $\beta$ -NMR and laser spectroscopy has been proposed at ISOLDE, and will provide information regarding

the ground-state configurations in the K isotopes from  $N=29$  to  $N=32$  [126]. Proton transfer reactions would provide the spectroscopic factors necessary to disentangle the proton single-particle contributions to excited states in  $^{49,50}\text{K}$ . Knowledge of the parentage of these states would further clarify the relative spacing of the  $\pi 1d_{3/2}$  and  $\pi 2s_{1/2}$  orbitals, and the appropriate strength of the cross-shell proton-neutron tensor interactions.

There is evidence of a new region of deformation developing in the  $^{24}\text{Cr}$ ,  $^{25}\text{Mn}$  and  $^{26}\text{Fe}$  isotopes near  $N=40$ , as the neutron  $1g_{9/2}$  orbital drops in energy with increased occupation of the proton  $1g_{7/2}$  orbital. The present results extended the knowledge in the Mn isotopic chain at  $N=36$ . Within this region, further  $\beta$ -decay studies of the Cr isotopes beyond  $N=36$  into the Mn daughters would provide an important extension of the knowledge in this isotopic chain. It appears that collectivity in the Mn isotopes does not occur until  $N=38$ , as was the case in the Fe isotopic chain. Determination of the level densities in the odd- $A$   $^{63,65}\text{Mn}$ , which is achievable through  $\beta$  decay, could provide the experimental signature for developing collectivity in the Mn isotopes. Future facilities will also prove critical in this region, in pushing spectroscopy of isotopes in the Cr, Mn and Fe chains to larger neutron excess.

## 6.2.2 The NSCL $\beta$ Counting System with Digital Data Acquisition

The NSCL  $\beta$  Counting System provides a means for determining critical  $\beta$ -decay properties needed to test nuclear structure models far from the valley of stability. The work presented in this dissertation is an example of the value both isomeric and  $\beta$ -delayed  $\gamma$ -ray spectroscopy with the combination of the BCS + SeGA can play in characterizing the evolution of nuclear shell structure as a function of isospin. However, planned improvements to the BCS will serve to expand its capabilities.

A digital data acquisition system (DDAS) has been developed at NSCL based

on the Pixie-16 Digital Gamma Finder (DGF) modules by XIA LLC [127]. When used with segmented germanium detectors such as SeGA, one of the greatest assets of digital data acquisition is the opportunity for pulse-shape analysis of digitized signals. Pulse shape analysis permits the localization of  $\gamma$ -ray interaction points to sub-segment resolution, which in turn permits more accurate Doppler corrections, critical for in-beam  $\gamma$  spectroscopy.

DDAS is being adapted for use with the BCS. Preliminary testing of the BCS dual-gain preamplifiers with DDAS has shown that the system is compatible with the fast ( $\sim 300$  ns rise time) output signals of these preamplifiers. With correct settings of the DDAS energy filter parameters, the resolution achieved with DDAS was comparable to, or slightly better than that achieved with the standard BCS analog electronics. Figure 6.1 illustrates the  $^{228}\text{Th}$  spectra obtained for a single strip in a 1 mm SSSD using both DDAS and the standard BCS analog electronics. The main advantage in using digital data acquisition for the BCS is the improved detection efficiency. The application of DDAS with the BCS silicon detectors is expected to reduce noise levels. This noise reduction will increase the detection efficiency of the BCS, since more of the low-energy  $\beta$  particles will produce true triggers. A gain in efficiency will also be realized due to the zero dead-time option of DDAS – data storage buffers permit readout of the modules with no dead-time losses. In addition to the gains in efficiency, the ability to capture and record waveforms will expand the possibilities for the use of the BCS in charged-particle decay studies, where short-lived ( $\sim \mu\text{s}$ ) charged particle decays may be characterized via detailed waveform analysis [128].

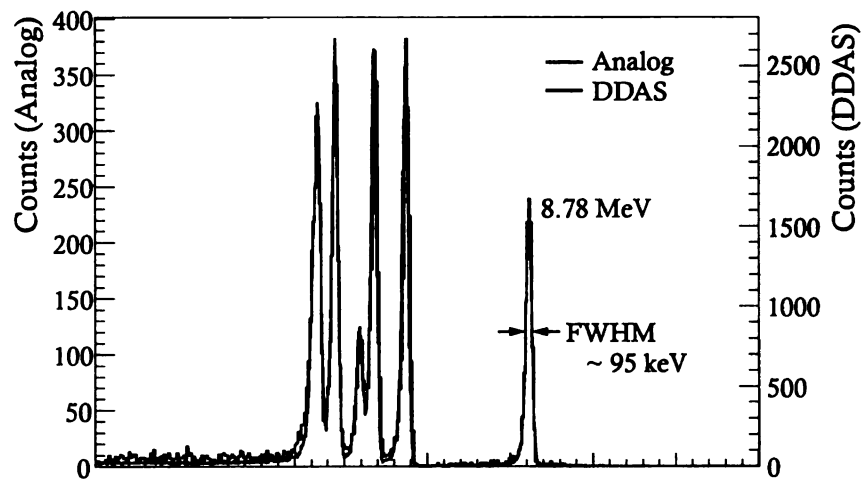


Figure 6.1:  $^{228}\text{Th}$   $\alpha$  spectrum collected in a single strip of a 1 mm thick SSSD using DDAS (red line) and the standard analog BCS electronics. The resolution achieved in DDAS is comparable to that obtained with the analog electronics.

# Bibliography

- [1] D.R. Lide. *CRC Handbook of Chemistry and Physics*. CRC Press, Inc., Florida, 1996.
- [2] R.B. Firestone. *Table of Isotopes*, edited by Virginia S. Shirley (Wiley, New York, 1996).
- [3] K.S. Krane. *Introductory Nuclear Physics*. John Wiley & Sons, Inc., New York, 1988.
- [4] W. Loveland, D.J. Morrissey, and G.T. Seaborg. *Modern Nuclear Chemistry*. John Wiley & Sons, Inc., New Jersey, 2006.
- [5] O. Haxel, J.H.D. Jensen, and H.E. Suess. *Phys. Rev.*, **75**:1766, 1949.
- [6] M.G. Mayer. *Phys. Rev.*, **75**:1969, 1949.
- [7] A. Navin, D.W. Anthony, T. Aumann, T. Baumann, D. Bazin, Y. Blumenfeld, B.A. Brown, T. Glasmacher, P.G. Hansen, R.W. Ibbotson, P.A. Lofy, V. Madalena, K. Miller, T. Nakamura, B.V. Pritychenko, B.M. Sherrill, E. Spears, M. Steiner, J.A. Tostevin, J. Yurkon, and A. Wagner. *Phys. Rev. Lett.*, **85**:266, 2000.
- [8] A. Gade, P. Adrich, D. Bazin, M.D. Bowen, B.A. Brown, C.M. Campbell, J.M. Cook, S. Ettenauer, T. Glasmacher, K.W. Kemper, S. McDaniel, A. Obertelli, T. Otsuka, A. Ratkiewicz, K. Siwek, J.R. Terry, J.A. Tostevin, Y. Utsuno, and D. Weisshaar. *Phys. Rev. Lett.*, **99**:072502, 2007.
- [9] E.K. Warburton, J.A. Becker, and B.A. Brown. *Phys. Rev. C*, **41**:1147, 1990.
- [10] L. Gaudefroy, O. Sorlin, D. Beaumel, Y. Blumenfeld, Z. Dombrádi, S. Fortier, S. Franchoo, M. Gélín, J. Gibelin, S. Grévy, F. Hammache, F. Ibrahim, K.W. Kemper, K.-L. Kratz, S.M. Lukyanov, C. Monrozeau, L. Nalpas, F. Nowacki, A.N. Ostrowski, T. Otsuka, Yu.-E. Penionzhkevich, J. Piekarewicz, E.C. Pollacco, P. Roussel-Chomaz, E. Rich, J.A. Scarpaci, M.G. St. Laurent, D. Sohler, M. Stanoiu, T. Suzuki, E. Tryggestad, and D. Verney. *Phys. Rev. Lett.*, **97**:092501, 2006.
- [11] A. Huck, G. Klotz, A. Knipper, C. Miehé, C. Richard-Serre, G. Walter, A. Poves, H.L. Ravn, and G. Marguier. *Phys. Rev. C*, **31**:2226, 1985.

- [12] A. Gade, R.V.F. Janssens, D. Bazin, R. Broda, B.A. Brown, C.M. Campbell, M.P. Carpenter, J.M. Cook, A.N. Deacon, D.-C. Dinca, B. Fornal, S.J. Freeman, T. Glasmacher, P.G. Hansen, B.P. Kay, P.F. Mantica, W.F. Mueller, J.R. Terry, J.A. Tostevin, and S. Zhu. *Phys. Rev. C*, **74**:021302(R), 2006.
- [13] R.V.F. Janssens, B. Fornal, P.F. Mantica, B.A. Brown, R. Broda, P. Bhattacharyya, M.P. Carpenter, M. Cinausero, P.J. Daly, A.D. Davies, T. Glasmacher, Z.W. Grabowski, D.E. Groh, M. Honma, F.G. Kondev, W. Królas, T. Lauritsen, S.N. Liddick, S. Lunardi, N. Marginean, T. Mizusaki, D.J. Morrissey, A.C. Morton, W.F. Mueller, T. Otsuka, T. Pawlat, D. Seweryniak, H. Schatz, A. Stolz, S.L. Tabor, C.A. Ur, G. Viesti, I. Wiedenhöver, and J. Wrzesiński. *Phys. Lett. B*, **546**:55, 2002.
- [14] J.I. Prisciandaro, P.F. Mantica, B.A. Brown, D.W. Anthony, M.W. Cooper, A. Garcia, D.E. Groh, A. Komives, W. Kumarasiri, P.A. Lofy, A.M. Oros-Peusquens, S.L. Tabor, and M. Wiedeking. *Phys. Lett. B*, **510**:17, 2001.
- [15] P. Federman and S. Pittel. *Phys. Lett.*, **69B**:385, 1977.
- [16] R.F. Casten. *AIP Conf. Proc.*, **238**:67, 1991.
- [17] T. Otsuka, R. Fugimoto, Y. Utsuno, B.A. Brown, M. Honma, and T. Mizusaki. *Phys. Rev. Lett.*, **87**:082502, 2001.
- [18] T. Otsuka, T. Suzuki, R. Fujimoto, H. Grawe, and Y. Akaishi. *Phys. Rev. Lett.*, **95**:232502, 2005.
- [19] R.F. Casten. *Nuclear Structure from a Simple Perspective*. Oxford University Press, Inc., New York, 1990.
- [20] C.A. Bertulani and P. Danielewicz. *Introduction to Nuclear Reactions*. Institute of Physics Publishing, London, 2004.
- [21] V. Paar. *Nucl. Phys.*, **A331**:16, 1979.
- [22] V.L. Alexeev, B.A. Emelianov, A.I. Egorov, L.P. Kabina, D.M. Kaminker, Yu.L. Khazov, I.A. Kondurov, E.K. Leushkin, Yu.E. Loginov, V.V. Martynov, V.L. Rumiantsev, S.L. Sakharov, P.A. Sushkov, H.G. Börner, W.F. Davidson, J.A. Pinston, and K. Schreckenbach. *Nucl. Phys.*, **A297**:373, 1978.
- [23] T.W. Burrows. *Nucl. Data Sheets*, **107**:1747, 2006.
- [24] R.F. Casten, J. Zhang, N.V. Zamfir, M.A. Caprio, H. Zhang, and F. Du. *Phys. Lett. B*, **481**:1, 2000.
- [25] S. Raman, C.H. Malarkey, W.T. Milner, C.W. Nestor Jr., and P.H. Stelson. *Atom. Data and Nucl. Data Tables*, **36**:1, 1987.
- [26] L. Grodzins. *Phys. Lett.*, **2**:88, 1962.

- [27] F.S. Stephens, R.M. Diamond, J.R. Leigh, T. Kammuri, and K. Nakai. *Phys. Rev. Lett.*, **29**:438, 1972.
- [28] D.-C. Dinca, R.V.F. Janssens, A. Gade, D. Bazin, R. Broda, B.A. Brown, C.M. Campbell, M.P. Carpenter, P. Chowdhury, J.M. Cook, A.N. Deacon, B. Fornal, S.J. Freeman, T. Glasmacher, M. Honma, F.G. Kondev, J.-L. Lecouey, S.N. Liddick, P.F. Mantica, W.F. Mueller, H. Olliver, T. Otsuka, J.R. Terry, B.A. Tomlin, and K. Yoneda. *Phys. Rev. C*, **71**:041302(R), 2005.
- [29] N.K. Glendenning. *Direct Nuclear Reactions*. World Scientific Publishing Co. Pte. Ltd., Singapore, 2004.
- [30] I.J. Thompson and F.M. Nunes. *Nuclear Reactions for Astrophysics*. Cambridge University Press, New York, 2009.
- [31] S.N. Liddick, P.F. Mantica, R. Broda, B.A. Brown, M.P. Carpenter, A.D. Davies, B. Fornal, T. Glasmacher, D.E. Groh, M. Honma, M. Horoi, R.V.F. Janssens, T. Mizusaki, D.J. Morrissey, A.C. Morton, W.F. Mueller, T. Otsuka, J. Pavan, H. Schatz, A. Stolz, S.L. Tabor, B.E. Tomlin, and M. Wiedeking. *Phys. Rev. C*, **70**:064303, 2004.
- [32] A. Bürger, T.R. Saito, H. Grawe, H. Hübel, P. Reiter, J. Gerl, M. Górska, H.J. Wollersheim, A. Al-Khatib, A. Banu, T. Beck, F. Becker, P. Bednarczyk, G. Benzoni, A. Bracco, S. Brambilla, P. Bringel, F. Camera, E. Clément, P. Doornenbal, H. Geissel, A. Görge, J. Grębosz, G. Hammond, M. Hellström, M. Honma, M. Kavatsyuk, O. Kavatsyuk, M. Kmiecik, I. Kojouharov, W. Korten, N. Kurz, R. Lozeva, A. Maj, S. Mandal, B. Million, S. Muralithar, A. Neusser, F. Nowacki, T. Otsuka, Zs. Podolyák, N. Saito, A.K. Singh, H. Weick, C. Wheldon, O. Wieland, M. Winkler, and the RISING Collaboration. *Phys. Lett. B*, **622**:29, 2005.
- [33] M. Honma, T. Otsuka, B.A. Brown and T. Mizusaki. *Phys. Rev. C*, **65**:061301(R), 2002.
- [34] M. Honma, T. Otsuka, B.A. Brown, and T. Mizusaki. *Eur. Phys. J. A*, **25**:499, 2005.
- [35] A. Poves, J. Sánchez-Solano, E. Caurier, and F. Nowacki. *Nucl. Phys. A*, **694**:157, 2001.
- [36] S.N. Liddick, P.F. Mantica, R.V.F. Janssens, R. Broda, B.A. Brown, M.P. Carpenter, B. Fornal, M. Honma, T. Mizusaki, A.C. Morton, W.F. Mueller, T. Otsuka, J. Pavan, A. Stolz, S.L. Tabor, B.E. Tomlin, and M. Wiedeking. *Phys. Rev. Lett.*, **92**:072502, 2004.
- [37] S.M. Fischer, C.J. Lister, D.P. Balamuth, R. Bauer, J.A. Becker, L.A. Bernstein, M.P. Carpenter, J. Durell, N. Fotiadis, S.J. Freeman, P.E. Garrett, P.A. Hausladen, R.V.F. Janssens, D. Jenkins, M. Leddy, J. Ressler, J. Schwartz, D. Svelnys, D.G. Sarantites, D. Seweryniak, B.J. Varley, and R. Wyss. *Phys. Rev. Lett.*, **87**:132501, 2001.

- [38] C.J. Lister, M. Campbell, A.A. Chishti, W. Gelletly, L. Goettig, R. Moscrop, B.J. Varley, A.N. James, T. Morrison, H.G. Price, J. Simpson, K. Connel, and O. Skeppstedt. *Phys. Rev. Lett.*, **59**:1270, 1987.
- [39] C.J. Lister, P.J. Ennis, A.A. Chishti, B.J. Varley, W. Gelletly, H.G. Price, and A.N. James. *Phys. Rev. C*, **42**:R1191, 1990.
- [40] B. Blank and P.H. Regan. *Nucl. Phys. News*, **10**:20, 2000.
- [41] Z. Janas, C. Chandler, B. Blank, P.H. Regan, A.M. Bruce, W.N. Catford, N. Curtis, S. Czajkowski, Ph. Dessagne, A. Fleury, W. Gelletly, J. Giovino, R. Grzywacz, M. Lewitowicz, C. Longour, C. Marchand, Ch. Miehé, N.A. Orr, R.D. Page, C.J. Pearson, M.S. Pravikoff, A.T. Reed, M.G. Saint-Laurent, J.A. Sheikh, S.M. Vincent, R. Wadsworth, D.D. Warner, and J.S. Winfield. *Phys. Rev. Lett.*, **82**:295, 1999.
- [42] M. Hannawald, T. Kautzsch, A. Wöhr, W.B. Walters, K.-L. Kratz, V.N. Fedoseyev, V.I. Mishin, W. Böhmer, B. Pfeiffer, V. Sebastian, Y. Jading, U. Köster, J. Lettry, H.L. Ravn, and the ISOLDE Collaboration. *Phys. Rev. Lett.*, **82**:1391, 1999.
- [43] P. Adrich, A.M. Amthor, D. Bazin, M.D. Bowen, B.A. Brown, C.M. Campbell, J.M. Cook, A. Gade, D. Galaviz, T. Glasmacher, S. McDaniel, D. Miller, A. Obertelli, Y. Shimbara, K.P. Siwek, J.A. Tostevin, and D. Weisshaar. *Phys. Rev. C*, **77**:054306, 2008.
- [44] O. Sorlin, C. Donzaud, F. Nowacki, J.C. Angélique, F. Azaiez, C. Bourgeois, V. Chiste, Z. Dlouhy, S. Grévy, D. Guillemaud-Mueller, F. Ibrahim, K.-L. Kratz, M. Lewitowicz, S.M. Lukyanov, J. Mrasek, Yu.-E. Penionzhkevich, F. de Oliveira Santos, B. Pfeiffer, F. Pougheon, A. Poves, M.G. Saint-Laurent, and M. Stanoiu. *Eur. Phys. J. A*, **16**:55, 2003.
- [45] R. Broda, B. Fornal, W. Królas, T. Pawlat, D. Bazzacco, S. Lunardi, C. Rossi-Alvarez, R. Menegazzo, G. de Angelis, P. Bednarczyk, J. Rico, D. De Acuña, P.J. Daly, R.H. Mayer, M. Sferrazza, H. Grawe, K.H. Maier, and R. Schubart. *Phys. Rev. Lett*, **74**:868, 1995.
- [46] O. Sorlin, S. Leenhardt, C. Donzaud, J. Duprat, F. Azaiez, F. Nowacki, H. Grawe, Zs. Dombrádi, F. Amorini, A. Astier, D. Baiborodin, M. Belleguic, C. Borcea, C. Bourgeois, D.M. Cullen, Z. Dlouhy, E. Dragulescu, M. Górska, S. Grévy, D. Guillemaud-Mueller, G. Hagemann, B. Herskind, J. Kiener, R. Lemmon, M. Lewitowicz, S.M. Lukyanov, P. Mayet, F. de Oliveira Santos, D. Pantalica, Yu.-E. Penionzhkevich, F. Pougheon, A. Poves, N. Redon, M.G. Saint-Laurent, J.A. Scarpaci, G. Sletten, M. Stanoiu, O. Tarasov, and Ch. Theisen. *Phys. Rev. Lett*, **88**:092501, 2002.
- [47] N. Bree, I. Stefanescu, P.A. Butler, J. Cederkäll, T. Davinson, P. Delahaye, J. Eberth, D. Fedorov, V.N. Fedosseev, L.M. Fraile, S. Franchoo, G. Georgiev, K. Gladnishki, M. Huyse, O. Ivanov, J. Iwanichi, J. Jolie, U. Köster, Th. Kröll,

- R. Krücken, B.A. Marsh, O. Niedermaier, P. Reiter, H. Scheit, D. Schwalm, T. Sieber, J. Van de Walle, P. Van Duppen, N. Warr, D. Weisshaar, F. Wenander and S. Zemlyanoy. *Phys. Rev. C*, **78**:047301, 2008.
- [48] S. Leenhardt, O. Sorlin, M.G. Porquet, F. Azaiez, J.C. Angélique, M. Belleguic, C. Borcea, C. Bourgeois, J.M. Daugas, C. Donzaud, I. Deloncle, J. Duprat, A. Gillibert, S. Grévy, D. Guillemaud-Mueller, J. Kiener, M. Lewitowicz, S.M. Lukyanov, F. Marie, N.A. Orr, Yu.-E. Penionzhkevich, F. de Oliveira Santos, F. Pougheon, M.G. Saint-Laurent, W. Shuying, Yu. Sobolev, and J.S. Winfield. *Eur. Phys. J. A*, **14**:1, 2002.
- [49] N. Aoi, H. Suzuki, E. Takeshita, S. Takeuchi, S. Ota, H. Baba, S. Bishop, T. Fukui, Y. Hashimoto, H.J. Ong, E. Ideguchi, K. Ieki, N. Imai, H. Iwaski, S. Kanno, Y. Kondo, T. Kubo, K. Kurita, K. Kusaka, T. Minemura, T. Motobayashi, T. Nakabayashi, T. Nakamura, T. Nakao, M. Niikura, T. Okumura, T.K. Ohnishi, H. Sakurai, S. Shimoura, R. Sugo, D. Suzuki, M.K. Suzuki, M. Tamaki, K. Tanaka, Y. Togano, and K. Yamada. *Nucl. Phys.*, **A805**:400c, 2008.
- [50] N. Aoi, E. Takeshita, H. Suzuki, S. Takeuchi, S. Ota, H. Baba, S. Bishop, T. Fukui, Y. Hashimoto, H.J. Ong, E. Ideguchi, K. Ieki, N. Imai, M. Ishihara, H. Iwasaki, S. Kanno, Y. Kondo, T. Kubo, K. Kurita, K. Kusaka, T. Minemura, T. Motobayashi, T. Nakabayashi, T. Nakamura, T. Nakao, M. Niikura, T. Okumura, T.K. Ohnishi, H. Sakurai, S. Shimoura, R. Sugo, D. Suzuki, M.K. Suzuki, M. Tamaki, K. Tanaka, Y. Togano, and K. Yamada. *Phys. Rev. Lett.*, **102**:012502, 2009.
- [51] K. Kaneko, Y. Sun, M. Hasegawa, and T. Mizusaki. *Phys. Rev. C*, **78**:064312, 2008.
- [52] L. Gaudefroy, A. Obertelli, S. Péru, N. Pillet, S. Hilaire, J.-P. Delaroche, M. Girod, and J. Libert. *Phys. Rev. C*, **80**:064313, 2009.
- [53] D.E. Appelbe, C.J. Barton, M.H. Muikku, J. Simpson, D.D. Warner, C.W. Beausang, M.A. Caprio, J.R. Cooper, J.R. Novak, N.V. Zamfir, R.A.E. Austin, J.A. Cameron, C. Malcolmson, J.C. Waddington, and F.R. Xu. *Phys. Rev. C*, **67**:034309, 2003.
- [54] A.N. Deacon, S.J. Freeman, R.V.F. Janssens, F.R. Xu, M.P. Carpenter, I.R. Calderin, P. Chowdhury, N.J. Hammond, T. Lauritsen, C.J. Lister, D. Seweryniak, J.F. Smith, S.L. Tabor, B.J. Varley, and S. Zhu. *Phys. Lett. B*, **622**:151, 2005.
- [55] S.J. Freeman, R.V.F. Janssens, B.A. Brown, M.P. Carpenter, S.M. Fischer, N.J. Hammond, M. Honma, T. Lauritsen, C.J. Lister, T.L. Khoo, G. Mukherjee, D. Seweryniak, J.F. Smith, B.J. Varley, M. Whitehead, and S. Zhu. *Phys. Rev. C*, **69**:064301, 2004.

- [56] D. Steppenback, A.N. Deacon, S.J. Freeman, R.V.F. Janssens, S. Zhu, M.P. Carpenter, P. Chowdhury, M. Honma, T. Lauritsen, C.J. Lister, D. Seweryniak, J.F. Smith, S.L. Tabor, and B.J. Varley. *Phys. Rev. C*, **81**:014305, 2010.
- [57] J.J. Valiente-Dobón, S.M. Lenzi, S.J. Freeman, S. Lunardi, J.F. Smith, A. Gottardo, F. Della Vedova, E. Farnea, A. Gadea, D.R. Napoli, M. Axiotis, S. Aydin, D. Bazzacco, P.G. Bizzeti, A.M. Bizzeti-Sona, G. Benzoni, D. Bucurescu, L. Corradi, A.N. Deacon, G. de Angelis, E. Fioretto, B. Guiot, M. Ionescu-Bujor, A. Iordachescu, S. Leoni, N. Mărginean, R. Mărginean, P. Mason, R. Menegazzo, D. Mengoni, B. Million, G. Montagnoli, R. Orlandi, F. Recchia, E. Sahin, F. Scarlassara, R.P. Singh, A.M. Stefanini, D. Steppenbeck, S. Szilner, C.A. Ur, B.J. Varley, and O. Wieland. *Phys. Rev. C*, **78**:024302, 2008.
- [58] L. Gaudefroy, O. Sorlin, C. Donzaud, J.C. Angélique, F. Azaiez, C. Bourgeois, V. Chiste, Z. Dlouhy, S. Grévy, D. Guillemaud-Mueller, F. Ibrahim, K.-L. Kratz, M. Lewitowicz, S.M. Lukyanov, I. Matea, J. Mrasek, F. Nowacki, F. de Oliveira-Santos, Yu.-E. Penionzhkevich, B. Pfeiffer, F. Pougheon, M.G. Saint-Laurent, and M. Stanoiu. *Eur. Phys. J. A*, **23**:41, 2005.
- [59] O. Sorlin, C. Donzaud, L. Axelsson, M. Belleguic, R. Béraud, C. Borcea, G. Canchel, E. Chabanat, J.M. Daugas, A. Emsallem, M. Girod, D. Guillemaud-Mueller, K.-L. Kratz, S. Leenhardt, M. Lewitowicz, C. Longour, M.J. Lopez, F. de Oliveira Santos, L. Petizon, B. Pfeiffer, F. Pougheon, M.G. Saint-Laurent, and J.E. Sauvestre. *Nucl. Phys.*, **A669**:351, 2000.
- [60] G. Friedlander, J.W. Kennedy, E.S. Macias, and J.M. Miller. *Nuclear and Radiochemistry, 3rd Edition*. John Wiley & Sons, Inc., New York, 1981.
- [61] T. Kibédi, T.W. Burrows, M.B. Trzhaskovskaya, P.M. Davidson, and C.W. Nestor Jr.. *Nucl. Instrum. Methods Phys. Res. A*, **589**:202, 2008.; Internal conversion calculator available online at: <http://physics.anu.edu/nuclear/bricc/>.
- [62] D.J. Morrissey, B.M. Sherrill, M. Steiner, A. Stolz, and I. Wiedenhöver. *Nucl. Instrum. Methods Phys. Res. B*, **204**:90, 2003.
- [63] A. Stolz, T. Baumann, T.N. Ginter, D.J. Morrissey, M. Portillo, B.M. Sherrill, M. Steiner, and J.W. Stetson. *Nucl. Instrum. Methods Phys. Res. B*, **241**:858, 2005.
- [64] J.I. Prisciandaro, A.C. Morton, and P.F. Mantica. *Nucl. Instrum. Methods Phys. Res. A*, **505**:140, 2003.
- [65] J.B. Stoker.  *$\beta$ -Decay Half-life of the  $rp$ -Process Waiting-Point Nuclide  $^{84}\text{Mo}$*  Ph.D. thesis, Michigan State University, 2009.
- [66] W.F. Mueller, J.A. Church, T. Glasmacher, D. Gutknecht, G. Hackman, P.G. Hansen, Z. Hu, K.L. Miller, and P. Quirin. *Nucl. Instrum. Methods Phys. Res. A*, **466**:492, 2001.

- [67] S.N. Liddick. *Beta-Decay Studies of Neutron-Rich Nuclides and the Possibility of an  $N=34$  Subshell Closure* Ph.D. thesis, Michigan State University, 2004.
- [68] R. Grzywacz, R. Béraud, C. Borcea, A. Emsallem, M. Glogowski, H. Grawe, D. Guillemaud-Mueller, M. Hjorth-Jensen, M. Houry, M. Lewitowicz, A.C. Mueller, A. Nowak, A. Plochocki, M. Pfützner, K. Rykaczewski, M.G. Saint-Laurent, J.E. Sauvestre, M. Schaefer, O. Sorlin, J. Szerypo, W. Trinder, S. Viteritti, and J. Winfield. *Phys. Rev. Lett.*, **81**:766, 1998.
- [69] S.N. Liddick, P.F. Mantica, R. Broda, B.A. Brown, M.P. Carpenter, A.D. Davies, B. Fornal, M. Horoi, R.V.F. Janssens, A.C. Morton, W.F. Mueller, J. Pavan, H. Schatz, A. Stolz, S.L. Tabor, B.E. Tomlin, and M. Wiedeking. *Phys. Rev. C*, **72**:054321, 2005.
- [70] P.F. Mantica, A.C. Morton, B.A. Brown, A.D. Davies, T. Glasmacher, D.E. Groh, S.N. Liddick, D.J. Morrissey, W.F. Mueller, H. Schatz, A. Stolz, S.L. Tabor, M. Honma, M. Horoi, and T. Otsuka. *Phys. Rev. C*, **67**:014311, 2003.
- [71] P.F. Mantica, B.A. Brown, A.D. Davies, T. Glasmacher, D.E. Groh, M. Horoi, S.N. Liddick, D.J. Morrissey, A.C. Morton, W.F. Mueller, H. Schatz, A. Stolz, and S.L. Tabor. *Phys. Rev. C*, **68**:044311, 2003.
- [72] P.R. Bevington, and D.K. Robinson *Data Reduction and Error Analysis for the Physical Sciences 2<sup>nd</sup> ed.*. McGraw-Hill, Boston, 1992.
- [73] G.F. Grinyer. *High Precision Measurements of  $^{26}\text{Na}$   $\beta^-$  Decay* Masters thesis, The University of Guelph, 2004.
- [74] R. Brun and F. Rademakers. *ROOT: A Data Analysis Framework*. Available online at: <http://root.cern.ch>.
- [75] S. McDaniel, A. Gade, R.V.F. Janssens, D. Bazin, B.A. Brown, C.M. Campbell, M.P. Carpenter, J.M. Cook, A.N. Deacon, D.-C. Dinca, S.J. Freeman, T. Glasmacher, P.G. Hansen, B.P. Kay, P.F. Mantica, W.F. Mueller, J.R. Terry, J.A. Tostevin, and S. Zhu. *Phys. Rev. C*, **81**:024301, 2010.
- [76] P.F. Mantica, R. Broda, H.L. Crawford, A. Damaske, B. Fornal, A.A. Hecht, C. Hoffman, M. Horoi, N. Hoteling, R.V.F. Janssens, J. Pereira, J.S. Pinter, J.B. Stoker, S.L. Tabor, T. Sumikama, W.B. Walters, X. Wang, and S. Zhu. *Phys. Rev. C*, **77**:014313, 2008.
- [77] M. Langevin, C. Détraz, D. Guillemaud-Mueller, A.C. Mueller, C. Thibault, F. Touchard, G. Klotz, C. Miehé, G. Walter, M. Epherre, and C. Richard-Serre. *Phys. Lett.*, **130B**:251, 1983.
- [78] L. Coraggio, A. Covello, A. Gargano, and N. Itaco. *Phys. Rev. C*, **80**:044311, 2009.

- [79] National Nuclear Data Center LOGFT web program. Available online at <http://www.nndc.bnl.gov/logft/>.
- [80] G. Audi, A.H. Wapstra, and C. Thibault. *Nucl. Phys.*, **A729:337**, 2003.
- [81] B. Fornal, S. Zhu, R.V.F. Janssens, M. Honma, R. Broda, P.F. Mantica, B.A. Brown, M.P. Carpenter, P.J. Daly, S.J. Freeman, Z.W. Grabowski, N.J. Hammond, F.G. Kondev, W. Królas, T. Lauritsen, S.N. Liddick, C.J. Lister, E.F. Moore, T. Otsuka, T. Pawlat, D. Seweryniak, B.E. Tomlin, and J. Wrzesiński. *Phys. Rev. C*, **70:064304**, 2004.
- [82] T. Dörfler, W.-D. Schmidt-Ott, T. Hild, T. Mehren, W. Böhmer, P. Möller, B. Pfeiffer, T. Rauscher, K.-L. Kratz, O. Sorlin, V. Borrel, S. Grévy, D. Guillemaud-Mueller, A.C. Mueller, F. Pougheon, R. Anne, M. Lewitowicz, A. Ostrowsky, M. Robinson, and M.G. Saint-Laurent. *Phys. Rev. C*, **54:2894**, 1996.
- [83] S. Zhu, R.V.F. Janssens, B. Fornal, S.J. Freeman, M. Honma, R. Broda, M.P. Carpenter, A.N. Deacon, B.P. Kay, F.G. Kondev, W. Królas, J. Kozemczak, A. Larabee, T. Lauritsen, S.N. Liddick, C.J. Lister, P.F. Mantica, T. Otsuka, T. Pawlat, A. Robinson, D. Seweryniak, J.F. Smith, D. Steppenbeck, B.E. Tomlin, J. Wrzesiński, and X. Wang. *Phys. Lett. B*, **650:135**, 2007.
- [84] H.L. Crawford, R.V.F. Janssens, P.F. Mantica, J.S. Berryman, R. Broda, M.P. Carpenter, N. Cieplicka, B. Fornal, G.F. Grinyer, N. Hoteling, B.P. Kay, T. Lauritsen, K. Minamisono, I. Stefanescu, J.B. Stoker, W.B. Walters, and S. Zhu. *To be published*.
- [85] R. Broda, W. Królas, B. Fornal, A. Gadea, N. Marginean, L. Corradi, A.M. Stefanini, J. Wrzesiński, T. Pawlat, S. Beghini, G. De Angelis, M. Carpenter, F. Della Vedova, E. Farnea, E. Fioretto, B. Guiot, R.V.F. Janssens, S. Lunardi, P. Mantica, P. Mason, G. Montagnoli, D.R. Napoli, R. Orlandi, I. Pokrovskiy, E. Sahin, F. Scarlassara, S. Szilner, C.A. Ur, M. Trotta, J.J. Valiente-Dobon, and S. Zhu. *Annual Report 2006 INFN-LNL-217*, ISSN 1828-8545 (Legnaro, 2007).
- [86] R. Broda, J. Wrzesiński, A. Gadea, N. Mărginean, B. Fornal, L. Corradi, A. Stefanini, W. Królas, T. Pawlat, B. Szpak, S. Lunardi, J.J. Valiente-Dobon, D. Mengoni, E. Farnea, S. Beghini, M.P. Carpenter, G. De Angelis, F. Della Vedova, E. Fioretto, B. Guiot, R.V.F. Janssens, P.F. Mantica, P. Mason, G. Montagnoli, D.R. Napoli, R. Orlandi, I. Pokrovskiy, E. Sahin, F. Scarlassara, S. Szilner, C.A. Ur, M. Trotta, and S. Zhu. *To be published*.
- [87] M. Lewitowicz, J.M. Daugas, R. Grzywacz, L. Achouri, J.C. Angélique, D. Baborodin, R. Bentida, R. Béraud, C. Bingham, C. Borcea, W. Catford, A. Em-sallem, G. de France, M. Glogowski, H. Grawe, D. Guillemaud-Mueller, M. Houry, S. Hurskanen, K.L. Jones, R.C. Lemmon, A.C. Mueller, A. Nowak, F. de Oliveira-Santos, A. Płochocki, M. Pfützner, P.H. Regan, K. Rykaczewski, M.G. Saint-Laurent, J.E. Sauvestre, M. Sawicka, M. Schaefer, G. Sletten, O. Sorlin,

- M. Stanoiu, J. Szerypo, W. Trinder, S. Viteritti, and J. Winfield. *Nucl. Phys.*, **A654:687c**, 1999.
- [88] J.M. Daugas. Ph.D. thesis, Caen University, 1999.
- [89] M.R. Bhat. *Nucl. Data Sheets*, **88:417**, 1999.
- [90] F. Ameil, M. Bernas, P. Armbruster, S. Czajkowski, Ph. Dessagne, H. Geissel, E. Hanelt, C. Kozhuharov, C. Miede, C. Donzaud, A. Grewe, A. Heinz, Z. Janas, M. de Jong, W. Schwab, and S. Steinhäuser. *Eur. Phys. J. A*, **1:275**, 1998.
- [91] E. Runte, K.-L. Gippert, W.-D. Schmidt-Ott, P. Tidemand-Petersson, L. Ziegeler, R. Kirchner, O. Klepper, P.O. Larsson, E. Roeckl, D. Schardt, N. Kafrell, P. Peuser, M. Bernas, Ph. Dessagne, M. Langevin, and K. Rykaczewski. *Nucl. Phys.*, **A441:237**, 1985.
- [92] J. Bron, H.W. Jongsma, and H. Verheul. *Phys. Rev. C*, **11:966**, 1975.
- [93] S. Bhattacharyya, M. Rejmund, A. Navin, E. Caurier, F. Nowacki, A. Poves, R. Chapman, D. O'Donnell, M. Gelin, A. Hodsdon, X. Liang, W. Mittig, G. Mukherjee, F. Rejmund, M. Rousseau, P. Roussel-Chomaz, K.-M. Spohr, and Ch. Theisen. *Phys. Rev. C*, **79:014313**, 2009.
- [94] B.A. Brown, private communication.
- [95] D.E. Alburger, E.K. Warburton, and B.A. Brown. *Phys. Rev. C*, **30:1005**, 1984.
- [96] U. Fister, R. Jahn, P. von Neumann-Cosel, P. Schenk, T.K. Trelle, D. Wenzel, and U. Wienands. *Nucl. Phys.*, **A569:421**, 1994.
- [97] F. Ajzenberg-Selove, R.E. Brown, E.R. Flynn, and J.W. Sunier. *Phys. Rev. C*, **32:756**, 1985.
- [98] A. Gade, R.V.F. Janssens, D. Bazin, B.A. Brown, C.M. Campbell, M.P. Carpenter, J.M. Cook, A.N. Deacon, D.-C. Dinca, S.J. Freeman, T. Glasmacher, B.P. Kay, P.F. Mantica, W.F. Mueller, J.R. Terry, and S. Zhu. *Phys. Rev. C*, **73:037309**, 2006.
- [99] B. Fornal, R.V.F. Janssens, R. Broda, N. Marginean, S. Beghini, L. Corradi, M.P. Carpenter, G. De Angelis, F. Della Vedova, E. Farnea, E. Fioretto, A. Gadea, B. Guiot, M. Honma, W. Królas, T. Lauritsen, S. Lunardi, P.F. Mantica, P. Mason, G. Montagnoli, D.R. Napoli, T. Otsuka, T. Pawlat, G. Pollarolo, F. Scarlassara, A.M. Stefanini, D. Seweryniak, S. Szilner, C.A. Ur, M. Trotta, J.J. Valiente-Dobón, J. Wrzesiński, and S. Zhu. *Phys. Rev. C*, **77:014304**, 2008.
- [100] S.P. Pandya. *Phys. Rev.*, **103:956**, 1956.
- [101] F. Nowacki and A. Poves. *Phys. Rev. C*, **79:014310**, 2009.
- [102] Y. Utsuno, T. Otsuka, B.A. Brown, M. Honma, and T. Mizusaki. *AIP Conf. Proc.*, **1120:81**, 2009.

- [103] Y. Utsuno, T. Otsuka, T. Mizusaki, and M. Honma. *Eur. Phys. J. Special Topics*, **150**:187, 2007.
- [104] S. Hinds and R. Middleton. *Nucl. Phys.*, **84**:651, 1966.
- [105] F. Touchard, P. Guimbal, S. Büttgenback, R. Klapisch, M. De Saint Simon, J.M. Serre, C. Thibault, H.T. Duong, P. Juncar, S. Liberman, J. Pinard, and J.L. Vialle. *Phys. Lett.*, **108B**:169, 1982.
- [106] T. Otsuka, T. Suzuki, M. Honma, Y. Utsuno, N. Tsunoda, K. Tsukiyama, and M. Hjorth-Jensen. *Phys. Rev. Lett.*, **104**:012501, 2010.
- [107] A. Gade, B.A. Brown, D. Bazin, C.M. Campbell, J.A. Church, D.C. Dinca, J. Enders, T. Glasmacher, M. Horoi, Z. Hu, K.W. Kemper, W.F. Mueller, T. Otsuka, L.A. Riley, B.T. Roeder, T. Suzuki, J.R. Terry, K.L. Yurkewicz, and H. Zwahlen. *Phys. Rev. C*, **74**:034322, 2006.
- [108] T. Ishii, M. Asai, A. Makishima, M. Matsuda, S. Ichikawa, T. Kohno, and M. Ogawa. *CNS-REP*, **64**:27, 2004.
- [109] L.G. Multhauf, K.G. Tirsell, S. Raman, and J.B. McGrory. *Phys. Lett.*, **57B**:44, 1975.
- [110] E.K. Warburton. *Phys. Rev. C*, **44**:1024, 1991.
- [111] O. Sorlin, D. Guillemaud-Mueller, R. Anne, L. Axelsson, D. Bazin, W. Böhmer, V. Borrel, Y. Jading, H. Keller, K.-L. Kratz, M. Lewitowica, S.M. Lukyanov, T. Mehren, A.C. Mueller, Yu.E. Penionzhkevich, F. Pougheon, M.G. Saint-Laurent, V.S. Salamatin, S. Shoedder, and A. Wöhr. *Nucl. Phys. A*, **583**:763, 1995.
- [112] S. Grévy, J.C. Angélique, P. Baumann, C. Borcea, A. Buta, G. Canchel, W.N. Catford, S. Courtin, J.M. Daugas, F. de Oliveira, P. Dessagne, Z. Dlouhy, A. Knipper, K.L. Kratz, F.R. Lecolley, J.L. Lecouey, G. Lehrsenneau, M. Lewitowicz, E. Liénard, S. Lukyanov, F. Maréchal, C. Miehé, J. Mrazek, F. Negoita, N.A. Orr, D. Pantelica, Y. Penionzhkevich, J. Péter, B. Pfeiffer, S. Pietri, E. Poirier, O. Sorlin, M. Stanoiu, I. Stefan, C. Stodel, and C. Timis. *Phys. Lett. B*, **594**:252, 2004.
- [113] B.A. Brown and B.H. Wildenthal. *Ann. Rev. Nucl. Part. Sci.*, **38**:29, 1988.
- [114] T.T.S. Kuo and G.E. Brown. *Nucl. Phys.*, **A114**:241, 1968.
- [115] S. Nummela, P. Baumann, E. Caurier, P. Dessagne, A. Jokinen, A. Knipper, G. Le Scornet, C. Miehé, F. Nowacki, M. Oinonen, Z. Radivojevic, M. Ramdhane, G. Walter, J. Äystö, and the ISOLDE Collaboration. *Phys. Rev. C*, **63**:044316, 2001.1
- [116] C.N. Davids, D.F. Geesaman, S.L. Tabor, M.J. Murphy, E.B. Norman, and R.C. Pardo. *Phys. Rev. C*, **17**:1815, 1978.

- [117] D.E. Appelbe, R.A.E. Austin, G.C. Ball, J.A. Cameron, B. Djerroud, T.E. Drake, S. Flibotte, C.D. O'Leary, A. Melarangi, C.E. Svensson, J.C. Waddington, and D. Ward. *Eur. Phys. J. A*, **8**:153, 2000.
- [118] N.G. Puttaswamy, W. Oelert, A. Djalois, C. Mayer-Böricke, P. Turek, P.W.M. Glaudemans, B.C. Metsch, K. Heyde, M. Waroquier, P. van Isaker, G. Wenes, V. Lopac, and V. Paar. *Nucl. Phys.*, **A401**:269, 1983.
- [119] M. Oinonen, U. Köster, J. Äystö, V. Fedoseyev, V. Mishin, J. Huikari, A. Jokinen, A. Nieminen, K. Peräjärvi, A. Knipper, G. Walter, and the ISOLDE Collaboration. *Eur. Phys. J. A*, **10**:123, 2001.
- [120] E. Caurier, Code ANTOINE, Strasbourg, 1989; E. Caurier and F. Nowacki. *Acta Phys. Pol.*, **30**:705, 1999.
- [121] S.N. Liddick, P.F. Mantica, B.A. Brown, M.P. Carpenter, A.D. Davies, M. Horoi, R.V.F. Janssens, A.C. Morton, W.F. Mueller, J. Pavan, H. Schatz, A. Stolz, S.L. Tabor, B.E. Tomlin, and M. Wiedeking. *Phys. Rev. C*, **73**:044322, 2006.
- [122] L. Gaudefroy. *Study of the  $N=28$  shell closure in the nucleus  ${}^{46}_{18}\text{Ar}_{28}$  with neutron transfer reaction: applications to astrophysics and  $\beta\gamma$  spectroscopy of neutron rich nuclei around  $N=32/34$  and  $N=40$*  Ph.D. thesis, De L'Universite Paris XI Orsay, 2005.
- [123] A. Estradé. *Time-of-flight mass measurements of neutron rich isotopes at the NSCL* Ph.D. thesis, Michigan State University, 2010.
- [124] B.A. Brown. *Prog. Part. Nucl. Physics*, **47**:517, 2001.
- [125] O.B. Tarasov, D.J. Morrissey, A.M. Amthor, T. Baumann, D. Bazin, A. Gade, T.N. Ginter, M. Hausmann, N. Inabe, T. Kubo, A. Nettleton, J. Pereira, M. Portillo, B.M. Sherrill, A. Stolz, and M. Thoennessen. *Phys. Rev. Lett.*, **102**:142501, 2009.
- [126] G. Neyens, M. Bissell, M De Rydt, P. Lievens, C. Geppert, J. Kraemer, A. Krieger, and R. Neugart. *Ground-state properties of  $K$ -isotopes from laser and  $\beta$ -NMR spectroscopy*. Available online at <http://greybook.cern.ch/programmes/experiments/IS484.html>.
- [127] K. Starosta, C. Vaman, D. Miller, P. Voss, D. Bazin, T. Glasmacher, H. Crawford, P. Mantica, H. Tan, W. Hennig, M. Walby, A. Fallu-Labruyere, J. Harris, D. Breus, P. Grudberg, and W.K. Warburton. *Nucl. Instrum. Methods Phys. Res. A*, **610**:700, 2009.
- [128] R. Grzywacz. *Nucl. Instrum. Methods Phys. Res. B*, **204**:649, 2003.

MICHIGAN STATE UNIVERSITY LIBRARIES



3 1293 03063 6926